

Detailed Investigation of Negative Sequence Current Compensation Technique for Stator Shorted Turn Fault Detection of Induction Motors

by

Syaiful Bakhri

Thesis submitted for the degree of

Doctor of Philosophy

School of Electrical and Electronic Engineering
Faculty of Engineering, Computer and Mathematical Science

The University of Adelaide
Australia

March 2013



Contents

Contents	ii
Abstract.....	vi
Declaration.....	vii
Acknowledgement	viii
List of Figures	ix
List of Tables	xvii
List of Abbreviations and Symbols	
List of Abbreviations	xviii
List of Symbols.....	xix
Chapter 1.....	
Overview of Condition Monitoring of Induction Motors.....	1
1.1 Overview.....	1
1.2 Research Gaps	5
1.3 Objective of the Thesis	6
1.4 Contributions of the Thesis.....	7
1.5 Outline of the Thesis.....	8
Chapter 2.....	
Background Theory and Literature Review of Negative Sequence Shorted Turn Fault Monitoring	10
2.1 Introduction.....	10
2.2 Condition Monitoring of Stator Shorted Turn Faults	11
2.3 Theory of Negative Sequence Components	14
2.3.1 Overview of Phasor Theory	14
2.3.2 The Sequence Components Calculation	17
2.3.3 Power Decomposition Techniques (PDT) sequence components calculation	21
2.4 Literature Review of Negative Sequence Monitoring	25

2.4.1 The Initial Utilization of Negative Sequence Current Monitoring	26
2.4.2 Admittance Calculation	30
2.4.3 Impedance Calculation and Look up Table	31
2.4.4 Semi-empirical Formula Methods	31
2.4.5 Neural Network Approaches.....	33
2.4.6 Sequence Impedances Monitoring.....	36
2.4.7 Sequence Impedances Matrix Monitoring.....	37
2.5 Conclusion	39
Chapter 3
Induction Motor Models and Determination of Motor Parameters	41
3.1 Introduction.....	41
3.2 Induction Motor Model.....	41
3.2.1 Modeling of Induction Motors.....	41
3.2.2 The Asymmetrical MCC model.....	48
3.3 Machine Parameters, Motor Simulations and Experimental Results	58
3.3.1 Machine characteristic and parameters	58
3.3.2 Comparison of Simulation and Experimental Results	67
3.4 Conclusion	71
Chapter 4	72
Investigation of Measurement Error of Negative Sequence Components.....	72
4.1 Introduction.....	72
4.2 Measurement Issues in Condition Monitoring	72
4.2.1 The Characteristic of the System Components.....	73
4.2.2 System Calibrations	75
4.3 Measurement Issues in Negative Sequence Monitoring.....	79
4.3.1 The negative sequence analysis including the phase angle corrections.....	79
4.3.2 The effect of temperature on the measurement.....	82
4.4 On-line Calibration	85
4.5 Conclusion	93
Chapter 5	95
Investigation of Stator Shorted Turn Fault.....	95
5.1 Introduction.....	95

5.2 Shorted Turn Simulation.....	95
5.3 The Shorted Turn Experiments.....	103
5.4 The Detailed Analysis of the Disturbances of Shorted Turn Faults	109
5.4.1 The Inherent Asymmetry	109
5.4.2 The Voltage Unbalance.....	111
5.4.3 The Effect of Load Variations	117
5.5 The Effect of Other Faults on the Negative Sequence Current Monitoring	126
5.5.1 Eccentricity Faults	126
5.5.2 Broken Rotor Bar Faults	129
5.6 Conclusion	132
Chapter 6	134
Negative Sequence Compensation technique for Stator Shorted Turn Faults ..	134
6.1 Introduction.....	134
6.2 The Comparison of Negative Sequence Current Compensation Techniques..	134
6.3 The New Compensation Methods for Negative Sequence Current Estimation	
139	
6.3.1 Compensation of Voltage Unbalance and Inherent Asymmetry	140
6.3.2 Compensation of Voltage Unbalance and Inherent Asymmetry under	
Different Motor Loading.....	143
6.4 Conclusion	150
Chapter 7	152
General Conclusions and Recommendations	152
7.1 Conclusions.....	152
7.2 Recommendations.....	156
References.....	157
Appendix.....	163
A.1 Steady State Induction Motor Model.....	163
A.1.1 DC Test	165
A.1.2 Block Rotor Test	165
A.1.3 No Load Test.....	166
A.2 Dynamic Motor Model's Parameters.....	168
A.2.1 The Motor Model Inductances	168

A.2.2 The Inductances of the Stator Fault Model.....	170
A.2.3 Resistance of The Rotor Asymmetry Model.....	170
List of Publications	172

Abstract

Online condition monitoring is preferred specifically in critical induction machines for timely analysis of their health and to predict any incipient failures. Negative sequence current monitoring is one of the well-known condition monitoring applications that capable of identifying stator faults in induction motor as well as producing fast and reliable results using a simple measurement technique. However, the technique is sensitive to asymmetrical sources of negative sequence, not only due to motor faults but also due to the disturbances such as sensor calibration, inherent non-idealities (such as inherent machine asymmetries), external effects (such as load change and supply voltage unbalances).

This thesis addresses the limitations in shorted turn fault detection while considering real system disturbances and non-linearities using a dynamic motor model which is also verified by the experimental studies. The thesis provides a comprehensive investigation of various negative sequence contributors such as measurement asymmetry, inherent asymmetry, voltage unbalance, shorted turn faults, eccentricity and broken rotor bar faults under load variations, and presents practical results. To allow accurate shorted turn fault detection, this thesis also provides an effective phasor compensation technique for these disturbances. A new detailed compensation by demonstrating step-by-step disturbance extraction to obtain the real negative sequence current due to shorted turn faults are also presented. It is demonstrated that this technique allows even a single stator shorted turn faults to be detected as well as successfully eliminating the effect of inherent asymmetry and voltage unbalances under motor load variations.

Declaration

I certify that this work contains no material which has been accepted for the award of any other degree or diploma in my name, in any university or other tertiary institution and, to the best of my knowledge and belief, contains no material previously published or written by any other person, except where due reference has been made in the text. In addition, I certify that no part of this work will, in the future, be used in a submission in my name, for any other degree or diploma in any university or other tertiary institution without the prior approval of the University of Adelaide and where applicable, any partner institution responsible for the joint-award of this degree.

I give consent to this copy of my thesis, when deposited in the University Library, being made available for loan and photocopying, subject to the provisions of the Copyright Act 1968.

I also give permission for the digital version of my thesis to made available on the web, via the University's digital research repository, the Library Search and also through web search engines, unless permission has been granted by the University to restrict access for a period of time

Signed : _____ Date : 12-07-2013

Acknowledgement

Firstly, I wish to express sincere gratitude to my principal supervisor Associate Professor Dr. Nesimi Ertugrul for his guidance, inspiration, motivation, support and knowledge during my research. He encourages my study since the beginning, from the PhD application processes until end of my study. He also gives essential support to obtain scholarship for my PhD.

I would like to thank to Associate Professor Dr. Wen L. Soong for the inspiration, guidance, discussion and suggestion that have enriched this project. He also provide valuable support for me to deal with my family related problem.

I also wish to thank Prof Muslum Arkan for the discussion and motor model development.

I am thankful Dr. Said Al Sarawi and Dr. Brian Ng for the inspiration during my research.

I would like also to thank all the technical staff for their help and assistance during my research in power laboratory.

I would like to thank and acknowledge Ms Ann Nobel for the editorial assistance during my thesis writing.

I am grateful to every member of the School of Electrical and Electronic Engineering, and staff of University of Adelaide Graduate Centre, who has helped me during my stay here.

Thanks to my family, my beloved wife, and my children, for their love, support, patience, encouragement, and understanding during my studies. Thanks also to my relatives in Indonesia for supporting me throughout my study.

Syaiful Bakhri

March 2013

List of Figures

Figure 1.1 Distribution of common faults of electric motors according to (a) EPRI survey results (b) IEEE-IAS survey results and (c) survey result in a petrochemical industry.	1
Figure 1.2 The summary of previous studies and the research opportunities for negative sequence components.	4
Figure 2.1 Various stator faults (a) turn-to-turn , (b) shorted coils, (c) phase-to-phase, (d) grounded at edge of faults, (e) grounded at slots, and (f) total phase damage [20].	13
Figure 2.2 Phasor definition under pure sinusoidal current waveform.....	15
Figure 2.3 Graphical analysis of the DFT algorithm to obtain phasors.....	16
Figure 2.4 Graphical waveform illustrations of the sequence component methods.	18
Figure 2.5 Graphical illustrations of the sequence operator h	19
Figure 2.6 Graphical analysis of the positive, negative and zero sequence system of phasors.	20
Figure 2.7 Graphical illustrations of the PDT methods.	23
Figure 2.8 Various causes of negative sequence current.	27
Figure 2.9 Compensation techniques based on phasor calculations. The negative sequence current due to stator faults is extracted from observed negative sequence current, negative sequence caused by voltage unbalance, and negative sequence due to inherent asymmetry.....	28
Figure 2.10 Predicted (circle and cross) and measured supply (line) of positive sequence, negative sequence and short circuit current for (a) one coil short-circuited and (b) a phase-to-phase short circuit [22].	29
Figure 2.11 (a) Neural network based negative sequence-based fault detection, and (b) the feed forward neural network [26].	34
Figure 2.12 Flowchart of (a) COT for training and monitoring mode and (b) training algorithm of QGMT [28].	35
Figure 2.13 Several factors that influence the sequence impedance matrix.	38

Figure 3.1 Induction motor model (a) T Equivalent Circuit, (b) Multiple Coupled Circuit (MCC), (c) Magnetic Equivalent Circuit (MEC) method, and (d) Finite Element Method (FEM).....	42
Figure 3.2 Winding arrangement of two-pole, 3-phase, wye-connected symmetrical induction machine [64].	48
Figure 3.3 Stator basic voltage equations.	49
Figure 3.4 Rotor basic voltage equations.....	50
Figure 3.5 The complete induction motor simulation block model.....	57
Figure 3.6 Induction motor single phase full equivalent circuit.....	59
Figure 3.7 Photograph of the experimental setup with the motor under test and dynamometer.....	59
Figure 3.8 The measured and calculated motor quantities of the test motor.	61
Figure 3.9 Block rotor voltage estimation considering the saturation in the closed rotor slot.....	62
Figure 3.10 Test results of the unbalance operation in (a) block rotor voltage, (b) block rotor current, (c) no load voltage and (d) no load current.....	64
Figure 3.11 As a function of slip, simulated and experimental results of (a) stator current, (b) power input, (c) power factor, (d) power output, (e) motor efficiency, and (f) motor torque.	66
Figure 3.12 (a) The simulated three-phase stator current during start up of the healthy ideal motor, and (b) three-phase stator currents showing comparison of the simulated (line) and experimental (dashed line) results.....	68
Figure 3.13 (a) The positive and negative sequence current as a function of time of the healthy motor, and (b) the zoom of the negative sequence current.	69
Figure 3.14 (a) Comparison of positive sequence stator current of T-model and positive current of dynamic model as a function of speed showing the experimental confirmation results (circle), (b) the comparison of developed torque of steady state T-model and Asymmetrical MCC Model vs rotor speed at normal rotor inertia.	70
Figure 4.1 An example of (a) Current Sensor and (b) Voltage Sensor.....	73
Figure 4.2 A complete hardware structure of a condition monitoring system.	73
Figure 4.3 Measurement setup for voltage and current calibration.	75
Figure 4.4 System calibration of (a) voltage channels, and (b) current channels.	76

Figure 4.5 Response analysis of the actual signals and the calibrated signals: (a) voltage measurements, (b) current measurements, (c) the magnitude error in voltage measurements, (d) the magnitude error in current measurements, (e) relative angle error of voltage measurements, and (f) the relative angle error in current measurements.	78
Figure 4.6 Angle displacement for the sequence component analysis of the measurement system.	79
Figure 4.7 Magnitudes of the negative sequence components due to the measurement system asymmetry, (a) current, (b) voltage, and (c) their angle. Note that for the angle analysis, the reference angle V_p is 90^0	80
Figure 4.8 The test setup for the hot and cold measurement.	82
Figure 4.9 The effects of the hot and cold operation on (a) stator current positive sequence components I_p and V_p , (b) magnitude of stator current negative sequence I_n , (c) magnitude of voltage negative sequence V_n , (d) the angle of I_n and I_p (e) the angle of V_n and V_p where the reference angle V_p is 90^0	84
Figure 4.10 On-line calibration system.....	86
Figure 4.11 Step by step on-line calibration showing (a) the measured stator current phasor including (b) the three-phase waveform; (c) the phasor diagram after calibrations including (d) the waveform; (e) the resultant current ($i_a+i_b+i_c$) before and after zero sequence eliminations; (f) the measured i_q and i_d compare with the reference value.	87
Figure 4.12 The phasor representation of differential gain compensation showing (a) general case of current components, (b) sequence components with differential gain current using three current sensors (c) sequence components using two current sensors [72]......	89
Figure 4.13 Online differential gain estimation system [72].	90
Figure 4.14 Experimental test of online calibration showing (a) the estimated gain of the symmetrical measurement gains, (b) the response of estimated gain calculation when different measurement gains are introduced, and (c) the ratio of actual gain and estimated gain.....	92
Figure 5.1 Shorted turn configurations in dq axis frame.	96

Figure 5.2 A sample simulation results under 5 shorted turn fault and with 0.5 Ω external resistance and under full load: (a) the positive sequence current, (b) the negative sequence current, (c) the short circuit current (d) the electromagnetic torque and (e) the rotor speed.	100
Figure 5.3 Short circuit simulation study under various values of external resistance	101
Figure 5.4 Negative sequence current of shorted turn simulation under various external resistances	102
Figure 5.5 The test setup showing (a) an adjustable shorted turn terminal block of the motor under test and (b) the external shorted circuit cable with a current clamp.....	104
Figure 5.6 The illustration of the stator windings of the test motor with shorted turns.	104
Figure 5.7 The fault current in the shorted turns versus the fraction of shorted turns under main supply voltage variation: experimental (circles) and simulated (solid lines).....	105
Figure 5.8 The experimental results under healthy and faulty operation under no load but at various fault levels (a) 1.7%, (b) 3.1%, (c) 5.3%, and (d) 7.1% shorted winding turn faults.	107
Figure 5.9 (a) The magnitude and (b) the phasors of the negative sequence and the positive sequence currents showing the experimental results (triangle) and the simulation results (line) as a function of the shorted winding turns.	107
Figure 5.10 Negative sequence current under voltage variation showing (a) the magnitude of inherent asymmetry and (b) the phasor diagram; the voltage unbalances which are indicated by (c) negative sequence voltage and (d) the phasor trajectory.....	110
Figure 5.11 The experimental results for different level of voltage unbalances factors including the healthy state.....	112
Figure 5.12 Comparison of positive and negative sequence magnitude currents of voltage unbalance and inherent asymmetry; showing the simulation (line) and the experimental results (circle), (a) magnitude variations and (b) phasor representation.	112

Figure 5.13 The inherent asymmetry graphical calculation using interpolations displaying the negative sequence voltage (left) and the negative sequence current (right).	114
Figure 5.14 Comparison of positive and negative sequence magnitude currents with and without inherent asymmetry (a) and the phasor representation (b) including the calculated inherent asymmetry (symbol \square).	115
Figure 5.15 Three-phase phasor representation of negative sequence current under voltage unbalance (a) before inherent asymmetry calculation, (b) without inherent symmetrical components, and (c) with 120^0 shift of phase <i>a</i> and <i>b</i> , showing the simulation results (line) and experimental results (circle, triangle and square for the three-phases).	116
Figure 5.16 The effect of load variations in a healthy motor: simulations (solid lines) and test results (circle and cross).	118
Figure 5.17 The effect of load variations on the negative sequence current under voltage unbalance using varying external resistors $r_{ext}=0.25\Omega$ (triangle), $r_{ext}=0.5\Omega$ (diamond), $r_{ext}=1\Omega$ (square), $r_{ext}=2\Omega$ (circle) and $r_{ext}=4\Omega$ (star).	119
Figure 5.18 The voltage unbalance analysis using external resistors, $r_{ext}=0.25\Omega$ (triangle), $r_{ext}=0.5\Omega$ (diamond), $r_{ext}=1\Omega$ (square), $r_{ext}=2\Omega$ (circle) and $r_{ext}=4\Omega$ (star) under load variations showing (a) the observed voltage unbalance factor (VUF), and (b) magnitude of the negative sequence impedance.	120
Figure 5.19 The effect of load variations and voltage unbalances after the inherent asymmetry eliminations: (a) the magnitude (b) phasor and (c) the relative magnitude of the stator currents between the phases I_a-I_b and I_b-I_c	122
Figure 5.20 The effect of load variations on the negative sequence under various level of shorted turn faults: (a) the magnitude of I_n , (b) phasor diagram of I_n under the shorted turn faults of 0% (triangle), 1.7% (diamond), 3.5% (square), 5.3% (circle) and 7.1% (star).	123
Figure 5.21 The analysis of load variations under various level of shorted turn faults of: 0% (triangle), 1.7% (diamond), 3.5% (square), 5.3% (circle) and 7.1% (star), (a) the corresponding voltage unbalance factors and (b) the negative sequence impedances.	124

Figure 5.22 Types of eccentricities in rotating machines.	126
Figure 5.23 The section view of induction motor including the arrangement for static Eccentricity experiments.....	127
Figure 5.24 The experimental results of the static eccentricity faults with the severity level of +0.1 mm, +0.05 mm, -0.05 mm, and -0.1 mm, showing (a) the magnitude of the current and (b) the plot of trajectory and (c) the negative sequence impedance as a function of load.....	128
Figure 5.25 The section of the motor used during the test indicating the slot type...	130
Figure 5.26 The experimental results of the broken rotor bar faults (1,2 and 4 broken bars) showing (a) the magnitude and (b) the trajectory of the negative sequence current as a function of load.....	131
Figure 6.1 The experimental results of the shorted turn faults under voltage unbalances and inherent asymmetry.	135
Figure 6.2 Shorted turn negative sequence current using the least square admittance, voltage unbalance and inherent asymmetry compensation.....	136
Figure 6.3 Shorted turn negative sequence currents after voltage unbalance compensation based on negative sequence impedance, showing (a) magnitude, (b) phasor trajectory.....	137
Figure 6.4 Shorted turn negative sequence current after the voltage unbalance and the load compensation based on the empirical formulas.	139
Figure 6.5 The measured negative sequence currents under voltage unbalance variations showing (a) the magnitude and (b) the phasor plot.....	140
Figure 6.6 The negative sequence current after voltage unbalance elimination: (a) the magnitude and (b) phasor diagram.....	142
Figure 6.7 The negative sequence after inherent asymmetry elimination showing (a) the magnitude and (b) the phasor diagram.....	143
Figure 6.8 The negative sequence current of 1.7% shorted turn faults under load variation and voltage unbalance employing external resistors, $r_{ext}=0\Omega$ (triangle), $r_{ext}=1\Omega$ (diamond), $r_{ext}=2\Omega$ (square), $r_{ext}=4\Omega$ (circle), showing (a) the magnitude and (b) the phasor trajectory.....	144
Figure 6.9 The negative sequence current of 3.5% shorted turn faults under load variation and voltage unbalance employing external resistors, $r_{ext}=0\Omega$	

(triangle), $r_{ext}=1\Omega$ (diamond), $r_{ext}=2\Omega$ (square), $r_{ext}=4\Omega$ (circle), showing (a) the magnitude and (b) the phasor trajectory.	144
Figure 6.10 The negative sequence current of 5.3% shorted turn faults under load variation and voltage unbalance employing external resistors, $r_{ext}=0\Omega$ (triangle), $r_{ext}=1\Omega$ (diamond), $r_{ext}=2\Omega$ (square), $r_{ext}=4\Omega$ (circle), showing (a) the magnitude and (b) the phasor trajectory.	145
Figure 6.11 The negative sequence current under 1.7% shorted turn faults after the elimination of the load-voltage unbalance using $r_{ext}=0\Omega$ (triangle), $r_{ext}=1\Omega$ (diamond), $r_{ext}=2\Omega$ (square), $r_{ext}=4\Omega$ (circle), showing (a) the magnitude and (b) phasor trajectory.	146
Figure 6.12 The negative sequence current under 3.5% shorted turn faults after the elimination of the load-voltage unbalance using $r_{ext}=0\Omega$ (triangle), $r_{ext}=1\Omega$ (diamond), $r_{ext}=2\Omega$ (square), $r_{ext}=4\Omega$ (circle), showing (a) the magnitude and (b) phasor trajectory.	147
Figure 6.13 The negative sequence current under 5.3% shorted turn faults after the elimination of the load-voltage unbalance using $r_{ext}=0\Omega$ (triangle), $r_{ext}=1\Omega$ (diamond), $r_{ext}=2\Omega$ (square), $r_{ext}=4\Omega$ (circle), showing (a) the magnitude and (b) phasor trajectory.	147
Figure 6.14 The negative sequence current of 1.7% shorted turn fault after the voltage unbalance and the inherent asymmetry elimination, using $r_{ext}=0\Omega$ (triangle), $r_{ext}=1\Omega$ (diamond), $r_{ext}=2\Omega$ (square), $r_{ext}=4\Omega$ (circle), showing (a) the magnitude and (b) the phasor trajectory.....	148
Figure 6.15 The negative sequence current of 3.5% shorted turn faults after the voltage unbalance elimination using $r_{ext}=0\Omega$ (triangle), $r_{ext}=1\Omega$ (diamond), $r_{ext}=2\Omega$ (square), $r_{ext}=4\Omega$ (circle), showing (a) the magnitude and (b) the phasor trajectory	149
Figure 6.16 The negative sequence current of 5.3% shorted turn fault after voltage unbalance eliminations using $r_{ext}=0\Omega$ (triangle), $r_{ext}=1\Omega$ (diamond), $r_{ext}=2\Omega$ (square), $r_{ext}=4\Omega$ (circle), showing (a) the magnitude and (b) the phasor trajectories	149
Figure A.1 Induction motor full equivalent circuit.....	163
Figure A.2 Induction motor full equivalent circuit referred to stator frequency	164
Figure A.3 The DC motor test set up.....	165

Figure A.4 Block rotor test equivalent circuit	165
Figure A.5 No load test equivalent circuit.....	166

List of Tables

Table 2.1 Negative Sequence Research.....	25
Table 3.1 Modeling Studies of Induction Motors.....	45
Table 3.2 Comparison of induction motor models	47
Table 3.3 Name plate of the motor test for Y connections.	60
Table 3.4 Calculated parameters.....	65
Table 4.1 Sensor parameters	74
Table 4.2 Voltage and Current Channels Calibration.....	76
Table 5.1 The resistance of shorted turn for 5 turns	105

List of Abbreviations and Symbols

List of Abbreviations

AI	Artificial Intelligence
BF	Butterworth filter
COT	Continual On-line training
CUR	Current Unbalance Ratio
DAQ	Data Acquisition System
DC	Direct Current
DFT	Discrete Fourier Transform
DMRM	Dynamic Mesh Reluctance Modelling
FEM	Finite Element Method
FFT	Fast Fourier Transform
HP	High-pass filter
I	Integral
LF	Low-pass filter
MCCM	Multiple Couple Circuit Model
MEC	Magnetic Equivalent Circuit
MWFA	Modified Winding Function Approach
NEMA	National Electrical Manufacturers Association
PDT	Power Spectral Decomposition Technique
PI	Proportional-Integral
RSH	Rotor Slot Harmonics
PVUR	Phase Voltage Unbalance Ratio
QGMT	Quasi-Global Minimum Training
RMS	Root Mean Square
SOFM	Self Organizing Feature Map
VUF	Voltage Unbalance Factor
WFA	Winding Function Approach

List of Symbols

$0, p, n$	Subscript symbols for zero, positive, and negative sequence components
a, b, c	Subscript symbols for the quantities in abc three-phase system
α and β	Subscript symbols for the quantities in reference frame
av	Subscript symbol for average values
δ	delay angle
g	Subscript symbol for the air gap of motor
h	Operator for symmetrical components ($e^{j\frac{2\pi}{3}}$)
ia	Subscript symbols for inherent asymmetry
in	Subscript symbols for measurement asymmetry
i and v	Instantaneous current and voltage
i, v	Superfix symbols for current and voltage related
I, V, Z, Y	Magnitude values for current, voltage, impedance and admittance
I, V, Z, Y	Phasor values for current, voltage, impedance and admittance
I_m	Peak amplitude of the current signal
L, X	Magnitude value for inductance and reactance
m, s, l, v	Subscript symbols denoting motor, supply, load and voltage related p
p	Operator for d/dt
N or $N_r N_s$	Number of stator and rotor winding turns
ϕ	Phase angle
p, q	Instantaneous active and reactive powers
P, Q	Fundamental active and reactive powers
q, d	Subscript symbols for the vector quantities in $q-d$ reference frame
ref	Subscript symbol for reference quantities
sf	Subscript symbol for shorted turn fault
sh	Subscript symbol for shorted turn
s, r	Subscripts symbols for the quantities of stator and rotor
T_s	Supply period quantities
T	3 to 2 transformation matrix
T	Symbol for torque quantities
μ_0	Permeability of free space

ψ and λ	Flux linkages
ω_s ω_r	Angular synchronous and rotor speed
x, y	Real and imaginary part of phasor (or complex number)
f	Supply frequency
f	Rotation frequency

Chapter 1

Overview of Condition Monitoring of Induction Motors

1.1 Overview

The induction motor is one of the most popular electric machines, and is widely employed in various industries. The induction motor population is around 85% of the total electric machine population. Industries have utilized them for various applications because of their high reliability, low maintenance, low-cost and simple operation.

Although the induction motor's construction has been refined continuously since its first development, motor faults cannot be avoided. This is because induction motors are subject to environmental hazards and to excessive mechanical or electrical stress during operation. Imperfect manufacture, poor installation, or mechanical defects may initiate various motor faults. These may affect all primary components of the induction motor such as rotor, stator and bearings.

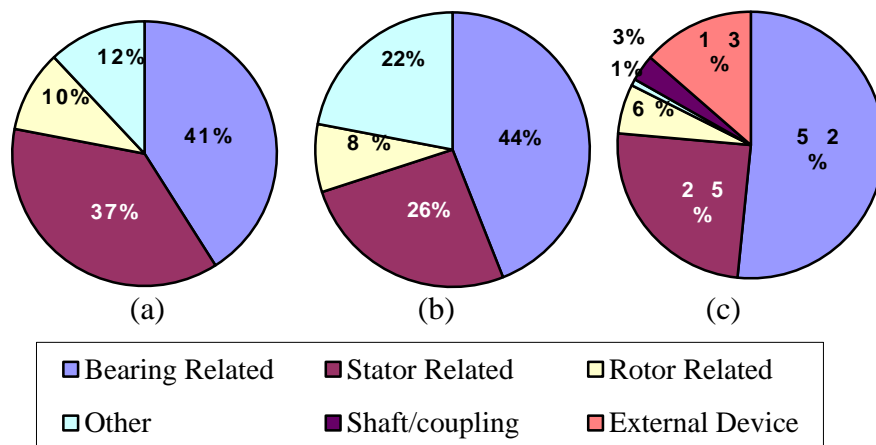


Figure 1.1 Distribution of common faults of electric motors according to (a) EPRI survey results (b) IEEE-IAS survey results and (c) survey result in a petrochemical industry.

Several literature reviews have detailed the common faults of induction motors which are summarized in Figure 1.1 [1-3]. These faults can be categorized into five common problems such as bearing related faults, stator related faults, rotor faults, eccentricity related faults, and mechanical faults (soft foot, misalignment, and mechanical unbalance). Among these faults, 41% of the total motor failures are bearing-related faults, followed by stator-related faults, about 37% [1]. The stator-related fault is the biggest contributor in term of electrical-related faults. In stator-related faults, if a small fault in a motor is not detected in a timely manner, complete motor failure may occur more quickly than with other faults. Therefore, an appropriate maintenance strategy, such as condition monitoring, needs to be employed to identify stator related faults as early as possible. The importance of the stator maintenance strategy also leads this research to focus on condition monitoring of stator faults.

A condition monitoring technique is effectively a maintenance strategy which provides information about potential faults or unidentified failures, to keep the induction motor in operation for longer time periods. Unlike other maintenance strategies, condition monitoring can be carried out without time restrictions and aims to anticipate any catastrophic failure. Basically, two condition monitoring strategies can be implemented. The first strategy can be applied while the motor is running, and is known as the on-line technique. The second strategy can be applied after stopping the motor, and is known as the off-line condition monitoring technique.

On-line diagnostic methods are preferred mainly in critical machines to predict any incipient failures. Various on-line diagnostic methods have been proposed in the literature, including signature analysis of the stator current, vibration monitoring, flux leakage monitoring, and negative sequence components of voltage and current [4, 5]. In addition to these methods, sequence components are also applied as an online method.

Sequence component monitoring is based on the identification of asymmetrical behavior in a machine [6]. In this method, any unidentified unbalanced three-phase voltage or current phasors are transformed to a set of three simple independent balanced component phasors: positive sequence, negative sequence, and zero sequence phasors. The positive sequence component always exists in such machines because of the supply voltage. However, negative sequence component will only exist under asymmetrical voltage supply or under motor faults. The negative sequence

component can be utilized to monitor the health as well as the supply voltage unbalances in induction machines.

In addition, it can be reported here that sequence monitoring can offer fast and reliable monitoring compared with other methods, since it is non-invasive, simple, and requires less computation. The negative sequence monitoring does not require advanced signal processing which in turn may also not require advanced condition monitoring devices. The method is also highly responsive and reliable to detect asymmetrical machine faults such as shorted turns and eccentricity. Furthermore, unlike other monitoring techniques, sequence component monitoring provides opportunities to increase the accuracy of the results through non-idealities and non-linearity compensation techniques [7].

Despite the advantages however, the sequence components monitoring technique presents various challenges for research in this field. For example, the measured negative sequence may contain inherent non-idealities (such as asymmetries in real machines) and is sensitive to external effects (such as load changes and supply variations). As stated previously, the negative sequence current component can be produced by unbalanced supply voltages which is very likely in practical applications, or by saturation in the machine, or by inherent winding asymmetry, or due to eccentricity [8]. Furthermore, the negative sequence current in the machine is also affected in a non-linear fashion by the loads, or by balanced supply voltage variations or by temperature variations. In other words, to identify the real faults of the induction motor, the negative sequence component analysis needs to be conducted carefully. In order to eliminate the above secondary fault effects, various compensation methods for voltage unbalance and other inherent non-idealities using look-up table databases, empirical formulas, or neural networks have been proposed in the literature. These studies are summarized below in Figure 1.2.

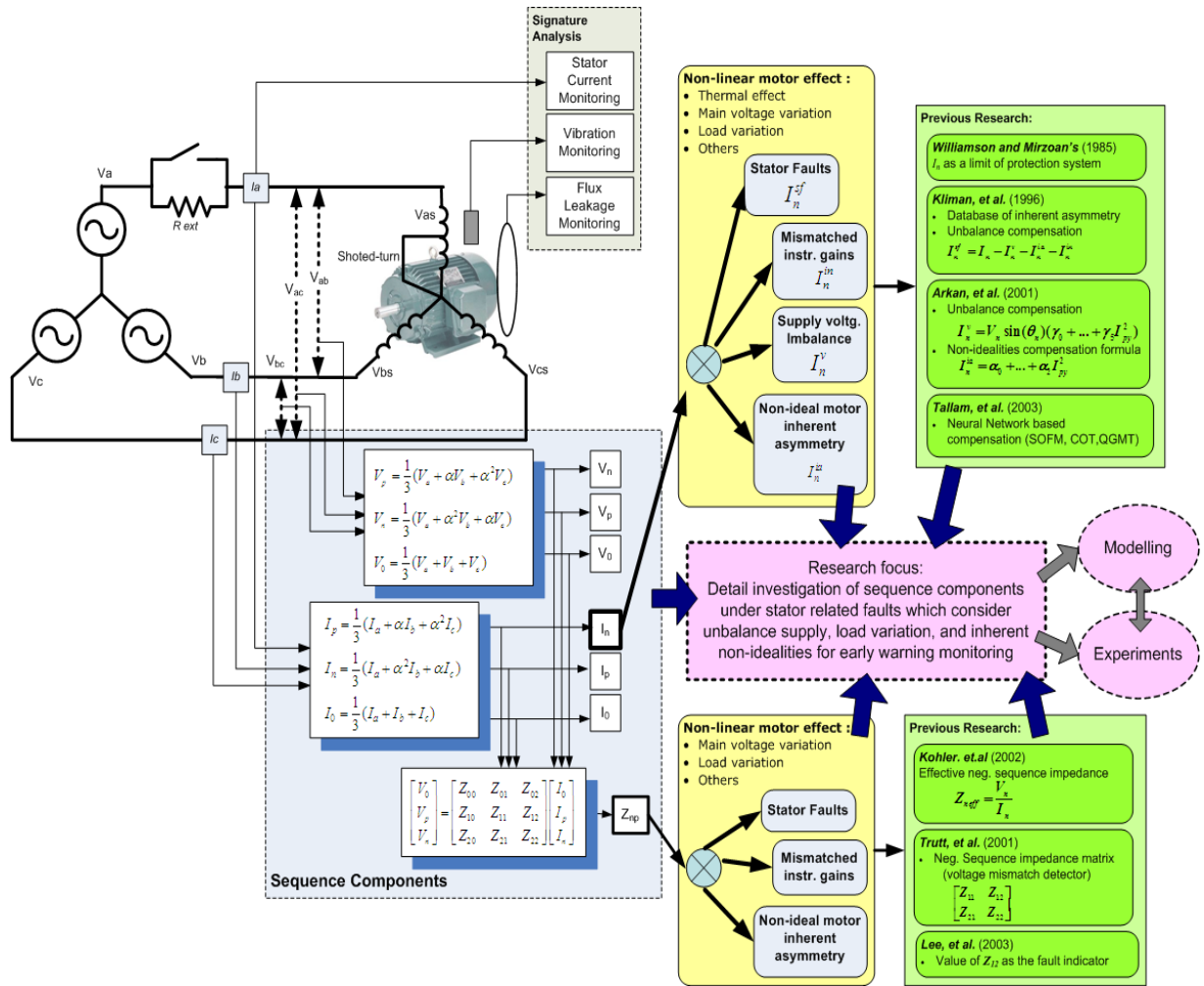


Figure 1.2 The summary of previous studies and the research opportunities for negative sequence components.

As it seen in Figure 1.2, a shorted turn in one phase of the motor and the basic measurement system utilizing the symmetrical components information are captured by using the three line current and three line voltage transducers. As also illustrated in the figure, negative sequence current, positive sequence, and zero sequence current can be extracted from the three current measurements. As summarized in the figure, the voltage and current transformations can be carried out using the symmetrical component analysis method, which converts a set of asymmetrical phasors into three symmetrical sets.

It can be noted here that there is a research potential to utilize various components of the sequence analysis in condition monitoring such as the negative sequence, the zero sequence, the negative sequence impedance analysis, or the full impedance matrix. The negative sequence compensation method can also be developed to obtain the true sequence components of induction motor faults. It can be

reported here that the true negative sequence is unaffected by disturbances or non-idealities in the machine such as voltage unbalance and other inherent non-idealities. The summary figure also illustrates the disturbance compensation of sequence components technique using look-up databases, empirical formula or neural networks.

The previous research summarized in Figure 1.2 highlight several important research directions in negative sequence analysis. One of the major shortcomings is that there is no detailed investigation of the negative sequence technique in shorted turn faults, while taking into account voltage unbalance, load variation and inherent asymmetry.

1.2 Research Gaps

Previous studies on negative sequence methods mainly had a narrow approach, which simply addressed a specific method under ideal measurement and test conditions. In addition, there was a lack of detailed studies covering the multiple faults and loading effects. There is a need to perform further investigation of inherent asymmetry elimination, which was not clearly demonstrated in the phasor domain under load variations. In addition, negative sequence components due to inherent asymmetry have not been excluded from the measured negative sequence signal and analyzed in detail. Note that this inherent asymmetry due to negative sequence can be employed as a baseline value to improve the accuracy of further negative sequence analysis.

Therefore, it can be noted here that a step by step investigation of voltage unbalance disturbances is also needed for accuracy of the method. Unlike in [8], the detailed investigation of voltage unbalance in the phasor domain can be done by considering variation of voltage unbalance as well as its characteristics under load variations. It is expected that this can result in better understanding of magnitude and angle interaction between the fault components and the disturbances. Such comprehensive investigation can show the effect of the phase angle of voltage unbalance, inherent asymmetry or shorted turn faults, which was simplified by the previous research using compensation formulas.

It is envisaged that the effects of disturbances on shorted turn fault detection needs special attention due to the critical nature of the faults. Furthermore, there is a

need to investigate the effect of single disturbances, as well as the combination of multiple disturbances to stator fault detection under phasor analysis. In order to gain a comprehensive analysis, it is also necessary to compare various compensation techniques, as this strategy can lead to a simple and practical compensation of these disturbances. A step by step compensation method can be adopted to show the intermediate results as each may have varying degrees of effect on the results.

It is envisaged that it is also needed to utilize a motor model to strength the fault analysis. However, the motor model, unlike in [9], has to be employed to provide experimental confirmations or analytical explanations of the motor behavior under both healthy and faulty conditions. The detailed induction motor model can also enable better understanding of motor faults and disturbance due to its ability to examine unlimited motor test and fault scenarios without causing motor damage.

The detailed investigation proposed will demonstrate the thorough analysis of the sequence components' capacity to detect shorted turn faults. It can also detect the presence of disturbances such as load, voltage unbalance and inherent asymmetry. Such a complete approach can differentiate clearly the turn faults from the disturbances. The approach can be adopted to separate other faults such as broken rotor bar or eccentricity from shorted turn faults if they occur at the same time. Previous research limitations, and the research opportunities, which have been pointed out, lead to the objective of this thesis, which will be stated in the following section.

1.3 Objective of the Thesis

The negative sequence components have a unique interaction due to shorted turn fault and various disturbances which can be explained by experimental as well as simulation model. However, motor model and experimental confirmation due to the combination of shorted turn, voltage unbalance, load variation or inherent asymmetry including their interactions has not been clearly discussed. In the previous studies, the experimental results were usually presented to justify that the model can be applied for a specific induction motor. Therefore, the first aim of this thesis is to present the effects of shorted turn faults, voltage unbalance, load and inherent asymmetries on negative sequence components using induction motor modeling and the experimental verification.

As was demonstrated in the literature, negative sequence measurement is one of the crucial methods for condition monitoring of induction motors. For example, three-phase voltage and current measurement systems may produce different output gain signals due to inaccurate channel calibration. This instrumentation gain asymmetry produces inaccurate measured negative sequence components which may lead to false alarms. Although the measurement asymmetry is important, it has not been studied sufficiently as it is critical for accurate condition monitoring. Therefore, the second aim is to investigate the accurate measurement of negative sequence components, while considering practical sensor limitations, the accuracies, and measurement noise and sensitivity.

Furthermore, various research about negative sequence analysis as presented in Figure 1.2 has concerned with obtaining the true negative sequence component due shorted turn faults using various disturbance compensation techniques. These studies range from a simple technique such as a look-up database to advanced analysis such as neural networks. However, these studies have presented very limited information about the effect of any disturbances on negative sequence analysis. Therefore, the third aim of this research is to investigate the effect of faults on negative sequence and compensation techniques for various disturbance factors such as voltage imbalance, load variations, and inherent asymmetries by using analytical methods, computer simulation, and experimental results. It is foreseen that this final aim will lead to simple compensation techniques that can be used for sequence component analysis.

1.4 Contributions of the Thesis

The primary contributions of the thesis can be listed as follows:

Detailed investigation of the negative sequence condition monitoring for the induction motor

- Investigation of the measurement issues to minimize negative sequence component error due to instrumentation asymmetry for accurate and realistic condition monitoring results.
- Investigation of single and combined multiple negative sequence contributors, such as inherent asymmetry, voltage unbalance, and shorted turn faults as a

function of load on negative sequence components, both using induction motor model and experimental results.

Development of simple new compensation methods of negative sequence condition monitoring for the induction motor

- Detailed comparison of previous compensation methods based on negative sequence component techniques.
- Investigation of a new and simplified method of inherent asymmetrical compensation to provide accurate baseline analysis for condition monitoring, followed by compensation techniques to eliminate the effect of negative sequence due to voltage unbalance disturbances and load variation that are present in any practical motor system.

1.5 Outline of the Thesis

This thesis is divided into seven chapters. The chapters following this chapter can be summarized as follows: Chapter 2 provides background theory and a literature review of the negative sequence method used in shorted turn monitoring. This chapter provides fundamental techniques of phasor and negative sequence calculation. The chapter also compares and discusses previous condition monitoring techniques based on negative sequence components.

Chapter 3 provides a comprehensive understanding of the induction motor model and machine parameters. This chapter discusses various models from the steady state T model to the dynamic finite element model. The dynamic asymmetrical multiple coupled circuit model is also given in the chapter. The accuracy of this motor model relies on the accuracy of the machine parameters. Therefore, experimental results, calculations and analysis to obtain appropriate machine parameters are explained. The chapter delivers confirmation results of the steady state model and experiments to show the performance of dynamic coupled circuit model.

To provide a better understanding of instrumentation asymmetry, the investigation of measurement issues on negative sequence components is carried out in Chapter 4. The first section in this chapter presents instrumentation characteristics for condition monitoring purposes and presents how the calibration of the measurement system is conducted. The effect of instrumentation gain asymmetry,

either the magnitude or angle signals, to negative sequence components is also discussed. The magnitude and angle correction of the signals for minimum negative sequence errors due to instrument asymmetry are presented. Furthermore, the effects of hot and cold measurement are also presented in this section. Finally, the chapter also briefly explains an approach for on-line calibration which is able to correct the measurement system errors for any induction motor.

In Chapter 5, the comprehensive investigation of stator shorted turn faults is presented. In this chapter, the induction motor test set up for the shorted turn fault experiment is explained. The shorted turn motor model based on the previous healthy motor model in Chapter 3 is demonstrated. The shorted turn experimental results are also presented to confirm the motor model developed. Furthermore, detailed investigation of the disturbances (inherent asymmetry and voltage unbalance) is presented. This chapter also discusses in detail how to eliminate the effect of the inherent asymmetry in induction motors. Furthermore, the negative sequence due to inherent asymmetry, voltage unbalance and shorted turn faults are examined under various motor loading cases. In this chapter, the effect of these negative sequence contributors is presented using phasor magnitude as well as phasor trajectory plots. The chapter also demonstrates the contribution of other faults to negative sequence currents including eccentricity faults and broken rotor bar faults.

Chapter 6 discusses the compensation of disturbances in the detection of shorted turn faults. The chapter provides a detailed comparison of three previous stator current negative sequence compensation techniques. A new detailed step by step development in compensation of voltage unbalance and inherent asymmetry to extract the negative sequence due to shorted turn faults are also given in Chapter 6. Finally, the load variation is examined to show the effect of load to voltage unbalance, inherent asymmetry and shorted turn faults.

Chapter 7 presents the main conclusion of this research, and provides possible future improvements for condition monitoring based on the negative sequence current.

Chapter 2

Background Theory and Literature Review of Negative Sequence Shorted Turn Fault Monitoring

2.1 Introduction

In the previous chapter, the significance of stator faults condition monitoring was briefly explained. A summary of literature survey study about sequence components in condition monitoring purposes was given in Figure 1.2. Therefore, it can be seen that there is a need for comprehensive understanding of the previous studies. It is expected that such background knowledge will help further investigation of the asymmetrical analysis of the sequence components of the induction motor under faults as well as under disturbances such as voltage unbalance or inherent asymmetry. The chapter will provide a literature review, and will outline essential theory suitable for further research.

In the first section of the chapter, condition monitoring of shorted turn faults in induction motor is given. The second section provides the basic theory of negative sequence components, and the theory of phasor calculation technique that is required to determine the sequence components is also presented. Furthermore, selected negative sequence calculation techniques, i.e. Fortescue's method for steady state monitoring cases and Power Decomposition Technique for the dynamic operation, are also explained. The final section of this chapter will present literature review of previous condition monitoring studies focusing preliminary on how to separate the measured negative sequence from the disturbances. It can be noted here, the previous condition monitoring studies are negative sequence current, negative sequence admittance, negative sequence impedance, sequence matrix impedance, semi empirical formula as well as neural network approaches.

2.2 Condition Monitoring of Stator Shorted Turn Faults

As it is mentioned previously, faults of an induction motor can be identified when the capability of the motor is decreasing in relation to the rated performance. The decrease of performance in early faults may be due to various factors, such as normal wear, poor design, poor mounting or poor alignment, wrong use, environmental hazards, or a combination of these [3]. These early faults may occur in every part of the motor, especially in electromechanical parts such as the stator or rotor. If a fault(s) is not detected timely, this may lead to a complete shutdown not only of the motors but also of the plants such as in petrochemical industry, material handling, nuclear power plant, or water treatment facility.

As shown previously in Figure 1.1, among the common faults, stator related faults have attracted many researchers in the field of condition monitoring of induction motors. These types of faults challenge researchers for several reasons, which are summarized in the following paragraphs.

Firstly, the stator related faults have constituted to approximately 38% of total motor faults [1-3], which are usually caused by electrical stresses. Recently, several improvements of the winding insulations have been made in premium-efficiency class motors to reduce winding faults. However, a recent paper [10, 11] has shown that there is not a significant increasing of the stator winding reliability, except for a large population of small motors (1-20 hp) which were built before The Energy Policy Act (EPAAct) for motors in USA, in 1997 that had higher winding and stator temperature limit. This means that stator shorted turn still needs serious attention in condition monitoring.

The second reason is that motor experts believe that the time between early stage and catastrophic failures in shorted turn faults is relatively short compared with other motor faults [7]. Even though little information has been found to identify the time to failure, this can vary from a second to an hour, depending on the size of the motor. This is a serious concern when a short circuit of a few turns in phase winding occurs as the protection might not work when the heating has accumulated and created an immediate change to damage the stator cores. This short time to failure also leads to the importance of on-line stator fault monitoring.

Due to a relatively short time to anticipate the complete motor failure, both accurate motor modeling and experiment confirmation are required to study such fault. Research shows that motor fault experiments are not an easy task [12]. However, the easiest way to predict motor behavior under various stages of stator faults is through accurate induction motor modeling. Several modeling techniques have been demonstrated, such as the winding function approach, also known as the Multiple Couple Circuit Model (MCCM) [13-15], and dynamic reluctance approaches also known as the Magnetic Equivalent Circuit (MEC) method [16], and Finite Element method [17]. In terms of accuracy, all these models require accurate machine parameters that are not readily available by the manufacturers. In addition, several assumptions must be included to approximate the real behavior of the motors, such as unbalanced operating conditions, skewing, slotting, air gap variations, and saturation. In case of motor faults experimental studies, it was also highlighted in [12] that the experiments have not been carried out extensively for various motor sizes and operating conditions. To protect the motor, resistors are usually applied to the stator terminal or by reducing the supply voltage during the experiments. Both techniques may eliminate the saturation effect exists in real machines. This means that both the model and experiment validation still needs further development for on-line and early detection stator fault monitoring.

Tavner and Penman in [18] classified stator-related faults into two groups: stator winding faults and stator core faults. Two main locations are identified for stator winding faults. The first location is end winding portion faults, which can be in the form of local damage, fretting, contamination, cracking, displacement of insulations, or any turn-to-turn faults caused by any damage to winding. The second location is slot portion faults such as fretting of insulation, and displacement of conductors. In the case of stator core faults, the faults are grouped as lamination faults (such as core hot spot and core slackening), frame faults (such as frame vibration, circulating currents) and earth faults.

Thomson and Fenger in [19] explained the biggest concern in relation to the winding faults caused by short circuits which basically can be used to represent other specific faults. Various real stator faults are illustrated in Figure 2.1 where small faults may propagate into complete winding faults.

NOTE:
This figure/table/image has been removed
to comply with copyright regulations.
It is included in the print copy of the thesis
held by the University of Adelaide Library.

Figure 2.1 Various stator faults (a) turn-to-turn , (b) shorted coils, (c) phase-to-phase, (d) grounded at edge of faults, (e) grounded at slots, and (f) total phase damage [20].

Thomson and Fenger in [19] also suggested that the pre-warning of failures, which can be in the form of phase-to-phase and phase-to-earth short, could be identified early by continuous evaluation of the turn-to-turn and shorted coils. In other words, one of the key issues in preventing catastrophic winding failures in induction motors is monitoring turn-to-turn within or between coils of the same phase.

To actively monitor early turn-to-turn faults, several techniques have been proposed. In [6], fourteen different on-line methods were presented, including their advantages and disadvantages. The methods can be categorized as temperature monitoring, high-frequency impedance, sequence components, signature analysis, Artificial Intelligence (AI)-based methods and partial discharge method. Among all the techniques presented, the sequence-based methods are the most promising techniques which can be applied for early on-line monitoring. The sequence methods can be in the form of voltages, currents, and impedance machines utilizing negative sequence, sequence matrix, or zero sequence.

The sequence-based detection method has several advantages compared with the other shorted turn on-line detection methods:

1. The sequence-based method is suitable for on-line real time monitoring due to its processing speed. The technique is non-invasive, simple, and there is no need for complex computations such as FFT [6].
2. Early detection of induction motors can be done immediately. If any asymmetry occurs due to the turn-to-turn faults, the sequence components will provide immediate accurate results [7].
3. Due to its high sensitivity to detect any asymmetrical changes simultaneously, the sequence components also indicate any change beyond the stator fault asymmetry. The sequence components can also be caused by voltage unbalance, saturation, winding asymmetry, and eccentricity faults. To eliminate and separate the effect of these, the active procedure can be carried out to extract the negative sequence due the stator faults from the disturbances. Unlike most condition monitoring, the separation procedure, known as compensation techniques, can be easily implemented to improve the accuracy.

These advantages especially for shorted turn faults, make negative sequence a better candidate to be used in online condition monitoring. In order to comprehend the negative sequence monitoring techniques, a basic understanding of negative sequence components is necessary, including how to calculate the negative sequence components and the phasor extractions from the measurement waveform signals, which will be will discussed below.

2.3 Theory of Negative Sequence Components

2.3.1 Overview of Phasor Theory

The sequence components analysis requires phasor representation to simplify the current or voltage signal calculation. The phasor calculation allows the essential information to be retained for monitoring or diagnostic applications. The phasor for electrical analysis aims to display the sinusoid waveform in a simple, easy to understand manner. The pure waveform of an electrical current $i(t)$ can be illustrated in Figure 2.2.

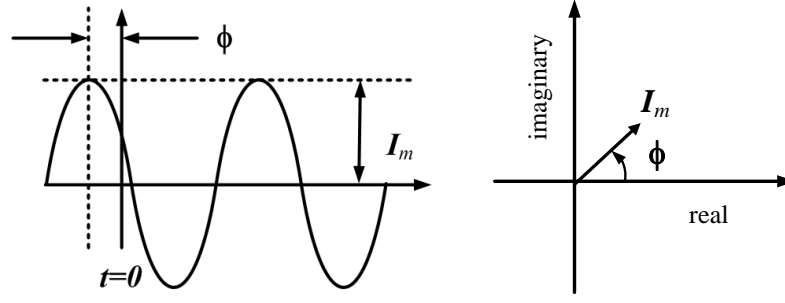


Figure 2.2 Phasor definition under pure sinusoidal current waveform.

The figure displays phasor definition of a current under pure sinusoidal waveform $i(t)$ such as given below.

$$i(t) = I_m \cos(\omega t + \phi) \quad (2.1)$$

This current equation is also presented in the mathematical equations given below, where ϕ is phase angle in radian, I_m is peak amplitude of the current signal and ω is the frequency in radian per second.

$$i(t) = \text{Re}\{I_m e^{j(\omega t + \phi)}\} = \text{Re}\left[\{e^{j(\omega t)}\} I_m e^{j\phi}\right] \quad (2.2)$$

The phasor representation of a current waveform can be obtained from this equation, as illustrated in Figure 2.2. The magnitude of the phasor is equal to Root Mean Square (RMS) value of the I_m , and the phase angle is assumed arbitrary, depending on the choice of $t=0$.

$$\mathbf{I} = \left(I_m / \sqrt{2}\right) e^{j\phi} = \left(I_m / \sqrt{2}\right) [\cos \phi + j \sin \phi] \quad (2.3)$$

This equation however cannot be applied directly to real condition monitoring signals since such signal waveforms may contain disturbances or be corrupted by other frequencies. In this case, the interested single frequency, which is usually the fundamental frequency, can be extracted from the measured signals to produce a phasor. To do such extraction in the data sampled system, the Fourier Transform technique is required. One of the prominent techniques for phasor implementation is Discrete Fourier Transform (DFT). The phasor presentation using DFT is given in Figure. 2.3.

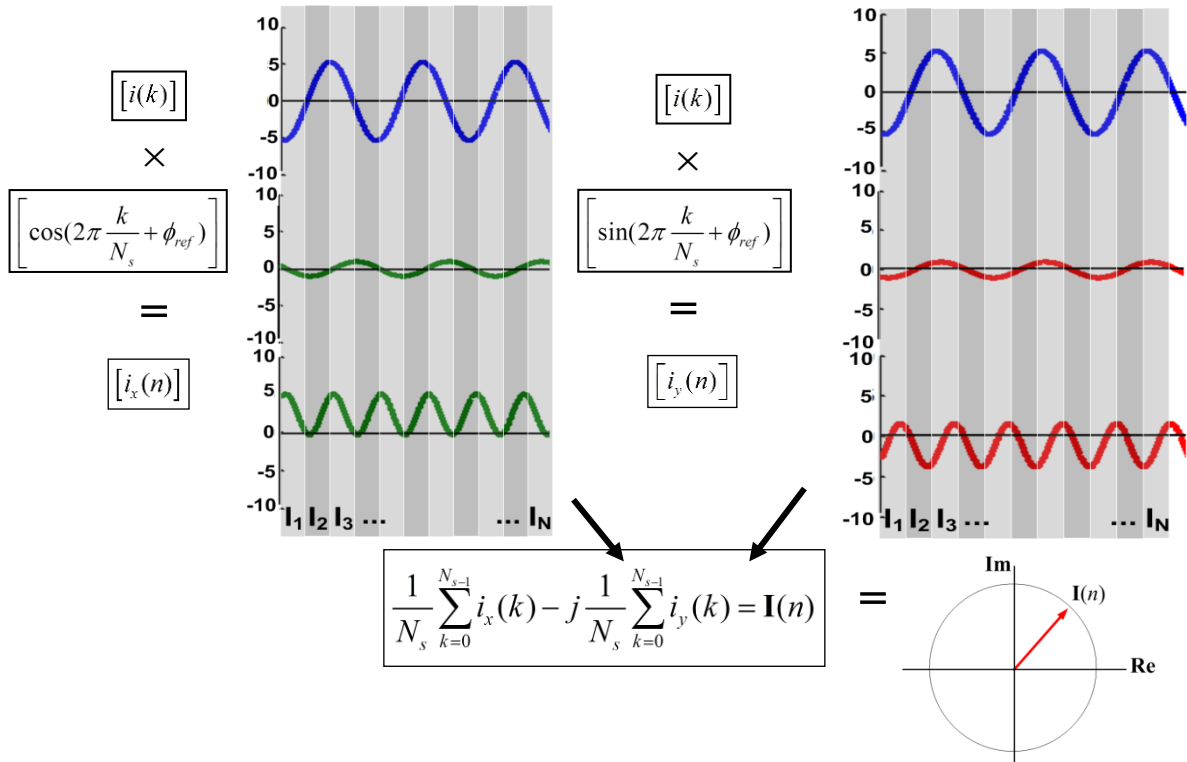


Figure 2.3 Graphical analysis of the DFT algorithm to obtain phasors.

As can be seen from Figure 2.3, the DFT technique means that the phasor is assumed to represent unchanging signals over a certain time span, called the data window. Like a filtering technique, the phasor is calculated at discrete instants in the time domain, or discrete steps in the frequency domain, using the rectangular window function. The waveform is sampled N_s times per cycle, where N_s is the number of samples, k represents the sample number in the time domain, and n is the frequency over the sampling period. The ϕ_{ref} is the reference of the phase angle in radian. The i_x and i_y denote the real and imaginary part of the phasor respectively. The figure shows that the phasor of the RMS electrical current (I), which is sampled at a rate N_s sample per sampling frequency cycle, is defined as the result of the sampled signals multiplied by a sin and a cosine term. The fundamental components of the phasor then can be given as in Figure 2.3

$$i_x(n) + ji_y(n) = \mathbf{I}(n) \quad (2.4)$$

where

$$i_x(n) = \frac{\sqrt{2}}{N_s} \sum_{k=0}^{N_s-1} i(k) \cos(kn\theta),$$

$$i_y(n) = \frac{\sqrt{2}}{N_s} \sum_{k=0}^{N_s-1} i(k) \sin(kn\theta),$$

$$k = 0 \text{ to } N_s-1$$

$$\theta = 2\pi / N_s, \text{ and}$$

$$\phi_{ref} = 0 \text{ for assumption that first sampled is at } t = 0.$$

The gained phasors is than calculated over the data window of the specific period by averaging techniques. Static window, moving average window, discrete mean value or other techniques can be employed for the averaging to improve the results, especially in real time environments.

The phasors obtained from three-phase current or voltage signals require further calculation to obtain the sequence components. The calculation is to simplify the analysis especially under asymmetrical phasor representations. The following section discusses the negative sequence calculation for further condition monitoring applications.

2.3.2 The Sequence Components Calculation

Sequence components can be obtained from asymmetrical analysis which has been presented in [21]. This asymmetrical component method simplifies the application of conventional general circuit analysis for multiple phases under various voltage unbalances. The general circuit analysis is usually implemented under symmetrical conditions. In other words, the mutual impedance of a motor can be assumed balanced and, therefore, multiple phase circuit can be easily treated as a single circuit. However, under asymmetrical voltage unbalance, the mutual impedance, as well as the self-impedance, cannot be assumed to be exactly alike. Therefore, using general circuit analysis, complex simultaneous multiple phase equations should be employed.

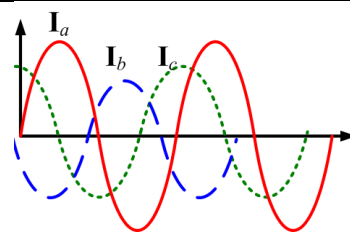
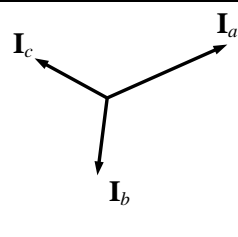
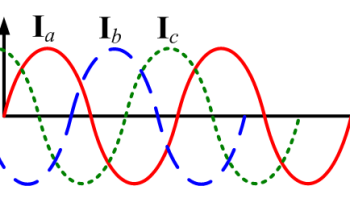
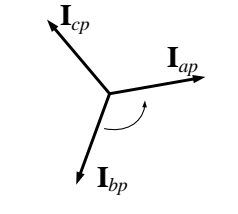
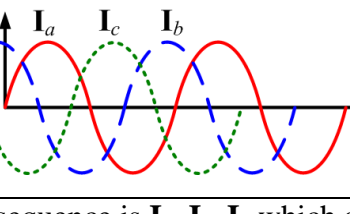
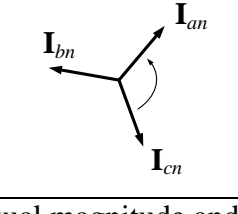
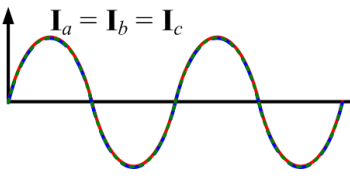
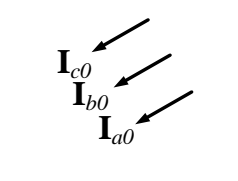
	Waveforms	Phasors
Unbalanced Voltages =		
	The measured unbalanced waveform and phasor with the sequence I_a, I_b, I_c	
Positive Sequence +		
	The sequence is I_a, I_b, I_c which are of equal magnitude and are set apart 120° from each other	
Negative Sequence +		
	The sequence is I_a, I_c, I_b which are of equal magnitude and are set apart 120° from each other	
Zero Sequence		
	The I_a, I_b, I_c is in phase and may be of equal magnitude	

Figure 2.4 Graphical waveform illustrations of the sequence component methods.

Different to the general circuit analysis, the asymmetrical component analysis can be done by building the analytical solution of three fundamental symmetrical balanced sequence components from the three unbalanced phasors. In other words, three sets containing three-phase unbalanced phasors or a total of nine phasors are required. This means that each of the symmetrical balanced sequence components are built up from a set of three unbalanced phasors. These sets of three-phase phasors are negative sequence, positive sequence, and zero sequence. This concept will produce three independent balanced sequence component phasors. Because none of the sequence component phasors react on the others, analysis or interpretation of the

system, especially for condition monitoring, can be done individually for each component.

The three sequence components can be added to produce the original three-phase phasors as illustrated in Figure 2.4. The Figure shows that the three unbalanced phasors (voltage or current phasors) are produced by positive, negative and zero sequences. The positive sequence which has sequence \mathbf{I}_a , \mathbf{I}_b , and \mathbf{I}_c is also known as the supply current phasor. It denotes the existence of supply phasors with the reference axis fixed to the generated current supply. In the contrary direction of the positive sequence, the negative sequence follows the anti-clockwise sequence, \mathbf{I}_a , followed by \mathbf{I}_c , and \mathbf{I}_b , with phase angle displacement $\pm 120^\circ$. In addition, the zero sequence without any phase displacement will reach the maximum value at the same time. The balanced system produces only positive sequence, while the negative sequence or the zero sequence occurs on unbalance or asymmetrical systems. Under asymmetrical faults, the magnitude and angle of the sets of sequence components phasors will change according to the faults, which can be useful for fault analysis.

In Figure 2.4, it is shown that the phasors were displaced 120° . This displacement value is used to represent the sequence operator called h .

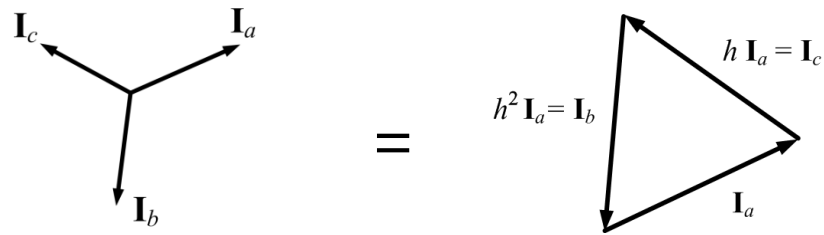


Figure 2.5 Graphical illustrations of the sequence operator h .

It is shown in Figure 2.5 that operator h can be used to designate phase (\mathbf{I}_b and \mathbf{I}_c) to \mathbf{I}_a , and produce an equilateral triangle if the phasor is added together. The sequence operator h has the following properties:

$$h = e^{j\frac{2\pi}{3}} \text{ or } h = 1\angle 120^\circ; \quad h^2 = 1\angle 240^\circ; \quad h^3 = 1$$

$$0 = 1 + h + h^2$$

This operator, then, is employed in the form three sequence components phasor, as explained below.

$$\mathbf{I}_a = \mathbf{I}_{ap} + \mathbf{I}_{an} + \mathbf{I}_{a0} = \mathbf{I}_p + \mathbf{I}_n + \mathbf{I}_0 \quad (2.5)$$

$$\mathbf{I}_b = \mathbf{I}_{bp} + \mathbf{I}_{bn} + \mathbf{I}_{b0} = h^2 \mathbf{I}_p + h \mathbf{I}_n + \mathbf{I}_0 \quad (2.6)$$

$$\mathbf{I}_c = \mathbf{I}_{cp} + \mathbf{I}_{cn} + \mathbf{I}_{c0} = h \mathbf{I}_p + h^2 \mathbf{I}_n + \mathbf{I}_0 \quad (2.7)$$

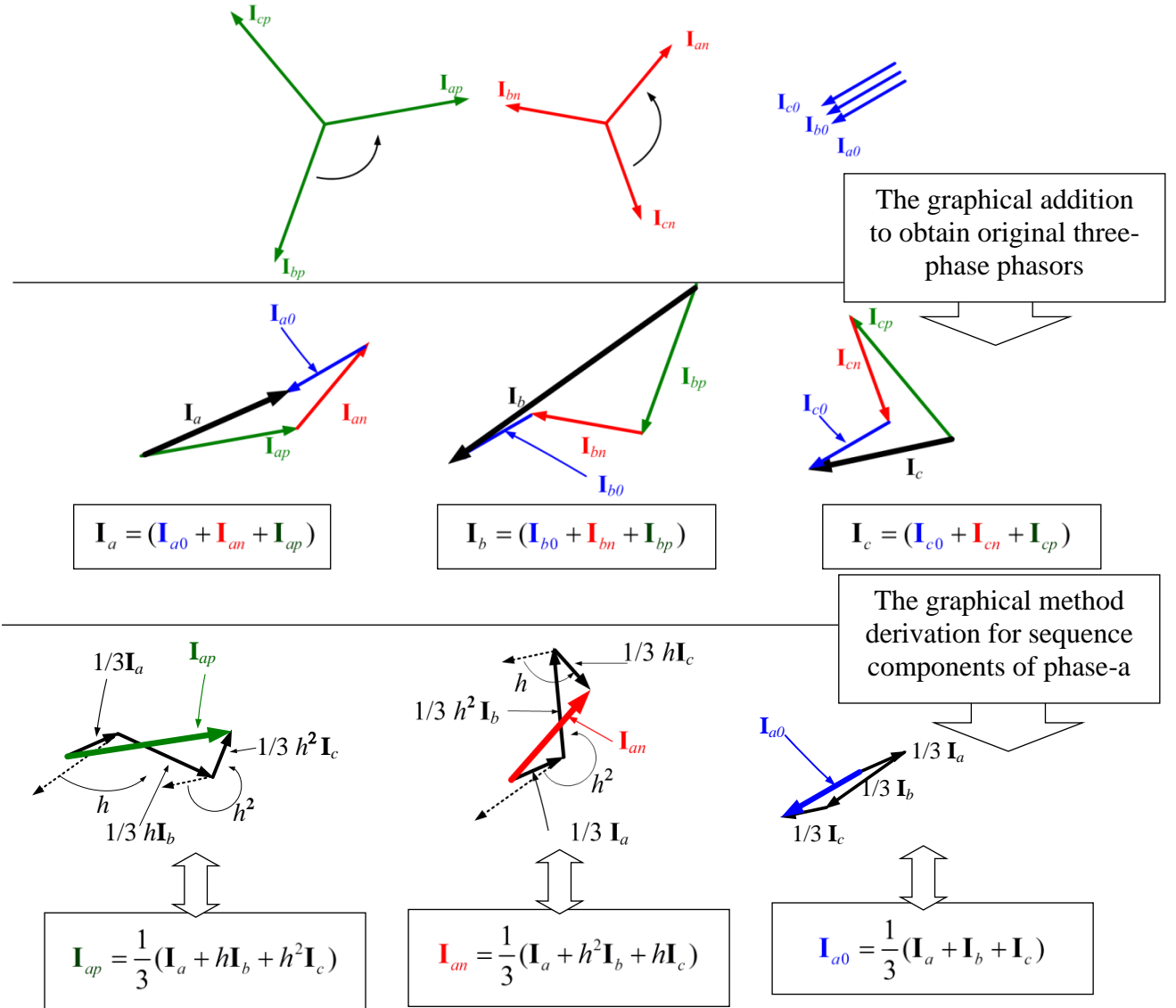


Figure 2.6 Graphical analysis of the positive, negative and zero sequence system of phasors.

Equation 2.5, 2.6 and 2.7 can be written in matrix form as given in Equation 2.8 below.

$$\begin{bmatrix} \mathbf{I}_a \\ \mathbf{I}_b \\ \mathbf{I}_c \end{bmatrix} = \begin{bmatrix} 1 & 1 & 1 \\ h^2 & h & 1 \\ h & h^2 & 1 \end{bmatrix} \cdot \begin{bmatrix} \mathbf{I}_p \\ \mathbf{I}_n \\ \mathbf{I}_0 \end{bmatrix} \quad (2.8)$$

where, (\mathbf{I}_0) = zero sequence, (\mathbf{I}_p) = positive sequence, and (\mathbf{I}_n) = negative sequence.

The sequence components can be obtained from the Equation 2.8 as shown below.

$$\begin{bmatrix} \mathbf{I}_p \\ \mathbf{I}_n \\ \mathbf{I}_0 \end{bmatrix} = \frac{1}{3} \begin{bmatrix} 1 & h & h^2 \\ 1 & h^2 & h \\ 1 & 1 & 1 \end{bmatrix} \cdot \begin{bmatrix} \mathbf{I}_a \\ \mathbf{I}_b \\ \mathbf{I}_c \end{bmatrix} \quad (2.9)$$

To give a better understanding, the current equations are illustrated graphically in Figure 2.6. This figure presents the graphical illustrations to provide understanding of the phasor calculation of the sequence components. The first row, from left to right, shows positive, negative and zero sequence phasors. The positive sequence is labeled according to sequence \mathbf{I}_{ap} , \mathbf{I}_{bp} and \mathbf{I}_{cp} while the negative sequence is \mathbf{I}_{an} , \mathbf{I}_{bn} and \mathbf{I}_{cn} . The second row demonstrates the graphical addition of each sequence component to obtain the original phasors. For example, the current phase \mathbf{I}_a consists of the positive sequence \mathbf{I}_{ap} , the negative sequence \mathbf{I}_{an} and zero sequence \mathbf{I}_{a0} . The third row gives an idea how the sequence components can be gained graphically from the previous original phasors. It should be noted from Figure 2.6 that operator α multiplying a vector will rotate the specific phase 120° counter clockwise while the h^2 operator rotates the phase 240° counter clockwise. The last row shows that $1/3\mathbf{I}_a$ is added to $1/3\mathbf{I}_b$ after the vector is shifted 120° by operator h . The results are then added to $1/3\mathbf{I}_c$, after the phasor is rotated 240° counter clockwise by operator h^2 to obtain the positive sequence component \mathbf{I}_{ap} .

It should be emphasized here that the sequence component calculation which requires variables in phasor representation shown in Equation 2.9 has only applicable for steady state cases. Therefore, to study transient cases various dynamic negative sequence calculations have been proposed. One of them is Power Decomposition Technique (PDT) which utilizes arbitrary three-phase signals in time domain by interpreting the energy conservation theorems in two-dimension ordinates.

2.3.3 Power Decomposition Techniques (PDT) sequence components calculation

Another simple sequence components extraction from the measurement signal is the power decomposition technique, shown in Figure 2.7. This technique provides alternatives to obtain direct symmetrical components positive and negative sequence based on the concept of power distribution in two dimensions. The implementation of

PDT (Power Spectral Decomposition Technique) to extract the sequence components in real-time environment, free from harmonics, and useful for transient analysis are presented in [8]. The method requires simultaneous sampling of three-phase instantaneous current signals. Furthermore, balanced sinusoidal voltage for references is also defined to produce instantaneous power. The calculation results are positive sequence power and negative sequence power phasors. Finally, the positive or negative sequence current or voltage phasor was gained from the complex arrangement of these power phasors. The following equations and graphs briefly discuss this method. It should be noted that γ and ρ suffixes represent the two-axis orthogonal coordinates fixed relative to the stator. The N_s in $k = 0,1,2\dots N_s-1$ is the number of samples per supply cycle.

$$\begin{bmatrix} i_\gamma(k) \\ i_\rho(k) \end{bmatrix} = \frac{2}{3} \begin{bmatrix} 1 & -\frac{1}{2} & -\frac{1}{2} \\ 0 & \frac{\sqrt{3}}{2} & -\frac{\sqrt{3}}{2} \end{bmatrix} \begin{bmatrix} i_a(k) \\ i_b(k) \\ i_c(k) \end{bmatrix} \quad (2.10)$$

$$\begin{bmatrix} u_\gamma(k) \\ u_\rho(k) \end{bmatrix} = \frac{2}{3} \begin{bmatrix} 1 & -\frac{1}{2} & -\frac{1}{2} \\ 0 & \frac{\sqrt{3}}{2} & -\frac{\sqrt{3}}{2} \end{bmatrix} \begin{bmatrix} u_a(k) \\ u_b(k) \\ u_c(k) \end{bmatrix} \quad (2.11)$$

Here the i_a , i_b , and i_c are the instantaneous current signals and u_a , u_b , and u_c are unitless pseudovoltages of instantaneous balanced sinusoidal positive sequence which are locked to the positive sequence supply voltage. These waveforms are transformed into two phase quantity i_α , i_β , and u_α , u_β . It should be noted that u_α , and u_β may be obtained from a look-up table as unit-amplitude of sinusoidal and cosinusoidal terms as given in Equation 2.12

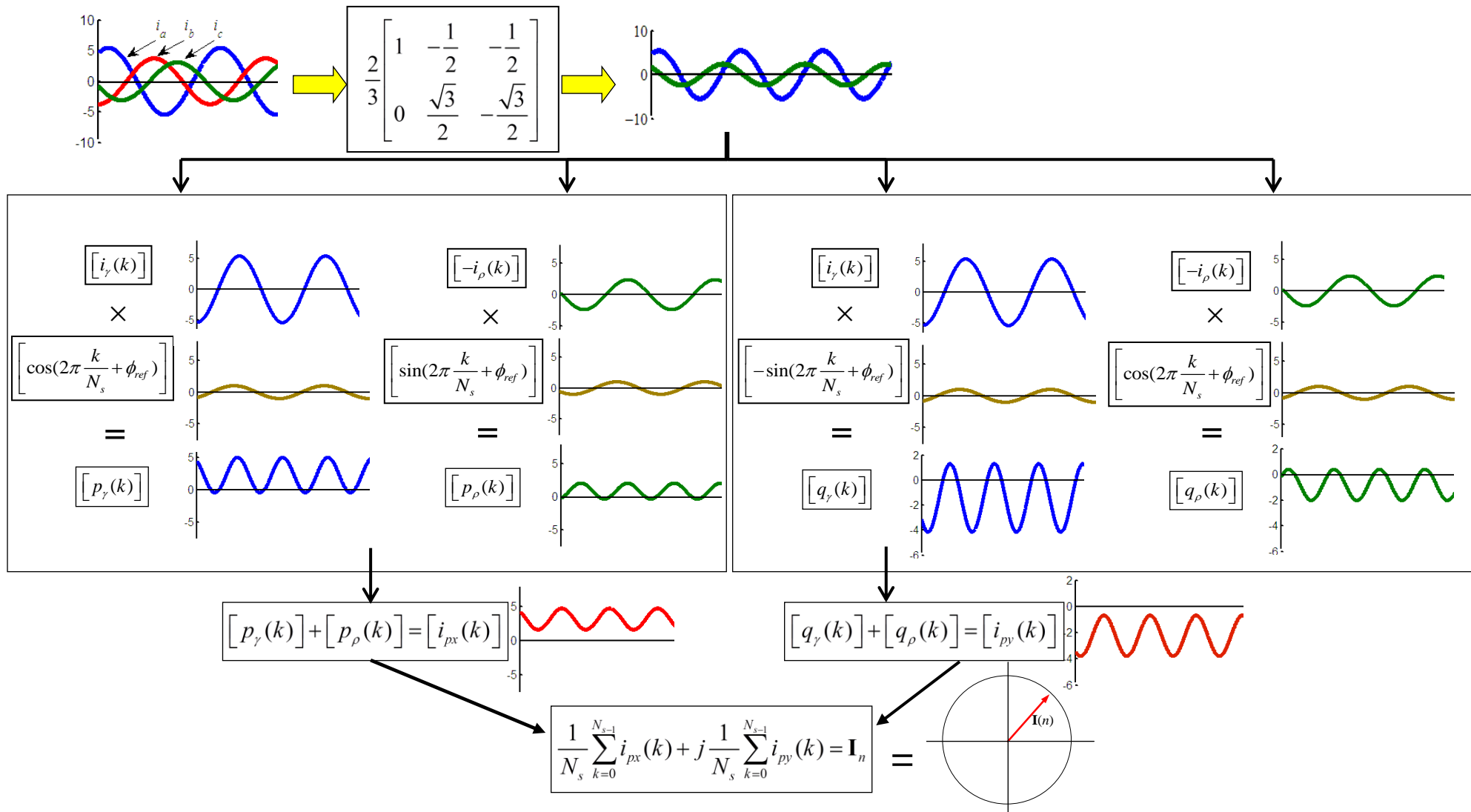


Figure 2.7 Graphical illustrations of the PDT methods.

$$u_p(k) = \left[\cos\left(2\pi \frac{k}{N_s} + \phi_{ref}\right) \right] \text{ and } u_q(k) = \left[\cos\left(2\pi \frac{k}{N_s} + \phi_{ref}\right) \right] \quad (2.12)$$

The instantaneous real power $p(k)$ and the imaginary reactive power $q(k)$ then can be given by,

$$\begin{bmatrix} p_\gamma(k) \\ p_\rho(k) \end{bmatrix} = \begin{bmatrix} u_\gamma(k) & 0 \\ 0 & u_\rho(k) \end{bmatrix} \begin{bmatrix} i_\gamma(k) \\ i_\rho(k) \end{bmatrix} \quad (2.13)$$

$$\begin{bmatrix} q_\gamma(k) \\ q_\rho(k) \end{bmatrix} = \begin{bmatrix} -u_\gamma(k) & 0 \\ 0 & u_\rho(k) \end{bmatrix} \begin{bmatrix} i_\gamma(k) \\ i_\rho(k) \end{bmatrix} \quad (2.14)$$

For the positive and negative sequence current

$$\mathbf{I}_n = P_{\gamma n} + jQ_{\gamma n} = I_{nx} + jI_{ny} \quad (2.15)$$

$$\mathbf{I}_p = P_{\gamma p} + jQ_{\gamma p} = I_{px} + jI_{py} \quad (2.16)$$

where,

$$P_{\gamma n} = P_\gamma - P_\rho = -P_{\rho n}, \quad Q_{\gamma n} = Q_\gamma - Q_\rho = -Q_{\rho n}, \quad P_{\gamma p} = P_\gamma + P_\rho = P_{\rho p}, \quad \text{and } Q_{\gamma p} = Q_\gamma + Q_\rho = Q_{\beta p}$$

The P_γ , P_ρ , Q_γ and Q_ρ are active (P) and reactive components (Q), obtained from one cycle of the average of pseudo power quantities. Although they are named power quantity, these active and reactive components practically have unit of current. In the case of voltage analysis, exactly the same procedures can be applied and the current signals are replaced by voltage signals.

The previous sub sections have provided fundamental knowledge of the phasor theory, negative sequence calculations theory, and the real time phasor with negative sequence PDT calculations. This basic knowledge will further support investigations in comparing the previous research, which will be covered in the following sections. Several reviews and research papers have highlighted the earlier developments in sequence component methods, including compensation methods, modeling, and experimental methods. The summary of research on negative sequence, effective sequence impedance, and sequence impedance matrix is presented in the following sections.

2.4 Literature Review of Negative Sequence Monitoring

Various studies have been carried out which are applicable to condition monitoring of induction motors. Most of these studies addressed the possibility of the sequence components being removed from any disturbances. This is not provided by any other fault detection method. The following table illustrates the summary of the research in this area. This is followed by a detailed discussion in the following sub sections.

Table 2.1 Negative Sequence Research

Sub Sections	Natural Unbalance	Voltage Unbalance	Load variation	Shorted Turn Fault	Authors
2.4.1	-	Developed the asymmetry equation	-	-	Fortescue [21]
2.4.1	-	-	Study was under various speed	Gives correlation between negative sequence and stator fault	Williamson and Mirzoan's [22]
2.4.2	Compensation of non-linearity (including inherent asymmetry) using look-up database	Compensation using $Z_{n-motor}$ which was assumed unaffected by load variation and stator shorted turn	Unaffected by load variation	stator shorted turn detection I_n^{sf}	Kliman [7, 23]
2.4.3	Compensation using complex constants (k) $I_n = k_1 V_p + k_2 V_n$	Compensation using complex constants (k) $I_n = k_1 V_p + k_2 V_n$	k is load dependent	Stator shorted turn detection I_n^{sf}	Tallam [24]
2.4.4	Compensation based on minimization of thermal effect by eliminating the current phase $I_{sn} = \frac{V_{sn} \sin \theta_n}{X_{hn}}$	Compensation using semi empirical quadratic function of reactance (X_{hn}) which was calculated at no and full load $X_{hn}^{-1} = \gamma_0 + \gamma_1 V_{a2} + \dots$	Compensation using semi empirical quadratic function $I_{mnlv} = \alpha_0 + \alpha_1 I_{px} + \dots$ $\alpha_2 I_{px}^2 + \alpha_3 I_{py} + \alpha_4 I_{py}^2$	Stator shorted turn detection $I_n^{sf} = I_n - I_{sn} - I_{mnlv}$	Arkan [8, 9, 25]
2.4.5	Compensation using Neural network	Compensation using Neural network	Compensation using Neural network	Stator shorted turn detection I_n^{sf}	Tallam [26-28]
2.4.6	Need to be perfectly balanced	Need a balanced voltage supply	Load is not affected	Effective impedance: $Z_{n-eff} = \frac{V_n}{I_n}$	Kohler, Sottile [29, 30]
2.4.7	Independent of inherent asymmetry	Independent of voltage imbalances	Calculation was made under speed variation	Impedance matrix Z_{np}	Lee[31], Trutt [32]

The Table shows various approaches which use negative sequence components as the indicator for condition monitoring. The negative sequence current components and negative sequence impedance are the most developed fault detection methods in the sequence component analysis. The following sub sections will discuss in greater detail the research indicated in Table 2.1.

2.4.1 The Initial Utilization of Negative Sequence Current Monitoring

As mentioned in the previous section, the negative sequence current (\mathbf{I}_n) as well as the positive sequence current (\mathbf{I}_p) and zero sequence current (\mathbf{I}_0) can be extracted from the three-phase current measurements. The equations above were firstly introduced by Fortescue [21]. Fortescue has investigated balance phasors called symmetrical components, which can be used to understand the unbalanced system in a system of balanced phasors.

Unlike the original three-phase current phasors, the three symmetrical phasors component discussed previously can be treated independently. For current and voltage in the symmetrical circuits, each sequence does not react with any other sequence. In other words, each sequence voltage only produces the same sequence current under balanced voltage supply conditions. This behavior can further simplify the symmetrical related problems. The independent characteristic of sequence components also provides advantages to isolate the specific sequence, which has the greatest influence with the induction motor during the operation. For example, the negative sequence supply voltage tends to affect significantly the net torque of induction motors, while the grounding phenomena relate to the zero sequence.

In the case of stator shorted turn fault, unfortunately, other non-idealities and operation conditions may also produce similar negative sequence. These non-idealities and operation conditions mean that shorted turn detection based on the negative sequence needs further research to eliminate these non-idealities. The contribution of non-idealities and operation interactions into overall negative sequence can be illustrated in Figure 2.8.

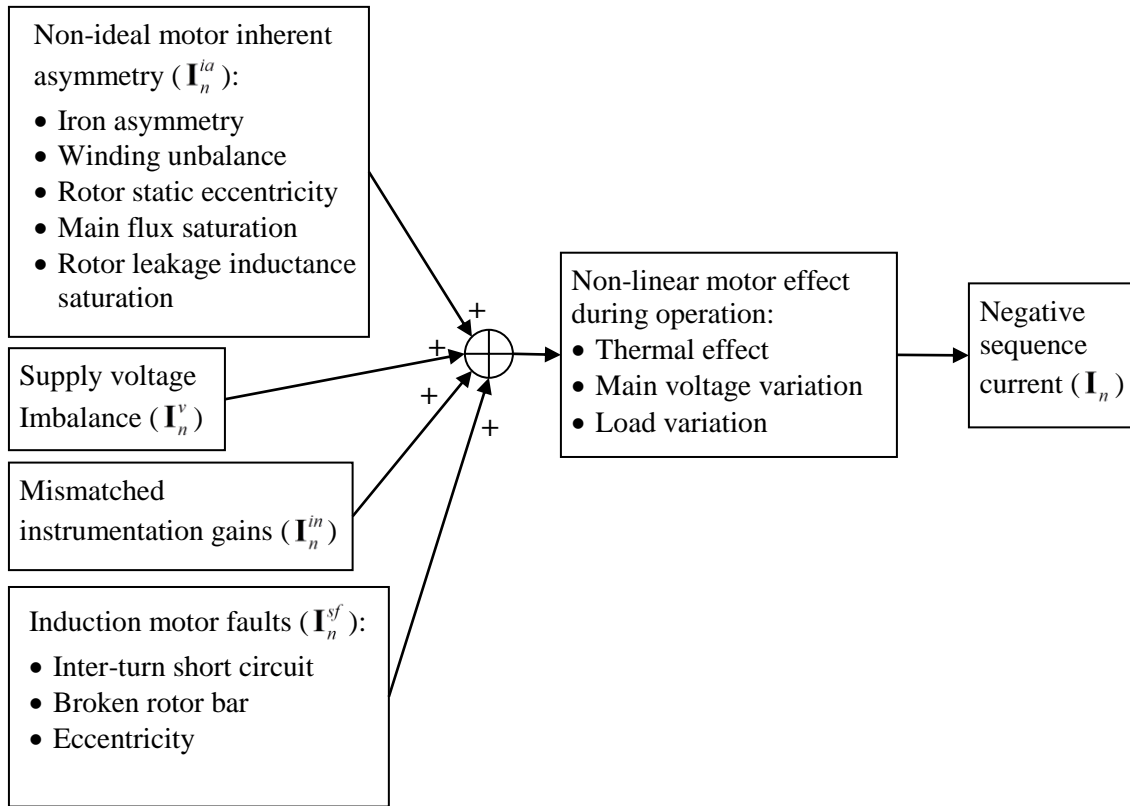


Figure 2.8 Various causes of negative sequence current.

Figure 2.8 illustrates the various causes that may contribute to increase negative, or produce similar symptoms, in negative sequence current. It should be noted that the negative sequence also exists in healthy machines [24], because of voltage imbalance, non-ideal inherent asymmetry of the induction motor, and instrumentation asymmetry. The negative sequence current increases significantly due to induction motor faults (such as the stator shorted turn fault). Because of these factors, the negative sequence current can be more complex when the non-linear characteristic of the induction motor involves, due to either load variations, main voltage variations, or the increasing of motor temperature during the operation. The real stator shorted turn can be obtained by eliminating any unintended negative sequence contribution illustrated in Figure 2.9. The figure illustrates that the real negative sequence due to stator current faults (\mathbf{I}_n^{sf}) can be extracted from the measured negative sequence (\mathbf{I}_n) after eliminating it from negative sequence due to voltage unbalance (\mathbf{I}_n^v), motor inherent asymmetry (\mathbf{I}_n^{ia}) and instrumentation asymmetry (\mathbf{I}_n^{in}).

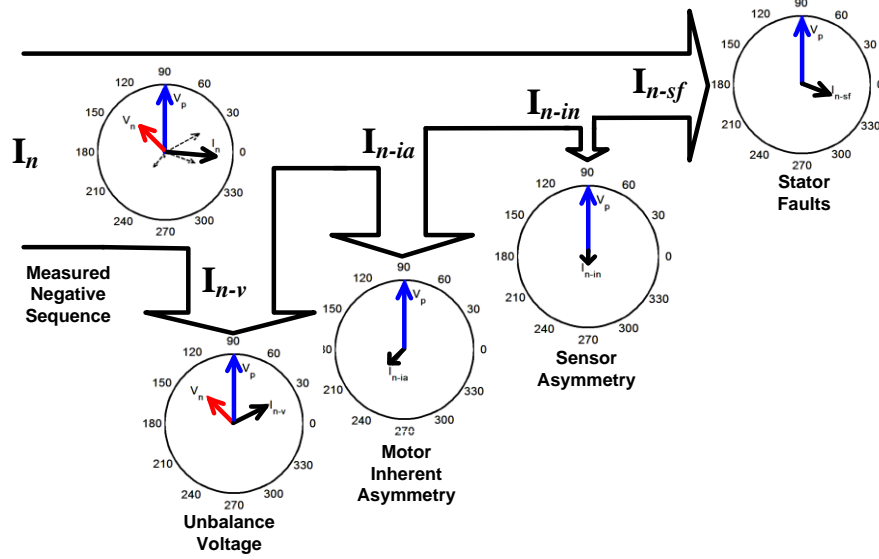


Figure 2.9 Compensation techniques based on phasor calculations. The negative sequence current due to stator faults is extracted from observed negative sequence current, negative sequence caused by voltage unbalance, and negative sequence due to inherent asymmetry.

Because of the contribution of these non-ideal and non-linear factors, the real negative sequence calculation of the stator shorted turn fault can be illustrated in Equation 2.17. It should be noted that load variations are not presented clearly in this equation as the previous research indicates [7] that each disturbance such as inherent asymmetry and voltage unbalance may be treated individually as functions of load variation.

$$\mathbf{I}_n = \mathbf{I}_n^v + \mathbf{I}_n^{ia} + \mathbf{I}_n^{in} + \mathbf{I}_n^{sf} \quad (2.17)$$

$$\mathbf{I}_n^{sf} = \mathbf{I}_n - \mathbf{I}_n^v - \mathbf{I}_n^{ia} - \mathbf{I}_n^{in} \quad (2.18)$$

The research in [22] inspires further sequence-based research in the field of condition monitoring. It was suggested in [22] that known value negative sequence could be implemented for trip limit of the protection system as well as for fault detection. Figure 2.11 shown below illustrates the result of measurements that were carried out in [22].

NOTE:

This figure/table/image has been removed to comply with copyright regulations. It is included in the print copy of the thesis held by the University of Adelaide Library.

Figure 2.10 Predicted (circle and cross) and measured supply (line) of positive sequence, negative sequence and short circuit current for (a) one coil short-circuited and (b) a phase-to-phase short circuit [22].

Figure 2.10 (a) and 2.10 (b) show that the negative sequence can be applied as an indicator of shorted turn fault. Firstly, it was reported that there is a correlation between negative sequence and stator shorted turn [22], and the negative sequence currents show different responses according to the type of stator current faults. As indicated in [22] that negative sequence current is a better indicator than positive sequence current as verified by the test results and computer model. Figure 2.10 also shows that the negative sequence current is not significantly affected by the motor's speed. Therefore, the negative sequence indicator may still be obtained accurately in various speed and load fluctuations. Note that although the short circuit currents (I_{sh}) under a turn-to-turn fault are also illustrated in Figure 2.10. They can not be accessed and measured directly, hence can not be used for on-line condition monitoring purposes.

2.4.2 Admittance Calculation

Few research studies have been reported in literature to compensate for any unintended negative sequence contributors. In [24], the contribution of inherent asymmetry and voltage unbalance to negative sequence components through negative admittance of a single phase steady state model are reported, which are given below.

$$\mathbf{I}_n = Y_n \mathbf{V}_n ; \mathbf{I}_p = Y_p \mathbf{V}_p \quad (2.19)$$

where \mathbf{I}_n = negative sequence current, \mathbf{I}_p = positive sequence current, \mathbf{Y}_n = negative sequence admittance, \mathbf{Y}_p = positive sequence admittance, \mathbf{V}_n = negative sequence voltage, and \mathbf{V}_p = positive sequence voltage.

The inherent asymmetry was also affected by load variation. Therefore, the negative sequence current that can be estimated by the compensation of the voltage unbalance and inherent asymmetry, and can be given by

$$\mathbf{I}_n^{v+ia} = k_1 \mathbf{V}_p + k_2 \mathbf{V}_n \quad (2.20)$$

Here, k_1 and k_2 are the load dependent complex numbers obtained from six sets of data under five load variations of a healthy machine. This technique also means that the k_1 and k_2 constants depend on motor design, construction, any motor deterioration during operation, measurement error and motor's operation slip. In addition, the saturation of motor is assumed the functions of positive and negative sequence voltage. Under an experimentally simulated shorted turn fault, the estimated negative sequence current in Equation 2.20 can be eliminated to obtain portion of stator fault negative sequence current using the measured negative sequence current. The experimental results of this technique using a transient model of induction motor are also given in [24]. Although this is a promising simple compensation technique, and an accurate motor model, no detailed information is given in [24] about detailed interactions of the inherent asymmetry and voltage unbalance. In addition, the results are given to present the magnitude analysis and under no load and rated load only, which are not sufficient to demonstrate the behavior of shorted turn fault under disturbances.

2.4.3 Impedance Calculation and Look up Table

In [7], the compensation of unbalance voltage supply (\mathbf{I}_n^v) was performed by measuring the actual negative sequence voltage \mathbf{V}_n and negative impedance of the motor, Z_n . In this technique, the negative sequence impedance was assumed unaffected by load variation and stator shorted turn fault. Hence, the Equation 2.17 is transformed into Equation 2.21 below.

$$\mathbf{I}_n^{sf} = \mathbf{I}_n - \frac{\mathbf{V}_n}{Z_n} - \mathbf{I}_n^{ia} - \mathbf{I}_n^{in} \quad (2.21)$$

In [7, 23], the non-ideal and non-linear behavior of induction motors in a healthy condition was also examined. The negative sequence current due to non-idealities (\mathbf{I}_n^{ia}) were modelled in a database. The database consisted of a two dimensional map which is a function of positive sequence current and positive sequence voltage, and can be used to eliminate non-ideal and non-linear motor characteristics in a real time. In this studies, the positive sequence voltage and current were used because of their sensitivity to load and voltage supply variations. In [23], a specific threshold for \mathbf{I}_n^{sf} was also defined to trigger the protection level of the motor under test. The threshold was defined as the multiple of combinations of the \mathbf{I}_n^{sf} variance and the line current variance.

2.4.4 Semi-empirical Formula Methods

The limitation of Z_n for the voltage compensations are reported in [8, 9, 25]. The Z_n for unbalance voltage compensation is not constant in many motors.

$$Z_n = \frac{\mathbf{V}_n}{\mathbf{I}_n} = R_n + jX_n \quad (2.22)$$

The resistive R_n and the reactive X_n component of the Z_n which is given above may vary due to various factor such as temperature. In order to overcome this weaknesses an approach was proposed in [8] to calculate the I_n^v as the functions of X_n and the phase angle θ_n .

$$I_n^v = \frac{V_n^v \sin \theta_n}{X_n} \quad (2.23)$$

where, $\theta_n = \text{atan} \left(\frac{X_n}{R_n} \right) = \text{atan} \left(\frac{V_{nx}}{V_{ny}} \right) - \text{atan} \left(\frac{I_{nx}}{I_{ny}} \right)$,

V_{px} , V_{py} are real and imaginary value of positive sequence voltage.

It was reported in [8] that the value of X_n varies due to the degree of unbalance supply and load. To overcome this problem, several factors of inherent non-idealities and non-linearity in the form of a semi-empirical formula was considered in [8]. The X_n was resolved into the equation

$$X_n^{-1} = \gamma_0 + \gamma_1 V_n + \gamma_2 \sin 2\phi_n + \gamma_3 \cos 2\phi_n + \gamma_4 I_{px} + \gamma_5 I_{py}^2 \quad (2.24)$$

where,

γ_0 , γ_1 , γ_2 , γ_3 , γ_4 and γ_5 are constants,

I_{px} , I_{py} are real and imaginary value of positive sequence current, and ϕ_n (orientation of unbalance voltage) = $\text{atan} \left(\frac{V_{nx}}{V_{ny}} \right)$.

In the Equation 2.24 several factors are represented, such as voltage imbalance and its orientation (V_{nx} and ϕ_n respectively), geometrical static eccentricity (sin and cos of ϕ_n), variation of magnetizing current due to main flux saturation (I_{py}) and load change (I_{px}). Therefore, the above equation can be rewritten as

$$I_n^v = V_n \sin(\theta_n) (\gamma_0 + \gamma_1 V_n + \gamma_2 \sin 2\phi_n + \gamma_3 \cos 2\phi_n + \gamma_4 I_{px} + \gamma_5 I_{py}^2) \quad (2.25)$$

Specific non-linear characterization of induction motor with load and main voltage variation in case of a healthy motor condition and zero unbalance supply is also discussed in [8]. It was indicated that in the ideal construction and in a healthy motor, the negative sequence does not exist neither under load nor under main voltage variation. However, due to the asymmetrical non-idealities of the motor, such as variation in the degree of saturation of motor iron or grain orientation of the steel, the negative sequence current which is labeled I_{mly} may occur. The semi-empirical formula for this negative sequence characterization is given below

$$I_{mnlv} = \alpha_0 + \alpha_1 I_{px} + \alpha_2 I_{px}^2 + \alpha_3 I_{py} + \alpha_4 I_{py}^2 \quad (2.26)$$

$$I_n^{sf} = I_n - I_n^v - I_{mnlv} \quad (2.27)$$

where, $\alpha_0, \alpha_1, \alpha_2, \alpha_3,$ and α_4 are constant.

Both Equation 2.25 and 2.26 are used to characterize the motor, which can be given as in Equation 2.27. It was reported in [8] suggested that the γ parameter is determined under supply voltage unbalance, and then calculated under load and main voltage variation. Under real-time conditions, the Recursive Least Square method was used in [8] to obtain the parameter estimation recursively.

Despite the extensive research, studies given in [8, 9, 25], there is a need for further improvement. This is because the characterization was recommended only for young and healthy motors, and the method needs improvement for “old” or existing motors. In addition, the phase angle θ_n parameter in Equation 2.25 was assumed only when phase of \mathbf{I}_n^v and \mathbf{I}_n are similar. However, the \mathbf{I}_n^{ia} and \mathbf{I}_n^{sf} contribution may shift the total phase angle which need to be investigated.

2.4.5 Neural Network Approaches

Instead of using a semi-empirical formula, the neural network approach was proposed in [26] to eliminate any non-linear and non-ideal effects. In this research an unsupervised off-line SOFM (Self Organizing Feature Map) neural network and feed-forward neural network were utilized.

NOTE:
 This figure/table/image has been removed
 to comply with copyright regulations.
 It is included in the print copy of the thesis
 held by the University of Adelaide Library.

Figure 2.11 (a) Neural network based negative sequence-based fault detection, and (b) the feed forward neural network [26].

As can be seen in Figure 2.11(a), the feed forward neural network was used to determine accurately the estimated negative sequence current ($\mathbf{I}_{sn(est)}$) due to inherent asymmetry and unbalance voltage ($\mathbf{I}_n^{in} + \mathbf{I}_n^v$). The feed forward network captured positive sequence voltage (\mathbf{V}_{sp}), negative sequence voltage (\mathbf{V}_{sn}) and positive sequence current (\mathbf{I}_{sp}) in cartesian form of phasors which gives a total of 5 input vectors. The feed forward neural network is detailed in Figure 2.11(b). The Linear and Tanh activation functions were employed to determine the estimated negative sequence current $\mathbf{I}_{sn(est)}$ based on specific weight matrix (\mathbf{W}_1 and \mathbf{W}_2) which were characteristic of the induction motor under various training conditions.

The neural network was trained off-line under varying magnitude and phase of negative sequence, varying load condition, varying fault impedance and number of shorted turn faults. In order to visualize the current condition of the motor, an unsupervised SOFM was implemented, which was trained by the Kohonen network based on the \mathbf{I}_n^{sf} input and magnitude of negative sequence voltage $|\mathbf{V}_n|$. The SOFM classifies the input either into faulty, healthy, unbalanced voltage or into balanced voltage in order to establish the current condition of the motor. To obtain the shorted turn fault negative sequence \mathbf{I}_n^{sf} , the output of

the network estimated the negative sequence due to non-idealities, which subtracted the measured negative sequence \mathbf{I}_{sn} .

Several weaknesses of negative sequence monitoring based on unsupervised off-line SOFM and feed-forward neural network was also investigated in [27]. Firstly, the training required to cover range of operations to anticipate various possibilities of the motor condition. This practice requires extensive data and consumes significant computational resources. In addition, the technique, which is performed in off-line mode, was not suitable for anticipating any new and unknown faults in real condition monitoring. Therefore, the a second method was proposed in [27], namely Continual On-line training (COT), to overcome the off-line neural technique as given in Figure 2.12 (a).

NOTE:
This figure/table/image has been removed
to comply with copyright regulations.
It is included in the print copy of the thesis
held by the University of Adelaide Library.

Figure 2.12 Flowchart of (a) COT for training and monitoring mode and (b) training algorithm of QGMT [28].

The COT basically performs a training task and monitoring task at the same time. In order to do this, for each time interval the captured data was divided into one training section and several sections for monitoring purposes. The weight matrix updating of artificial neural network was carried out continuously considering previous data training. This means that not all the motor operation range was required for training, but only the area near the current operation. Since the COT has a small training data and does not have

a database to extensively track back the previous conditions, the neural network is found to be sensitive only when a significant fault severity level occurs in a short time. Further improvement was also made by introducing Quasi-Global Minimum Training (QGMT) shown in Figure 12.12 (b) [28]. The QGMT complements the weakness of COT using a limited dynamic database which is created and updated continuously only when there is a difference with the current state motor condition. This QGMT contains only recent operation information. Both of these neural networks were combined, but only one was operated for monitoring. For example, the QGMT was used for monitoring, and COT was activated for the motor protection system as soon as a large shift in motor operation occurred.

Research demonstrates the advantages of supervised as well as unsupervised neural network using small training data for negative sequence monitoring, such as low sensitivity to motor loading and unaffected by voltage unbalance. In real condition monitoring applications, however, neural network still requires a large training set of data for each induction motor and each type of faults under entire operating condition. This is because each of induction motor has its own motor characteristic and inherent asymmetry. Furthermore, the nature of neural network is like black box, where any physical relationship between variables or causes is not easy to be studied.

2.4.6 Sequence Impedances Monitoring

The difficulties in using the negative sequence current to identify the shorted turn faults have challenged researchers to explore other technique, namely effective negative-sequence impedance for fault indicators [29, 30]. The effective negative sequence impedance (Z_{neff}) is the ratio of negative sequence voltage (\mathbf{V}_n) and negative sequence current (\mathbf{I}_n) [33]. This ratio is constant for perfectly symmetrical induction motors. It is claimed in the same study that the ratio is significantly unaffected by motor's operating speed.

$$Z_{\text{neff}} = \frac{\mathbf{V}_n}{\mathbf{I}_n} \quad (2.28)$$

The simplicity of this technique has been demonstrated in [11, 29]. However, this technique requires a perfectly balanced supply, since the slightly imbalanced supply may

cause a false alarm in fault detection. Furthermore, to avoid interaction of different negative sequence faults due to shorted turn faults with various disturbances, the sensor gain signals and the induction motor constructions must be also symmetrical.

2.4.7 Sequence Impedances Matrix Monitoring

The sequence impedance matrix (Z_{xy}) was proposed in [31] to utilize the relation between the voltage and current sequence components, as given below.

$$\begin{bmatrix} \mathbf{V}_0 \\ \mathbf{V}_p \\ \mathbf{V}_n \end{bmatrix} = \begin{bmatrix} Z_{00} & Z_{0p} & Z_{0n} \\ Z_{p0} & Z_{pp} & Z_{pn} \\ Z_{n0} & Z_{np} & Z_{nn} \end{bmatrix} \begin{bmatrix} \mathbf{I}_0 \\ \mathbf{I}_p \\ \mathbf{I}_n \end{bmatrix} \quad (2.29)$$

The subscripts p , n and 0 in the above equation represent positive, negative and zero sequence. In the case of a perfect symmetrical motor without any non-idealities, the off-diagonal terms of this equation are zero. The sequence components also do not interact with each other. However, in a practical induction motor, the inherent asymmetry that defines the off-diagonal values are not zero. Therefore, it can be conclude that if there is no significant ground leakage, the zero sequence can be assumed zero. Therefore, the Equation 2.29 can be rewritten to represent this assumption.

$$\begin{bmatrix} \mathbf{V}_p \\ \mathbf{V}_n \end{bmatrix} = \begin{bmatrix} Z_{pp} & Z_{pn} \\ Z_{np} & Z_{nn} \end{bmatrix} \begin{bmatrix} \mathbf{I}_p \\ \mathbf{I}_n \end{bmatrix} \quad (2.30)$$

The impedance matrix Z_{xy} are affected by several factors, including motor constructions, operating speed and any winding faults, which represents the real condition of the motor. It should be noted here that, for a reliable result, the unbalanced voltage effect as well as operating speed should be considered in calculations to represent a realistic case for fault detection. Figure 2.13 summarizes the factors affecting the sequence impedance matrix.

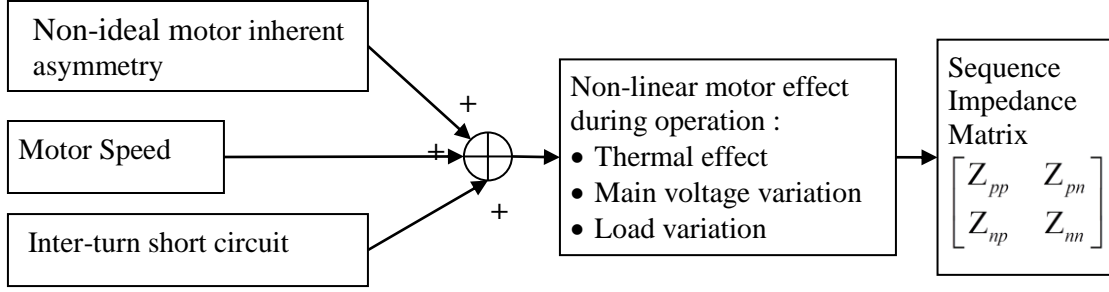


Figure 2.13 Several factors that influence the sequence impedance matrix.

The diagnosis in this monitoring technique is performed by identifying any changes of voltage deviation due to faults, known as voltage mismatch detector [32]. The matrix Z_{xy} is calculated from two separate tests at any same speed, under perfectly balanced motor and sensor. The obtained values of Z_{xy} as a function of various motor speeds are then stored as the reference values to represent the healthy motor condition.

For condition monitoring purposes, the line voltages and currents, \mathbf{V}_p , \mathbf{V}_n , \mathbf{I}_p and \mathbf{I}_n are captured simultaneously. At a given speed, the stored Z_{xy} with \mathbf{I}_p and \mathbf{I}_n are used to calculate the expected values of \mathbf{V}_p and \mathbf{V}_n . The measured and calculated voltages are then compared to find any mismatched values caused by any change in Z_{xy} due to the shorted turn faults.

Another approach based on sequence impedance matrix was also proposed in [31] using fault indicator impedance Z_{pn} . Similar to the mismatch detector [32], the tests are required to determine reference value of Z_{pn} . The Z_{pn} is determined from two independent tests at a certain speed. The first sequence components test ($\mathbf{I}_p^1, \mathbf{I}_n^1$ and \mathbf{V}_n^1) was done without any intentional unbalance voltage. Then, in the second test, the second sequence values ($\mathbf{I}_n^2, \mathbf{I}_n^2$ and \mathbf{V}_n^2) are obtained under unbalanced voltage. The calculated Z_{pn} value is given by

$$Z_{pn} = \frac{\mathbf{I}_n^2 \mathbf{V}_n^1 - \mathbf{I}_n^1 \mathbf{V}_n^2}{\mathbf{I}_p^1 \mathbf{I}_n^2 - \mathbf{I}_p^2 \mathbf{I}_n^1} \quad (2.31)$$

In [31], the Z_{pn} reference value, including sequence components of the balanced set, was stored as a function of speed. Note that the positive sequence Z_p can be used to represent the speed measurement. For monitoring purposes, the calculated Z_{pn} was

compared with the reference value. The deviation of this calculation can be utilized as an indication of the stator faults.

2.5 Conclusion

Several types of negative sequence based condition monitoring which have been discussed in this chapter providing opportunities for further improvements and industrial applications. The previous investigations mostly focus on finding the true value of negative sequence due to faults, either based on utilization of the sequence components or the artificial intelligent approaches.

This chapter provided an overview of the condition monitoring of stator shorted turn faults. The overview was followed by the basic theories of sequence components, which covered phasor extraction techniques, steady state asymmetrical and dynamic negative sequence component calculations. These theories provide valuable information to understand the condition monitoring of stator shorted turn faults based on negative sequence components. In addition, the detailed literature review provides a useful insight in negative sequence monitoring from the basic negative sequence utilization to the advanced techniques of compensations involving complex mathematical implementations.

It was concluded from the literature review that the research in negative sequence component currents received the most attention compared to other sequence techniques. The research in this area has mainly focused on how to obtain accurate results by eliminating the effect of disturbances. In order to achieve accurate results, the compensation approaches mainly aim to employ sequence component parameters or techniques, which are least sensitive to voltage unbalance, load variation, and inherent asymmetry. However, it was found out that there is a little attention given to compare different techniques to obtain the best results. In addition, the previous studies have not been utilized in a systematic manner to develop logical steps for better understanding of each technique. These challenges clearly address the objectives of this thesis which will be developed further in the following chapters of this thesis. As the first step, the next chapter develops the motor model and machine parameters, which aims to provide fundamental

definitions for accurate simulations and verifications for negative sequence detection in condition monitoring of induction motors.

Chapter 3

Induction Motor Models and Determination of Motor Parameters

3.1 Introduction

The introduction chapter of the thesis briefly explained the significance of motor models for fault detection. As expected with an accurate motor model, various faults can be identified and predicted more easily than by experiments. The wide range of faults and their severity levels may be simulated more economically and more safely than by experiments simply by changing their corresponding parameters. In addition, the models can also be used to gain better understanding of the steady state behavior of induction motors as well as their dynamic behavior and the electro-mechanical interactions inside the machine. In addition, the basic machine parameters are determined and analyzed to provide knowledge for further condition monitoring analysis.

3.2 Induction Motor Model

3.2.1 Modeling of Induction Motors

Obtaining an accurate motor model has been a very challenging research direction for many researchers. An ideal motor model should be able to represent a large range of real machines under entire operating conditions.

In addition, the model should have features that are required in condition monitoring, such as complexity, accuracies, sensitivities to faults, disturbances and noise robustness, and ease of integration to expert diagnostic techniques. These requirements also mean that every model may have certain positive characteristics that may suit to a given requirements. For example, a model may be suitable for detailed analysis of a specific fault, but it may be unable to show clearly analysis of any other fault.

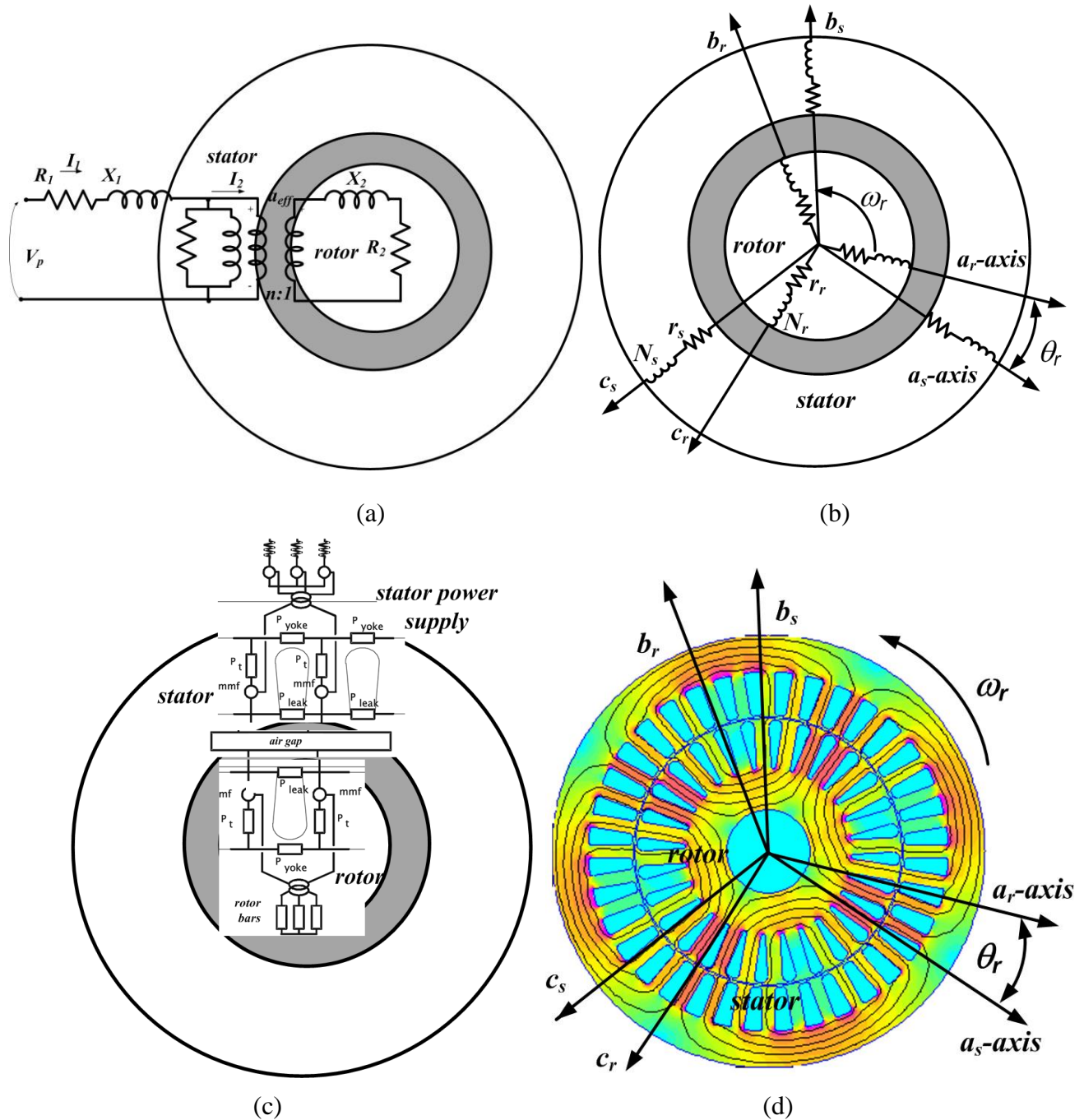


Figure 3.1 Induction motor model (a) T Equivalent Circuit, (b) Multiple Coupled Circuit (MCC), (c) Magnetic Equivalent Circuit (MEC) method, and (d) Finite Element Method (FEM).

In other cases, a model may be reliable for advanced condition monitoring, but require large computation resources, which may not be suitable in an early warning real time online system. Inappropriate model selection may also lead to false alarms when the

model is unable to cope with any disturbances or noise. Therefore, to prove its performance, the model must be validated with real time experiments. An experimental validation can also justify the potential capability of the model to be involved in a certain level of complexity of condition monitoring. Therefore, it is required to consider an induction motor modelling which can be implemented in the condition monitoring system. Figure 3.1 above summarizes various models of an induction motors which have been developed in the literature.

The best known model for understanding the characteristics of an induction motor is the steady state T model, or per-phase equivalent circuit as shown in the above figure. The T model is useful to predict the current, power and torque of induction motors. The T model can also incorporate iron loss, which cannot be done in conventional dq dynamic methods. The T model is widely employed by field analysts and motor designers. Detail of the use of this model to predict the motor parameters is given in Appendix A.1. Despite its advantages, however, the T model cannot be implemented directly to three-phase AC source to obtain the dynamic behavior of the motor. Therefore, dynamic models are developed to overcome such limitations and to provide better understanding of induction motor operation.

As expected, the induction motor dynamic model provides a more realistic simulation tool than a steady state machine model, including the operation under three-phase source. This means that any three asymmetrical phenomena of multi phase motors can be studied in detail. Three of these dynamic models are named in Figure 3.1: Multiple Coupled Circuit (MCC), the Magnetic Equivalent Circuit (MEC) method, and the Finite Element Method (FEM).

In the case of the MCC model, which is also known as the Winding Function Method (WFM), the stator winding current, rotor bar current, and motor voltage are magnetically coupled using loop flux in relative motion [13, 34-37] as illustrated in Figure 3.1 (b). This magnetic coupling aims to simulate transfer of energy between the electrical and mechanical system. The magnetic coupling system also allows this model to determine mutual-inductance between stator winding and rotor loops. The model also considers the influence of stator harmonics because of the stator winding distribution and rotor slotting.

Detail of this model will be given in Chapter 4. This model has also been extended to multiple coupled circuits recently, which is known as the extension of Multiple Coupled Circuit Model (MCCM) [38] and Modified Winding Function Approach (MWFA) for better accuracy [39-41]. This model has been widely investigated and improved due to its suitability for induction motor modeling using simple mathematical functions. The saturations effect of stator inductance [42, 43], and interbar current [15] has been included in the recent studies.

Unlike the MCC, the MEC as shown in Figure 3.1 (c) provides a more detailed motor structure [16, 44-46], which includes multiple flux tubes of an electromagnetic system; each has its own permeance. These tubes are linked together to become a complete model of a magnetic circuit. Based on this technique, the induction motor can be broken down into small elementary magnetic circuits built in around stator and rotor teeth, slots, yokes, air gap, stator windings, and rotor bars. The stator and rotor parts are connected together by air gap modeling, while the magnetomotive force sources are introduced to make a connection between electrical and mechanical parts. Similar to the MCC, the MEC model has also been improved to response to some of the limitations, such as in Dynamic Mesh Reluctance Modeling (DMRM) [47, 48].

Among the motor models, the finite element based model Figure 3.1 (d) has the highest level of computational overhead. FEM uses numerical computation approaches to simulate machine behavior and faults. Several studies show that FEM may produce better and more detailed results, but requires a large amount of computation time [49-52].

Although there are alternative methods to simulate the induction motor, several aspects should be considered to determine the most appropriate model to be used in this research. These include the closeness of the behavior with the healthy and unhealthy motors, the accuracy of the results, the mathematical complexity, the speed of computation, and the requirements of the model output for further fault detection algorithms. For example, in terms of accuracy in relation to computation complexity, the traditional T-equivalent model has the fastest computation time, but it has the lowest accuracy compared with the FEM. On the other hand, the MCC and MEC have intermediate capacity both for the accuracy and computation time [42, 53].

Despite a large amount of research in induction motor models, detailed model validation with real machines has received little attention. For example, the MEC and the MCC model were made and compared in [54] for condition monitoring, but this was not followed by any validation with real machine operation covering entire operating range. Another investigation was undertaken in [55] regarding the FEM and Modified Winding Function Approach (MWFA) model, which is an extension of MCC. In this case, the MWFA showed acceptable results compared with the FEM approach, and had better computation time. However, the model comparison was carried out only to detect frequency of rotor slot harmonics (RSH) for sensorless estimation speed, and was not explored for various fault detection cases. It is clear that comprehensive analysis and validation are required to gain better understanding about the characteristics of a model to be the basis for further fault detection techniques.

Many studies have demonstrated the application of each individual model for fault detection analysis, including advantages and weaknesses for condition monitoring. The applications of these models for fault diagnosis are presented in Table 3.1. Detail comparison of advantages and weaknesses is presented in Table 3.2.

Table 3.1 Modeling Studies of Induction Motors

Faults	Motor Model		
	MCC	MEC	FEM
Stator shorted turn	[13-15]	[16]	[17]
Open circuit in stator winding	[43]		
Broken Rotor Bar	[37, 56]		[57, 58]
Eccentricity	[35]		[59, 60]

Based on comparison from these tables, in this thesis the MCC is selected for modeling purposes. This is because firstly, the model MCC can be extended significantly to simulate various specific mechanical as well as electrical faults. The MCC can be used to simulate stator, rotor and eccentricities faults. Secondly, the MCC has relatively simple mathematical functions and has the fastest computation time compare with MEC or FEM, which may be beneficial for further integration with real time on-line condition monitoring. Thirdly, the FEM may provide the best modeling results; however, if the MCC model can be fed with accurate input parameters the MCC model will deliver sufficient results for

sequence monitoring applications. Furthermore, comparing MCC and MEC, several papers [42, 53] have also mentioned that the performance of the MCC is better than the MEC in several cases. For example, the MCC model allows the study of combination between air gap length and winding distribution in induction motor. In other words, the behavior of the resultant of faults due to stator winding faults, rotor faults, and stator and rotor eccentricity in the resultant model can be determined. Therefore, the MCC-based model can be a promising method to simulate various faults, while the accuracy and computation performances are acceptable for monitoring purposes. In order to prove this, there is a need to understand the performance of this basic couple circuit model better.

Table 3.2 Comparison of induction motor models

Model No	Types	Advantages	Weakness
1	Multiple Coupled Circuit (MCC) [13, 34-37]	<ul style="list-style-type: none"> • Relatively fast computation time • Allows integration with real time control • Load disturbance may be overcome [61] 	<ul style="list-style-type: none"> • Considering several ideal assumptions, such as: air gap should be very small and state of operation far from saturation
2	Multiple Coupled Circuit Model with modification of space harmonic and saturation effect [42, 43]	<ul style="list-style-type: none"> • Considers space harmonic and saturation effect 	<ul style="list-style-type: none"> • Requires further development for broken rotor bar fault
3	Multiple Coupled Circuit incorporating interbar current [15]	<ul style="list-style-type: none"> • Applicable for various rotor incipient faults, including partial broken bar or bad contact between rotor bar of the iron core 	<ul style="list-style-type: none"> • Requires large computation time for large number of rotor and slices (smaller mesh)
4	Multiple Coupled Circuit With Modified Winding Function Approach (WFA).[13, 39-41]	<ul style="list-style-type: none"> • Has better accuracy than traditional MCC, but faster than FEM • Predicts several harmonics 	<ul style="list-style-type: none"> • Not suitable for torque control
5	Magnetic Equivalent Circuit (MEC)[16, 44, 45]:	<ul style="list-style-type: none"> • Close association with the physical field distribution (motor geometry, winding distribution, B-H characteristics) • Less intense computation than FEM 	<ul style="list-style-type: none"> • Not suitable for torque control • Requires accurate permeance parameter around air gap due to rotor and stator slotting • Complexity of the healthy and unhealthy induction motor model
6	Dynamic Mesh Reluctance Modeling (DMRM)[47, 48]	<ul style="list-style-type: none"> • Has better accuracy than MCC and faster than FEM 	<ul style="list-style-type: none"> • Not applicable for torque control • Requires further development for various faults, such as broken rotor bar
7	Finite Element Model (FEM) [59, 60, 62, 63]	<ul style="list-style-type: none"> • Provides detailed information about non-linear effect 	<ul style="list-style-type: none"> • Time consuming computation

3.2.2 The Asymmetrical MCC model

Among the dynamic models mentioned in Table 3.2, Multiple Couple Circuit (MCC)[64] is selected to be used in this research. Justification of this selection was given previously. One of the reasons is that the MCC has a significant capacity to be extended to handle various faults. For example, it can be extended to adapt winding inductances [64] and shorted turn [65] or broken rotor bar [66] faults.

NOTE:
This figure/table/image has been removed
to comply with copyright regulations.
It is included in the print copy of the thesis
held by the University of Adelaide Library.

Figure 3.2 Winding arrangement of two-pole, 3-phase, wye-connected symmetrical induction machine [64].

The basic model of an induction motor has two-pole, stator and rotor side, 3-phase, wye-connection. It can be shown in Figure 3.2 that the stator windings are identical windings with three equivalent turn N_s and resistance r_s . However, in this thesis each stator phase can be assumed to have a different number of turns, N_a , N_b , and N_c with uniform spatial displacement. The ω_r and θ_r illustrated in Figure 3.2 are the angular velocity and angular displacement of the rotor respectively. In addition, the ϕ_s denotes angular displacement of the stator. The rotor type, wound or squirrel cage, is also assumed having identical winding arrangement with equivalent number of turn N_r and equivalent resistance r_r . Other assumptions in this model are uniform air gap, displaced 120° and sinusoidally distributed stator and rotor windings, which

means that only the fundamental effect of the symmetrical windings is considered and all the harmonics effect can be ignored.

3.2.2.1 Basic Voltage Equations of the Machine Variables

The stator and rotor equations for a symmetrical idealized induction machine can be expressed using abc frames as shown in Figure 3.3 and 3.4 for both the stator and rotor with superscript s and r respectively. The flux linkages for both rotor and stator are also involved for the calculation of winding inductances and currents. This abc reference frame is transformed to $qd0$ frames to ease the calculations by employing reference frame transformations as indicated with appropriate subscript in equations. In order to do this, Park's Transformation matrix $\mathbf{T}_{qd0}(\theta)$ and its inverse $\mathbf{T}_{qd0}(\theta)^{-1}$ are applied to stator winding abc voltage. For the Park's transformation, it should be noted that the ω and θ are equal to zero and can be omitted because the q and as axis are assumed aligned.

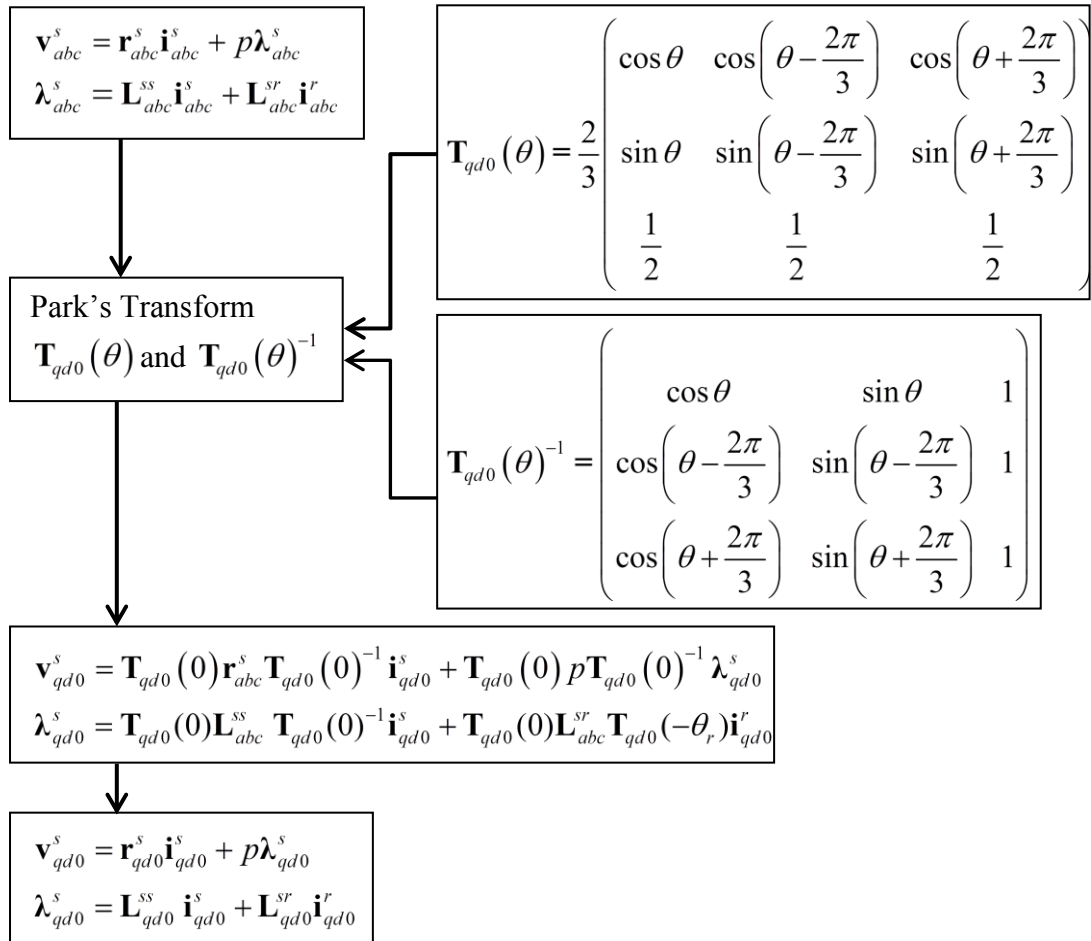


Figure 3.3 Stator basic voltage equations.

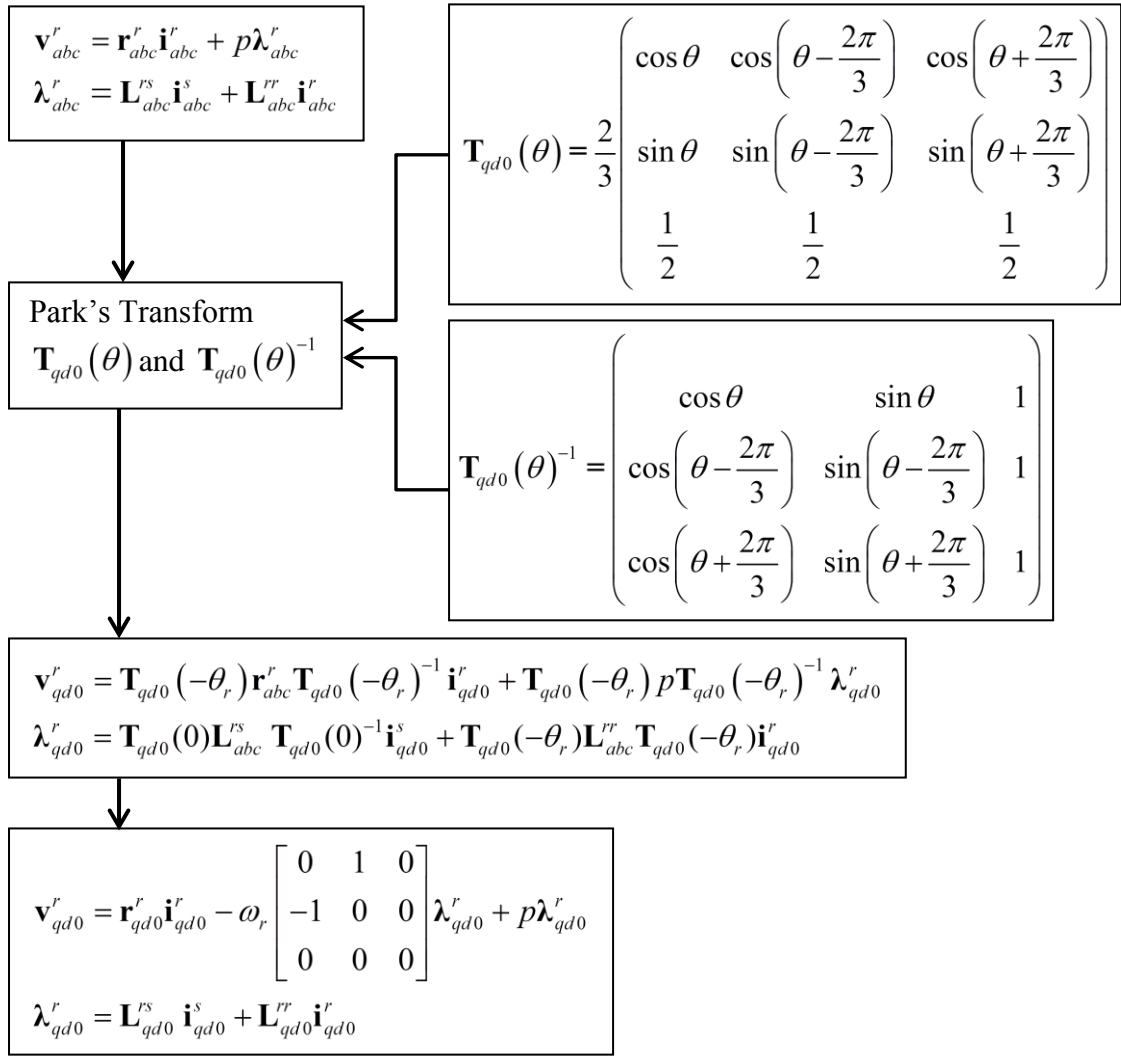


Figure 3.4 Rotor basic voltage equations.

Several variables in figures are given below:

\mathbf{v}_{abc}^x = three-phase voltage of stator (superscript s) or rotor (superscript r),

\mathbf{i}_{abc}^x = three-phase current of stator (superscript s) or rotor (superscript r),

\mathbf{r}_{abc}^x = winding resistances of stator (superscript s) or rotor (superscript r),

$\boldsymbol{\lambda}_{abc}^x$ = three-phase flux leakage of stator (superscript r) or rotor (superscript r),

\mathbf{L}_{abc}^x = three-phase stator self-inductances (superscript ss), rotor self-inductances (superscript rr) or mutual-inductances (superscript sr or rs),

θ_r = rotor angle, and $p = d/dt$.

The same variables are also applied after Park's Transformation, as indicated using subscript $dq0$.

As shown in the above figures, the voltage across stator and rotor windings includes the voltage drops due to resistor components and the non linear differential of voltage behavior due to inductances. Note that the differential flux leakage is transformed into an arbitrary reference frame using Park's Transformation in the equations. Because of these transformations, the stator and rotor variables will be referred to specific rotor frames to remain stationary while rotating at any specific angular velocity. This technique aims to simplify the complexity by eliminating the time-varying inductances which in turn also reduces further potential trigonometric calculation, specifically for the inductances.

The final equations of the voltage and flux leakage equations (λ) after transformations both for stator are also given in the equations. The resistances of the stator and rotor windings are given by Equation 3.1. Note that since the resistance of each rotor phase is similar in a balanced system, the rotor resistance can be assumed $r_{ar} = r_{br} = r_{cr} = r_r$. Therefore, the resistance matrix can be simplified as shown on the right hand side of the equation

$$\mathbf{r}_{qd0}^s = \begin{pmatrix} r_{11}^s & r_{12}^s & r_{13}^s \\ r_{21}^s & r_{22}^s & r_{23}^s \\ r_{31}^s & r_{32}^s & r_{33}^s \end{pmatrix}, \text{ and } \mathbf{r}_{qd0}^r = \begin{pmatrix} r_r & 0 & 0 \\ 0 & r_r & 0 \\ 0 & 0 & r_r \end{pmatrix} \quad (3.1)$$

Note that the stator and rotor resistances as well as the inductances should be determined accurately for a realistic motor model. Therefore, the following sub sections will demonstrate how to obtain these variables accurately.

3.2.2.2 Stator and Rotor Resistance

The transformation is also performed on all voltage equation components, including the stator and rotor resistances and the time varying inductances. The detail of the matrix element of the stator resistance after transformation from abc to $qd0$ frame, $\mathbf{r}_{qd0}^s = \mathbf{T}_{qd0}(0)\mathbf{r}_{abc}^{ss}\mathbf{T}_{qd0}(0)^{-1}$ is given in Equation 3.2.

$$\begin{aligned}
r_{11}^s &= \frac{2}{3} \left(r_{as} + \frac{1}{4} r_{bs} + \frac{1}{4} r_{cs} \right) \\
r_{12}^s &= r_{21}^s = \frac{\sqrt{3}}{6} (r_{bs} - r_{cs}) \\
r_{13}^s &= 2r_{31}^s = \frac{1}{3} (2r_{as} - r_{bs} - r_{cs}) \\
r_{22}^s &= \frac{1}{2} (r_{bs} + r_{cs}) \\
r_{23}^s &= -\frac{1}{2} r_{12}^s \\
r_{32}^s &= -r_{12}^s \\
r_{33}^s &= \frac{1}{3} (r_{as} + r_{bs} + r_{cs})
\end{aligned} \tag{3.2}$$

where N_a , N_b , and N_c are the effective number of turns of the winding a , b , and c respectively. N_s is used for reference turn number in the case of a symmetrical turn motor. The stator resistances of the windings are $r_{as} = (N_a/N_s)r_s$, $r_{bs} = (N_b/N_s)r_s$, and $r_{cs} = (N_c/N_s)r_s$.

In the case of symmetrical rotor resistance, the results of transformation $\mathbf{r}_{qd0}^r = \mathbf{T}_{qd0}(-\theta_r)\mathbf{r}_{abc}^r\mathbf{T}_{qd0}(-\theta_r)^{-1}$ can be assumed similar in each phase. Therefore, the r_{ar} , r_{br} and r_{cr} can be written equal to r_r , and the other elements can be considered zero.

3.2.2.3 Stator and Rotor Flux Linkages and Inductances

The winding inductances under symmetrical stator and rotor windings, are given below.

$$\begin{aligned}
\mathbf{L}_{abc}^{ss} &= \begin{bmatrix} L_{asas} & L_{asbs} & L_{ascs} \\ L_{bsas} & L_{bsbs} & L_{bscs} \\ L_{csas} & L_{csbs} & L_{cscs} \end{bmatrix}, \\
\mathbf{L}_{abc}^{rr} &= \begin{bmatrix} L_{arar} & L_{arbr} & L_{arcr} \\ L_{brar} & L_{brbr} & L_{brcr} \\ L_{crar} & L_{crbr} & L_{cr cr} \end{bmatrix}, \\
\mathbf{L}_{abc}^{rs} &= \left[\mathbf{L}_{abc}^{sr} \right]^T \\
\mathbf{L}_{abc}^{sr} &= \begin{bmatrix} L_{asar} \cos \theta_r & L_{asbr} \cos \left(\theta_r + \frac{2\pi}{3} \right) & L_{ascr} \cos \left(\theta_r - \frac{2\pi}{3} \right) \\ L_{bsar} \cos \left(\theta_r - \frac{2\pi}{3} \right) & L_{bsbr} \cos \theta_r & L_{bscr} \cos \left(\theta_r + \frac{2\pi}{3} \right) \\ L_{csar} \cos \left(\theta_r + \frac{2\pi}{3} \right) & L_{csbr} \cos \left(\theta_r - \frac{2\pi}{3} \right) & L_{cscr} \cos \theta_r \end{bmatrix}
\end{aligned} \tag{3.3}$$

Here the superscripts *ss* and *rr* indicate the self-inductances of stator and rotor respectively, while the *sr* and *rs* refer to the mutual-inductances. The stator self and mutual-inductances can be transformed from *abc* frame to *qd0* reference frame as given in Equation 3.4 and 3.5.

$$\mathbf{L}_{qd0}^{ss} = \begin{bmatrix} L_{11}^{ss} & L_{12}^{ss} & L_{13}^{ss} \\ L_{21}^{ss} & L_{22}^{ss} & L_{23}^{ss} \\ L_{31}^{ss} & L_{32}^{ss} & L_{33}^{ss} \end{bmatrix}, \text{ and } \mathbf{L}_{qd0}^{sr} = \begin{bmatrix} L_{11}^{sr} & L_{12}^{sr} & 0 \\ L_{21}^{sr} & L_{22}^{sr} & 0 \\ L_{31}^{sr} & L_{32}^{sr} & 0 \end{bmatrix} \tag{3.4}$$

$$\mathbf{L}_{qd0}^{rr} = \begin{bmatrix} L_{11}^{rr} & 0 & 0 \\ 0 & L_{22}^{rr} & 0 \\ 0 & 0 & L_{33}^{rr} \end{bmatrix}, \text{ and } \mathbf{L}_{qd0}^{rs} = \begin{bmatrix} L_{11}^{sr} & L_{12}^{sr} & \frac{1}{2} L_{31}^{sr} \\ L_{12}^{sr} & L_{22}^{sr} & -\frac{1}{2} L_{32}^{sr} \\ 0 & 0 & 0 \end{bmatrix} \tag{3.5}$$

Then, for a three-wire system, the flux linkages of stator and rotor windings becomes

$$\begin{bmatrix} \lambda_q^s \\ \lambda_d^s \\ \lambda_q^r \\ \lambda_d^r \end{bmatrix} = \begin{bmatrix} L_{11}^{ss} & L_{12}^{ss} & L_{11}^{sr} & L_{12}^{sr} \\ L_{21}^{ss} & L_{22}^{ss} & L_{21}^{sr} & L_{22}^{sr} \\ L_{11}^{sr} & L_{12}^{sr} & L_{11}^{rr} & 0 \\ L_{21}^{sr} & L_{22}^{sr} & 0 & L_{22}^{rr} \end{bmatrix} \begin{bmatrix} i_q^s \\ i_d^s \\ i_q^r \\ i_d^r \end{bmatrix} \tag{3.6}$$

The elements of stator self-inductances after transformations from \mathbf{L}_{abc}^{ss} to \mathbf{L}_{qd0}^{ss} , or $\mathbf{L}_{qd0}^{ss} = \mathbf{T}_{qd0}(0)\mathbf{L}_{abc}^{ss}\mathbf{T}_{qd0}(0)^{-1}$ are given below.

$$\left. \begin{aligned} L_{11}^{ss} &= \frac{2}{3} \left(L_{asas} + \frac{1}{4} L_{bsbs} + \frac{1}{4} L_{cscs} - L_{asbs} - L_{ascs} + \frac{1}{2} L_{bscs} \right) \\ L_{12}^{ss} &= \frac{1}{2\sqrt{3}} \left(L_{bsbs} - L_{cscs} - L_{asbs} + L_{ascs} \right) \\ L_{21}^{ss} &= \frac{1}{\sqrt{3}} \left(\frac{1}{2} L_{bsbs} - \frac{1}{2} L_{cscs} - L_{asbs} + L_{ascs} \right) \\ L_{22}^{ss} &= \frac{1}{2} \left(L_{bsbs} + L_{cscs} - 2L_{bscs} \right) \end{aligned} \right\} (3.7)$$

In the case of stator to rotor mutual-inductances, the transformation is given by $\mathbf{L}_{qd0}^{sr} = \mathbf{T}_{qd0}(0)\mathbf{L}_{abc}^{sr}\mathbf{T}_{qd0}(\theta_r)^{-1}$. Considering similar number of turn in each rotor phase (symmetrical rotor), the element of stator mutual-inductances will be $L_{asar} = L_{asbr} = L_{ascr} = L_{asr}$, $L_{bsar} = L_{bsbr} = L_{bscr} = L_{bsr}$, and $L_{csar} = L_{csbr} = L_{cscr} = L_{csr}$. Then the elements of these inductances can be given by

$$\left. \begin{aligned} L_{11}^{sr} &= L_{asr} + \frac{1}{4} L_{bsr} + \frac{1}{4} L_{csr} \\ L_{12}^{sr} &= L_{21}^{sr} = \frac{\sqrt{3}}{4} \left(L_{bsr} - L_{csr} \right) \\ L_{22}^{sr} &= \frac{3}{4} \left(L_{bsr} - L_{csr} \right) \end{aligned} \right\} (3.8)$$

For the rotor mutual-inductances, the element of rotor self-and mutual-inductances after transformations become

$$L_{11}^{rr} = L_{22}^{rr} = L_{lr} + \frac{3}{2} L_{mar} = L_{lr} + \frac{N_r^2}{N_s^2} L_m \quad (3.9)$$

Detail of how to obtain the stator and rotor inductances in each phase are given in Appendix A.2.1. The stator and rotor equations, and voltage equations including the flux linkages, are utilized in the induction motor model which will be discussed in the following sections.

3.2.2.4 The Induction Motor Model

For the modeling implementations, the voltage equations which contain differential equations are changed into the integration form. This integration technique

will ensure the numerical stability calculation of the custom written software such as MATLAB SIMULINK. Therefore, the compact form of the motor model in the stationary reference frame can be developed from flux linkages and reactances using $\psi = \omega_s \lambda$ and $X = \omega_s L$. Here ω_s is the synchronous angular velocity.

For a three-wire system, the flux linkages for stator and rotor circuits can be given by,

$$\psi_q^s = \omega_s \int (v_q^s - r_{11}^s i_q^s - r_{12}^s i_d^s) dt \quad (3.10)$$

$$\psi_d^s = \omega_s \int (v_d^s - r_{21}^s i_q^s - r_{22}^s i_d^s) dt \quad (3.11)$$

$$\psi_q^r = \int (\omega_r \psi_d^r - \omega_s r_r^r i_q^r) dt \quad (3.12)$$

$$\psi_d^r = -\int (\omega_r \psi_q^r + \omega_s r_r^r i_d^r) dt \quad (3.13)$$

where ω_t is speed of the machine, and T_{em} is electromagnetic torque. The transformed stator and rotor currents can be obtained by inverting Equation 3.6 :

$$\begin{bmatrix} i_q^s \\ i_d^s \\ i_q^r \\ i_d^r \end{bmatrix} = \begin{bmatrix} X_{11}^{ss} & X_{12}^{ss} & X_{11}^{sr} & X_{12}^{sr} \\ X_{21}^{ss} & X_{22}^{ss} & X_{21}^{sr} & X_{22}^{sr} \\ X_{11}^{sr} & X_{12}^{sr} & X_{11}^{rr} & 0 \\ X_{21}^{sr} & X_{22}^{sr} & 0 & X_{22}^{rr} \end{bmatrix}^{-1} \begin{bmatrix} \psi_q^s \\ \psi_d^s \\ \psi_q^r \\ \psi_d^r \end{bmatrix} \quad (3.14)$$

The speed of the machine and the rotor angle can be obtained from the load model of the induction motor, and given by

$$\omega_r(t) = \frac{P}{2J} \int (T_{em} + T_{mech} - T_{damp}) dt \quad (3.15)$$

$$T_{em} = \frac{3}{2} \frac{P}{2} \int (\lambda_d^s i_q^s - \lambda_q^s i_d^s) \quad (3.16)$$

$$\theta_r(t) = \int \omega_r(t) dt + \theta_r(0) \quad (3.17)$$

where P is the number of poles, T_{em} is the electromagnetic torque, T_{mech} is the externally applied mechanical torque in the direction of motor speed, T_{damp} is the damping torque in the opposite direction of the motor speed, and J is the total system inertia. The rotor angle θ_t can be obtained from integrating the motor speed as given

by Equation 3.17 where the initial rotor angle follows the stator reference phase, i.e. is equal to zero.

3.2.2.5 Voltage Supply Model

Three-phase supply voltage model is required to drive the induction motor model, which can allow to simulate balanced as well unbalanced voltage conditions.

$$\begin{aligned} v_{as} &= (|V_{ag}| - R_{cable_a} |i_a|) \cos(\omega_s t + \theta) \\ v_{bs} &= (|V_{bg}| - R_{cable_b} |i_b|) \cos(\omega_s t - 2\pi/3 + \theta) \\ v_{cs} &= (|V_{cg}| - R_{cable_c} |i_c|) \cos(\omega_s t + 2\pi/3 + \theta) \end{aligned} \quad (3.18)$$

where the $|V_{ag}|$, $|V_{bg}|$, and $|V_{cg}|$ are the magnitude of the supply phase voltages, and the θ is the initial phase angle of supply. The voltage drop in the terminal cable can be included in these equations. Therefore, the voltage supply models can be given by the voltage equation, where R_{cable_abc} and $|i_a|$, $|i_b|$, and $|i_c|$ are the cable resistor and the stator current outputs respectively. To obtain the dq reference frame of the induction motor, the voltage supply is then converted into qd two-axis space given by the following equations

$$v_q^s = \frac{2}{3} \left[v_{as} - \frac{1}{2}(v_{bs} + v_{cs}) \right] = \frac{2}{3} \left[v_{ag} - \frac{1}{2}(v_{bg} + v_{cg}) \right] \quad (3.19)$$

$$v_d^s = \frac{1}{\sqrt{3}} (-v_{bs} + v_{cs}) = \frac{1}{\sqrt{3}} (-v_{bg} + v_{cg}) \quad (3.20)$$

This voltage model is then involved in the software implementation of the induction motor model. The summary block diagram of the complete model is illustrated in Figure 3.5.

3.2.2.6 Implementation of the motor model

The induction motor model is developed using the supply voltage and the stator-rotor voltage equations including the resistor and reactance calculations. The final dynamic model is implemented in MATLAB SIMULINK. The block model is given in Figure 3.5.

Although the induction motor model was originally given in [67] and [9], this thesis provides improvements to simplify the model as well as to improve the reactance and resistance calculations. The voltage supply module was also improved to simulate voltage unbalance easily. The model is also fitted with DFT based sequence analysis as a comparison with the PDT analysis. Furthermore, for the comprehensive analysis, the stator current analysis is included in the improved model.

It is shown in the Figure 3.5 that the supply voltage with external adjustable magnitude and angle provides the dq voltage supply to the motor model. Various motor parameters such as resistance and inductance both for the rotor and the stator are calculated for the voltage equations. The motor model which contains the stator and the rotor voltage equations both for d -axis and q -axis generates the flux linkages at a specific rotor speed. This rotor speed is obtained from an electromechanical module using torque and speed calculations based on the external load information. The stator current of the induction motor in dq -axis are produced after multiplying the flux linkages information of the stator and the rotor circuit in dq -axis with the inverse matrix of the reactance. Finally, the three-phase stator current values are obtained after converting the dq stator current, into the abc reference current which in turn is analyzed using the PDT module for the sequence component fault detection.

3.3 Machine Parameters, Motor Simulations and Experimental Results

3.3.1 Machine characteristic and parameters

One of the important issues in an accurate motor model is to obtain the machine parameters accurately. As the model includes a number of machine parameter. The common rule is that the greater number of machine parameters required, the closer is the behavior of the motor model to the real machine.

Although the machine parameters can be found in the nameplate of an induction motor, they are not usually sufficient to develop a simulation model. Firstly, every machine has own inherent motor characteristics even though they have similar motor power rating. Secondly, certain machine parameters are not always available for the inputs to either steady state model or dynamic motor model. Therefore, it is

beneficial to determine additional parameters, such as leakage reactances for a better understanding of the motor's characteristics.

One of the ways to determine the machine parameters is by using equivalent circuit approaches. This technique is applied to provide basic parameters of a motor model, using simple single phase equivalent circuit. Figure 3.6 illustrates some of the important parameters that can be obtained using such equivalent circuit. These parameters are stator leakage reactance (X_1), rotor reactance (X_2), magnetizing reactance (X_m), stator resistance (R_1), and rotor resistance (R_2).

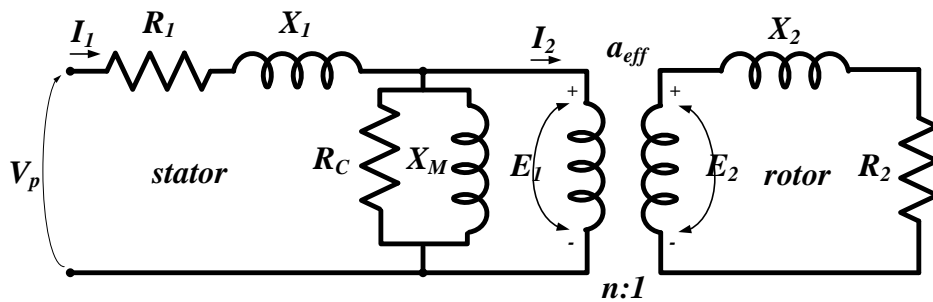


Figure 3.6 Induction motor single phase full equivalent circuit



Figure 3.7 Photograph of the experimental setup with the motor under test and dynamometer.

Based on the equivalent circuit shown in Figure 3.6, three experimental approaches can be carried out to obtain the parameters. These experiments are no load test, the block rotor test of induction motors, and the DC stator resistance measurement. The DC stator winding measurement determines the stator resistance R_1 . Under a block rotor test, the rotor is forced to reach a stationary state at $s=1$ by blocking the rotor rotation and increasing the supply current up until the rated current is reached. This test produces the reactance and the resistance information, such as the stator leakage reactance (X_1), the rotor reactance (X_2), and the rotor resistance (R_2).

The second test is the no load experiment, in which the induction motor is allowed to accelerate up to synchronous speed (slip close to zero). Using the stator power, current and reactive power measurements, the rotational losses, the friction and windage losses, the iron core losses and the magnetizing reactance (X_m) can be calculated. Details of this test is discussed in the Appendix A.1.

Note that the test set up shown in Figure 3.7 is used to obtain the motor parameters that also involved the complete data acquisition, the voltage and current sensors and the signal conditioning units. The details of the data acquisition system will be discussed in the next chapter. The motor under test was a 2.2 kW motor having the machine parameters as given below in Table 3.3..

Table 3.3 Name plate of the motor test for Y connections.

Output Power	2200 W	Rated speed	1415 rpm
Rated Frequency	50 Hz	Cos ϕ	0.8
Line Voltage	415 V	Number of poles	4
Rated Stator Current	4.9 A	Number of turns/phases	282 turns
Rotor Inertia	0.05 kg m ²		

No load and short circuit test results of the motor under test are given below in Figure 3.8.

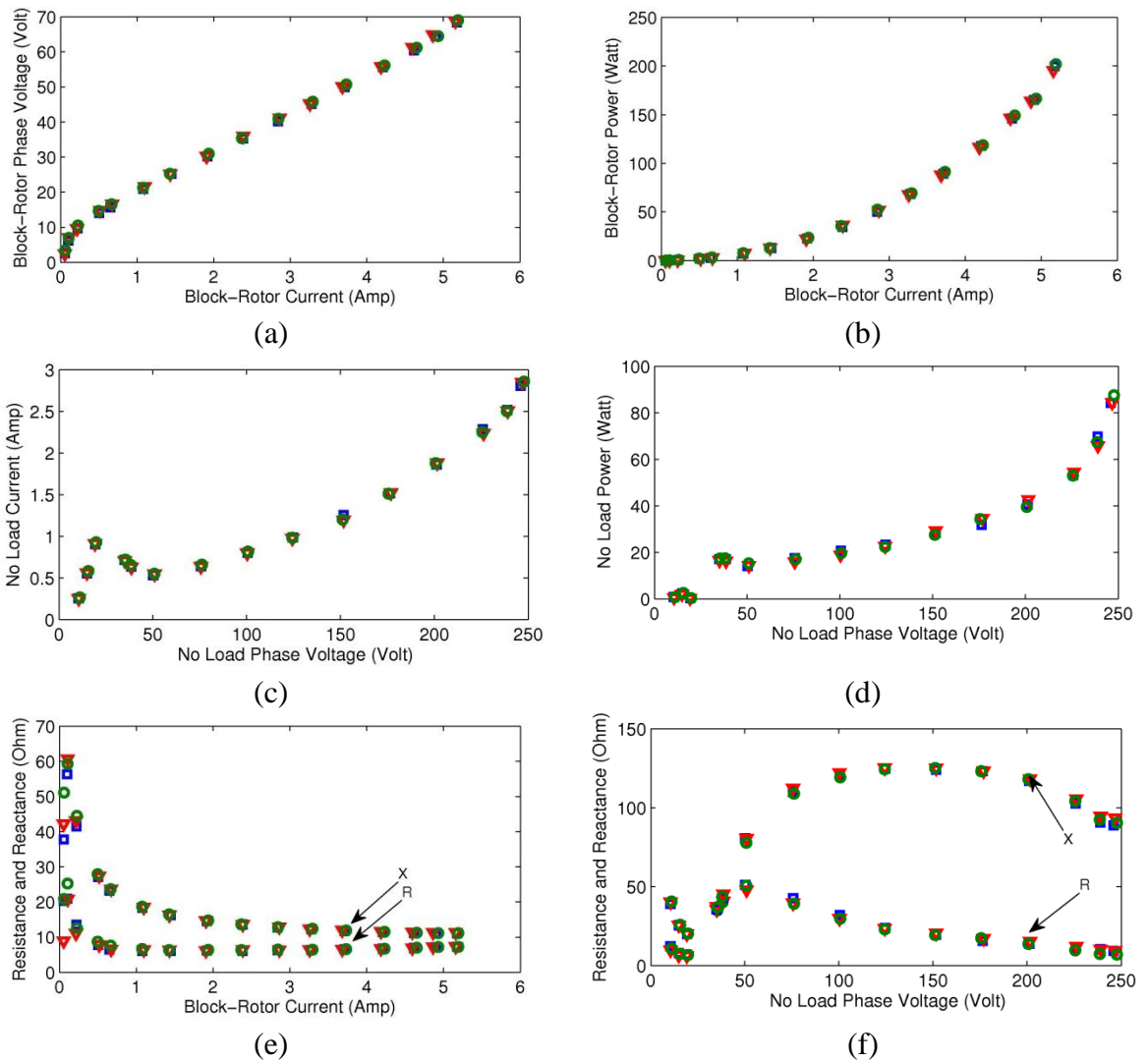


Figure 3.8 The measured and calculated motor quantities of the test motor.

For the block rotor test, several phenomena of the motor's operation can be identified. Figure 3.9 supports the idea that block rotor current usually less than six times of the full load motor current [68]. The block rotor current, which was calculated at rated voltage of 240 V, is about 20 Amp or about four times the rated motor current. Note the non-linear voltage in Figure 3.8 (a) which is due to the saturation of the induction motor. The saturation possibly occurs in the rotor slot wedges especially in the motor which has a type of closed rotor slot. This non-linearity shifts the starting voltage at low stator current. It should be noted that squirrel cage induction motors with power ratings up to several ten kilowatts are usually manufactured with closed rotor slot type construction.

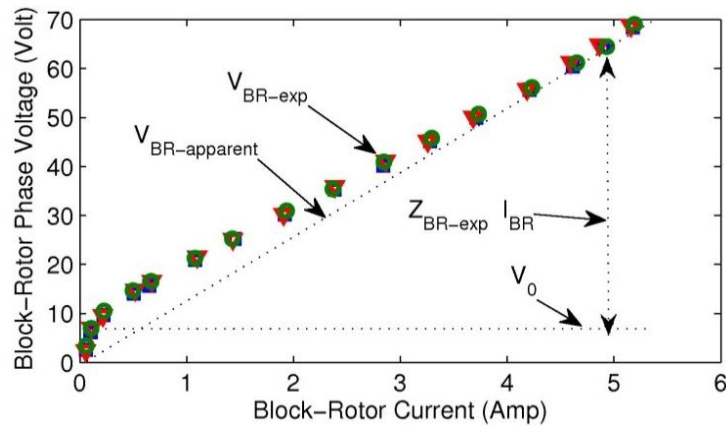


Figure 3.9 Block rotor voltage estimation considering the saturation in the closed rotor slot.

It is shown in Figure 3.9 that the voltage tends to drop at small currents, which in turn shows a non-linearity trend during block rotor tests. The trend will be relatively linear in open rotor slots [69] which is shown as $V_{BR\text{-apparent}}$ in Figure 3.9. In the closed rotor slots type, the saturation occurs due to a relatively high value of the slot bridge rotor radial thickness. In a small rotor current, the slot leakage flux tends to pass through the magnetic slot wedges, in turn creating high slot rotor leakage inductances. These high inductances, as it can be seen in Figure 3.9, will decrease in high current when the rotor slot bridge begins to be saturated. In Figure 3.9, this small voltage drop because of magnetic saturations of rotor slot bridges is illustrated as the voltage generator, called V_0 .

Such non-linearity is hard to avoid. Therefore, it needs to be considered in further analysis. Even though this phenomenon is not taken into account at the rated current operation, this small voltage drop, about 0.6 V, still needs to be considered for better estimation of various parameters in induction motors. One important aspect is that this voltage drop produces slightly different values of the stator reactance (X_1) and the rotor reactance (X_2) in Figure 3.6 between the experimental and ideal (apparent) value of V_{BR} . The correction of the parameters gives better accuracy in terms of simulation results of the induction motor dynamic model.

The presence of the leakage and magnetizing saturation can also be seen in the reactance measurement in Figure 3.8 (e) as the reactance decreases considerably as the current increases. This saturation can be contributed by leakage reactance from both the stator side as well as the rotor side. In the case of closed rotor slot reactance, it was reported that this decrease of total leakage inductance is contributed mainly from

bridge leakage inductance, followed by slot leakage, and air gap leakage inductance [70].

Unlike the block rotor measurement, the no load test shows relatively small saturation, as it can be seen in Figure 3.8 (c). Note that the plot of no load test can be separated into three regions. In the first region (below the 50 V), the stator current increases due to the stator flux leakage and magnetizing saturation. This increase reaches a peak at a certain value (around 20V) when the stator is capable to induce the rotor producing mechanical rotations. In the second region (between 50 V and 239 V), the stator phase current seems relatively linear. In the third region, the presence of core saturation can be identified from a sharp rise plot compare with the previous region at the rated phase voltage of 239 V.

In addition, no load test results in Figure 3.8 (c) also shows that the stator current is about 50% of the rated full load current at the rated line voltage. This ratio confirms that the typical induction motor at the no load current (between 25-60% of full load current) mostly due the magnetizing reactance as given in Figure 3.8 (f). Unlike in the lock-rotor test, in the no load test of Figure 3.8 (f), the reactance increases significantly, before slightly decreasing at around the rated voltage operations. The degree of change in the reactance may be mainly from the change in the magnetizing reactance (X_m) while a slight increasing of resistance at around 50 V may be from the resistance of the core loss (R_c) of the equivalent circuit model.

Another aim of the results presented in Figure 3.8 is to understand the motor behavior under variations of the supply voltage and current specifically under balanced/unbalanced system operation. The voltage and current unbalance are measured to ensure that the motor parameter characterizations are performed properly, as it leads to a better accuracy in the motor simulation studies. In addition, this voltage and current unbalance analysis may also provide base line information of the healthy motor up to rated supply voltage and current levels. As it can be seen in Figure 3.8, the three-phase supply voltage, current and power with respect to the average values do not shows significant changes. To calculate the voltage and current unbalance, the IEEE Standard 141 is selected. The voltage and current unbalance is calculated using Phase Voltage Unbalance Ratio (PVUR) and Current Unbalance Ratio (CUR) respectively as given in the equations.

$$\text{PVUR (\%)} = \frac{\text{Max. deviation from average phase voltage magnitude}}{\text{Average phase voltage magnitude}} \cdot 100\% \quad (3.21)$$

$$\text{PVUR (\%)} = \frac{\text{Max} \left[|V_a - V_{Pavg}|, |V_b - V_{Pavg}|, |V_c - V_{Pavg}| \right]}{V_{Pavg}} \cdot 100\%$$

$$\text{where } V_{Pavg} = \frac{V_a + V_b + V_c}{3}$$

$$\text{CUR (\%)} = \frac{\text{Max. deviation from average phase current magnitude}}{\text{Average phase current magnitude}} \cdot 100\% \quad (3.22)$$

$$\text{CUR (\%)} = \frac{\text{Max} \left[|I_a - I_{Pavg}|, |I_b - I_{Pavg}|, |I_c - I_{Pavg}| \right]}{I_{Pavg}} \cdot 100\%$$

$$\text{where } I_{Pavg} = \frac{I_a + I_b + I_c}{3}$$

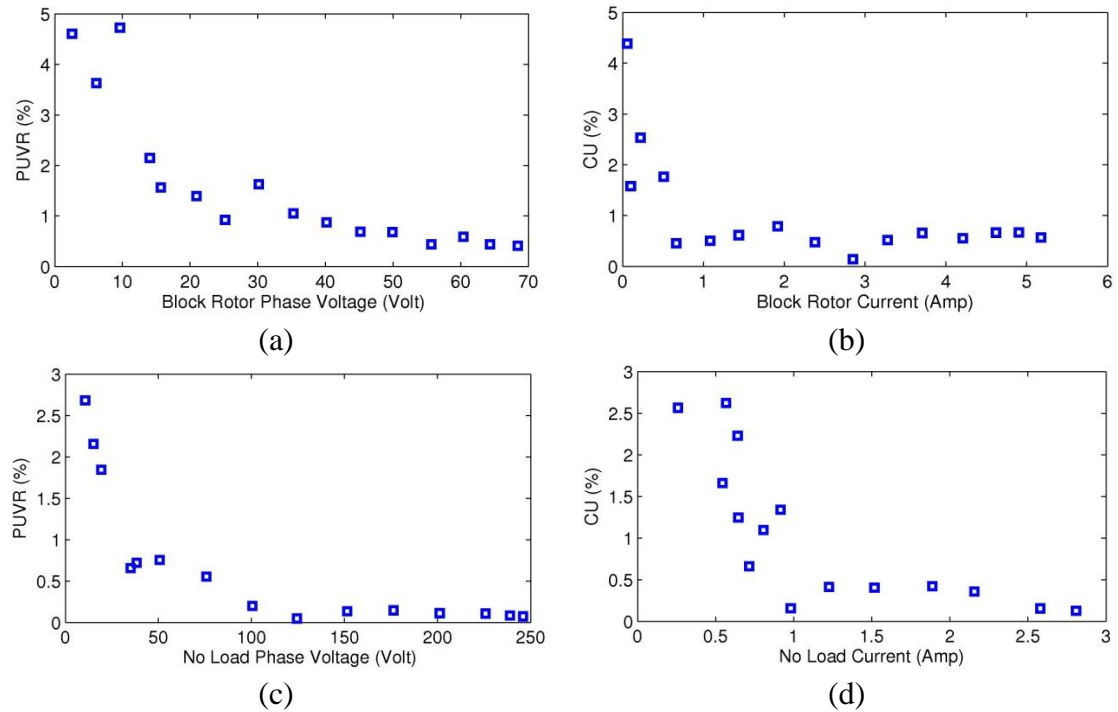


Figure 3.10 Test results of the unbalance operation in (a) block rotor voltage, (b) block rotor current, (c) no load voltage and (d) no load current.

Figure 3.10 shows the calculated results of the data presented in Figure 3.8 to analyze the unbalance in the machine. As shown in figure, high percentage of phase voltage unbalance and current unbalance ratio occurs at low supply voltage and motor current, which is about 5% for block rotor and 3% for the no load test. The rates decrease sharply before reaching a steady value as the symmetrical three-phase stator current and voltage are achieved. At the rated values, the phase voltage and the current

unbalanced ratio is less than 0.5% under no load test and less than 0.8% under block rotor test. Such rate of unbalance is acceptable in the test motor since the unbalance level is within the NEMA requirements (a maximum 2% or even 5%) [71].

It should be noted that a small level of unbalance is desirable at the rated operation for accurate determination of the induction motor parameters. For examples, the voltage unbalance may affect to sensitivity of the magnetizing current and rotor current motor parameters which will lead to a false magnetizing reactance parameter calculation. In this case the over voltage unbalance increases the magnetizing current while the under unbalance voltage reduces it.

Based on the data presented in Figure 3.8, inductances and resistances of the motor can also be obtained, which are used in a steady state equivalent circuit model. Table 3.4 summarizes the calculated motor parameters using the data in Figure 3.8.

Table 3.4 Calculated parameters.

Stator Winding Resistance	5.22 ohm	Stator Leakage Inductance	0.0148 mH
Referred Rotor Winding Resistance	4.65 ohm	Referred Rotor Leakage Inductance	0.0148 mH
Magnetising Inductance	0.312 mH	Rated line voltage	239.6 Volt
Rated output torque	14.85 N.m	Rated input power	2993.81 Watt
Air Gap Power	2332.16 Watt	Rated Efficiency	85.76%

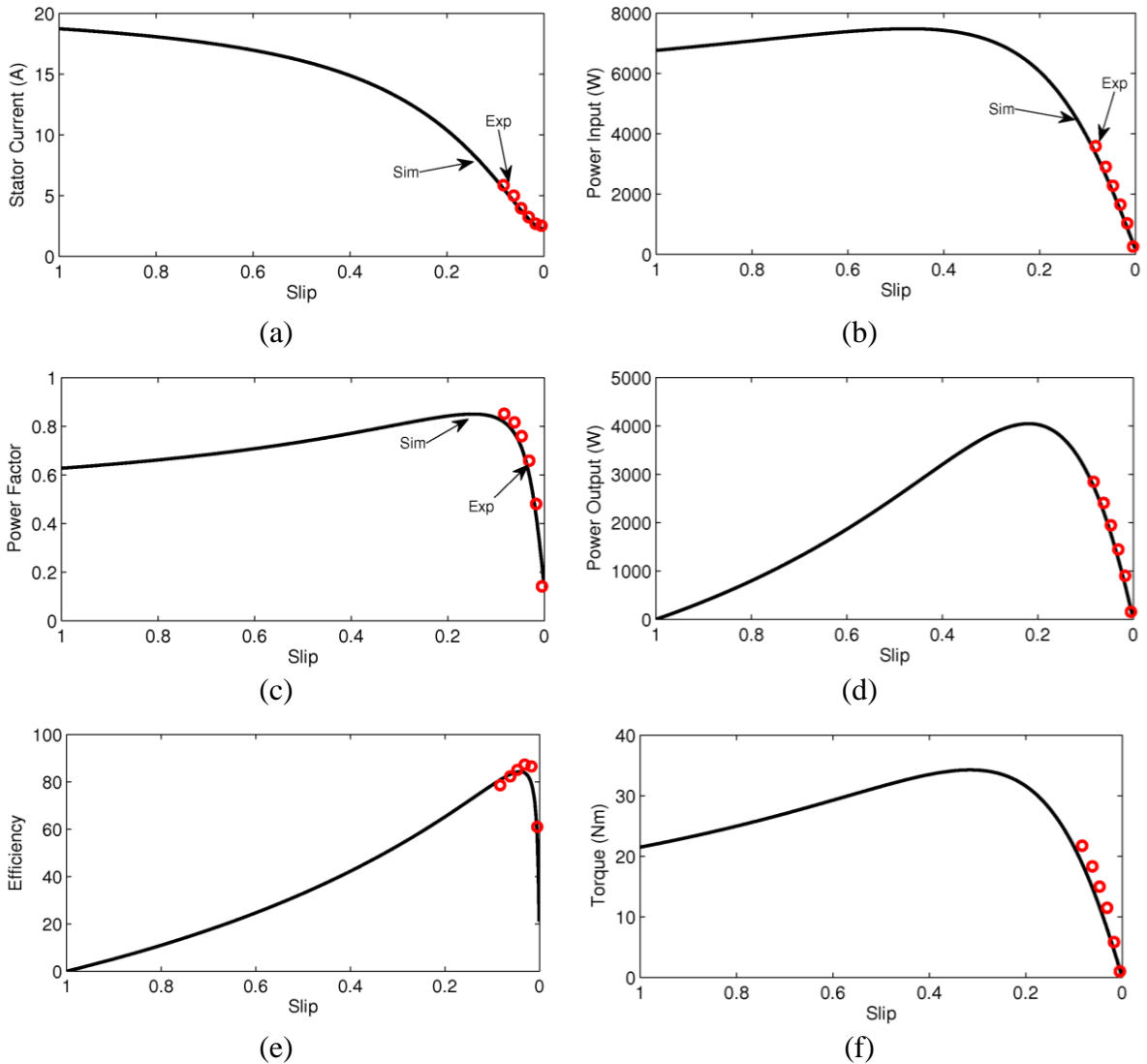


Figure 3.11 As a function of slip, simulated and experimental results of (a) stator current, (b) power input, (c) power factor, (d) power output, (e) motor efficiency, and (f) motor torque.

The typical simulated and experimental performance characteristics of the induction motor under test are given in Figure 3.11 including stator current, rotor current, power input, power output, torque, and efficiency as a function of slip.

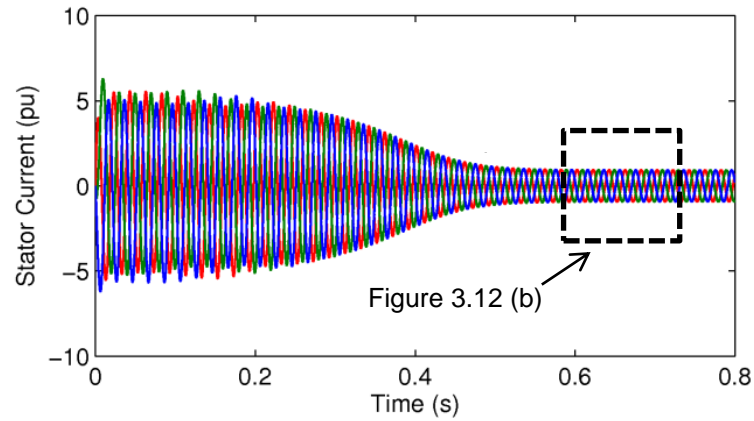
The stator current in Figure 3.11(a) shows the induction motor's stator current characteristics, where the starting current is 4 times of the rated current, which drops significantly at about 75% at the rated speed. Similarly, Figure 3.11(c) shows the power factor of the induction motor as a function of slip (or speed). In the case of no load, the power factor is relatively low due to the high magnetizing current. Then power factor increases with the increasing load, and drops significantly under lock rotor condition.

In the output power characteristic in Figure 3.11(d) the power output is zero at zero speed (and in the block rotor test), which increase about the twice the rated power at around 0.2 slip. Similarly, the efficiency increases proportionally with the motor speed which reaches to a maximum value at 0.1 slip, and then drops significantly under no load. Note that the motor operated efficiency is lower than the maximum possible ideal efficiency, of 94.3%. As seen in Figure 3.11(f), the starting torque is slightly smaller than the rated torque at rated slip of 0.0567, which is also known as the design operating point. The ratio of starting torque (locked rotor torque) and the full load torque is about 1.45 for the test motor, while the ratio between pull out torque is about twice (i.e. 2.3) the full load torque. Note that the motor torque in Figure 3.11 (f) shows similar variation as in the power factor.

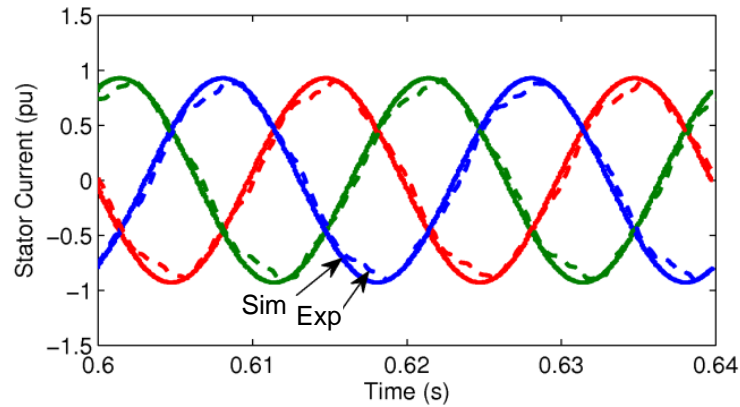
In terms of the model validations, Figure 3.11 (a) to (c) shows that the simulated stator current, power input and power factor characteristic match well to the measured data. At the rated slip, stator current, power input and power factor value are found very close to the nameplate data, which confirms that the model is capable of representing the induction motor characteristics. Note that the power output, efficiency and torque are not directly measured during the experiments. These parameters are derived from primary data shown in Figure 3.8. These approaches arguably can be different to the direct experimental measurement results. However, the technique itself is still beneficial for simplifying the motor performance assessment experiments, while the indirectly calculated values are still acceptable. Detail of these calculations can be found in Appendix A.1.

3.3.2 Comparison of Simulation and Experimental Results

The simulation results of the motor under test under starting operation are given in Figure 3.12 (a), and the simulated and experimental results under steady state operation are given in Figure 3.12 (b). The transient variation of the negative and positive sequence currents during starting up is shown in Figure 3.13. The equivalent T circuit model is employed in this section to compare with the performance of the Asymmetrical MCC Model. The motor model was simulated using the motor parameters which were given in Tables 3.1 and 3.2.



(a)



(b)

Figure 3.12 (a) The simulated three-phase stator current during start up of the healthy ideal motor, and (b) three-phase stator currents showing comparison of the simulated (line) and experimental (dashed line) results.

These results demonstrate that the motor models presented here are suitable to study steady state and dynamic behavior of the motor under test, and can be utilized in the negative sequence component analysis. Figure 3.12 (a) shows the asymmetries of the three-phase stator current due to a start up transient. An enlarged figure in Figure 3.12 (b) is given to illustrate three-phase steady state stator current under fully loading condition. Similar magnitude and phase plots between the simulation and experimental results validate the applicability of the Asymmetrical MCC Model. It should be noted in Figure 3.12 (b) that small “ripple” in experimental results might be due to voltage unbalance or any other inherent asymmetry of induction motor.

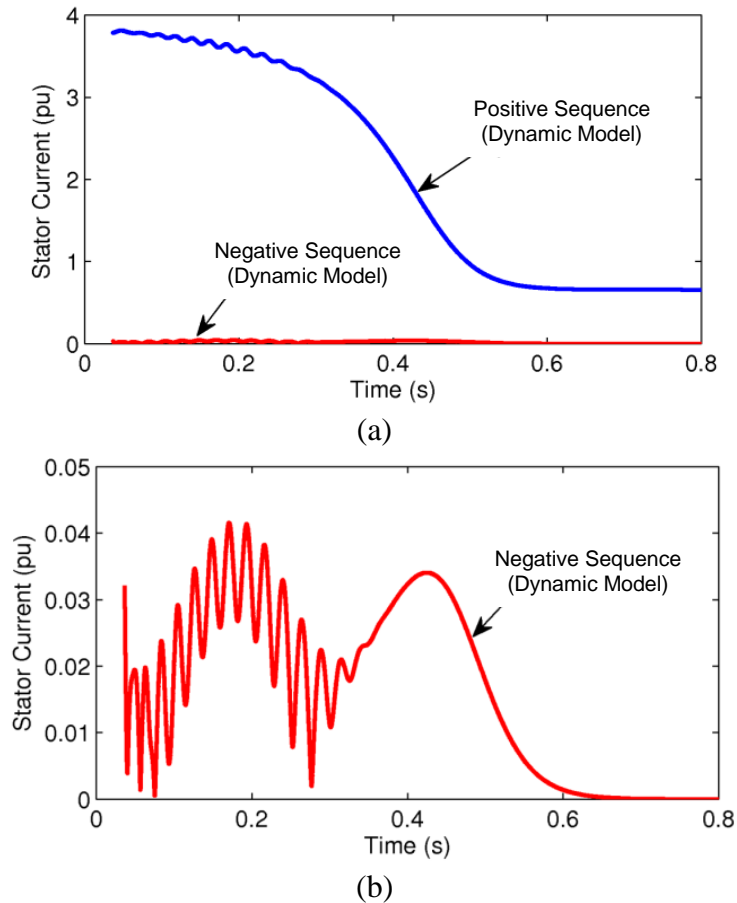
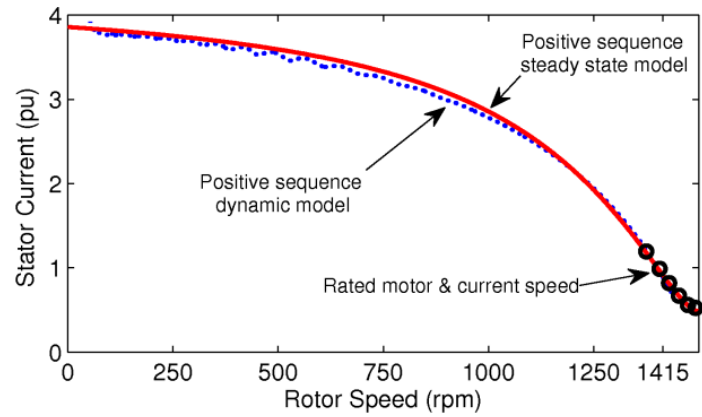
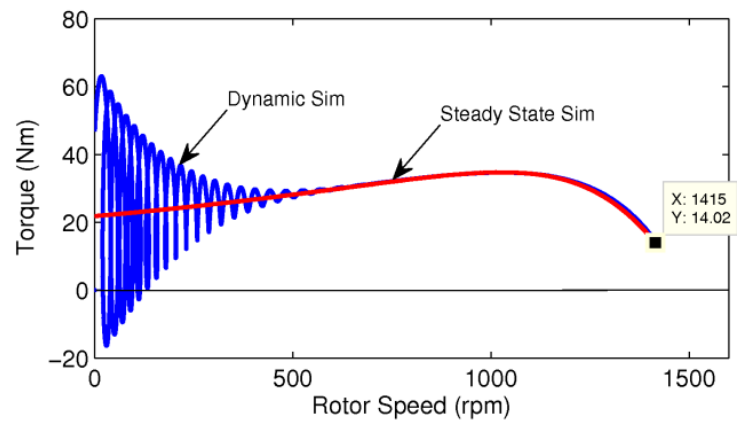


Figure 3.13 (a) The positive and negative sequence current as a function of time of the healthy motor, and (b) the zoom of the negative sequence current.

Sequence components analysis of the stator current of Figure 3.12 is given in Figure 3.13. Figure 3.13 (a) separates the transient operation into positive and negative sequence components. Note that during the starting transient the positive sequence current is about four times the steady state rated current. The negative sequence component is given in Figure 3.13 (b) after scaling the y-axis value. Note that after full speed is reached, due to the symmetrical current, the negative sequence component is equal to zero.



(a)



(b)

Figure 3.14 (a) Comparison of positive sequence stator current of T-model and positive current of dynamic model as a function of speed showing the experimental confirmation results (circle), (b) the comparison of developed torque of steady state T-model and Asymmetrical MCC Model vs rotor speed at normal rotor inertia.

In figures 3.14 (a) and 3.14 (b) the dynamic model was compared with the simple steady state T-equivalent model. The comparison between the steady-state and the dynamic model in Figure 3.14 (a) illustrates that the rated currents between the dynamic and the steady-state models are very close to the experimental value at 4.9 A. Figure 3.14 (b) shows that the transient torque of the dynamic model at rated speed, 14.02 Nm, is very close to the steady state rated torque of 13.82 Nm which is also similar to estimated torque 14.847 Nm based on the name plate data. These results highlight that the dynamic model behavior could be similar to the induction motor.

3.4 Conclusion

This chapter demonstrated the investigation of an induction motor model which utilizes the Asymmetry MCC model as well as the steady state equivalent circuit model. The Asymmetry MCC model is selected based on the literature review of various models of induction motor which are suitable for on-line condition monitoring. Furthermore, detailed investigation of the motor machine parameters provides comprehensive information for the accurate motor models to simulate a real healthy motor during the starting transient as well as during the steady state operation. The experimental results are given to validate the accuracy of the models. It can be concluded that the performance simulation of the motor is matching closely to the experimental results. In other words, the stator current and the voltage supply of the motor model can be used in condition monitoring. It was also demonstrated that the accurate model allows us to utilize motor operation under overload conditions that is not possible in real machine. The practical measurement issues of the negative sequence monitoring will be studied in the following chapter.

Chapter 4

Investigation of Measurement Error of Negative Sequence Components

4.1 Introduction

Although a number of studies has been reported in the literature about the fault diagnosis using negative sequence component, very limited research has been discussed the effect of measurement error on the accuracy of fault detections. It was found that an accurate measurement system is essential to avoid any false alarm, as well as to reduce the negative sequence components due to instrumentation asymmetry.

Therefore, this chapter aims to address this research challenge by investigating measurement issues of sequence components under healthy condition and due to inherent asymmetry in the practical induction motors. In this chapter, a systematic method is presented which included a detailed analysis of the effect of measurement techniques on negative sequence components. The measurement technique involves the calibration steps as well as an on-line calibration method. The chapter also highlights the effectiveness of sequence components in fault detection after the measurement issues are considered.

4.2 Measurement Issues in Condition Monitoring

In terms of condition monitoring practice, the measurements of stator currents allow us to obtain specific parameters, which can be utilized to determine the physical condition of an induction motor. The measurements also aim to ensure that any change in the motor behavior can be quantified correctly to avoid misdiagnosis.

Therefore, several important aspects of measurement need to be considered in such study. These include a good understanding the characteristics of measurement components and understanding of the system calibration including the operating principle of the transducers and the overall accuracy of the system. These aspects will be discussed in the following sections to provide the fundamental principles for the investigations of the effect of instrumentations asymmetry on the negative sequence components.

4.2.1 The Characteristic of the System Components

The measurement system for condition monitoring consists several hardware components including suitable sensors and a data acquisition system. Figure 4.1 illustrates a current transducer and a differential voltage sensor which are used in this study. Figure 4.2 is also provided to illustrate the data acquisition and processing. Note that a data acquisition task contains a multiplexer, a sample and hold function, which can be built from a high speed amplifier, and an Analog to Digital Converter (ADC).

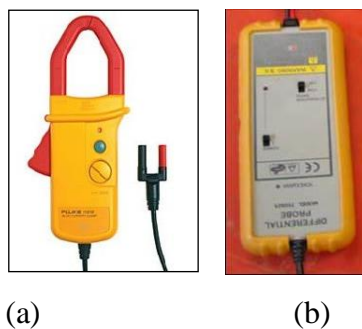


Figure 4.1 An example of (a) Current Sensor and (b) Voltage Sensor.

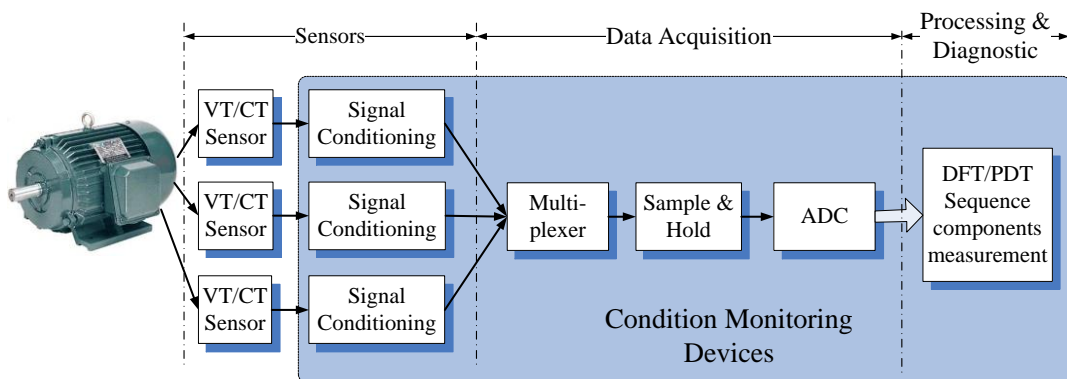


Figure 4.2 A complete hardware structure of a condition monitoring system.

The specifications of the amount and voltage sensor are listed in the Table 4.1. The current measurements are done by sensing the motor currents caused by asymmetrical related problems or specific motor faults. In other words, magnetic flux due to a fault induces fault current components in the stator winding which also results in modulation of the motor supply current.

Table 4.1 Sensor parameters

Measured Quantity	Sensor Type	Sensor Model	Input Range	Voltage Output
Current	Hall Effect Sensor	LEM LTA 50P/SP1 1:1000	0 to ± 50 A	500mV/Amp
Voltage	Differential Isolation Voltage Amplifiers	ISO122P isolation voltage Amplifier	0 to ± 600 V	10mV/V

As shown in Figure 4.2, after the transducers capture the voltage and current signals, signal conditioning block amplifies and filters the original signals. The signal amplification includes a gain amplifier hardware module which has three different gains (1x 10x and 100x). An eight channel 8th order low pass Butterworth analog filter was employed to satisfy the Nyquist Theorem by adjusting the sampling rate at least two times the highest frequency in the measured signals. The filter also has a selectable cut off frequency of 100 Hz or 2 kHz. As expected, this filter avoided any aliasing issues by removing any unwanted high frequency signals. In next step, filtered signals are converted to digital data using the A/D converter, 12 bit resolution at 5 MHz simultaneous sampling.

In this study, the analog sensor signals are sampled at 2000 Hz, which was sampled at 40,000 samples to obtain a 0.05 Hz resolution, with sampling time of 20s. This sampling frequency was found to be sufficient to identify the negative sequence component, which only requires fundamental frequency. In practice, this measurement setting can be simplified according to the hardware capacity as long as the fundamental frequency is captured correctly. However, in this research, the simultaneous sampling and high resolution capture of a large number of samples are useful for the detailed signal analysis to study the measurement errors.

The accuracy of measurement system is also considered in this research. This data acquisition system has minimum voltage sensitivity up to 0.098 mV with current

transducer (voltage output 500 mV/Amp), or equal with 0.196 mA (0.00004 pu of rated stator current). Furthermore, for the voltage transducer with the voltage output 5 mV/V, the minimum voltage sensitivity of line-to-line voltage supply measurement will be 9.8 V or 0.0236 pu. This value is suitable to handle the accuracy of measurement especially for the instrumentation asymmetry which will be discussed in the following section.

4.2.2 System Calibrations

To ensure the accuracy of the overall measurement, sensor calibration is carried out by applying a known input. The target aim is to obtain the same output for the same input signal. Hence, the calibration was done to all three channels of voltage and the current inputs. The measurement circuit configuration is given in Figure 4.3

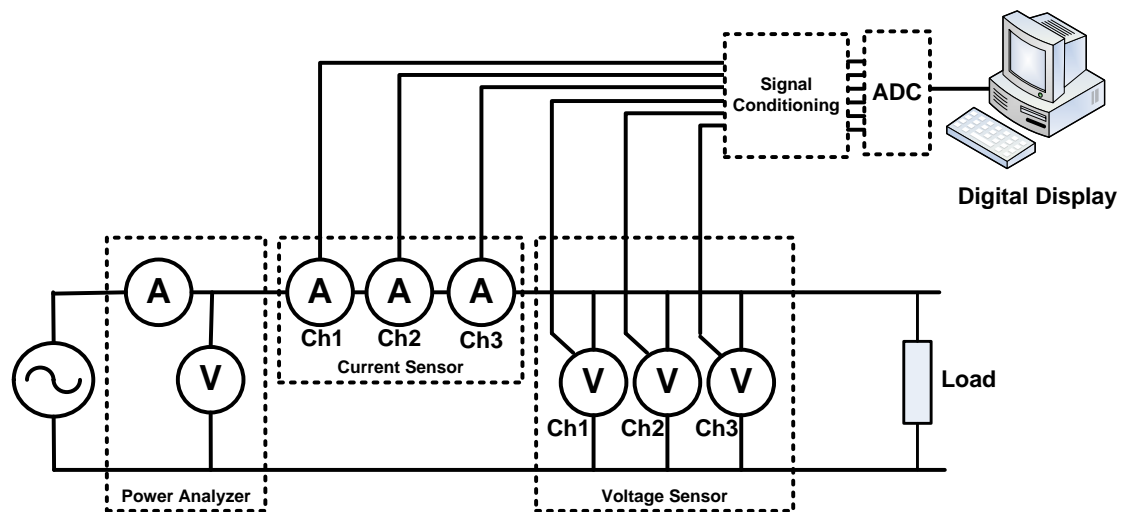


Figure 4.3 Measurement setup for voltage and current calibration.

Note that Figure 4.3 shows a commercial power analyzer which is used as a reference to determine the voltage and current values for calibrations. Three current sensor channels were connected in series to the same voltage source, while three voltage sensor channels were connected in parallel. This configuration ensures that all sensors captured the same current and voltage quantities.

System calibration was done by comparing the observed standard true values of voltage and current from the power analyzer, and the corresponding voltage and current sensor values from the DAQ system. Note that the system calibration not only covers the sensors, but also all other devices in the measurement system. The results are illustrated in Figure 4.4.

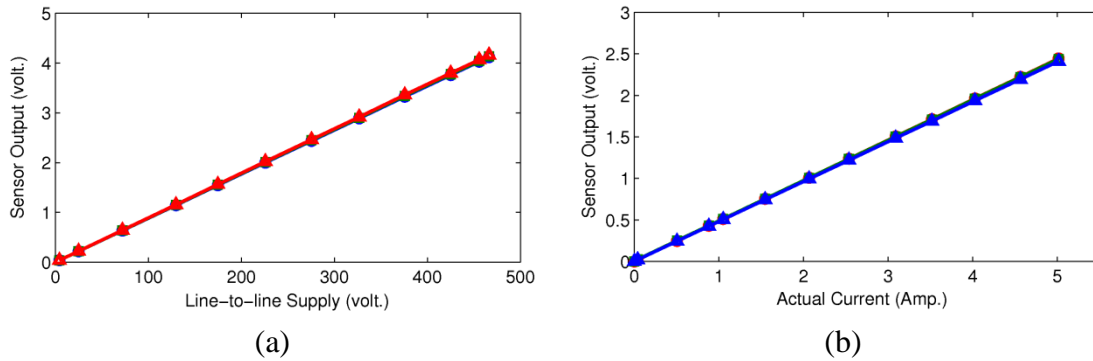


Figure 4.4 System calibration of (a) voltage channels, and (b) current channels.

Figure 4.4 (a) shows the voltage global calibration graph of three-channel voltage measurement systems, while Figure 4.4 (b) is for the current channels. The line voltages and the line currents are the input predictor/regressor shown in these figures. The digital output of the measurement system from the computers is the response parameter for both calibrations. The calibration plots (Figure 4.4) and the calibration equations (Table 4.2) illustrate that three voltage and the current graphs are very similar. This demonstrates that the data can be used for further measurements.

Table 4.2 Voltage and Current Channels Calibration

Parameters	Channel A	Channel B	Channel C
Voltage	$y = 2.4e^{-5} + 8.84e^{-3}x$	$y = 1.06e^{-3} + 8.88e^{-3}x$	$y = 4.56e^{-4} + 8.93e^{-3}x$
Current	$y = -4.93e^{-5} + 0.489x$	$y = -8.19e^{-4} + 0.49x$	$y = -1.07e^{-4} + 0.488x$

Figure 4.4 shows that the intercept of all calibration equation are small, and can be considered as zero. In other words, the calibration equations do not consider any offset to be implemented for the measurement. The coefficient test is carried out to understand the adequacy of the calibration model using the linear regression least square method. To show this adequacy, the hypothesis “t” tests of the slope and intercept coefficients can be done. In the case of voltage channel A, the t coefficient of slope ($8.84e^{-3}$), i.e. $t = 1915.5$ is bigger than probability of value $t_{10,0.05} = 1.812$ (at 95% confidence interval for 12 sample data observation, and 2 parameters estimated) which is considered zero ($P \approx 0$). The probability points out that the straight-line model is adequate, or it has a strong linear relationship between x and y variables. In addition, the statistical test also shows the high probability of the t intercept coefficient. Given the t coefficient of the intercept ($2.4e^{-5}$), i.e. $t = 0.0177$ and

hypothesis at $t_{10,0.05}$, the high probability ($P = 0.986$) shows that the intercept is equal to zero and should be not rejected, which justifies the previous offset assumption.

Furthermore, three other indicators also support the goodness-of-Fit statistic, the residual mean error ($\hat{\sigma}^2$) which close to zero ($6.5e^{-6}$), coefficient of determination (R^2) close to unity (0.99), and the degree of freedom adjusted (R^2) close to 1. These values represent an appropriate fit model for further application in prediction. These similar statistical conclusions are also obtained for other voltage and current channels. It can be concluded that the regression analysis of calibrated channels shows a linear respond of the measurement system and significant relationship between the predictor, line-to-line voltage or current supply, and the response, the voltage output of measurement system.

The measurement system calibration can also be validated experimentally using the residual test in addition to the previous statistical test. The residual error which is defined by the difference between the actual observation value and the corresponding response values from calibrated channels, can be assessed visually as given in Figure 4.5.

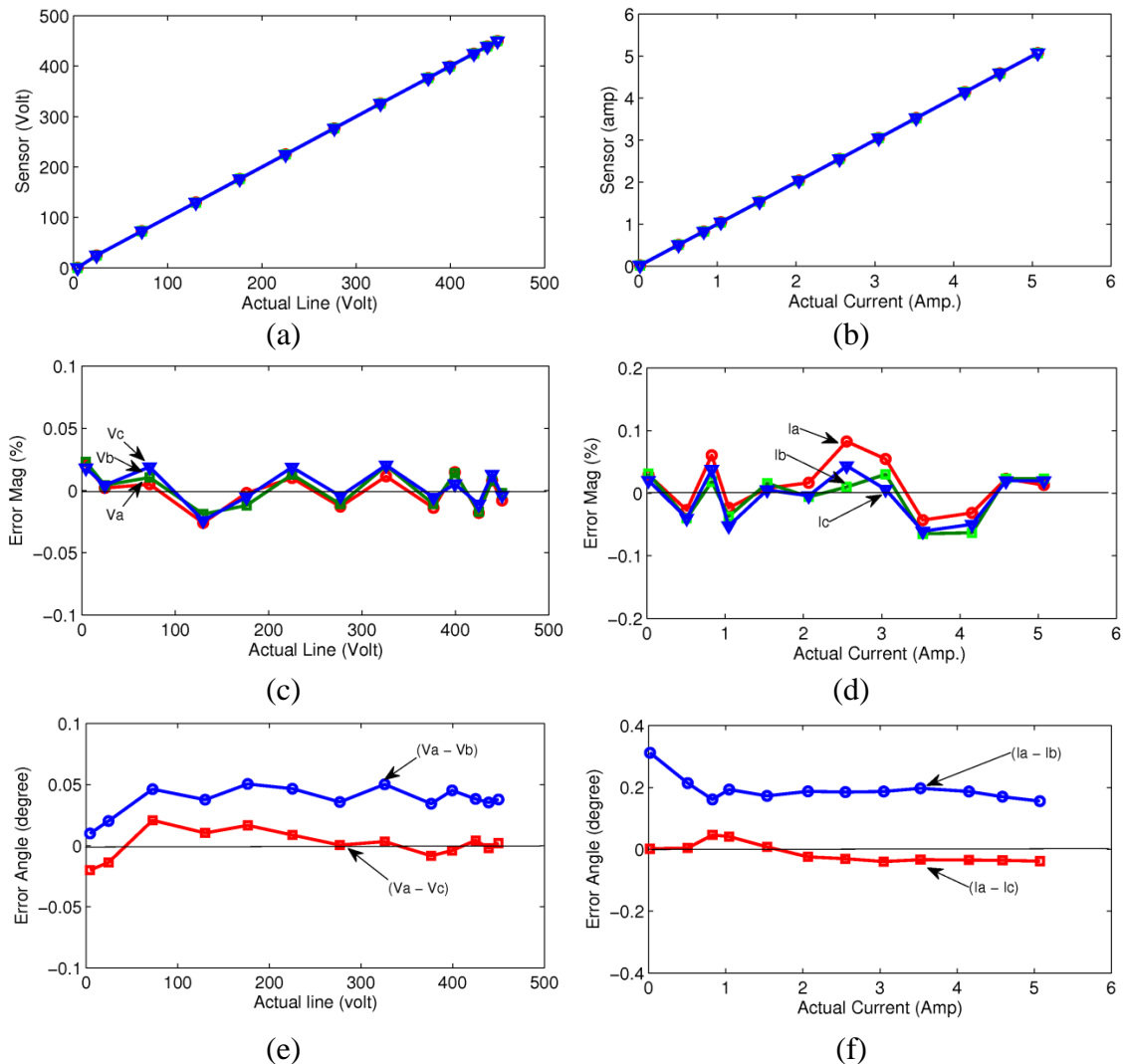


Figure 4.5 Response analysis of the actual signals and the calibrated signals: (a) voltage measurements, (b) current measurements, (c) the magnitude error in voltage measurements, (d) the magnitude error in current measurements, (e) relative angle error of voltage measurements, and (f) the relative angle error in current measurements.

Figure 4.5 shows the comparison of voltage and current measurements between the actual values and the output values of each calibrated channel. A second test has also been performed to obtain the error using the calibration equations of each channel. The error is calculated using the data obtained in the condition monitoring system and the output of the power analyzer, which is then given as a percentage of ideal full scale output. Note that, this error percentage is the ratio between the error and the full scale reading output. Figure 4.5 (a) and (b) illustrates the magnitude comparison of the current and voltage measurements respectively.

Figure 4.5 (b) and (c) shows that in terms of line voltage, the error percentage is relatively small, less than 0.1% or 0.12 V reference to the rated phase voltage, and

less than 0.1% or 0.0049 A reference to the rated current. These values can be considered acceptable for the current sequence component analysis. Note that the error analysis gives confidence that the system has acceptable accuracy in terms of the magnitude analysis for the sequence analysis. Figure 4.5 (b) and (c) also illustrates that the calculated error does not appear to be predictable, which demonstrates that the previous regression model is adequate since it does not require any additional term for the calibration equation

In addition, Figure 4.5 (e) and (f) illustrates the angle analysis of voltage and current measurement respectively. The angle error analysis is defined as the relative angle difference between two phase, such as between V_a-V_b and V_a-V_c . The ideal results show that the voltage channels have smaller difference compared to the current channels. The phase a and phase c are found to have similar angles, a constant 0.05° difference to the voltage channels and a constant 0.2° difference for the current channels. Although these are relatively small differences, a new technique has also presented in this study to reduce the error to increase the accuracy of the sequence analysis. The simple technique can be implemented by subtracting the difference with the angle difference around the rated value. In order to understand the effect of this correction, the negative sequence analysis based on this sensor calibration is implemented and shown in the next section.

4.3 Measurement Issues in Negative Sequence Monitoring

4.3.1 The negative sequence analysis including the phase angle corrections

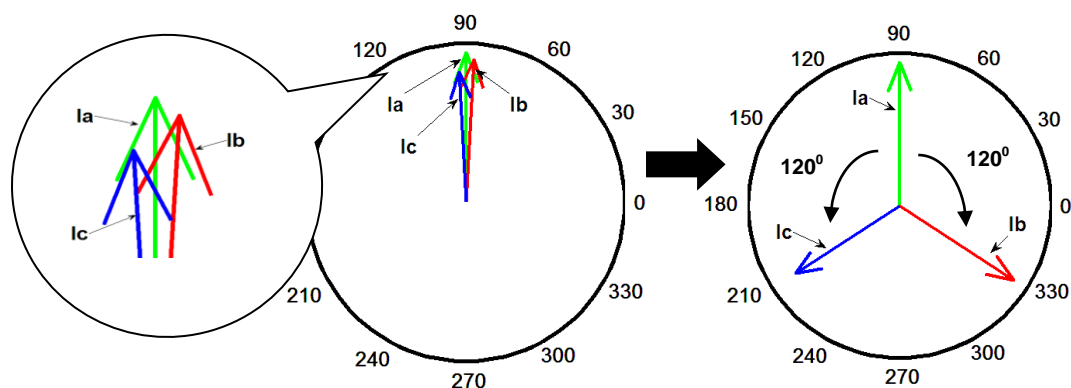


Figure 4.6 Angle displacement for the sequence component analysis of the measurement system.

The negative sequence analysis of the measurement system is presented in this section. The previous data measurement using the test set-up shown in Figure 4.3 is employed in the sequence analysis. Note that since the three-phase current and voltage measurements are obtained from the same source, the three-phase phasors have behavior close to the zero sequence components, which are given in Figure 4.6.

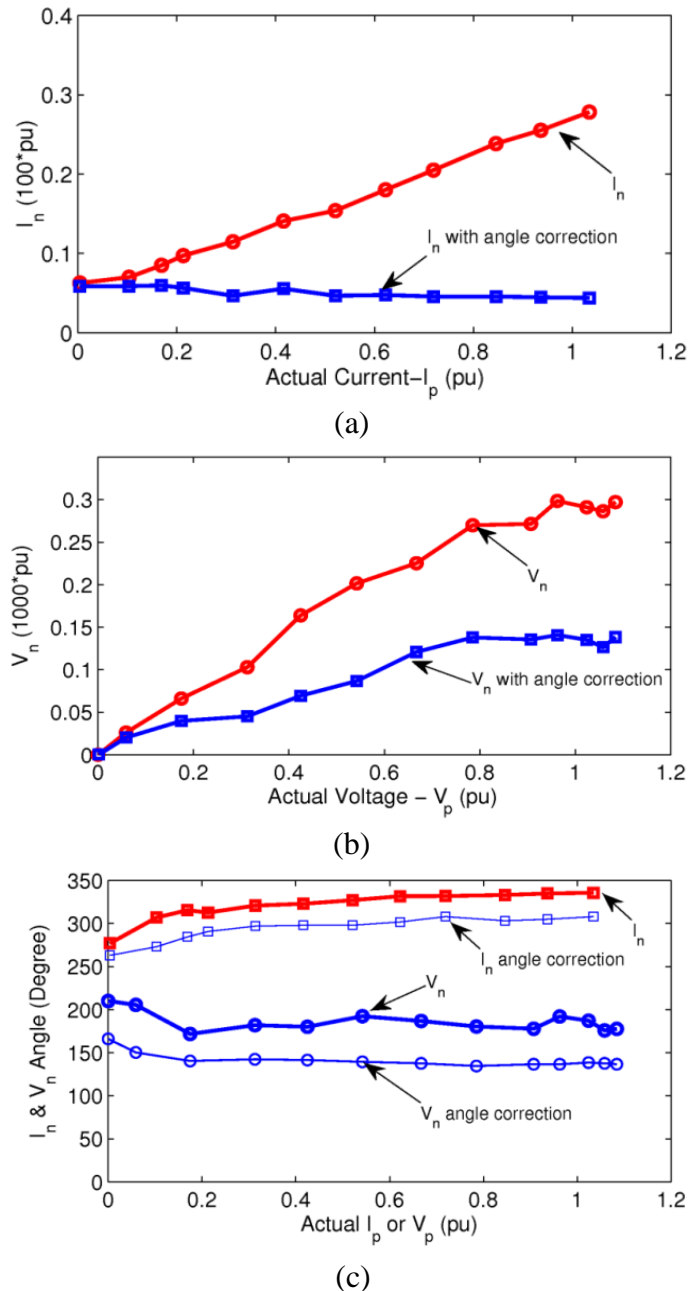


Figure 4.7 Magnitudes of the negative sequence components due to the measurement system asymmetry, (a) current, (b) voltage, and (c) their angle. Note that for the angle analysis, the reference angle V_p is 90^0 .

The most left figure in Figure 4.6 illustrates the original phasors of three current channels, which has a relatively similar angle direction to the zero sequence

components. In order to obtain the negative sequence component phasors, the two phasors, I_b and I_c are displaced 120° from I_a as shown. Note that this displacement provides a phasor sequence resembling the phasor sequence of the negative sequence component, and this technique identifies the negative sequence components since the measurement system has no disturbances, especially due to the voltage unbalance. The results of the angle displacements are illustrated in Figure 4.6.

Figure 4.7 demonstrates the effect of measurement on the magnitude of the negative sequence components. The negative sequence components are presented using per unit value where the base quantity is the rated values of the induction motor under test. Figure 4.7 (a) shows that the negative sequence of the measurement system tends to increase proportionally with the current or supply voltage. Referring to the previous error analysis figure, the significant contributor to the negative sequence component is likely to be the angle differences. Figure 4.7 (a) also demonstrates the relatively similar negative sequence current after the angle correction. This similar value can be assumed as the actual value of the negative sequence due to measurement system asymmetry. The constant value is relatively small, less than 0.0005 pu or 0.00245 A at the rated voltage. This value can also be used as the minimum detectable negative sequence component for the stator current.

In terms of negative sequence voltage analysis, Figure 4.7 (b) presents the effect of the asymmetrical instrumentation. The result shows that the measured negative sequence voltage is very small compared with the voltage supply operation where the maximum value is about 0.0003 pu or 0.07188 V. The voltage negative sequence does not indicate any offset around the 0 V which indicates that the voltage unbalance does not exist. The accuracy of the negative sequence voltage value can also be increased by applying the angle correction as in the current measurement correction. The results of the negative sequence voltage after angle correction are also presented in the Figure 4.7 (b). Unlike the current negative sequence, the angle correction of the voltage negative sequence does not completely eliminate the negative sequence voltage. However, the negative sequence voltage has unchanged around the rated phase voltage. This phenomenon, as for current measurements, can also be used to determine the minimum detectable negative sequence voltage in the condition monitoring.

Figure 4.7 (c) illustrates the angle shift of the negative sequence components due to the three-phase angle phasor corrections. The negative sequence current angles shift about 30° , while it is about 40° in the voltage. These shifts show that small differences of the phasor angle between each phase, such as 0.2° for current and 0.05° for voltage, are sufficient to produce significant phase angle differences in sequence component analysis. Fortunately, the magnitude of the current and the voltage negative sequence component is relatively small. Therefore, it is considered that the negative sequence due to angle error may not affect the overall phasor. This will be considered in the following chapters. In addition, the effect of the temperature variation both in the instrumentation and the motor under test will be investigated.

4.3.2 The effect of temperature on the measurement

The measurement set up used in this section is given below in Figure 4.8.

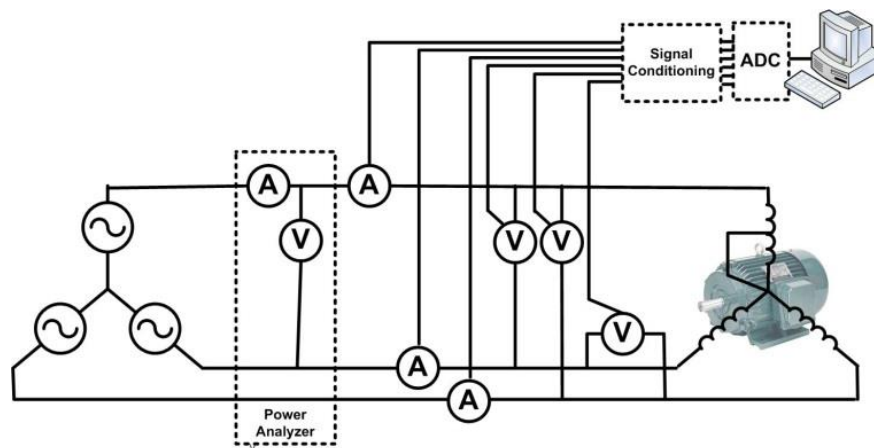
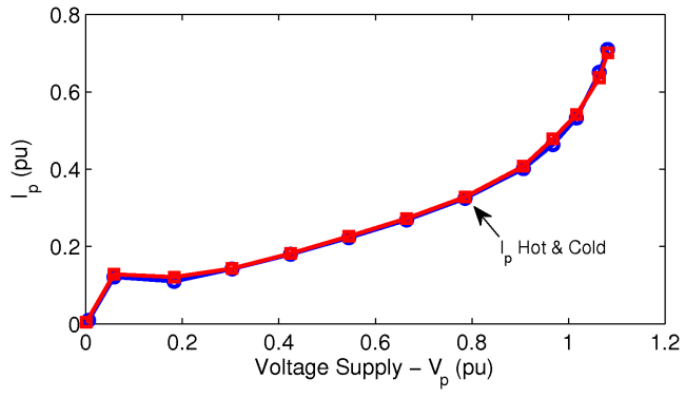
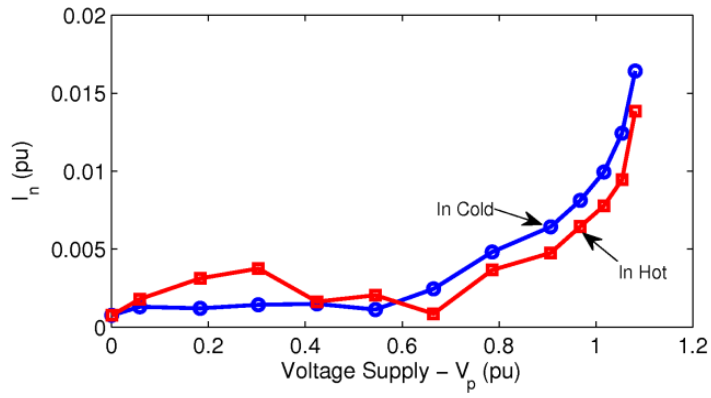


Figure 4.8 The test setup for the hot and cold measurement.

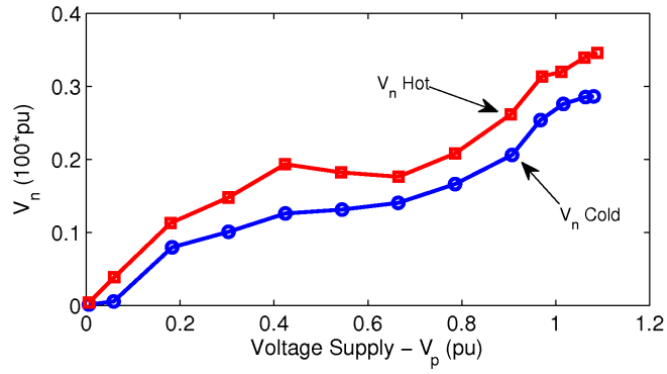
Using this test arrangement, two separate tests were carried out. In the first tests, the no load cold test, the data is captured during the first 15 minutes after the induction motor, including the measurement system, is turned on. The no load hot measurements were obtained after operating the motor at full load condition for about half an hour. After the full-load operation, the test motor was uncoupled from the DC load and the measurement were performed under no load condition. The tests were carried out by varying the supply voltages step by step up to more than the rated voltage supply voltage. The tests demonstrate the effect of hot and cold operation, and can also be used to study voltage variation effects on the negative sequence. The test results of the analysis are presented in Figures 4.9.



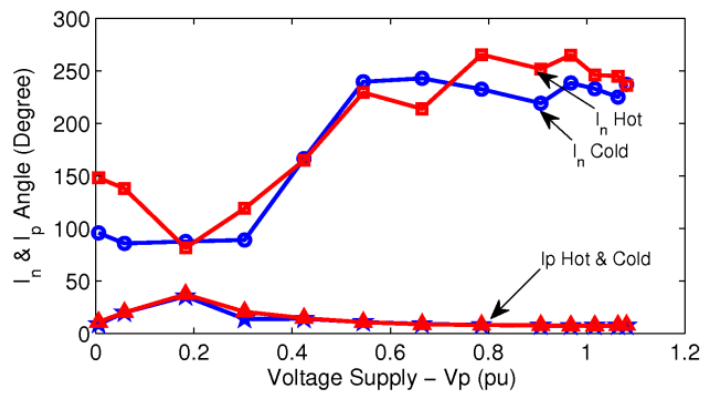
(a)



(b)



(c)



(d)

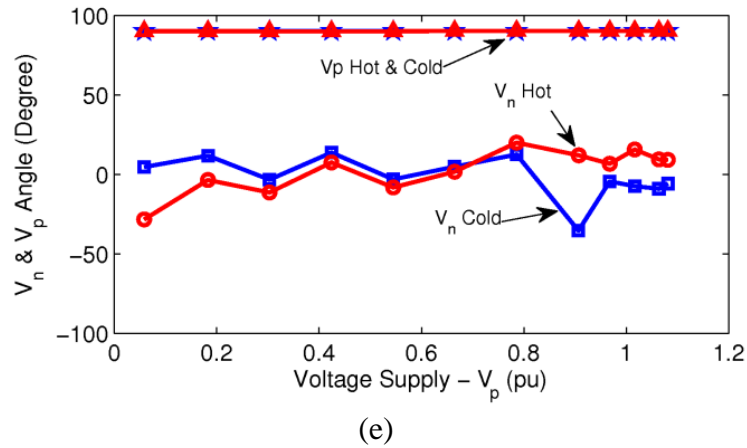


Figure 4.9 The effects of the hot and cold operation on (a) stator current positive sequence components I_p and V_p , (b) magnitude of stator current negative sequence I_n , (c) magnitude of voltage negative sequence V_n , (d) the angle of I_n and I_p (e) the angle of V_n and V_p where the reference angle V_p is 90° .

Figure 4.9 illustrates the effect of hot and cold operation on negative sequence components. It was found that the positive sequence components are not effected under hot and cold operation. The results also confirm the saturation effect as it was discussed in Chapter 3 for the machine parameter investigations.

Figure 4.9 (b) and (c) show the two components of the negative sequence which are due to inherent machine and measurement asymmetries. To determine the percentage of each contributor, the measured negative sequence are compared with the negative sequence arising from measurement only. It was found that in the case of stator current, the negative sequence due to measurement issues was around 0.0025 A, while the total measured negative sequence at the no load rated voltage (see Figure 4.9), is about 0.034 A. These results indicate that the negative sequence due to measurement issues is about 7.4% of the total measured negative sequence of the healthy motor. This value denotes that the remaining percentage may be due to the inherent asymmetry of the induction motor or the voltage supply unbalance. Hence, negative sequence voltages will be examined in the later chapters.

In Figures 4.9 b and c, the effects of hot and cold measurement on the current negative sequence components and the voltage negative sequence, are shown respectively. Note that the negative sequence current component can be identified clearly above 0.7 pu value of voltage supply. The cold measurement gives a higher negative sequence value than the hot measurement. The difference is about 0.0022 pu value at the rated current, or there is a decrease of about 28% at the rated value reference to the cold measurement. Note that the difference may be caused by the

increase of winding resistance under the hot condition, which in turn lowers the stator current negative sequence. In case of the voltage, the negative sequence voltage under hot measurement has a larger value than in the cold test. The difference is about 0.00045pu or 0.108 V. This difference corresponds to 14% of the total measured negative sequence. This negative sequence voltage, even though it is small, indicates that voltage unbalance may contribute to the test results significantly.

The angle measurement results are given in Figure 4.9 (d) and 4.9 (e) for the negative sequence current and voltage respectively. In the case of positive sequence current and the voltage, there are no differences in phasor angle between the hot and the cold measurements. However, the current and voltage angle of the negative sequence show small and consistence differences between hot and cold measurements, especially around the rated voltage. The results indicates that hot measurement, changes both the magnitude of the negative sequence magnitude and the angle slightly. This confirms that it is necessary to investigate both magnitude and angle of phasors to obtain accurate results.

As the previous positive sequence graph, the negative sequence stator current also presents saturation as illustrated in Figure 4.9 (d) around the rated voltage. The sharp raise in the figure around the rated voltage also indicate that the negative sequence due to inherent asymmetry should be carefully mapped to the voltage variations. This approach avoids false identification of inherent asymmetry due to the small variations around the past varying region.

The comparison of Figure 4.9 and Figure 4.7 can provide an insight about to understand the percentage of each contributor. It was found that the negative sequence due to the measurement errors in this research is about 7.25% of the total measured negative sequence of the healthy motor. This value denotes that the remaining percentage may be due to the inherent asymmetry of the induction motor or may be due to the external voltage unbalance.

4.4 On-line Calibration

One of the challenges in the sequence measurement is how to measure the negative sequence components accurately under various conditions, which heavily relies on the calibration of measurement systems. For a new induction motor, the

calibration can be done easily by stopping the motor. However, for an existing and continuously running induction motor, understanding the motor's inherent asymmetry is not easy task. In this section, an online calibration method is introduced as a means of adjusting the gain as well as removing any zero sequences.

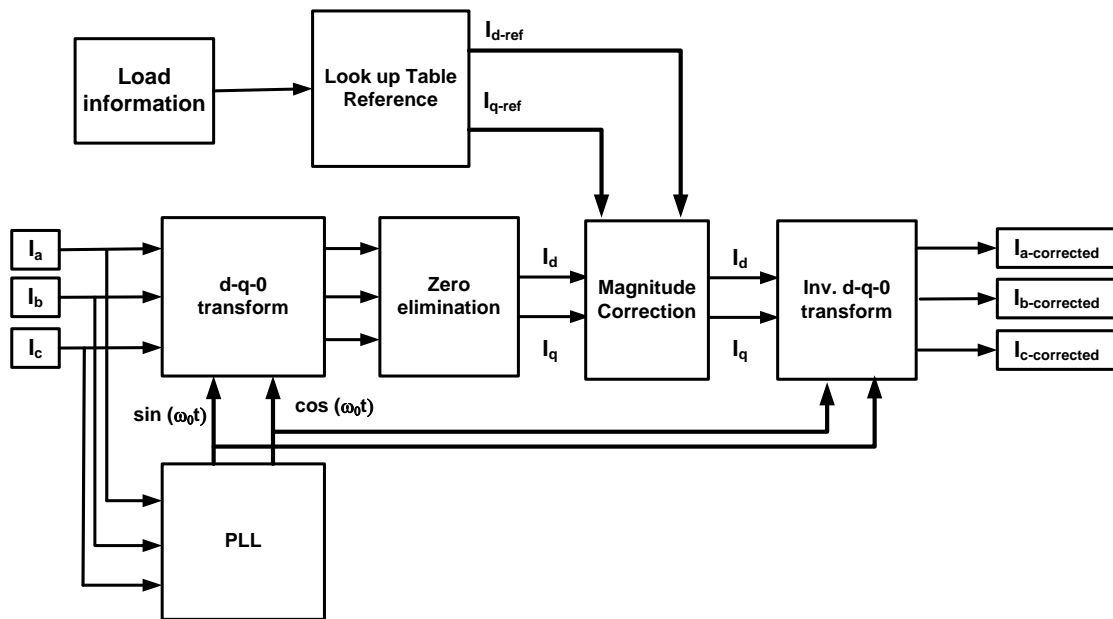


Figure 4.10 On-line calibration system.

Figure 4.10 shows a Simulink block diagram of the online calibration method developed in this study. As shown, the measured three-phase current signals are converted into dq0-frame to ease signal correction first, and then the 0-axis component is eliminated. To calibrate with the reference gain, the magnitude correction block varies the measured gain to match the reference gain for both i_q and i_d . The reference gain can be obtained from the Look up Table of the stator current i_q and i_d as a function of the measured motor load. The load percentage information can be obtained from the flux leakage measurements, power measurements, or stator current measurements. In the next step, the non gain of value for i_q and i_d , is utilized during the measurement for online calibrations. The deviation between the reference and the measured current is then added to the measured currents. After the online calibration, the currents in the dq-frame are converted back to the abc-frame using the invers function. The calibration steps are illustrated below in Figure 4.11.

Figure 4.11 illustrates the magnitude waveform and phasor diagram before and after online calibration including the correction technique under dq-frame.

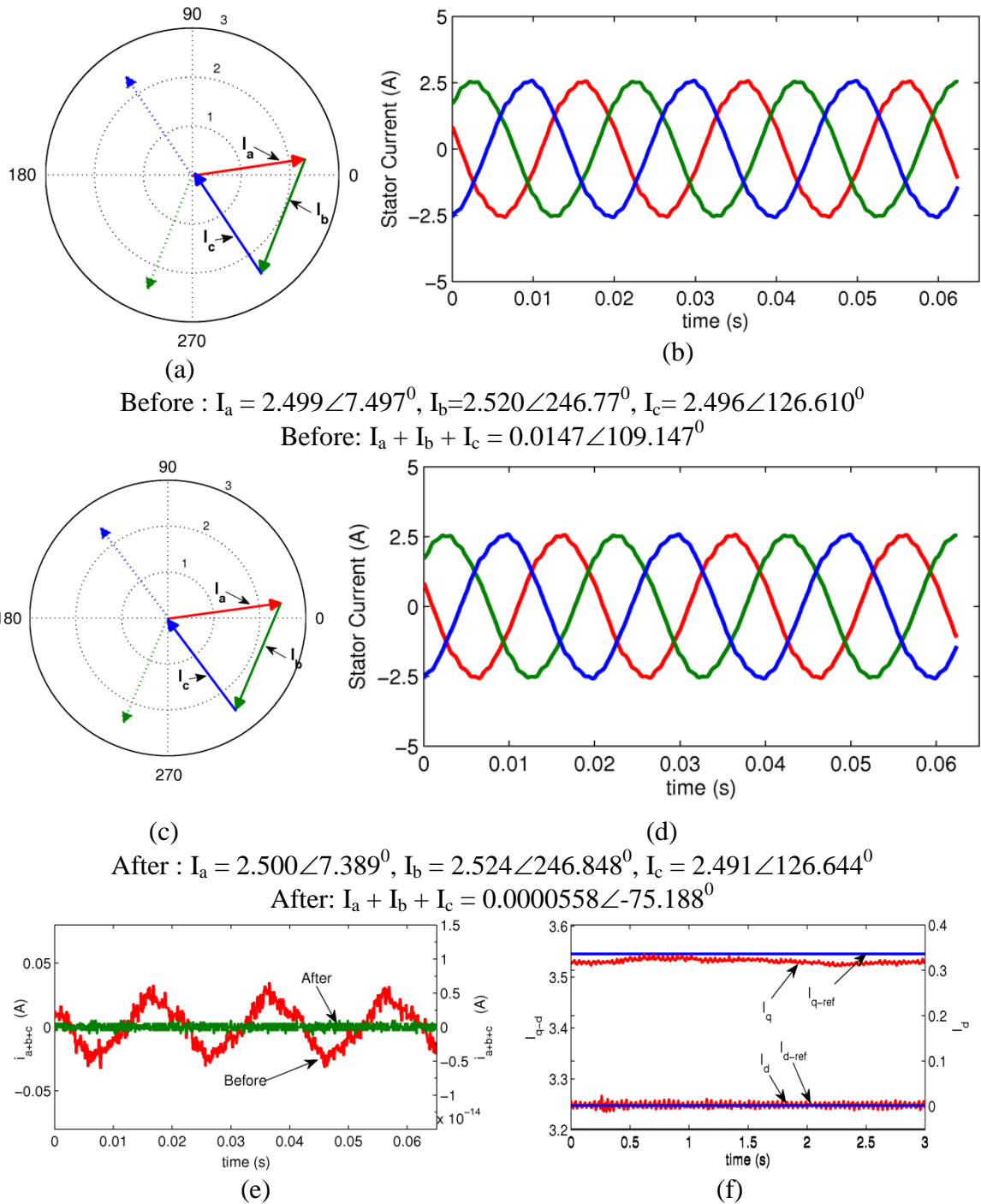


Figure 4.11 Step by step on-line calibration showing (a) the measured stator current phasor including (b) the three-phase waveform; (c) the phasor diagram after calibrations including (d) the waveform; (e) the resultant current ($i_a+i_b+i_c$) before and after zero sequence eliminations; (f) the measured i_q and i_d compare with the reference value.

The online calibration aims to correct the measured data which may contain measurement asymmetry or gain asymmetry through online calibration of the sensor system. Figure 4.10 indicate that the current magnitude can be corrected by comparing the measured signals (i_q and i_d) with the reference of the measurement database (i_q and

i_d) at various loads which also includes inherent asymmetry. This technique retains the baseline information of negative sequence due to motor's inherent asymmetry at various loading condition. However it eliminates unwanted measurement asymmetry.

Figure 4.11 (a) and (b) illustrates the phasor diagram and the actual waveforms of the measured signal respectively. Under ideal condition, the addition of three-phase phasors ($\mathbf{I}_a + \mathbf{I}_b + \mathbf{I}_c$) should produce a zero value for the resultant phasor. However, the resultant phasor is found to be $0.0147 \angle 109.147^\circ$. The corresponding waveform zero sequence current is shown in Figure 4.11 (e) indicates current variation between -0.025 and +0.025 A. The magnitude correction block function can adjust the measured signal according to the reference signals and produce the final results given in Figure 4.11 (c) and (d). Figure 4.11 (c) illustrates the I_a , I_b and I_c phasor after correction and the zero value of the resultant phasor. The resultant current after the zero sequence elimination is zero (green plot) as given in Figure 4.11 (e). Furthermore, Figure 4.11 (f) is given to compare the measured i_q and i_d and their reference values. The difference between the reference and the measured value is used for the online calibrations. The result confirms that the calibration of the signal using the previous baseline negative sequence data of a specific induction motor has been performed successfully.

Note that although the on-line calibration using previous baseline information can help to detect any additional negative sequence components due to faults, the magnitude of the corrected three-phase phasors are not perfectly similar (see Figure 4.11 (c)). This means that the measurement gains of the three current sensors need further corrections to achieve symmetrical balanced output signals in an online measurement system. The stator current correction both for adjusting the gain and the offset error has also been studied for various purposes [72-75]. However the application of negative sequence condition monitoring has not been reported previously. This research indicates that the on-line offset correction can be omitted as explained in Section 4.2.2. Therefore, the online offset correction will not be discussed.

The online scaling gain calibration is simplified by conversion of three-phase current signals to dq -axis. Figure 4.12 (a) illustrates the conversion of two or three-phase current to dq frame which contains positive and negative sequence current. It should be noted that the zero sequence component has been ignored in the figure.

$$\mathbf{I}_{dq} = \mathbf{I}_p + \mathbf{I}_n \quad (4.1)$$

where

$$\mathbf{I}_p = |i_p| e^{j(\omega t - \varphi)}$$

$$\mathbf{I}_n = |i_n| e^{j(-\omega t + \gamma)}$$

NOTE:
This figure/table/image has been removed to comply with copyright regulations. It is included in the print copy of the thesis held by the University of Adelaide Library.

Figure 4.12 The phasor representation of differential gain compensation showing (a) general case of current components, (b) sequence components with differential gain current using three current sensors (c) sequence components using two current sensors [72].

The figure illustrates that the resultant currents in dq axis consist of mean gain of three sensor channels (Σk_{abc}), a gain deviation vector (Δk) and the complex conjugate of the positive sequence (\mathbf{I}_p^*) as given in Equation 4.2. Note that φ is original phase angle of positive sequence and γ is original angle for negative sequence. The phasor conversion of three sensors-based channels, from abc frame to dq frame is illustrated in Figure 4.12 (b). The Figure 4.12 (a) and (b) will be explained later, since it proposes a further improvement for the previous calibration based on the baseline inherent asymmetry database.

Figure 4.12 (b) and (c) shows that the differential gain of the positive sequence component can be compensated according to the specific references. The main idea about the differential gain compensation is how to isolate the differential gain of three sensors from any unwanted asymmetry, and then to calculate the differential gain using a decoupling matrix system. The new current measurement gain is estimated after a regulator minimizes the calculated differential gains. The technique is illustrated in Figure 4.13.

NOTE:
This figure/table/image has been removed
to comply with copyright regulations.
It is included in the print copy of the thesis
held by the University of Adelaide Library.

Figure 4.13 Online differential gain estimation system [72].

In Figure 4.13, three current sensors from *abc*-axis are transformed into *dq0*-axis followed by calculation using first order low-pass (LF) and high-pass (HP) Butterworth filter (F) to isolate the positive sequence component from the negative sequence component. The complex conjugate positive sequence *dq0*-axis is useful to determine the angle of positive sequence component such as given in Figure 4.12 (b).

$$\mathbf{I}_{dq-abc} = \sum k_{abc} \mathbf{I}_p + \sum k_{abc} \mathbf{I}_n + k \Delta \mathbf{I}_p^* \quad (4.2)$$

$$\mathbf{I}_{dq-ab} = \sum k_{ab} \mathbf{I}_p + \frac{\sqrt{3}}{3} \Delta k_{ab} \mathbf{I}_p e^{j\xi} + \sum k_{ab} \mathbf{I}_n + \frac{2\sqrt{3}}{3} \Delta k_{ab} \mathbf{I}_p^* e^{j\phi} \quad (4.3)$$

where

$$k \Delta = -\frac{1}{2} \left[\Delta k_u + j \frac{\sqrt{3}}{3} (\Delta k_u - \Delta k_w) \right]$$

$$\sum k_{abc} = \frac{k_a + k_b + k_c}{3}, \sum k_{ab} = \frac{k_a + k_b}{2}, \sum k_{bc} = \frac{k_b + k_c}{2}, \Delta k_{ab} = \frac{k_a - k_b}{2},$$

$$\Delta k_{bc} = \frac{k_b - k_c}{2} \text{ and } k \text{ is a specific channel sensor gain}$$

Two sensor measurement channels, *ab* and *bc* channels in *dq*-axis, are employed to produce a pair of two differential error of isolated positive sequence gain as given in Figure 4.13. The implementation of two gain positive sequence channels is easier than the three channels. The phasor currents of positive and negative sequence component in case of *ab* channels are given in Figure 4.12 (c). This figure illustrates the additional terms due to the differential gain both for the positive sequence (green arrow phasor orthogonal to actual current, i.e. $\xi = \pi/2$) and the negative sequence

components. In negative sequence component, the additional term of differential gain is obtained by rotating the complex conjugate of positive sequence according to the measured value ($\phi = \pi/6$ in Figure 4.12 (c)). The complete phase shift parameters can be found in [72]. The same technique and the equation (Equation 4.3) can also be applied for the bc channels.

Figure 4.13 shows that the distortions of positive sequence gain discrepancies are also isolated by creating two vectors ϵ and η as given below.

$$\epsilon = \sum k_{abc} \sum k_{ab} |i_p|^2 + \mathbf{j} \frac{\sqrt{3}}{3} \Delta k_{ab} \sum k_{abc} \sum k_{ab} |i_p|^2 \quad 4.4$$

$$\eta = \sum k_{abc} \sum k_{bc} |i_p|^2 + \mathbf{j} \frac{\sqrt{3}}{3} \Delta k_{bc} \sum k_{abc} \sum k_{bc} |i_p|^2 \quad 4.5$$

The Equation 4.4 and 4.5 are created by multiplication of complex conjugate three-sensor-based positive sequence and two-sensor-based positive sequence. Figure 4.12 shows the isolation technique of the estimate two-sensor-based differential sensor between channel a and b (Δk_{ab}) and between b and c channels (Δk_{bc}) by multiplying $\sqrt{3}$ with the ratio of the imaginary terms and real terms of Equation 4.4 and 4.5. The decoupling matrix in Figure 4.13 illustrates the conversion of two-sensor-based differential matrix into the deviation of three-sensor-based matrix. The compensation employs Integral (I) or Proportional-Integral (PI) regulator to drive the estimated three-sensor-based differential error gain ($\Delta k_a, \Delta k_b$ and Δk_c) to zero. The PI regulator provides more stable steady state zero error while the integral (I) regulator provide more simpler mythology of gain selection [76]. Based on feed-forward information ($k_{a-(ref)}, k_{b-(ref)}, k_{c-(ref)}$) of design circuit parameters, the final estimated gain ($k_{a-(est)}, k_{b-(est)}, k_{c-(est)}$) is determined as one of the channels (i_a) as given below.

$$k_{(a)-est} = k_{(a)-ref} + \Delta k_{(a)-est} \quad 4.6$$

The estimated gain is then employed to determine an actual stator current as

$$i_{a-measured} = \frac{k_{(a)-actual}}{k_{(a)-est}} i_{a-actual} \quad 4.7$$

This technique can be employed to adjust the differential gain error which leads to negative sequence due to instrumentation asymmetry.

This technique is examined in detail and the preliminary results are given in Figure 4.14. In this research, the differential gain estimation of the captured stator current data is performed offline using simple model as indicated in the computation algorithm shown in Figure 4.13. The first experiment was performed by using the same gain value of 1A/500 mV for all sensors. The reference gain current and measurement gain are assumed 1A/500 mV and 1 A/A respectively.

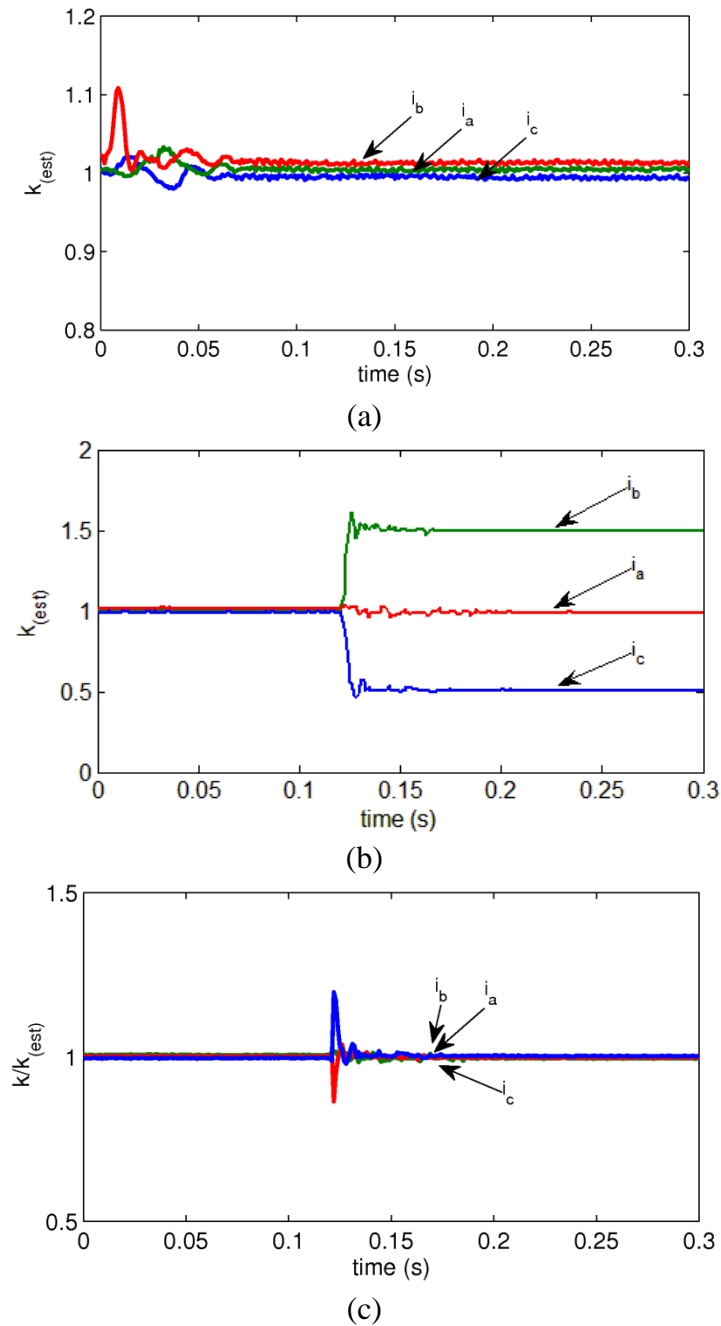


Figure 4.14 Experimental test of online calibration showing (a) the estimated gain of the symmetrical measurement gains, (b) the response of estimated gain calculation when different measurement gains are introduced, and (c) the ratio of actual gain and estimated gain.

The performance of differential gain estimation is demonstrated Figure 4.14. The estimated gains of the sensor indicate that the three-phase gain are not perfectly similar. The average of relative gain differences between the three sensors are within 2.2% after steady state.

A second experiment was performed to shows the response of the differential gain. The differential gain provides a guide how the implementation of online calibration based on three sensors measurements. Therefore, different extreme amplifications are employed in each sensor: 1A/500 mV, 1A/750 mV and 1A/250 mV. The reference gain is set at 1A/500 mV. The same input current (assuming that the current measurement gain is 1A/A) is applied to all three sensors. Figure 4.14 (b) illustrates the results of these extreme different gain amplification. The figure shows the changes in the estimated gain amplification ($k_{(b)-est} = 1.5$ and $k_{(c)-est} = 0.5$) after the different gain sensor is turned on as the sensors had similar gains in the previous state. This result indicates that new estimated gains are calculated immediately after different gains are identified in measured three-phase currents. The new estimated gains are adjusted according to the reference gain until the output of the measured current is same as the input current. The comparison with the assumed current measurement gain (1 A/A) is given in Figure 4.14 (c), which indicates that the model responds appropriately with the extreme gain changing during the measurements. These results demonstrate that the method developed can perform the calibration effectively. Further investigation is required to show the performance of the method in the negative sequence condition monitoring.

4.5 Conclusion

This chapter demonstrated one of the major issues, the measurement in condition monitoring of induction machine. The monitoring issues in negative sequence monitoring are also studied. System components characteristics and step by step system calibration under similar input voltage and current were also carried out in this chapter. The effect of calibration to the negative sequence current and voltage were discussed.

The negative sequence components due to measurement system are obtained using angle displacement technique. It was shown that angle correction of the stator current and voltage signals is very useful method to minimize the effect of the

negative sequence due to instrumentation asymmetry. Furthermore, hot and cold measurement has significant effect during the condition monitoring as it can contribute to negative sequence current.

The chapter also provided alternative methods for online condition monitoring such as simple negative sequence baseline adjustments and sensor gain corrections. It was concluded that measurement asymmetry affects the measured negative sequence if the calibration as well as the gain and the angle correction are not performed appropriately. Measurement analysis ensures the validity of the negative sequence condition monitoring of errors and motor's faults. In the next chapter, shorted turn machine faults and various other disturbances will be investigated to support the discussion of measurement errors.

Chapter 5

Investigation of Stator Shorted Turn Fault

5.1 Introduction

As stated previously shorted turn fault in the induction motors requires immediate action, as it is the biggest contributor in terms of electrical related faults. In this chapter, the negative sequence analysis of the stator shorted turn faults will be discussed. The experimental studies will be supported by the simulation models to better understand the effect of the shorted turn faults on the negative sequence. Furthermore, various disturbances for the shorted turn faults will also be discussed including inherent machine asymmetry and supply voltage unbalance. Both the shorted turn faults and these disturbances will also be investigated under load variation to obtain a better understanding of each negative sequence contributors.

5.2 Shorted Turn Simulation

The shorted turn faults are performed in the simulations based on the model given in Chapter 3. The other motor faults are also studied using the model presented in [9]. In this thesis, the model of the stator shorted turn fault is developed using an unequal number of shorted turns in each phase. The shorted turn is assumed in one phase composed of shorted number of turns (N_{sh}) and unshorted number of turn(s) (N_{us}) as the total number of turns is N_s .

$$N_s = N_{as} = N_{us} + N_{sh} \quad (5.1)$$

In a balanced machine, this total number of turn N_s is similar for the other phase N_{bs} and N_{cs} respectively. In order to facilitate the shorted turn calculation, as in Chapter 3, the shorted turn faults in the abc axis can be transferred to the $qd0$ axis. Figure 5.1 shows the shorted turn section of the motor faults in the dq axis frame.

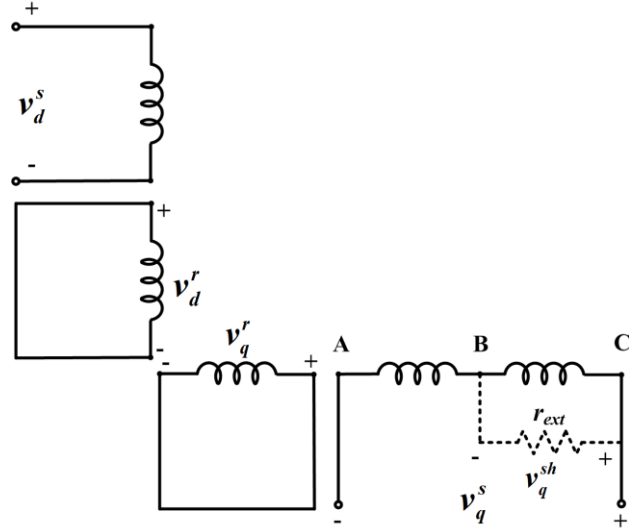


Figure 5.1 Shorted turn configurations in dq axis frame.

The above figure illustrates that the shorted turn fault occurred between point B and point C of the winding, which has winding between point A and point C in the q axis. The axis transformations given in the figure show that the shorted turn faults affect only part of the q axis. The figure also illustrates the external short circuit current limiting resistance r_{ext} , which can be used to include the simulation resistance of the external cable during the shorted turn fault experiments.

To include the shorted turn configuration in Figure 5.1 the previous model has been modified. As in the healthy machine model, some of the parameters of the fault model are also transformed from abc frame to $qd0$ axis frame. The parameters include the stator self-inductances, mutual-inductances, stator to rotor inductances and resistances. An additional flux linkage equation is added to the previous healthy model equations.

The inductances in the $qd0$ axis given previously in Equation 3.4 and 3.5 can be modified to obtain the stator self (\mathbf{L}_{qd0}^{ss}) and the mutual-inductances (\mathbf{L}_{qd0}^{sr}) and the rotor self (\mathbf{L}_{qd0}^{rr}) and the mutual-inductances (\mathbf{L}_{qd0}^{rs}) as below.

$$\mathbf{L}_{qd0}^{ss} = \begin{bmatrix} L_{11}^{ss} & 0 & L_{13}^{ss} \\ 0 & L_{22}^{ss} & 0 \\ L_{31}^{ss} & 0 & L_{33}^{ss} \end{bmatrix}, \mathbf{L}_{qd0}^{sr} = \begin{bmatrix} L_{11}^{sr} & L_{12}^{sr} & 0 \\ 0 & L_{22}^{sr} & 0 \\ L_{31}^{sr} & 0 & 0 \end{bmatrix} \quad (5.2)$$

$$\mathbf{L}_{qd0}^{rr} = \begin{bmatrix} L_{11}^{rr} & 0 & 0 \\ 0 & L_{22}^{rr} & 0 \\ 0 & 0 & L_{33}^{rr} \end{bmatrix}, \mathbf{L}_{qd0}^{rs} = \begin{bmatrix} L_{11}^{sr} & 0 & \frac{1}{2}L_{31}^{sr} \\ 0 & L_{22}^{sr} & 0 \\ 0 & 0 & 0 \end{bmatrix} \quad (5.3)$$

where

$$L_{11}^{ss} = (L_q^s + L_q^{ssh}) + (L_q^{sh} + L_q^{ssh}), L_{22}^{ss} = L_d^s$$

$$L_{11}^{sr} = L_q^{sr} + L_q^{shr}, L_{22}^{sr} = L_d^s$$

$$L_{11}^{rr} = L_q^r, L_{22}^{rr} = L_d^r$$

The self-inductance elements in the equations above are obtained by modifying Equation 3.7 and given by

$$\left. \begin{aligned} L_{11}^{ss} &= \frac{2}{3} \left(L_{asas} + \frac{1}{2} L_{bsbs} - 2L_{asbs} + \frac{1}{2} L_{bscs} \right) \\ &= \frac{2}{3} \left[\left(L'_{asas} + \frac{1}{2} L'_{bsbs} - 2L'_{asbs} \right) + (L_{assh} - L_{shbs}) \right] + \frac{2}{3} [L_{shsh} + (L_{assh} - L_{shbs})] \\ &= (L_q^s + L_q^{ssh})(L_q^{sh} - L_q^{ssh}) \\ L_{22}^{ss} &= \frac{1}{2} (L_{bsbs} + L_{cscs} - 2L_{bscs}) = L_{bsbs} - L_{bscs} = L_{ls} - L_m = L_d^s \end{aligned} \right\} (5.3)$$

Similarly, the stator and the rotor mutual-inductances, the transformed equations can be given using Equation 3.8 as

$$\left. \begin{aligned} L_{11}^{sr} &= L_{asr} + \frac{1}{4} L_{bsr} + \frac{1}{4} L_{csr} = L_{asr} + \frac{1}{2} L_{bsr} \\ &= \left(L'_{asr} + \frac{1}{2} L'_{bsr} \right) + L_{shar} = L_q^{sr} + L_q^{shr} \\ L_{22}^{sr} &= \frac{3}{4} (L_{bsr} - L_{csr}) = \frac{3}{2} L_{bsr} = L_d^s \end{aligned} \right\} (5.4)$$

The derivation of the self and mutual-inductances using the shorted and unshorted turn sections are given in Appendix A.2. Furthermore, based on the equations given above, to obtain the flux leakages of the squirrel cage motor, the matrix of inductances in Equation 3.4 and 3.5 can be modified as given in Equation 5.4.

$$\begin{bmatrix} \lambda_q^{sh} \\ \lambda_q^s \\ \lambda_d^s \\ \lambda_q^r \\ \lambda_d^r \end{bmatrix} = \begin{bmatrix} L_q^{sh} & L_q^{ssh} & 0 & L_q^{shr} & 0 \\ L_q^{ssh} & L_q^s & 0 & L_q^{sr} & 0 \\ 0 & 0 & 0 & L_d^s & 0 \\ L_q^{shr} & L_q^{sr} & 0 & L_q^r & 0 \\ 0 & 0 & L_d^{sr} & 0 & L_d^r \end{bmatrix} \begin{bmatrix} i_q^{sh} \\ i_q^s \\ i_d^s \\ i_q^r \\ i_d^r \end{bmatrix} \quad (5.4)$$

Note that the shorted turn model also affects the stator phase resistances. Hence the stator shorted turn phase resistance in one phase (phase a) can be given as

$$r_{as} = \left(\frac{N_a}{N_s} \right) r_s = \left(\frac{N_{us}}{N_s} \right) r_s + \left(\frac{N_{sh}}{N_s} \right) r_s = r_{as}' + r_{sh} \quad (5.5)$$

$$r_{bs} = r_{cs} = r_s$$

where r_{sh} is the shorted windings resistance, N_{us} is the unshorted section, N_{sh} is the number of turns of the shorted section and N_s is the number of turns of the stator winding. After transformations, the induction motor resistance can be expressed as below (see Appendix A.2).

$$\begin{pmatrix} r_q^{sh} \\ r_q^s \\ r_d^s \end{pmatrix} = \begin{pmatrix} \frac{2}{3} r_{sh} & 0 & 0 \\ 0 & r_{11}^s & r_{12}^s \\ 0 & r_{21}^s & r_{22}^s \end{pmatrix} \quad (5.6)$$

For the rotor side, the derivation of resistance elements, which have been transformed to the $qd0$ axis, can be found in Appendix A.2. Note that the rotor resistance terms developed here can also be implemented in the simulation of asymmetrical rotor by adding resistances to each element. The matrix element resistance in $qd0$ axis can be given by

$$\mathbf{r}_{qd0}^r = \begin{pmatrix} r_{11}^r & r_{12}^r & r_{13}^r \\ r_{21}^r & r_{22}^r & r_{23}^r \\ r_{31}^r & r_{32}^r & r_{33}^r \end{pmatrix} \quad (5.7)$$

Note that in case of the qd axis, the rotor elements considered are the first four matrix elements: r_{11} , r_{12} , r_{21} , and r_{22} . The basic voltage equations are implemented to simulate the dynamic induction motor. The previous voltage equations can be implemented to obtain the flux linkages. The flux linkage equations given in Equations 3.10 - 3.13 can be modified for three wire systems, and are given below.

$$\psi_q^{sh} = \omega_s \int (v_q^{sh} - r_{sh} i_q^{sh}) dt \quad (5.8)$$

$$\psi_q^s = \omega_s \int (v_q^s - v_q^{sh} - r_{11}^s i_q^s - r_{12}^s i_d^s) dt \quad (5.9)$$

$$\psi_d^s = \omega_s \int (v_d^s - r_{21}^s i_q^s - r_{22}^s i_d^s) dt \quad (5.10)$$

$$\psi_q^r = \int (\omega_r \psi_d^r - \omega_s r_{11}^r i_q^r - \omega_s r_{12}^r i_d^r) dt \quad (5.11)$$

$$\psi_d^r = - \int (\omega_r \psi_q^r + \omega_s r_{21}^r i_q^r + \omega_s r_{22}^r i_d^r) dt \quad (5.12)$$

The current components in the above equations can be obtained from the inductances matrix as a function of flux linkages and reactances, and can be obtained by inverting the Equation 5.4.

$$\begin{bmatrix} i_q^{sh} \\ i_q^s \\ i_d^s \\ i_q^r \\ i_d^r \end{bmatrix} = \begin{bmatrix} X_q^{sh} & X_q^{ssh} & 0 & X_q^{shr} & 0 \\ X_q^{ssh} & X_q^s & 0 & X_q^{sr} & 0 \\ 0 & 0 & X_d^s & 0 & X_d^{sr} \\ X_q^{shr} & X_q^{sr} & 0 & X_q^r & 0 \\ 0 & 0 & X_d^{sr} & 0 & X_d^r \end{bmatrix}^{-1} \begin{bmatrix} \psi_q^{sh} \\ \psi_q^s \\ \psi_d^s \\ \psi_q^r \\ \psi_d^r \end{bmatrix} \quad (5.13)$$

Using this motor model, various stator shorted turn faults can be studied together with additional disturbances such as voltage unbalance, inherent asymmetry or load variations. Then the motor model can be validated using the real data.

In order to investigate the dynamic behavior of the shorted turn fault, various fault parameters are applied to the motor model including 5 shorted turns, 0.5Ω external resistor and full load cases. The results are presented in Figure 5.2. Note that the figure illustrates the performances of the induction motor from start up to the steady state operation. Figure 5.2 (a) shows the positive sequence current of the induction motor as a function of time under the full load. Note that the negative sequence current (unlike the healthy machines as detailed in Chapter 3) shows significant asymmetry which can be identified by the large negative sequence oscillations during starting. It was found that the negative sequence current drops to 0.01 pu after reaching the steady-state speed. The short circuit current is given in Figure 5.2 (c) showing small difference between the transient starting part and the steady-state speed region where the current is about two times the rated current. This

observation shows that the short circuit current at the external short turn cable is significantly high and relatively unchanged, even during starting. The shorted turn also significantly affects the motor torque, which can be seen as small oscillations in the torque figure (see Figure 5.2 (d)).

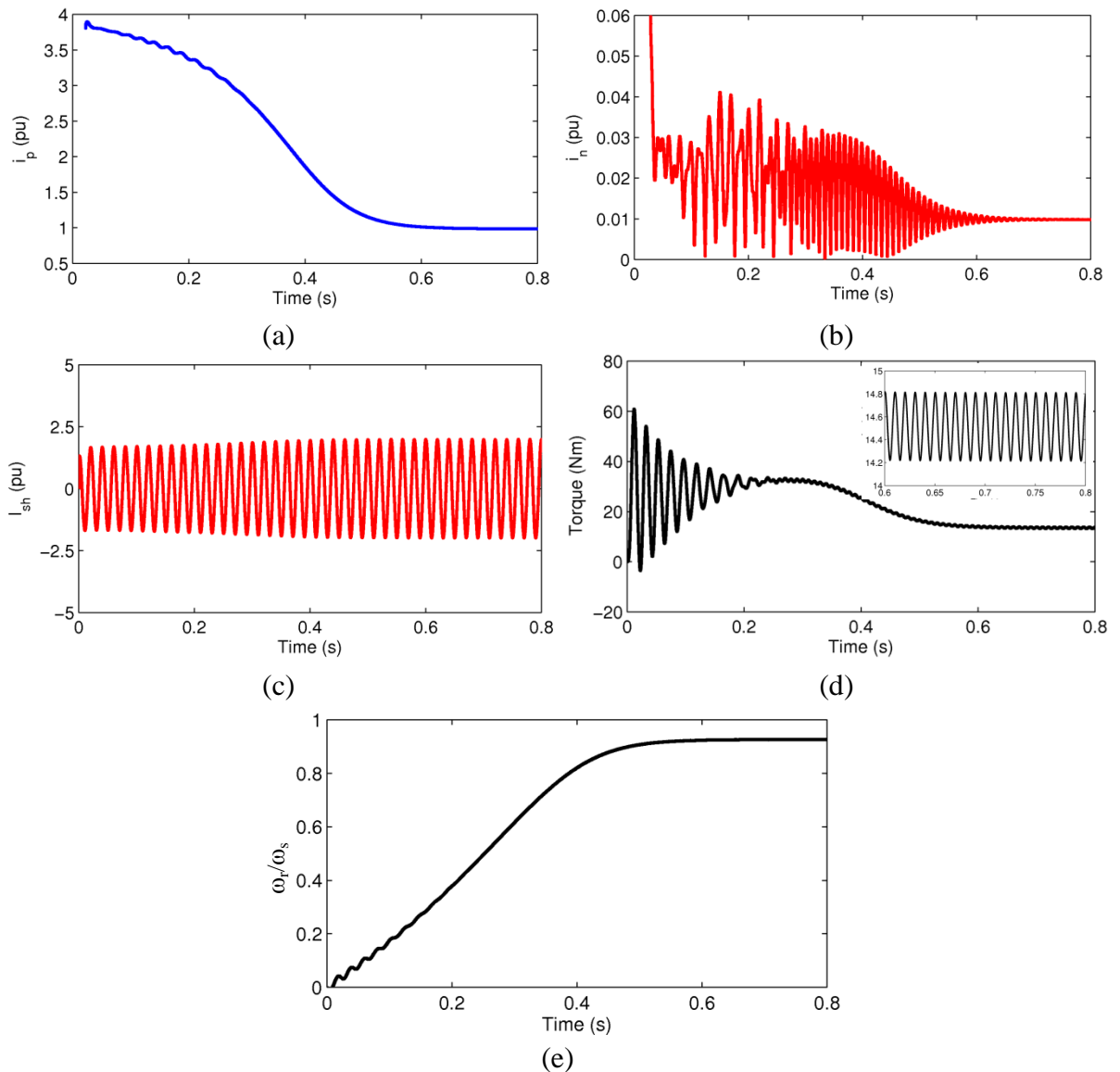


Figure 5.2 A sample simulation results under 5 shorted turn fault and with 0.5Ω external resistance and under full load: (a) the positive sequence current, (b) the negative sequence current, (c) the short circuit current (d) the electromagnetic torque and (e) the rotor speed.

Two distinct sections of Figure 5.2 can be explored further to analyze the negative sequence. Note that these sections are the effect of the external resistance to the short circuit currents and negative sequence currents. The analysis is shown in Figures 5.3 and 5.4.

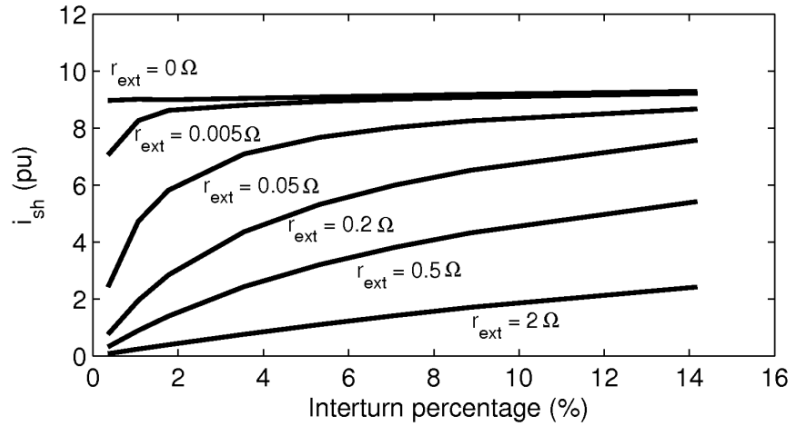


Figure 5.3 Short circuit simulation study under various values of external resistance

Figure 5.3 illustrates the simulation results of the short circuit current produced under varying external resistances, which is used to limit the current level in the winding. Note that under almost zero external resistance, the short circuit currents are approximately double the lock rotor current, and are relatively unaffected by the severity of fault. In addition, as expected, short circuit current reduces when the large value of external resistance is applied. The more external resistances are applied, the less shorted circuit current is generated. Under small value of external resistance (0.005Ω), the significant increases of short circuit current occurs below 2% turn faults before reaching to a steady value of about 9 pu. This result indicates that the short circuit current is almost independent of the percentage of the shorted turn, except at very low value below 2%. In other words, short circuits involving only a few turns can still generate large currents and result in rapid winding damage.

Figure 5.3 also confirms that the maximum shorted circuit current can be identified from the simple ratio of voltage supply and stator resistance in a single phase. As an example, for a rated voltage of 239.6V and the stator resistance of 5.22Ω , the short circuit current using the computer at small resistance is about 9.4 pu, which is similar to the results obtained using the computer model. This value is useful to determine the value of the winding current under the worst state of the shorted turn fault. In addition, it can be used for further analysis to study the negative sequences.

As a function of the inter turn percentage, Figure 5.4 is given to show that the negative sequence current value as a function of the interturn percentage. Note that the negative sequence current decreases as the external resistances increase. The external

current reduces the asymmetrical phenomena of the induction motor indicated by the decreases of negative sequences. Note that 0.5Ω external resistance can reduce the magnitude of shorted turn negative sequence current by about half. Both Figures 5.3 and 5.4 show that the external resistor to limit the current for shorted turn faults plays an important role to accurately identify the shorted turn current faults, especially for the negative sequence analysis.

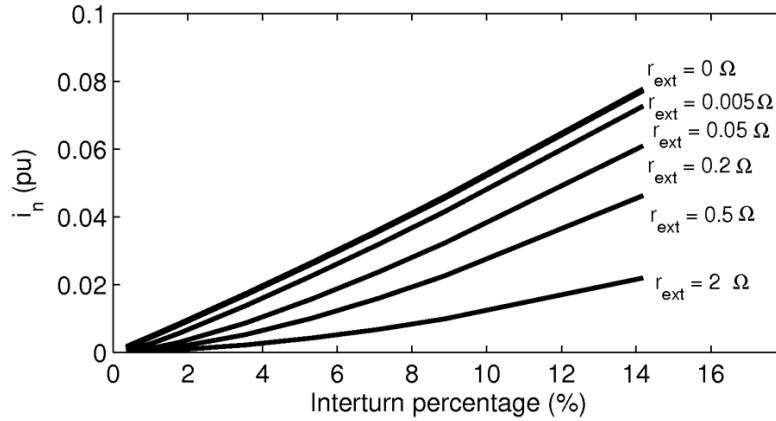


Figure 5.4 Negative sequence current of shorted turn simulation under various external resistances

Like the short circuit current, the shorted turn negative sequence current can also be calculated using the main parameters. It is explained in [12] that negative sequence current can be given by

$$I_n \cong \frac{N_{sh} V}{6N_s R_s} \quad (5.14)$$

where R_s is the stator resistance and V is the voltage supply. For example, for the motor parameters given previously under the rated voltage, and at 5 shorted turns or 10 shorted turns, the negative sequence is approximately 0.027 pu or 0.0523 pu respectively. This result also validates the simulation studies presented in Figure 5.4. However, the prediction also assumed that the external resistance is low.

Both the shorted turn negative sequence current and the short circuit current can be used to define other parameters. An approximation for negative sequence current can be given as a function of the short circuit current, which is based on the transformer theory and symmetrical components as given in [8].

$$I_n = 0.25 \frac{N_{sh}}{N_s} I_{sh} \quad (5.15)$$

Using this approximation, the calculated values of negative sequence currents from Figure 5.3 and the simulated results in Figure 5.4 were compared. The errors using these approaches are about 3% for small external resistances and 30.4% for large resistances. Although this approach mentioned in the literature, it is not intended for the prediction of the number of shorted turn. Instead, it is applied for the quick prediction of minimum sensitivity for stator shorted turn condition monitoring and for the threshold setting to avoid further faults. This is because short circuit currents can not be measured in real applications. For a sample calculation, in the case of the smallest shorted turn faults (i.e. one turn fault) and the highest allowable short circuit current at the rated current, the acceptable negative sequence current before rapid failure can be determined easily, which is about 4.3mA for the motor under test.

The previous motor simulations in this research have shown the applicability of the model to determine the short circuit current, the applicability of external resistance to control the short circuit current and the negative sequence current. In addition, the simple equations were provided to understand these quantities. In the next section, the motor short circuit experiment will be described in order to better understand the model in relation to the real faults.

5.3 The Shorted Turn Experiments

In order to validate the results of the dynamic model as well as understand the behavior of the induction motor under real shorted turn faults and disturbances, various experiments have been done using a test motor with multiple external terminals to introduce a known degree of shorted turn fault (see Figure 5.5 (a)). The test motor has an external panel to access 5, 10, 15 and 20 turns from the end of the stator winding in the phase *a* (R1-R5) and B (B1-B5), which corresponds with 1.7%, 3.5%, 5.3%, and 7.1% percentage of turn-to-turn faults. Therefore, to simulate a shorted turn fault, an external cable should be used to short circuit a pair of suitable terminals as shown in Figure 5.5 (b). For example, to create a 1.7% shorted turn in phase *a*, a cable is connected between R1 and R2; while to create a 3.5% shorted turn, the cable should be connected between R1 and R3. Note that, the detailed stator winding diagram is given in Figure 5.6 to illustrate the shorted turn method used in this research.

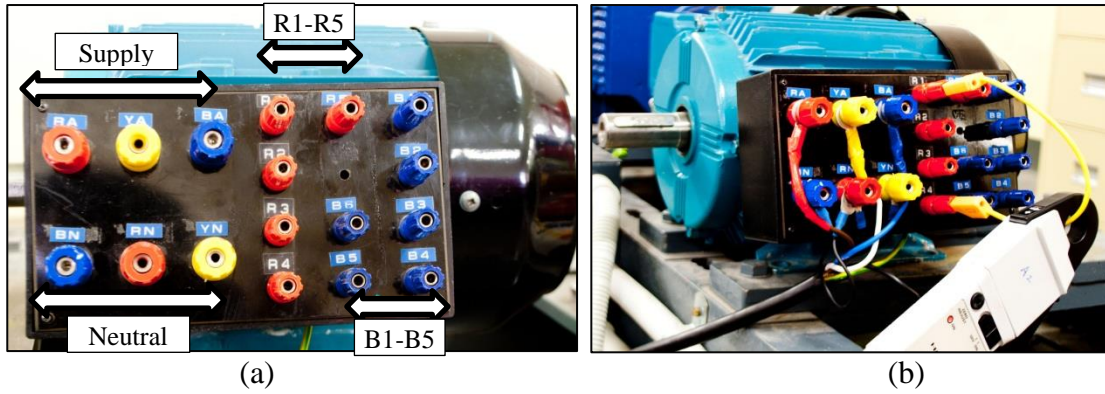


Figure 5.5 The test setup showing (a) an adjustable shorted turn terminal block of the motor under test and (b) the external shorted circuit cable with a current clamp.

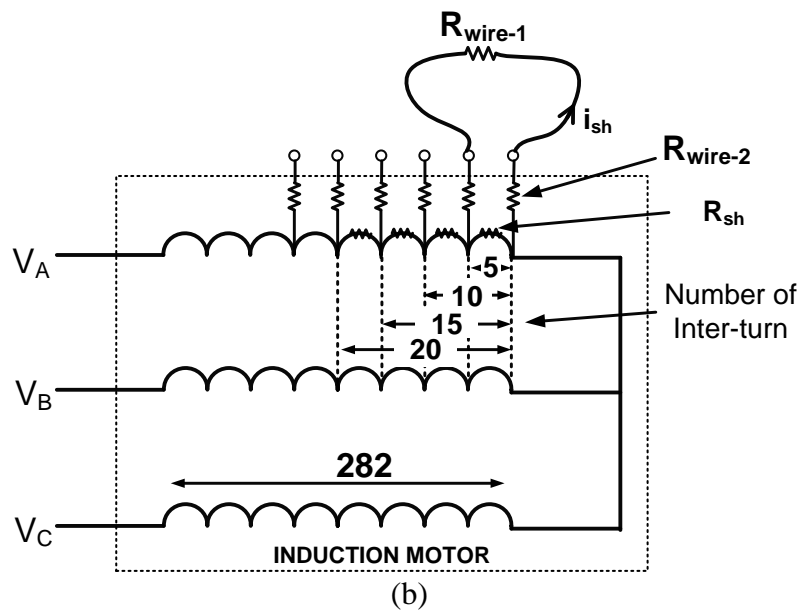


Figure 5.6 The illustration of the stator windings of the test motor with shorted turns.

Note that the motor has a total of 282 turns on each phase of the stator winding, with an additional external cable to introduce a turn fault. The resistance of the external cable is $R_{\text{wire-1}}$ which can be used to create either 5, 10, 15 or 20 shorted turns on the stator winding. In addition to this external connector resistance, there are two more external cables due to the tapping, $R_{\text{wire-2}}$ in the figure. The resistance of the actual shorted turn section is labeled as R_{sh} , and corresponding shorted turn current is i_{sh} .

An accurate measurement of the resistance of the entire shorted turn path is required to obtain accurate simulation results. The shorted turn resistances are measured and given in Table 5.1.

Table 5.1 The resistance of shorted turn for 5 turns

Resistance	Value
$R_{\text{wire-1}}$	0.0785Ω
$R_{\text{wire-2}}$	0.0233Ω
R_{sh}	0.0926Ω
$R_{\text{sh}} + 2R_{\text{wire2}}$	0.1391Ω

The four wires resistance measurement technique is used to measure R_{wire1} , and R_{wire2} is obtained by indirect measurements. The R_{sh} is obtained assuming that the resistance of 5 turns is a fraction of the total resistance across one phase, 5.22Ω. The R_{wire2} is obtained by subtracting R_{sh} from the measured total of $R_{\text{sh}}+2 R_{\text{wire2}}$. In the shorted turn fault simulations, the total of R_{wire1} and R_{wire2} (0.125Ω) is used. Note that this external resistance is applied to any other additional 5 shorted turn faults.

The shorted turn experiments and simulations were carried out by making variations of shorted turn faults under various supply voltages. The variations of the short circuit currents versus the percentage of the shorted turns at various supply voltages are illustrated in Figure 5.7 below.

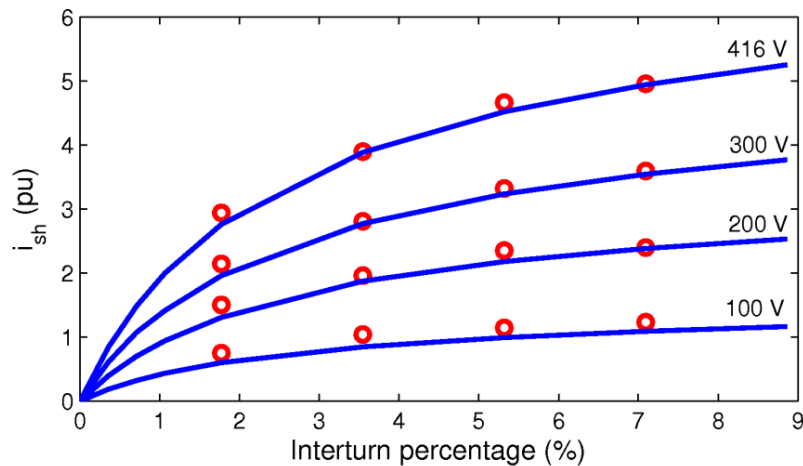


Figure 5.7 The fault current in the shorted turns versus the fraction of shorted turns under main supply voltage variation: experimental (circles) and simulated (solid lines).

Figure 5.7 shows that the fault currents are dependent on the number of shorted turns and the voltage supply. This behavior is quite similar to the experimental results in [24], where the short circuit currents increase with the number of shorted turns. In [9], similar trends are given. The short circuit currents are proportional to the number of shorted turns, especially when external limiting resistances are present. The simulation of the short circuit using zero external limiting resistance is also discussed

in [9], which is similar to results given in Figure 5.3. However, the results given in Figure 5.7 contradicts the results given in [77]. In [77], the short circuit currents increase sharply until a certain small number of shorted turns (8 turns), then decrease significantly with the number of shorted turn faults. The reason for this is that at a small number of shorted turns, the resistance dominates the short circuit current. However, with a large number of shorted turns, the reactances in turn take place and reduce the short circuit current values.

As shown in Figure 5.7 the short circuit current is relatively proportional to the percentage of the shorted turn faults. This behavior is quite different to the common rule for the short circuit current where the shorted turn current is usually independent of the turn percentage, unless in the case of a small number of turns. This usually occurs at a total external resistance bigger than 0.005Ω , as indicated in Figure 5.3. In other words, the smaller the total resistances for turn-to-turn faults, the circuit currents are independent of the number of the shorted turns, at a larger shorted turn percentages of 1%. In addition, the external resistance also reduces the short circuit currents as illustrated in Figure 5.3. This external resistance factors can be seen in Figure 5.7 where the short circuit current is almost equal to the block rotor current (see Figure 3.8). Figure 5.7 also shows that the voltage variation affects the short circuit currents significantly. Figure 5.7 also demonstrates that the motor model also takes into account the main voltage variations.

It can be conclude that the external resistance is useful to protect the induction motor while studying the shorted turn faults. However, the external resistor also reduces the short circuit current that is used as an indicator in condition monitoring. Despite this limitation, the level of short circuit current confirms that a small number of shorted turns can generate a large current that may result a complete winding damage and motor failure. Note that since the large short circuit current cannot be accessed from the measurements at the motor terminal, the negative sequence monitoring of shorted turn faults is an alternative method for fault detection.

The experimental results of the negative sequence currents under shorted turn faults are shown in Figure 5.8. The results were obtained at zero load by switching on and off the shorted turn faults via the external terminal to demonstrate the significance of the negative sequence current under faults and the healthy state of the motor under test. The magnitude of the negative sequence current during the experiments of

healthy conditions was found to be 0.003 pu. The smallest shorted turn fault value in this test is given in Figure 5.8 (a), which also demonstrates the magnitude of faulty and healthy condition that can be a simple indicator to detect the shorted turn faults in induction machines.

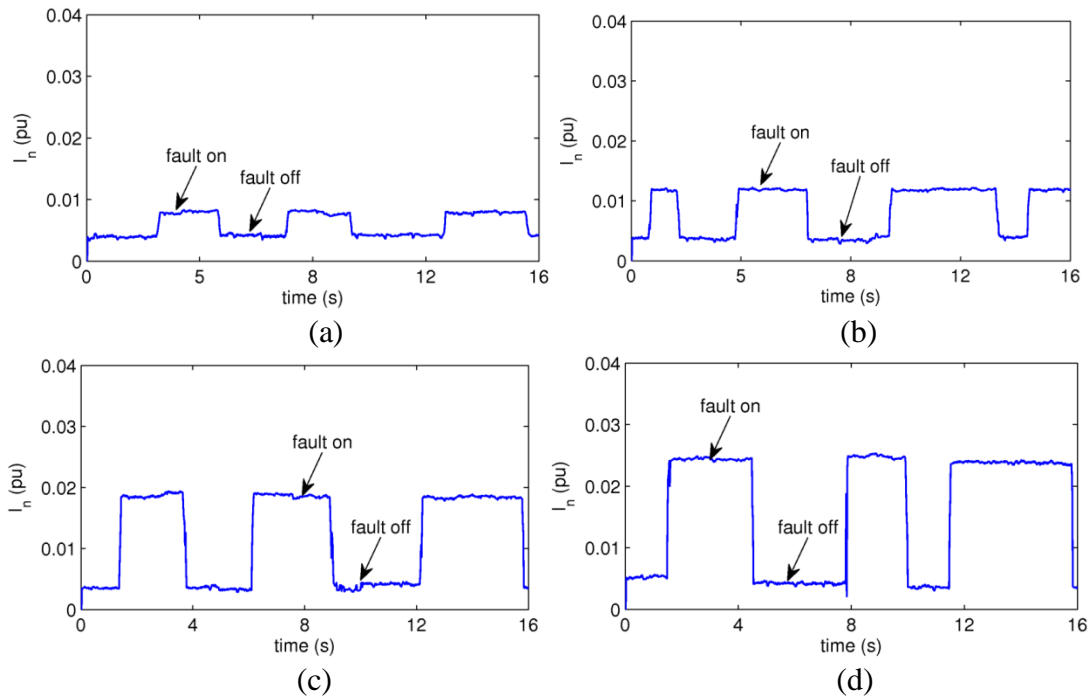


Figure 5.8 The experimental results under healthy and faulty operation under no load but at various fault levels (a) 1.7%, (b) 3.1%, (c) 5.3%, and (d) 7.1% shorted winding turn faults.

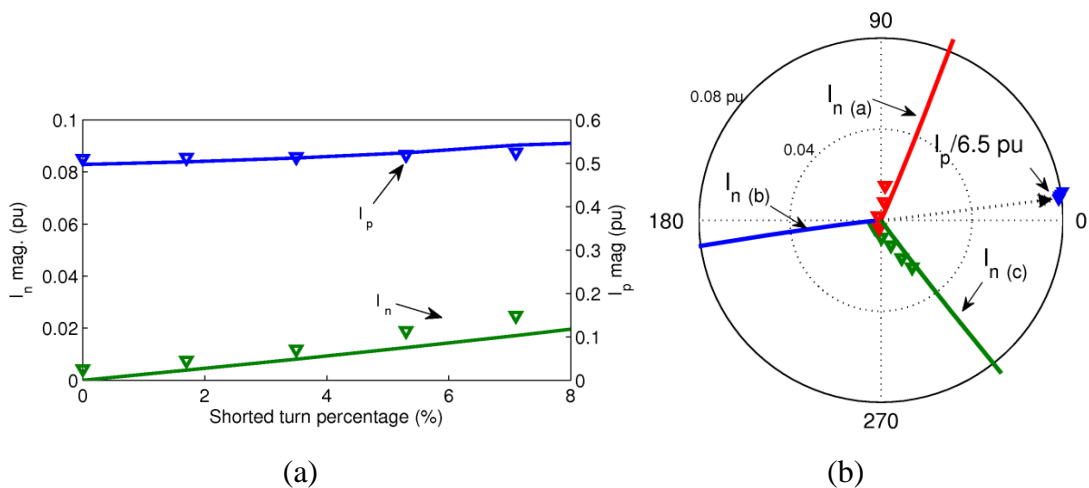


Figure 5.9 (a) The magnitude and (b) the phasors of the negative sequence and the positive sequence currents showing the experimental results (triangle) and the simulation results (line) as a function of the shorted winding turns.

The shorted turn faults, which are illustrated in magnitudes and phasors, are given in Figure 5.9. Note that the magnitudes of the negative sequence currents at no

load increase proportionally with the shorted turns winding, while the positive sequence stays relatively constant. The magnitude of the negative sequence currents measured as 0.008 pu, 0.012 pu, 0.019 pu and 0.025 pu for 1.7%, 3.5%, 5.3% and 7.1% shorted winding turns respectively. The trend line of the magnitude graph also indicates that for the motor under test, an increase of four times the shorted winding turn increases the shorted turn negative sequence current about three times.

The phase angle analysis in Figure 5.9 (b) shows the shorted turn faults in each motor phase. Note that the phase angle of the negative sequence current can be studied using the ratio of the supply phase voltage and the zero sequence impedance [78].

$$\mathbf{I}_n \approx \frac{N_{sh}}{3N_s} \mathbf{I}_{sh} \approx \frac{N_{sh}}{3N_s} \frac{\mathbf{V}_a}{Z_0} \quad (5.15)$$

The above equation is obtained using the symmetrical components under steady state equivalent circuit where the negative sequence current is composed of voltage unbalances and negative sequences due to unmodeled disturbances. This approach indicates that the simple analytical negative sequence can be obtained by neglecting the asymmetry due to the contributors of voltage unbalance or other unmodeled disturbances. The external resistance \mathbf{R}_{ext} was not considered in this approach and the negative sequence current angle was subtracted from the zero sequence angle obtained from the supply voltage's phase angle.

For the zero sequence impedance of $15.83 \angle 11.1^\circ$ and the voltage supply phase references of 90° and 210° for phase a and c , the negative sequence due to the shorted turn in phase a is estimated as -78.9° and 318.9° respectively. These values are similar to the experimental results and the motor model simulation results. This quick prediction of negative sequence current of the shorted turn shows that the phase of the shorted turn fault can be predicted from the location of phasor trajectory. The zero sequence impedance which represents the sum of asymmetrical phasor can also be a good indicator for the shorted turn faults as proposed in [78].

Note that the magnitudes of the negative sequence currents are also compared in Figure 5.9, in which the simulation results are higher than the test results. It was observed that excluding the healthy value (at 0%), there is a constant ratio of 0.44 between the test and the simulations results. In addition, as illustrated in Figure 5.9 (b), the phase angle of the negative sequence current has a reference angle started at a

small offset reference to the zero axis. These differences indicate the presence of various disturbances in measurements such as inherent asymmetry, voltage unbalances or other unwanted asymmetrical contributions. The differences may also be caused by the limitations of the induction motor model, such as the absence of saturation or the effect of temperature increases. To better understand the real shorted turn faults, the unwanted negative sequence currents, also known as disturbances in shorted turn monitoring will be discussed in the following section.

5.4 The Detailed Analysis of the Disturbances of Shorted Turn Faults

As stated previously in Chapter 2, the total measured negative sequence in shorted turn faults analysis can be influenced by various factors. These include inherent asymmetry, measurement asymmetry, voltage unbalance or other undetected faults. Measurement asymmetry has been discussed in the previous chapter, hence this chapter will study the other factors.

5.4.1 The Inherent Asymmetry

Inherent asymmetry in induction machines under healthy operation provides the baseline for negative sequence quantity which is also useful to understand other components of the negative sequence. Every practical machine presents a degree of inherent asymmetries due to the manufacturing imperfections. Inherent asymmetry may be caused by stator winding imbalances, rotor static eccentricities, iron saturations, closed rotor slots or other design related imperfections. Research also shows that inherent asymmetry maybe is a function of load, supply voltage and stator frequency [12]. In this research, because the motor was connected to the line voltage supply, the stator frequency will not affect the negative sequence due to the inherent asymmetry. However, it should be noted that the experiments do not eliminate other sources of the voltage unbalance which may occur. Therefore, the voltage unbalance factors which may affect the total inherent asymmetries will be considered.

In this thesis, the inherent asymmetries were examined under voltage variations, hot measurements, and no load conditions. The no load condition aims to avoid any asymmetrical disturbances which may be worst under load fluctuation. Hot measurement technique was used to minimize any negative sequence effects because

of temperature variations both in the motor and in instrumentations. It should be noted here that due to the complexity of the inherent asymmetry contribution, it is not easy to develop an accurate motor model that can represent the real condition of the machine. Therefore, the computer simulation is not employed in the inherent asymmetry analysis. The experimental results of the inherent asymmetries are given in Figure 5.10.

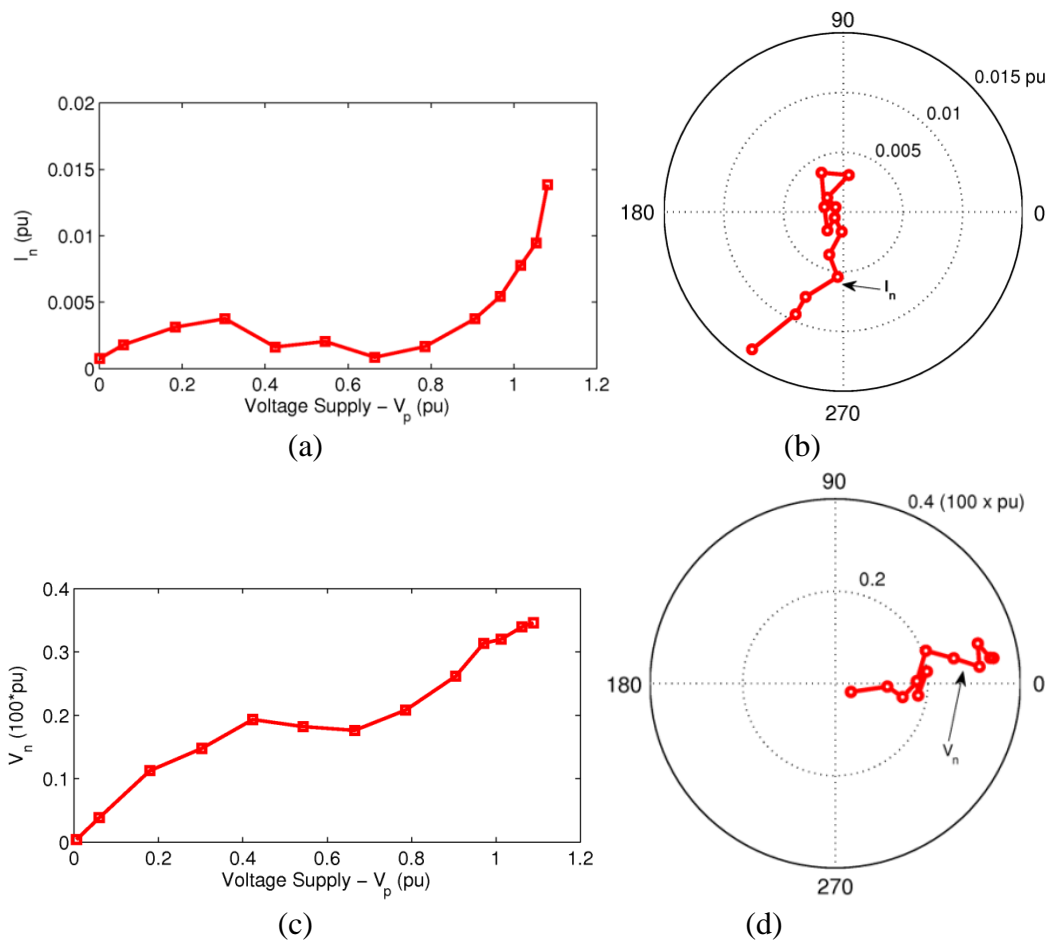


Figure 5.10 Negative sequence current under voltage variation showing (a) the magnitude of inherent asymmetry and (b) the phasor diagram; the voltage unbalances which are indicated by (c) negative sequence voltage and (d) the phasor trajectory.

Figure 5.10 shows negative sequence current due to the inherent asymmetry at various voltages. Note that the negative sequence current increases with the voltage supply variations (more than 0.6 pu), and below 0.6 pu, the negative sequence is mostly affected by high asymmetry since the rotor is not perfectly induced to rotate at synchronous speed. This can be understood from the phasor graph where the orientations of the phase angle are randomly less than 0.6 pu of the voltage supply. In this thesis, the voltage unbalance was around 0.24% at the rated voltage. This means

that the inherent asymmetry that contains a small voltage unbalance can be around $0.0078 \text{ pu} \angle 246^\circ$ at the rated voltage.

The effect of the voltage unbalance during the test can be seen in the negative sequence voltage in Figure 5.10 (c) and (d). It should be noted here that although the previous studies used the negative sequence current to show the inherent asymmetry trends [8, 79], the inherent asymmetry should be accompanied with the evaluation of the voltage unbalance as it was found in this study. This approach will ensure that the inherent asymmetry analysis is obtained accurately and free from other disturbances. The increase in the magnitude and the phasor quantity of the negative sequence voltage confirms that the presence of voltage unbalance is also relatively proportional to the supply voltage variation.

Figure 5.10 (a) and (b) also shows that the negative sequence current increases sharply after 0.8 pu of the voltage supply. This phenomenon may be caused by the saturation due to the characteristics of the close rotor slot type of the motor under test. The saturation effect has been previously described in Chapter 3. The real inherent asymmetry calculation which is free from voltage unbalance will be demonstrated in the next section.

5.4.2 The Voltage Unbalance

Unlike inherent asymmetry, which cannot be avoided and is always present in various operation conditions, the voltage unbalance in the machine can be easily identified and eliminated. The voltage unbalance test and simulation results are given in Figure 5.11 and Figure 5.12.

In this analysis, to measure the voltage unbalance, the Voltage Unbalance Factor (VUF) was defined which includes both magnitude and phase angle of the sequence components. The VUF is defined as the ratio of the negative sequence (V_n) and the positive sequence (V_p) voltage magnitudes given by

$$\% VUF = \frac{V_n}{V_p} \times 100 \% \quad (5.16)$$

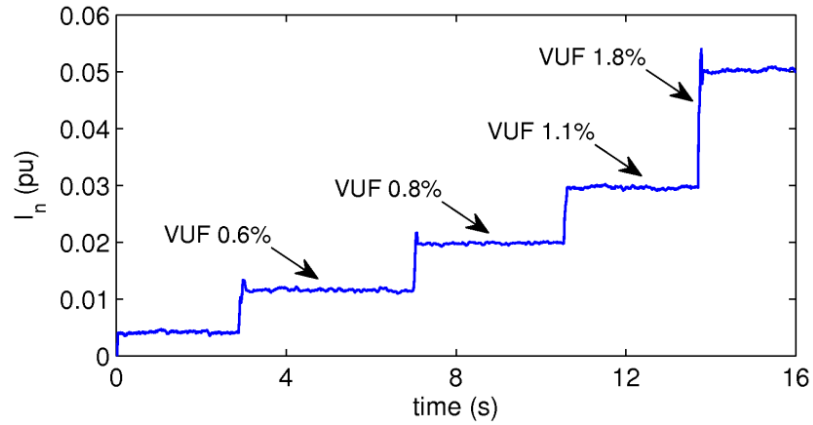


Figure 5.11 The experimental results for different level of voltage unbalances factors including the healthy state.

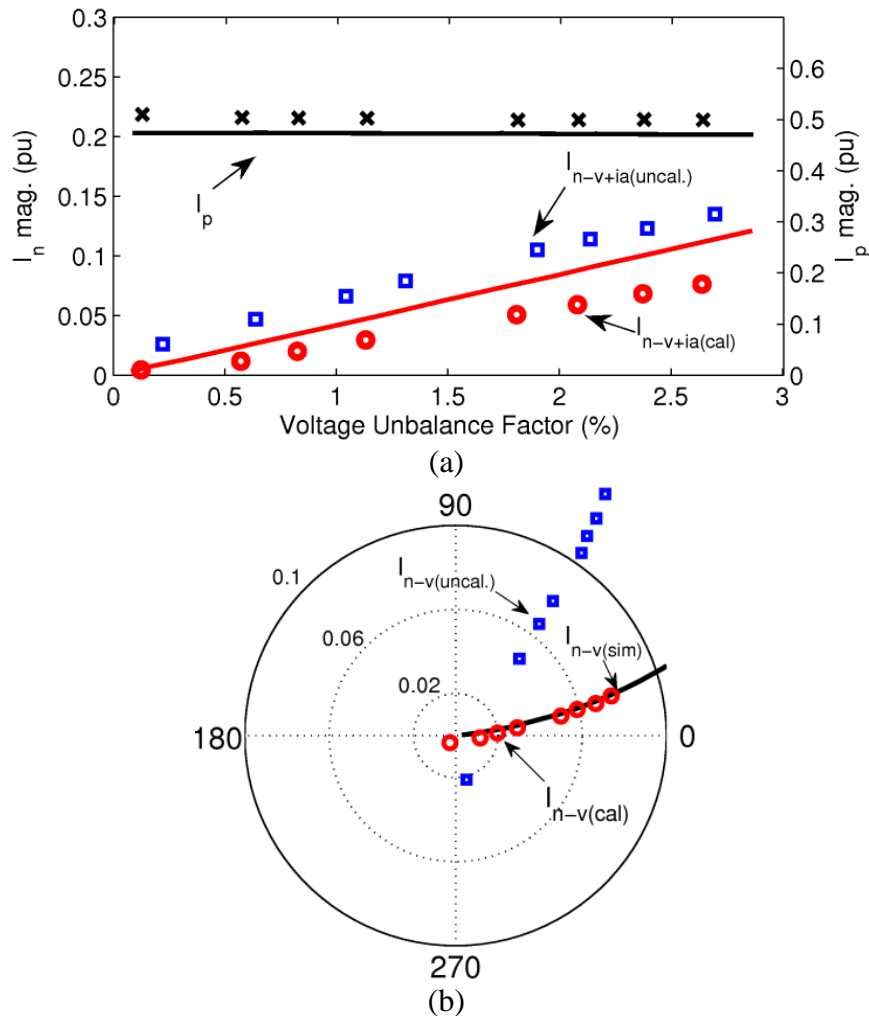


Figure 5.12 Comparison of positive and negative sequence magnitude currents of voltage unbalance and inherent asymmetry; showing the simulation (line) and the experimental results (circle), (a) magnitude variations and (b) phasor representation.

The voltage unbalance test and simulations were carried out by adding external resistors to a single motor phase or one phase of the motor while operating under no load. The magnitudes of positive and negative sequence currents are given in Figure 5.12 (a). The external resistances during the test were increased gradually to highlight the magnitude difference in each voltage unbalance. The external resistors were: 0.25Ω , 1Ω , 2Ω , 4Ω , 5Ω , 6Ω , and 7Ω which corresponds to a VUF of 0.6%, 0.8%, 1.1%, 1.8%, 2.1%, 2.4% and 2.6% respectively. Note that the differences in magnitude negative sequences in the figure can be distinguished clearly compare to the healthy condition.

Note also that in Figure 5.12, results (experiments and simulated) are given for both uncalibrated and calibrated voltage sensors. As it can be seen in the figure, the uncalibrated voltage sensors, which cause asymmetrical sensor gain, can easily lead to false alarm. The negative sequence current magnitudes of the simulation results show small differences reference to the experimental results, which may be due to various factors in the model such as saturation.

As shown in Figure 5.12, a small percentage of voltage unbalance may produce a significant negative sequence current. Unfortunately, in practice, small voltage unbalance is allowed during motor operation. For example, several motor operation standards tolerate up to 2% even 5% of voltage unbalance [71]. As seen in the figure, the negative sequence due to 2% of VUF can produce a false alarm during shorted turn fault detection.

Figure 5.12 (a) indicates that positive sequence currents decrease slightly with the increase in VUF %. Note that this trend is different from the result given in Figure 5.9 (a) for the shorted turn fault. It can be summarized here that such differences can be used as an indicator to classify the voltage unbalance under the shorted turn faults. However, combination of the shorted turn and the voltage unbalance faults can be difficult to be detected by using such indicator alone.

Furthermore, Figure 5.12 demonstrates the presence of inherent asymmetry. The experimental results show that the trending curve of the experimental negative sequence current does not intercept VUF axis at zero (around 0.4%). This represents the existence of negative sequence due to inherent asymmetry. This inherent asymmetry presence can also be clarified from the phasor diagram in Figure 5.12 (b).

Note that the first data circle (which is obtained without an additional external resistor in the voltage unbalance test) does appear at 231° while the other measured data points are on the opposite of the quadrant angle. In other words, the first data may represent the inherent asymmetry but it may still contain the voltage unbalance. Based on this investigation, the inherent asymmetry elimination can be carried out as illustrated in Figure 5.13.

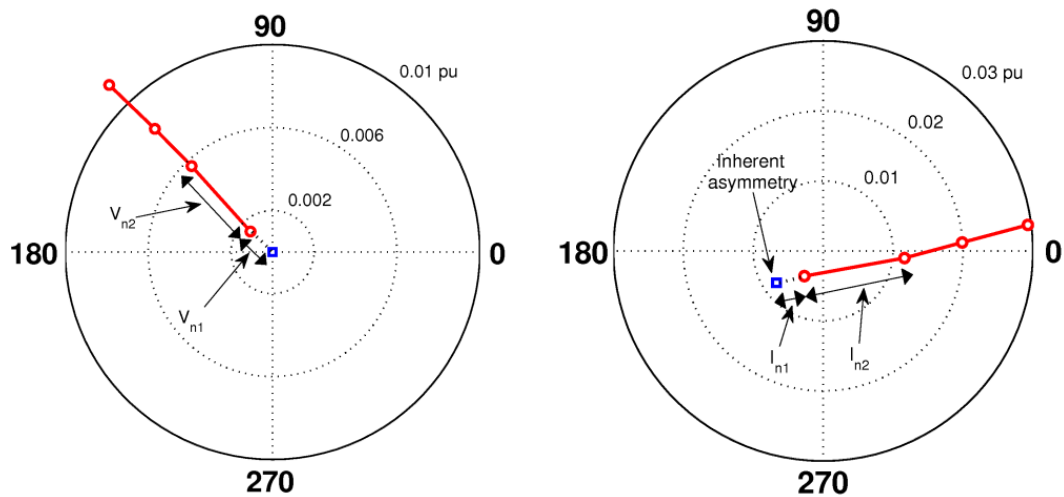


Figure 5.13 The inherent asymmetry graphical calculation using interpolations displaying the negative sequence voltage (left) and the negative sequence current (right).

The inherent asymmetry can be estimated as illustrated in Figure 5.13 that illustrates the part of Figure 5.12. The inherent asymmetry of the induction motor can be determined where the voltage unbalances do not exist or the VUF is equal to zero. The graphical interpolation is carried out to obtain a negative sequence current when the negative sequence of the voltage is zero. Figure 5.13 (left) shows that the quantity V_{n2} is the length between the healthy measured negative sequence voltage data and the negative sequence voltage for VUF of 5.3%. The negative sequence voltage length, V_{n1} is the length when the voltage unbalances do not exist. The negative sequence current due to inherent asymmetry is obtained by comparing the ratio of V_{n1} and V_{n2} , and the ratio between I_{n1} and I_{n2} . The phasor value of the negative sequence due to the inherent asymmetry is calculated as $0.0078 \text{ pu} \angle 211^\circ$ that is also marked in Figure 5.13 (right). This phasor value is applied to analyze the measured voltage unbalance data in Figure 5.12, which is given in Figure 5.14.

Figure 5.14 compares the voltage unbalance results before and after the inherent asymmetries. The magnitude of the inherent asymmetry can be seen in the figure as the square point at the zero voltage unbalance.

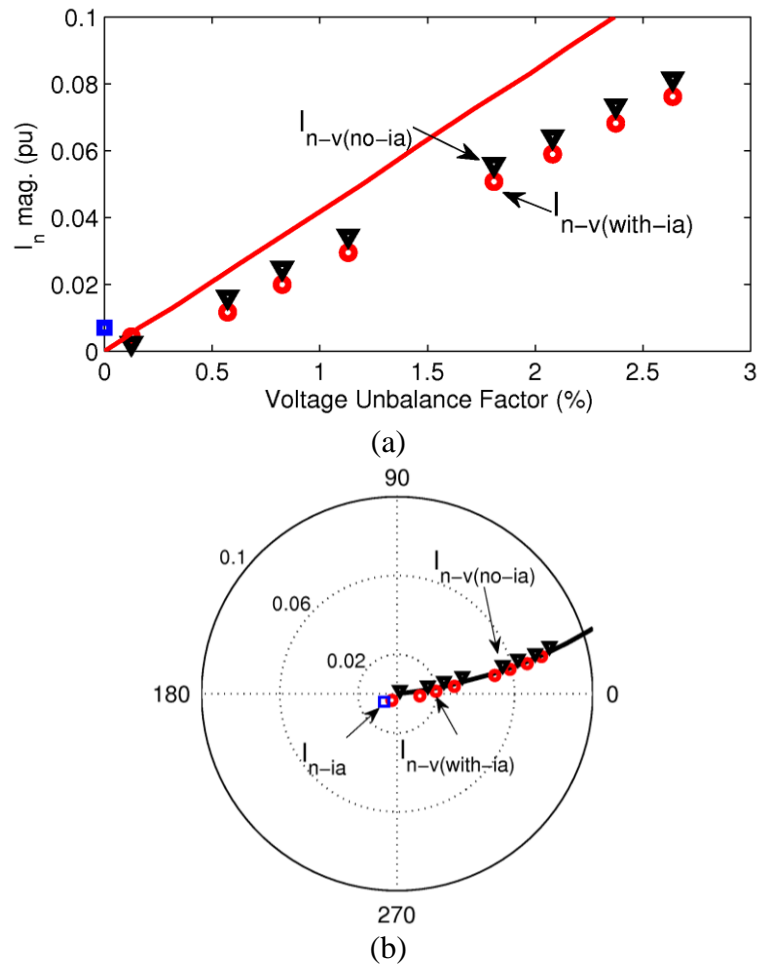


Figure 5.14 Comparison of positive and negative sequence magnitude currents with and without inherent asymmetry (a) and the phasor representation (b) including the calculated inherent asymmetry (symbol □).

Figure 5.14 shows that the series of final voltage unbalance data after inherent asymmetry eliminations are shifted toward the zero, seen as a triangle in Figure 5.14 (b). The inherent asymmetry is eliminated from the measured negative sequence current, resulting only in the real negative sequence due to the voltage unbalance interactions. Note that the phase angle due to the voltage unbalance changes slightly after the inherent asymmetry eliminations. Furthermore, for the simulation results, the phase angles show similarity with the experimental results as seen in the phasor domain. However, as shown in Figure 5.14 (a), significant differences between magnitudes of the negative sequence of the motor model and test results are still present. This may indicate that the model still requires further development to be close

to the experimental conditions, even though the experimental results are close to the ideal motor conditions. Figure 5.15 shows the voltage unbalance in all three-phases of the motor under test.

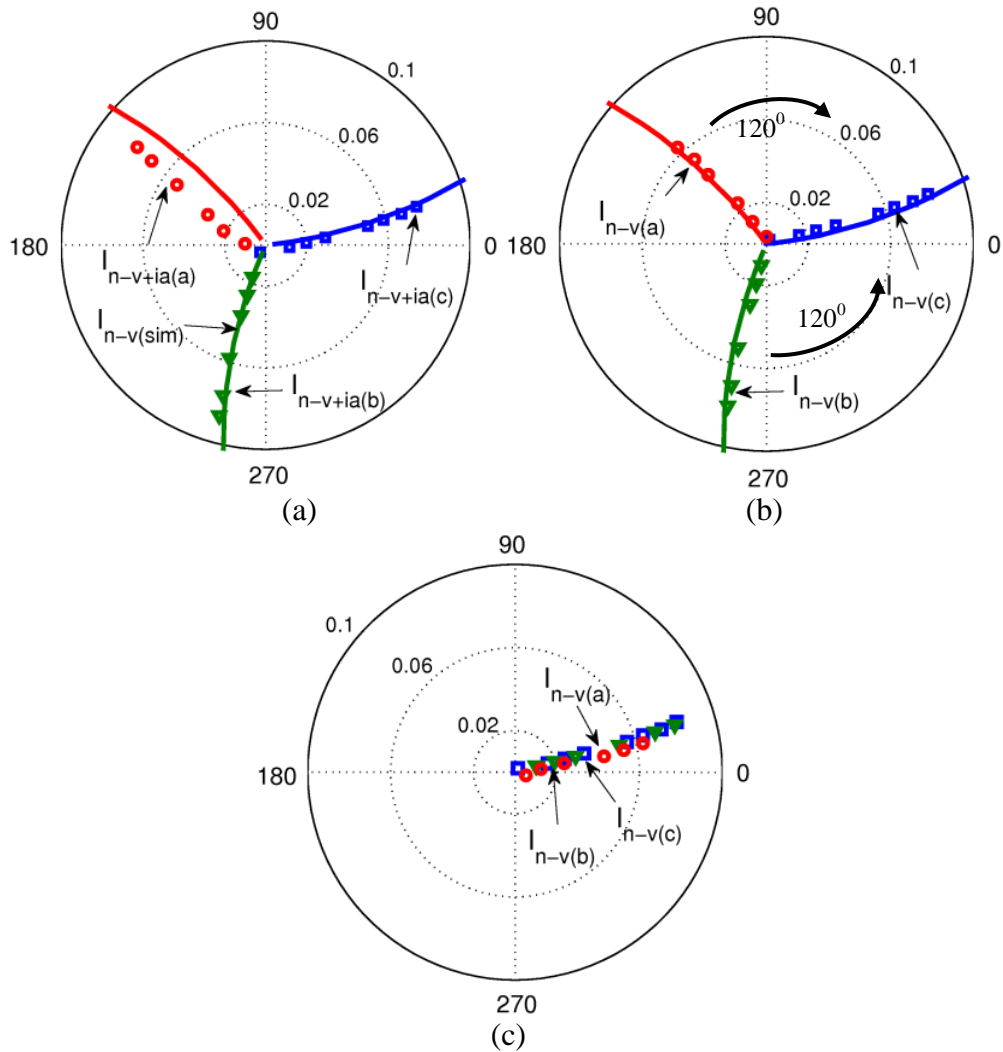


Figure 5.15 Three-phase phasor representation of negative sequence current under voltage unbalance (a) before inherent asymmetry calculation, (b) without inherent symmetrical components, and (c) with 120° shift of phase a and b , showing the simulation results (line) and experimental results (circle, triangle and square for the three-phases).

Figure 5.14 (a), illustrates the complete negative sequence currents when the voltage unbalance is applied to one phase. Note that the measured test data (symbols) of all three-phases is not at the origin. Figure 5.14 (b) illustrates the voltage unbalance data after the inherent asymmetry compensation as previously described, which shows the experimental results starting at the origin and matches with the simulation results. Figure 5.14 (c) shows the results after b - and c -phases rotated by 120° which should ideally overlap with a -phase. The results show that the effect of voltage unbalance is

similar for each phase and free from the inherent asymmetry. This voltage unbalance data can now be used for further compensation of the negative sequence current under supply voltage unbalance.

Unlike the angle analysis of the shorted turn faults in Figure 5.9, the angle of the negative sequence due to the voltage unbalance have different directions even though it has been initiated from the same phase. Like the shorted turn faults, the negative sequence of phase angle can be understood and predicted analytically from the steady state model given below [80].

$$\mathbf{I}_{n(A)}^v \approx -\frac{\mathbf{R}_{\text{ext}} \mathbf{I}_{as}}{3Z_n} \quad (5.17)$$

Considering that the angle of the negative sequence impedance of a healthy motor is around 270° , and the phase angles of the phasors \mathbf{I}_{as} , \mathbf{I}_{bs} , and \mathbf{I}_{cs} are around 6.5° , 241° , and 131° respectively, will result the voltage unbalance prediction angles around 83.5° , 211° , 341° . Note that these predictions have very large offset compare to the experimental and the simulation results. The Equation 5.17 shows that one of the crucial parameters, which determine the angle prediction, is the negative sequence impedance. The healthy machine's negative sequence impedance contains inherent asymmetry and can be a factor contributing to the accuracy of the angle predictions.

5.4.3 The Effect of Load Variations

The literature review in Chapter 3 has shown the importance of the load variations as can give non-linear effect on the measured negative sequence current. The measured negative sequence current can be produced by various negative sequence sources such as inherent motor asymmetry, voltage unbalance, eccentricity or shorted turn faults. It should be noted here that these sources have certain sensitivities to load variations. Therefore, the effects of load variations require specific attention. The effects of load variations on the negative sequence current are examined using a healthy machine and the results are given below in Figure 5.16.

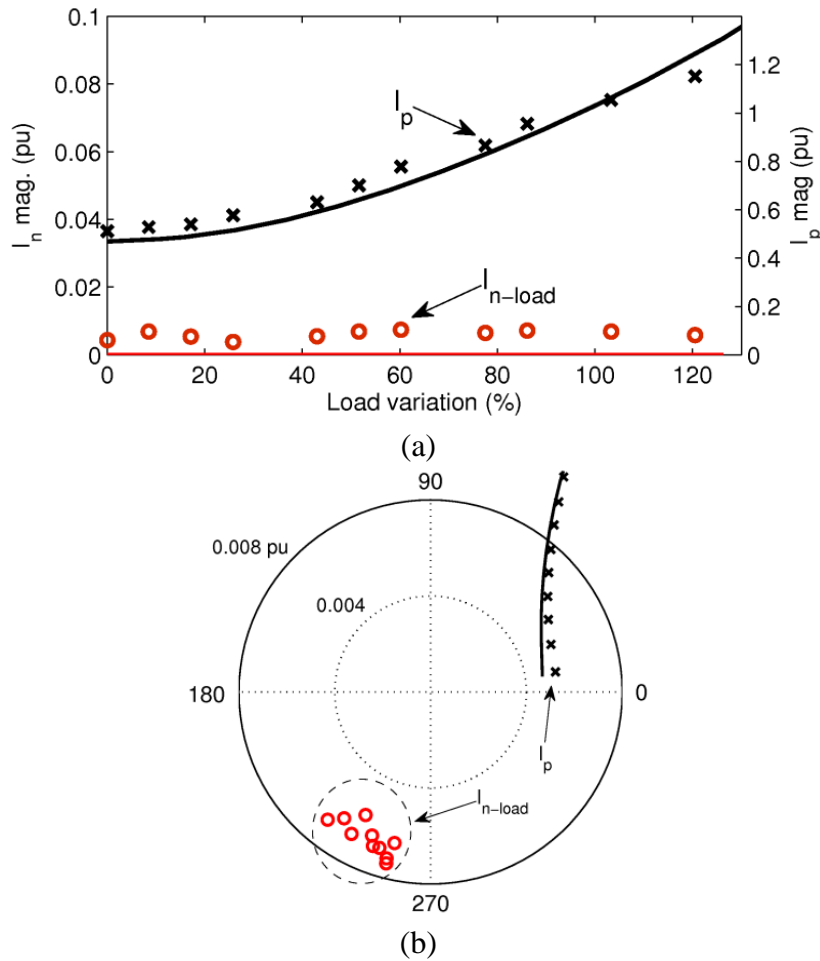


Figure 5.16 The effect of load variations in a healthy motor: simulations (solid lines) and test results (circle and cross).

The figure shows that the load variations produce significant level positive sequence currents, but much less effect on the negative sequence current components. Therefore, it can be concluded that the positive sequence current component can be useful in the identification of the load variation compensation.

The negative sequence current results in Figure 5.16 also highlight the effect of inherent asymmetry with load variations that the load variations have a little effect on the inherent asymmetry. The negative sequence current, which contains inherent asymmetry as well as a small percentage of voltage unbalance, is relatively constant (~ 0.0062 pu) from no load to above full load (120% of the rated load). The average of voltage unbalance is about 0.26% VUF (It is about 0.20% VUF at full load). Furthermore, the phasor patterns of the inherent asymmetry due to the load variation forms in a cluster around a constant angle (250° in this case) as shown in Figure 5.16 (b).

The effect of load variations were also studied at different voltage unbalance values which was introduced by varying external resistors. It was demonstrated that the voltage unbalance affects the negative sequences significantly. However, in practice, the load effect also occurs simultaneously as the voltage unbalance. To examine this, both simulation and experimental studied were performed using fixed external resistances of 0.25Ω , 1Ω , 2Ω and 4Ω to produce voltage unbalances as the load varied from no load to 123% of rated load and the results are given in Figure 5.17.

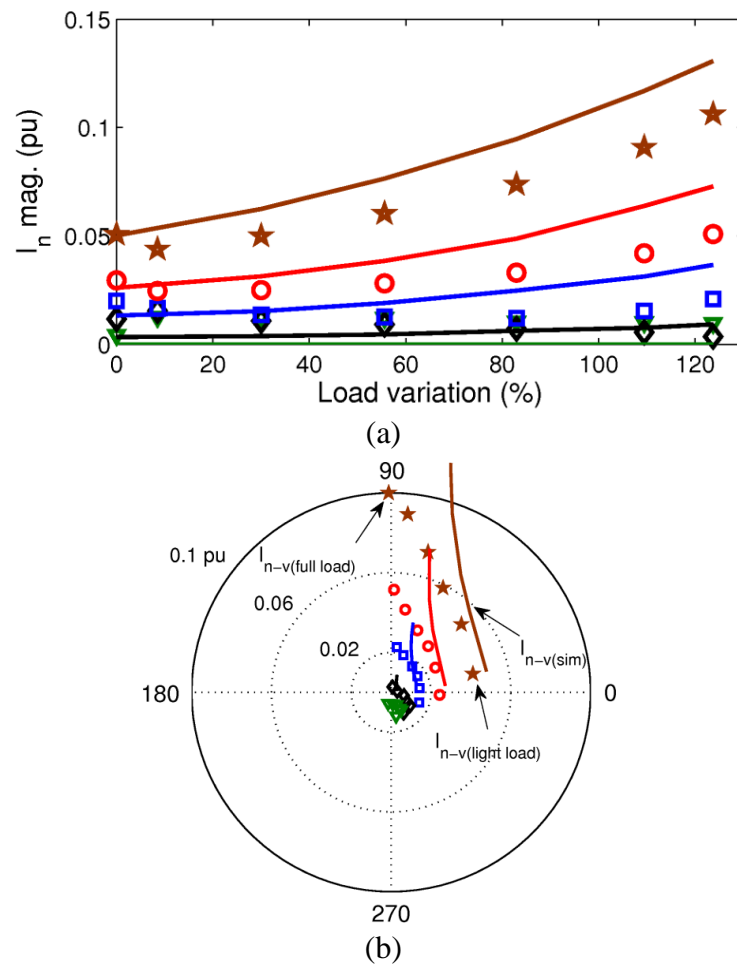


Figure 5.17 The effect of load variations on the negative sequence current under voltage unbalance using varying external resistors $r_{\text{ext}}=0.25\Omega$ (triangle), $r_{\text{ext}}=0.5\Omega$ (diamond), $r_{\text{ext}}=1\Omega$ (square), $r_{\text{ext}}=2\Omega$ (circle) and $r_{\text{ext}}=4\Omega$ (star).

The above figure shows that the load variations under a constant voltage unbalance tend to increase the negative sequence current components. The load variation doubles the magnitude of the negative sequence under the voltage unbalance, above the external resistance of 2Ω . The voltage unbalance also creates a degree of phase angle shift (about 86°) of the negative sequences current. Note that the increase

in the negative sequence magnitude and the angles may not be due to the voltage unbalances only. It can be observed in Figure 5.17 (b) that the negative sequence phase angles of the simulations and the test results appear in the same quadrant in the phasor graph. However, the differences between the simulation and experimental results may be due to several factors, such as the presence of inherent asymmetry in the motor under test, or the accuracy of the induction motor model (in terms of simultaneous inherent asymmetry and the voltage unbalance supply faults). Therefore, to understand the effect of the voltage unbalances, which are free from inherent asymmetry, further examination is carried out and the results are given Figure 5.18.

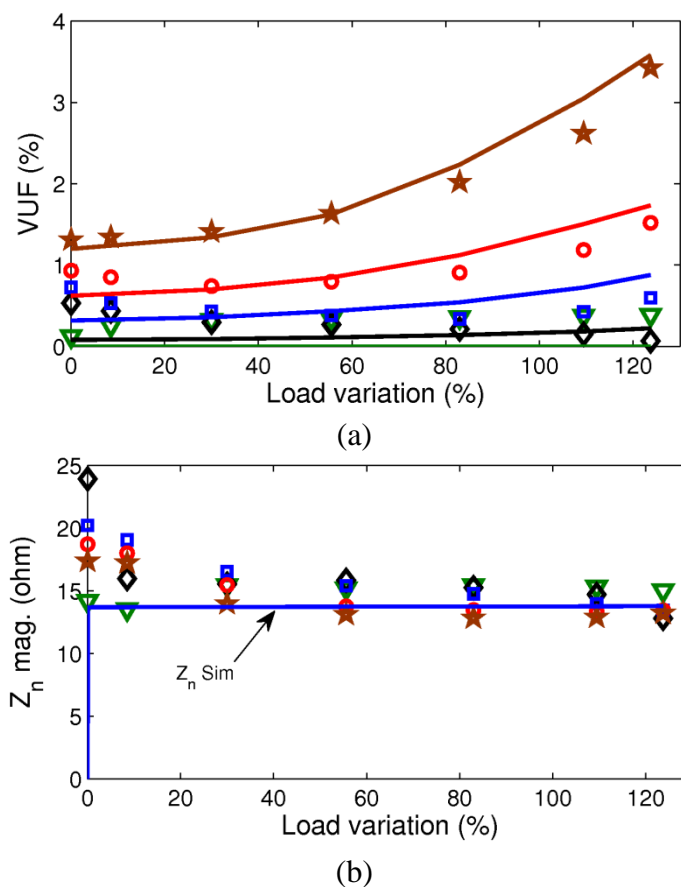


Figure 5.18 The voltage unbalance analysis using external resistors, $r_{ext}=0.25\Omega$ (triangle), $r_{ext}=0.5\Omega$ (diamond), $r_{ext}=1\Omega$ (square), $r_{ext}=2\Omega$ (circle) and $r_{ext}=4\Omega$ (star) under load variations showing (a) the observed voltage unbalance factor (VUF), and (b) magnitude of the negative sequence impedance.

Figure 5.18 shows that the voltage unbalances increase with the motor loading. The external resistors reduce the positive sequence voltages while increasing the negative sequence voltages. Note that the positive sequence voltage decreases with load because of the larger voltage drop across the external resistors. Furthermore, the

negative sequence voltage increases with the load due to the larger asymmetry in the three-phase voltage supply.

Figure 5.18 (b) also illustrates that the negative sequence impedance decreases slightly with load. It was found that the negative sequence impedances vary about 25% from no load to full load case. The negative sequence impedances ideally are not affected by the load variations as shown in the simulation study for the open slot rotor type motor. However, in the closed slot rotor type motor, the closed magnetic circuits around the slot can cause significant leakage flux not reaching the stator winding. This phenomenon produces high leakage reactance or high negative sequence impedance under light load. The impedance tends to decrease at higher motor loading since the irons that close the slots are saturated reducing the leakage flux proportionally. The figure also shows that the voltage unbalance variations present on impedance band of 2.4Ω at above the motor loading of 30%. This impedance band can be caused by the variation of negative sequence resistances due to the temperature effect. These two factors, i.e. iron saturation and winding resistance, can be crucial issues to implement the negative sequence impedances as an accurate parameter for fault detections.

To determine the level of voltage unbalance due to the external resistors, the measured negative sequence should be eliminated from other unwanted contributors such as the inherent asymmetry. Figures 5.19 shows the magnitude of the negative sequence current after the inherent asymmetries are removed.

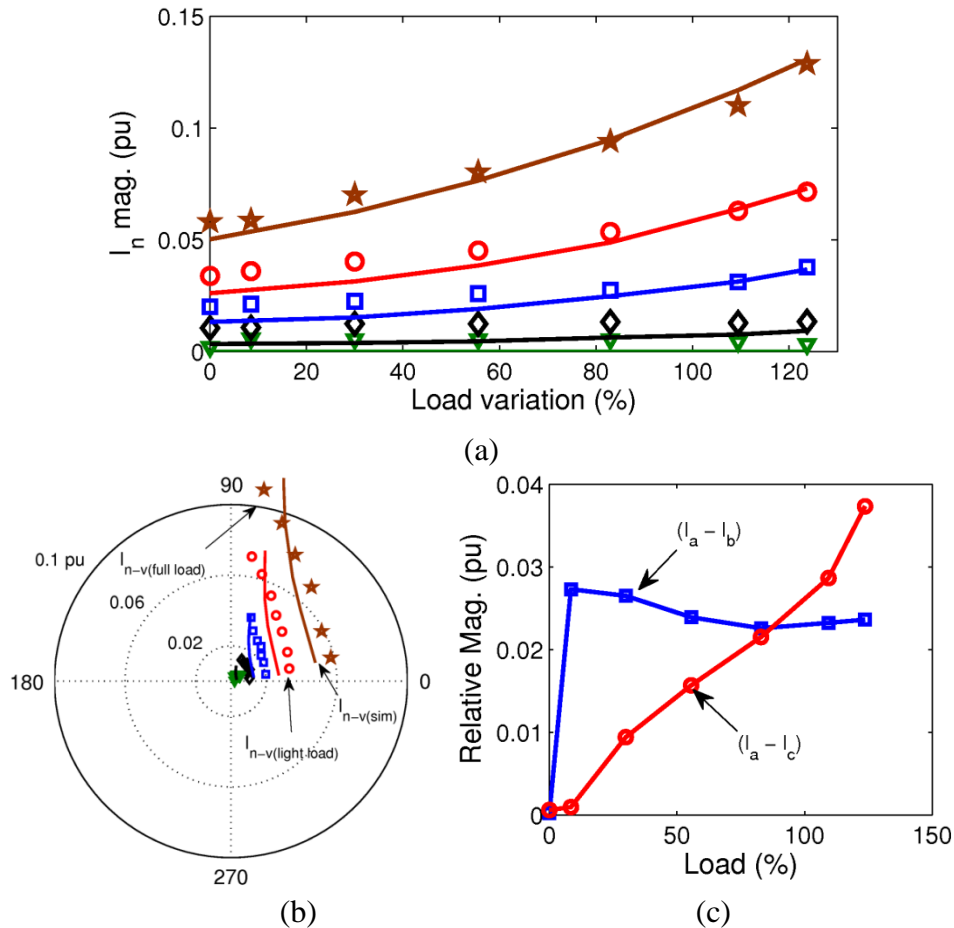


Figure 5.19 The effect of load variations and voltage unbalances after the inherent asymmetry eliminations: (a) the magnitude (b) phasor and (c) the relative magnitude of the stator currents between the phases I_a - I_b and I_b - I_c .

Figure 5.19 also clarifies that the true negative sequence current due to voltage unbalances increase with the load. The stator currents, which increase with the load, develop significant level of asymmetries among the three-phase current as shown in Figure 5.19 (c). Assuming that the negative sequence impedances of the induction motor and the input voltages are constant, the increase in the asymmetrical stator current together with the external resistor in one phase increases the negative sequence current. Note that the figure also shows smaller discrepancies between the experimental and simulated results as in Figure 5.17. The elimination of the inherent asymmetry also shifts the phase angle to the origin of the phasor diagram of the voltage unbalance.

The effect of the load on the shorted turn faults has also investigated in this research. The experiments have been carried out to simulate of the shorted turn faults under load variations. The load is varied from no load to full load with five steps of shorted turn faults: 0%, 1.7%, 3.5%, 5.3% and 7.1%.

Figure 5.20 illustrates these investigations, the negative sequence current under load variations. The shorted turn negative sequence current under no load was obtained when the rotor of the induction motor under test was uncoupled to any load. The motor loading was examined under seven different loading levels, from no load to 123% of the rated load. Figure 5.20 (a) demonstrates that the negative sequence magnitude of each shorted turn level can be visibly identified. The shorted turn negative sequence decreases slightly with the load variations, having opposite trend to the effect of motor loading under the voltage unbalance. In addition, the load effect slightly shifts the negative sequence angle between 30% and 80% of the rated load (about 6°). These magnitude and angle changes may be caused by the characteristics of the closed rotor type of the induction motor or the presence of static motor eccentricity.

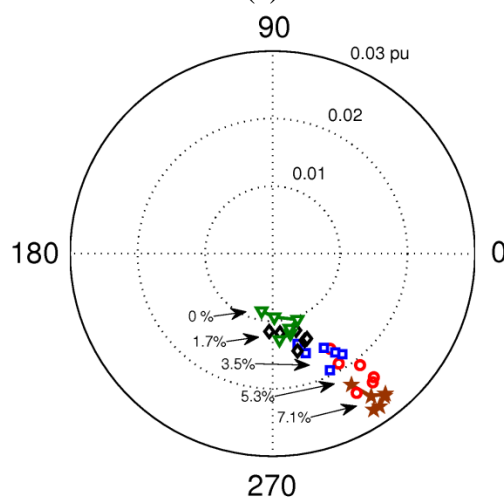
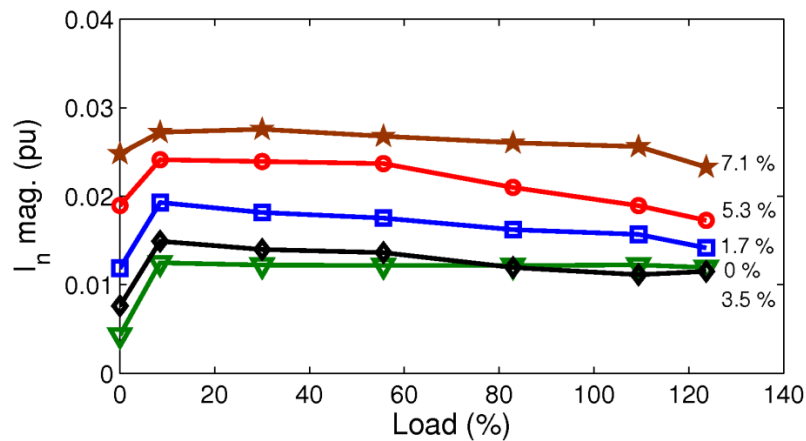


Figure 5.20 The effect of load variations on the negative sequence under various level of shorted turn faults: (a) the magnitude of I_n , (b) phasor diagram of I_n under the shorted turn faults of 0% (triangle), 1.7% (diamond), 3.5% (square), 5.3% (circle) and 7.1% (star).

Unlike the experimental results, the simulations of the shorted turn under load show a slightly increasing trend. This differences show the limitation of the model under various conditions of the induction motor which can be improved further considering various rotor types.

Figure 5.21 shows the results of the voltage unbalance analysis and the negative sequence impedances under various shorted turn faults and at various load levels. Figure 5.21 (a) demonstrates that voltage unbalance factor was maintained at similar level during motor loading. In other words, the effect of the voltage unbalance on the negative sequence current is minimal hence can be ignored.

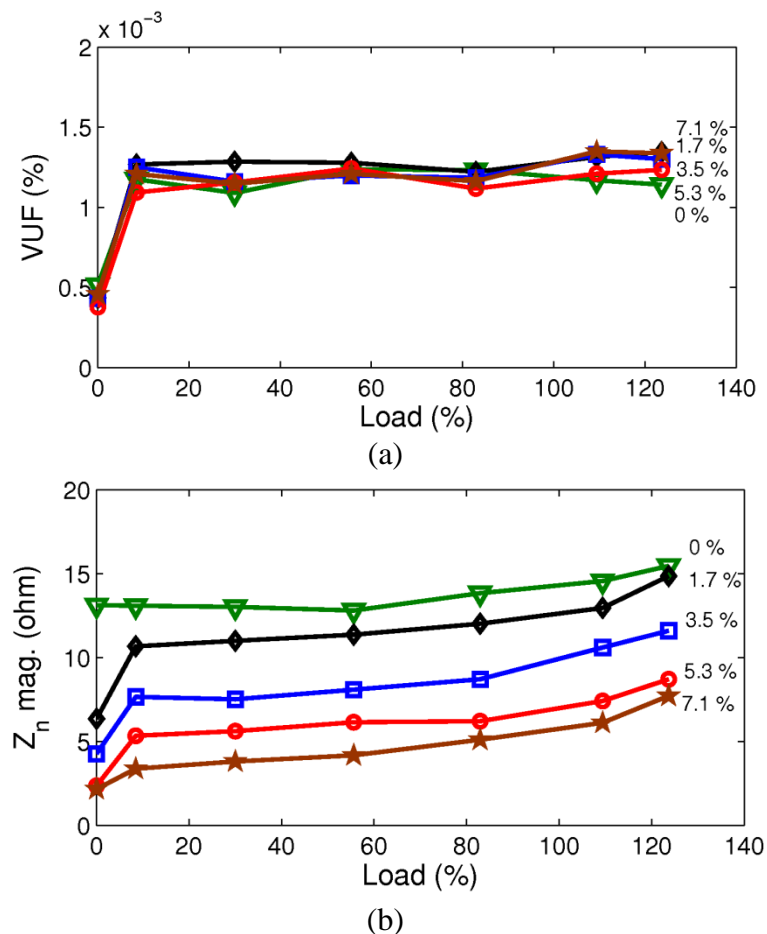


Figure 5.21 The analysis of load variations under various level of shorted turn faults of: 0% (triangle), 1.7% (diamond), 3.5% (square), 5.3% (circle) and 7.1% (star), (a) the corresponding voltage unbalance factors and (b) the negative sequence impedances.

The negative sequence impedance of the shorted turn faults during motor loading can be examined in Figure 5.21 (b). As it can be seen, the negative sequence impedances in each fault level can be distinguished clearly, which is different than the negative sequence impedance variations due to the voltage unbalance shown in Figure

5.18 (b). This negative sequence impedance variation can be implemented to differentiate between the shorted turn faults and voltage unbalance supply. The figure also shows that the higher level of the shorted turn faults, the negative sequence impedances gets smaller. This means that the higher levels of the shorted turn faults in one phase, the asymmetrical reactances of the three-phases also get higher. This negative sequence impedance characteristic can be also implemented for shorted turn fault indicator.

Figure 5.21 (b) illustrates that the negative sequence impedance rises gradually from no load to full load. This trend is different with the negative sequence impedance under the voltage unbalance in Figure 5.18 (b). This gradual increase of impedances may be due to two possible factors.

Firstly, the load current may cause the increase of impedances. As previously discussed, the closed rotor slot type may cause small decrease in negative sequence impedance under voltage unbalance around the rated load. However, under asymmetrical stator inductances due to the shorted turn faults, the asymmetry of the three-phase stator reactances as well as asymmetry of stator to rotor mutual reactances will occur. The mutual reactances, which rely on rotor angle from the integration of motor speed, increase with load. This gradual rise of reactances in turn will increase the total measured negative sequence impedances.

Secondly, the higher impedances at high motor loading conditions may also be caused by eccentricity. Unequal static air gap between stator and rotor will introduce additional inductances for rotor, stator as well as for the stator-rotor mutual-inductances. Under load variations, the stator inductance is fixed, however, rotor inductance will vary as a function of the rotor speed because the effect of non-uniform air gap permeance modulation. These additional inductances will increase the total negative sequence impedances with the motor loading according to the eccentricity severity level of the induction motors. Even though the eccentricity faults are not introduced deliberately, a very small eccentricity may occur during the manufacture.

In this section, a comprehensive analysis of load disturbances was carried out under the shorted turn faults as well as voltage unbalance or inherent asymmetry. The non linear effect of the load may influence the measured negative sequences currents. One of the important factors is identifying the type of the rotor and the presence of

eccentricity related faults in the rotor. This thesis will investigate the effects of the eccentricity faults in next chapter using the experimental work. However since the motor model did not include to simulate eccentricity related faults, it is not included in this study.

5.5 The Effect of Other Faults on the Negative Sequence Current Monitoring

As known, the induction motors may have various faults that may affect the asymmetry of induction motor operations, and causing negative sequence currents. Some of the major faults include the eccentricity, broken rotor bar and bearing related problems. Due to the availability of the experimental setup, this section will only discuss the eccentricity and the broken rotor bar fault. Note that these faults have not been studied in the literatures.

5.5.1 Eccentricity Faults

Eccentricity-related faults occur because rotor and stator is not positioned at the same centre either in radial or axial direction gap [81]. There are two types of eccentricity according to the rotor positions: static air-gap eccentricity and dynamic air-gap eccentricity. The static eccentricity occurs if the minimum air-gap length position is fixed in space (see Figure 5.22 (b)). In the dynamic eccentricity, however the centre of the rotor is not at the centre of rotation hence the position of the minimum air-gap rotates with the rotor (see Figure 5.22 (c)). In machines, both types of eccentricities usually occur at the same time.

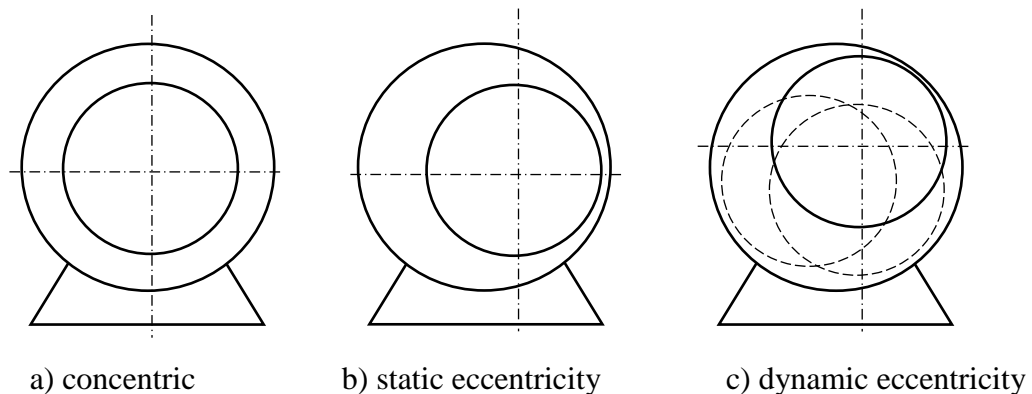


Figure 5.22 Types of eccentricities in rotating machines.

In Practice, in induction machines 5% or even 10% air gap eccentricity is allowed. However, the air-gap need to be kept as small as possible, not only reducing the noise or minimizing the unbalance magnetic pull but also preventing the rotor to damage the stator core and the windings [82, 83]. Since the induction motors have smaller air-gap than other types of electrical machines, the negative sequence current is very sensitive to the small changes of air-gap. In the case of static eccentricities, ovality of the stator core or incorrect positioning of the rotor or stator at the commissioning stage [84] may cause asymmetry during the motor operation. For the dynamic eccentricity, bearing wear or misalignment, a bent rotor shaft, incorrect manufacture of the components, or mechanical resonance at the critical speed [82] may also result in asymmetry in rotor.

In this thesis, a custom built induction motor with adjustable static eccentricity features used (see Figure 5.23). The degree of the static eccentricity is introduced by adjusting the position of the bearing housing at the custom-built end plate of the induction motor. In this setup, the bearing housing can be raised or lowered by two graduated screw to create a static eccentricity with a resolution up to 0.01 mm at either end of the rotor. For the motor under test, the air-gap of the rotor was measured 0.39 mm in one side. In the static eccentricity test, one bearing housing were raised +0.05 mm and +0.1 mm, then lowered -0.05 mm and -0.1 mm while the other end side is fixed at zero eccentricity (centered rotor).

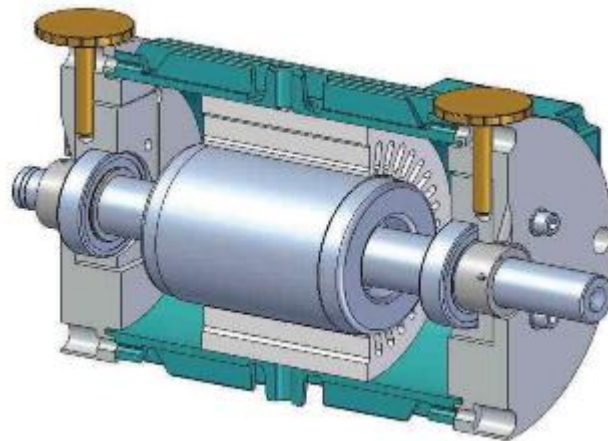


Figure 5.23 The section view of induction motor including the arrangement for static Eccentricity experiments.

The negative sequence currents due to the introduced eccentricity as function of motor loading are given in Figure 5.24. The experimental results show that the

static eccentricity produces negative sequence current even though its value is smaller than the value in the shorted turn faults.

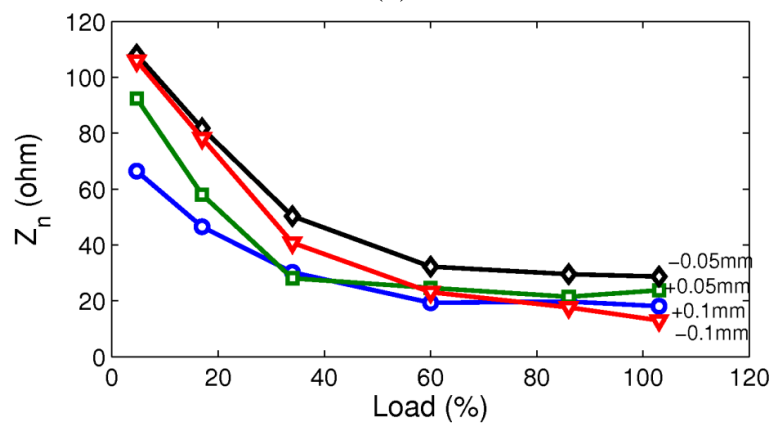
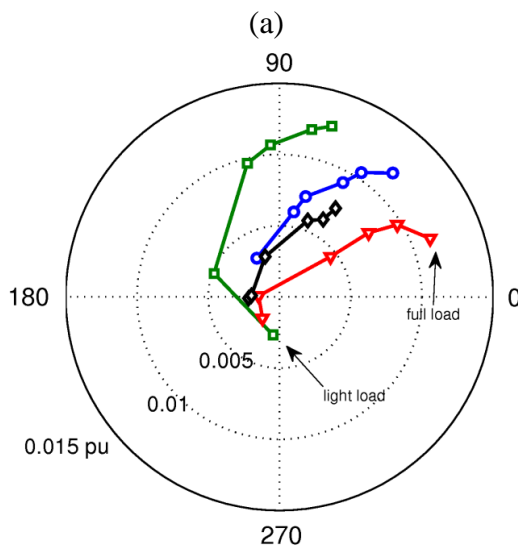
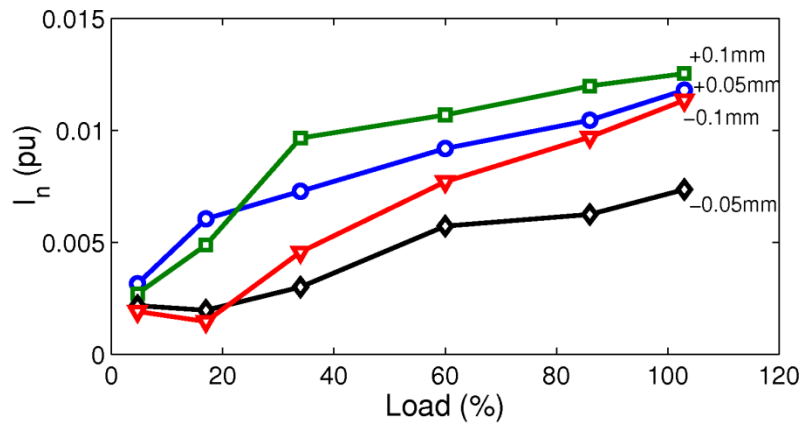


Figure 5.24 The experimental results of the static eccentricity faults with the severity level of +0.1 mm, +0.05 mm, -0.05 mm, and -0.1 mm, showing (a) the magnitude of the current and (b) the plot of trajectory and (c) the negative sequence impedance as a function of load.

The figure clearly indicates that the negative sequence current directly proportional to the air gap size due to the eccentricity. For example, +0.1 mm of static eccentricity level produces higher negative sequence currents than +0.05 mm of static eccentricity level. The negative sequence currents also increase steadily with the motor loading. These tests did not involve any voltage unbalance as observed from the steady negative sequence current results under the motor loading variation with an average VUF of 0.50%, 0.51%, 0.50% and 0.48% for the static eccentricity levels +0.05 mm, +0.1 mm, -0.05 mm and -0.1 mm respectively. This means that the measured negative sequence currents are free from the voltage unbalance influences. In other words, the negative sequence impedances slightly decrease and vary with the percentage of eccentricity under the motor loading. Note that the negative sequence impedance variation due to the eccentricity fault is opposite to the result obtained under shorted turn faults (see Figure. 5.21). The decrease in the asymmetrical negative sequence impedances with motor loading is due to the type of closed rotor as given in Figure 5.24 (c). The negative sequence impedances vary with the severity level of eccentricity faults at the same load level.

The static eccentricity also changes the angle of negative sequence current clockwise with the motor loading. These angle changes are different with the changes of angle under voltage unbalance using additional resistor (counter clockwise). This phasor trajectory can be used to identify any faults due to eccentricity by monitoring the increase of trend of magnitude and angle periodically.

5.5.2 Broken Rotor Bar Faults

A rotor related fault could be potential problems for the induction motor even though it is not immediately causing motor failures as in shorted turn faults. There two type of rotor faults in the squirrel cage induction machine [18]: rotor winding related problems (cracking in the rotor bars or at the cage end rings) and rotor body defects (cracking in the rotor body). Broken rotor and end ring faults, especially for die cast squirrel cage rotor, is almost impossible repair [85].

Several causes of the broken rotor bars and ring faults can be identified. The faults can be caused by manufacturing faults during casting, due to welding problems, or due to motor speed fluctuations [82, 86]. These causes can increase the resistances of the rotor circuit which in turn overheat the rotor bars initiating the rotor cracks.

Note that due to repetitive start/stop and motor speed fluctuations during operation, high currents also generate large forces on the rotor bars, which cause material fatigue resulting cracks between bars and ring. Besides these causes, voltage unbalance, single phase operation, contamination or corrosion, and vibration may also initiate the broken rotor bar faults. The broken rotor bar profile and the end-ring section is illustrated in the photo below, which is a like rotor piece used in the motor under test in this thesis.



Figure 5.25 The section of the motor used during the test indicating the slot type.

Note that Figure 5.25 shows a closed slot type of rotor that can significantly affect negative sequence current. During the test, the rotor bar was partially removed by drilling to simulate a broken rotor bar fault. The tests were performed using 1, 2 and 4 broken rotor bars, and the results are given in Figure 5.26.

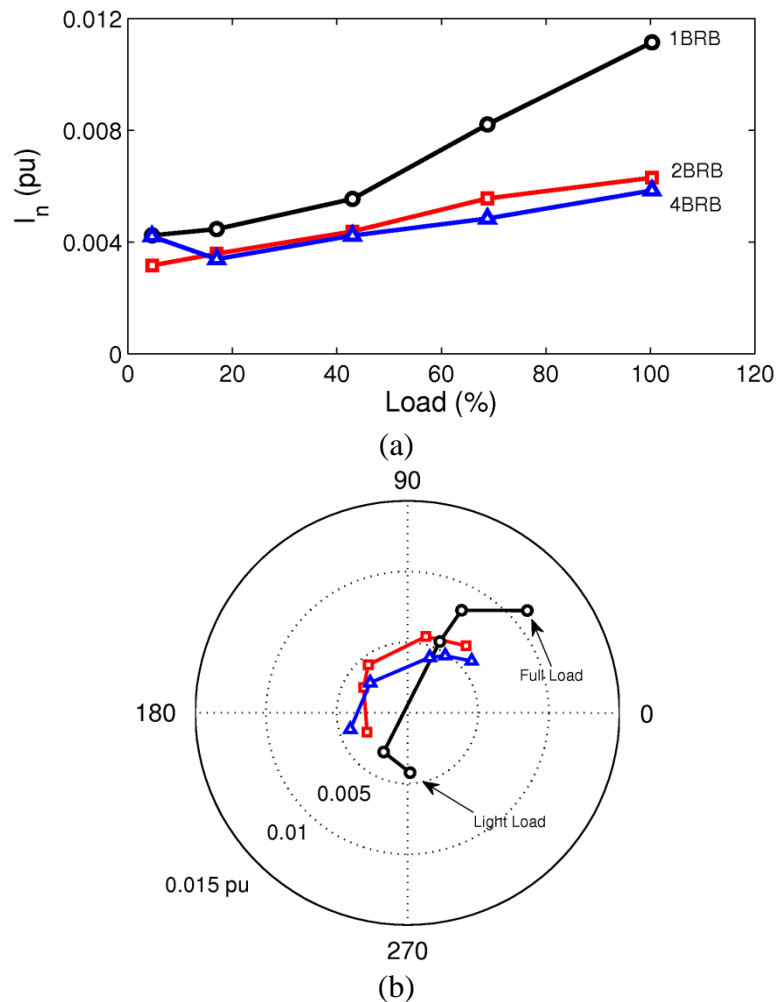


Figure 5.26 The experimental results of the broken rotor bar faults (1,2 and 4 broken bars) showing (a) the magnitude and (b) the trajectory of the negative sequence current as a function of load.

The results show that broken rotor bar faults have different asymmetrical effect on the negative sequence currents compare to other faults or disturbances. Unlike other asymmetrical sources, such as shorted turn faults, eccentricity or voltage unbalance, Figure 2.26 shows that the number of broken bars inversely proportional to the magnitude of negative sequence currents. The negative sequence current magnitude of two broken rotor bars is 55% smaller than the magnitude of the one broken bar. However, the negative sequence current magnitudes due to two broken rotor bars also look similar with four broken bars. This result indicates that the negative sequence current is not a good indicator for the faults having more than one broken rotor bar.

The magnitude variation in the negative sequence current is also visible in Figure 5.26 (b), from 0.004 pu under light load to 0.011 pu under full load. Note that similar magnitude variation is also observed under 1 broken rotor bar fault and with

1.7% shorted turn faults which indicates the difficulties to distinguish faults using the magnitude of negative sequence only. The polar plot analysis can help to differentiate the shorted turn faults (see Figure 5.20) which the angles are relatively constant with the load. However, in the broken rotor faults, the phasor angles changes clockwise from about 270° at low load to 45° at full load. The broken rotor bar faults also found to have relatively similar and unique phasor trajectory with eccentricity faults as given in Figure 5.24 (b). The such similarities in the phasor angle trajectory makes the identification of faults difficult specifically if two faults occur simultaneously. This indicates that further research is required to utilize the negative sequence method in the condition monitoring of induction motor that has both broken rotor bar and eccentricity fault simultaneously.

5.6 Conclusion

This chapter demonstrated a comprehensive investigation of negative sequence method to monitor shorted turn faults using both motor model and experimental results. The shorted turn computation model was developed based on the MCC model which utilized the real induction motor parameters. The effects of the shorted turn faults and the individual disturbances, (such as voltage unbalance and inherent asymmetry) on the negative sequence current were investigated.

It can be summarized that the negative sequence current increases with the level of shorted turn faults. In addition, the supply voltage unbalances also demonstrate similar increase in the negative sequence current. The magnitude of voltage unbalance may lead to false alarm if the source of negative sequence is not identified properly. The phasor trajectory of supply voltage unbalances and shorted turn faults can be used to differentiate the sources of negative sequences currents. It was also verified that both shorted turn faults and voltage unbalance generates negative sequence due to the inherent asymmetry. A simple graphical interpolation method was developed to interpret the level of negative sequence due to the inherent asymmetry.

The chapter revealed that compensation of the measured inherent asymmetry can improve the accuracy of measured negative sequence. It also demonstrated the effects of the negative sequence current contributors under varying motor load. It was demonstrated that the motor loading has non-linear effect on the measured negative

sequence. It was observed that the motor loading may change the negative sequence components depending on the motor structure, especially the type of rotor.

Other type of induction motor faults such as eccentricity and broken rotor bars are also investigated in this section, which help to understand the impact of simultaneous multiple faults on the negative sequence current. The eccentricity and broken rotor bars faults are found to affect negative sequence current that increases significantly with the motor loading. It was found that although the magnitude and angle of negative sequence phasor of both faults can be used to differentiate the shorted turn faults, the negative sequence current analysis is unable to classify the broken rotor and eccentricity if they occur at the same time.

Finally, it can be concluded that although this chapter provides comprehensive investigation of negative sequence current under various faults and disturbances and under motor loading, it is important to distinguish faults from disturbances. Therefore, the compensation techniques, which obtain negative sequence due the motor faults, will be discussed in the following chapter.

Chapter 6

Negative Sequence Compensation technique for Stator Shorted Turn Faults

6.1 Introduction

The literature review in Chapter 2 revealed several promising techniques to increase the applicability of the stator current negative sequence monitoring. The techniques to obtain the accurate negative sequence current included a simple look up table of the motor impedance and highly complex neural networks method. Although the advance mathematical approaches provide a good performance, this thesis considers much simpler approaches using the measured data. For example, the utilization of the measured negative sequence current, impedance, admittance, or semi empirical formula can be developed to compensate the disturbances or non-idealities in the machine. In this chapter, previous negative sequence monitoring methods will be compared to understand their performances and characteristics firstly, which will be followed by applications and improvements.

6.2 The Comparison of Negative Sequence Current Compensation Techniques

Three techniques that will be investigated are admittance techniques, negative impedances and semi empirical formulas as discussed in Section 2.3.2, 2.3.3 and 2.3.4 respectively. These techniques are selected due to their capacity to provide basic understanding of disturbance compensation. The techniques are tested using identical data to compare their performances accurately. The original test data is shown in Figure 6.1 where the combination of inherent asymmetry, shorted turn faults and supply voltage unbalances are introduced. The measurements were done under no load to obtain a baseline work to developed compensation techniques.

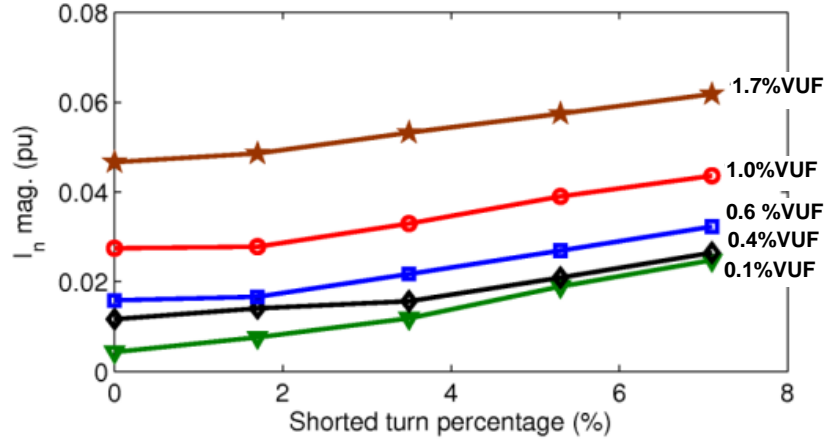


Figure 6.1 The experimental results of the shorted turn faults under voltage unbalances and inherent asymmetry.

Note that the figure illustrates the variation of the measured negative sequence current as a function of both the number of shorted turns and the voltage imbalance under no load conditions. As stated previously, the number of shorted turns was varied between 0 and 20 turns (which corresponds to a maximum of 7% shorted turns), and the voltage unbalance factor was varied from 0.1% to 1.7% in five steps which resulted 25 individual test conditions in total.

The first method that will be investigated is the admittance monitoring technique which was discussed previously in Section 2.3.2. This technique, which accommodates the compensation of motor loading and voltage unbalances, aims to obtain real negative sequence currents under phasor regression analysis. Negative sequence current under voltage unbalance and inherent asymmetry was calculated using the test results. In the test, the same voltage unbalance data given in Figure 5.17 was utilized. Five sets of data under different voltage unbalances (each containing seven different levels of load variations) were employed, which included no shorted turn faults. The complex constants of the admittances were determined using least square method given earlier in Equation 2.20. The calculated complex constants are given below in Equation 6.1. This equation was developed to determine the calculated negative sequence current that is due to the voltage unbalance and the inherent asymmetry using the measured positive sequence and negative sequence voltages. Then the negative sequence current due to the actual faults were calculated using the measured negative sequence current as given in Equation 6.2.

$$\mathbf{I}_n^{v+ia} = (0.0792 - 0.0294\mathbf{i}) + (-0.0025 - 0.0013\mathbf{i})\mathbf{V}_p - (5.7e-05 + 1.4e-5)\mathbf{V}_n \quad (6.1)$$

$$\mathbf{I}_n^{sf} = \mathbf{I}_n - \mathbf{I}_n^{v+ia} \quad (6.2)$$

The calculated negative sequence currents due to the shorted turn faults after the compensations are illustrated in Figure 6.2. Note that the voltage unbalance effect is removed from the measured negative sequence current even under the small percentage of voltage unbalance operation. In addition, the magnitudes of negative sequence currents decrease with the level of shorted turn faults. It is important to emphasize that these results do not look very accurate compare with the real machine operation where higher number of shorted turns produces higher negative sequence currents. The results shows that the negative sequence magnitudes appeared to be under the influence of load variations even though the experiments were performed under no load conditions.

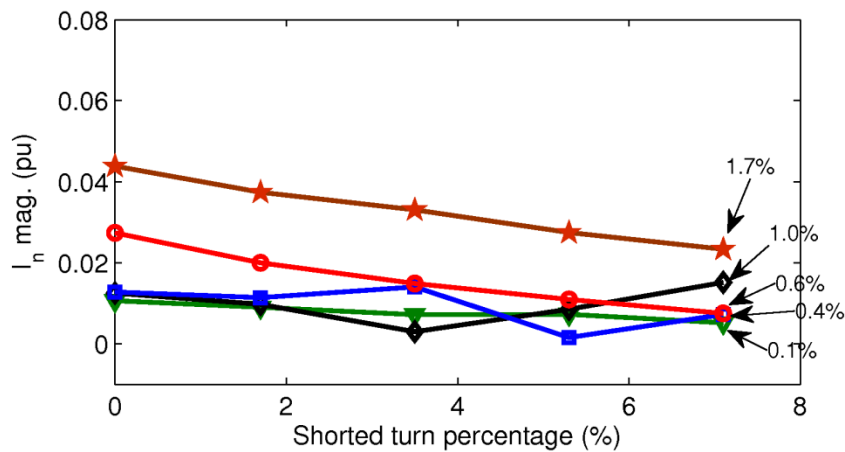


Figure 6.2 Shorted turn negative sequence current using the least square admittance, voltage unbalance and inherent asymmetry compensation.

The second compensation technique was performed using the negative sequence impedance of the healthy induction motor under test. The negative sequence impedances were employed to calculate the negative sequence current under voltage unbalances using the negative sequence voltage. The calculated negative sequence current was then applied to extract the shorted turn faults using the phasors. The calculated negative sequence currents due to the shorted turn faults are given in Figure 6.3. It should be noted that the negative sequence impedances in this technique are assumed unaffected by the motor loading or by the shorted turn faults. The look up table was also employed to obtain the negative sequence currents that are due to the inherent asymmetries in the motor under test.

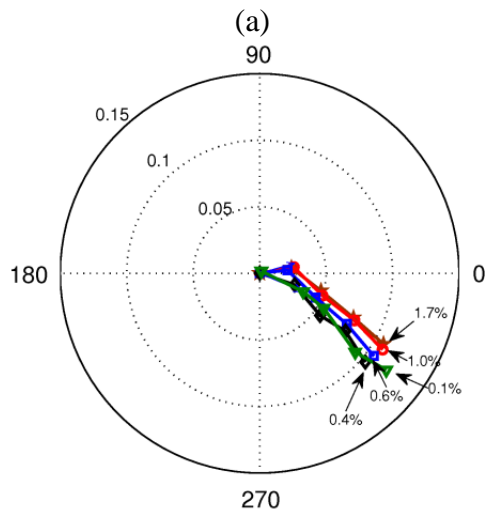
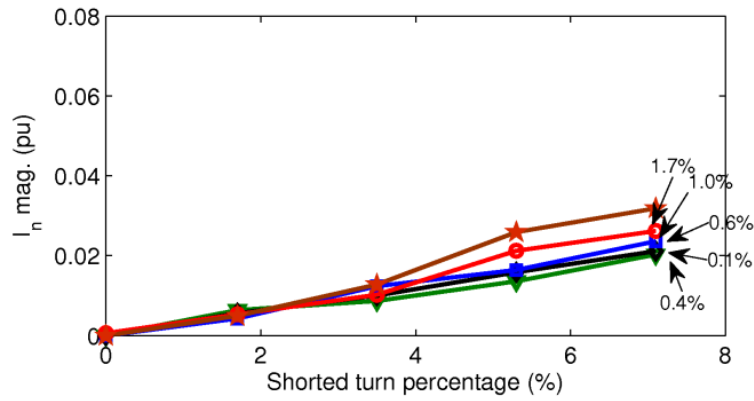


Figure 6.3 Shorted turn negative sequence currents after voltage unbalance compensation based on negative sequence impedance, showing (a) magnitude, (b) phasor trajectory.

As shown in the figure, the negative sequence currents increase with the level of shorted turn faults. The shorted turn negative sequences after compensation produce a small variation in the magnitude of negative sequence currents, which appear to be better than the previous compensation technique. However, the negative sequence currents vary significantly creating a significant standard deviation of the mean values at above 4% shorted turn faults. This large deviation may be caused by nonuniformity of the negative sequence impedances which (as given in Chapter 5) are affected by the shorted turn faults as well as the load variations. In addition, the phasor trajectory diagram representation of the negative sequence current which has not been discussed in literature, shows curved plot lines at small percentage of the shorted turn faults. These curved lines indicate that the inherent asymmetry may not be implemented precisely. In other words, the inherent asymmetry, which is gained

from look up table, are not extracted at zero value of negative sequence voltage as demonstrated in Section 5.4.2.

The next compensation technique was carried out based on semi empirical formula. In this approach, the induction motor was characterized under load variations, followed by voltage unbalance. This technique advances the previous techniques while analytical approaches to understand the shorted turn faults are still considered. Note that two empirical formulas were introduced as given previously in Equation 2.25 and 2.26 for voltage unbalance and load effect characterizations. Similar to the previous test, load and voltage unbalance characteristics were carried out using the identical data points. The inherent asymmetry and the voltage unbalance characterizations were performed first followed by the load characterization. The voltage unbalance and the inherent asymmetry characterizations employed negative sequence reactances to determine the negative sequence currents. Furthermore, the load characterization used real and imaginary positive sequence current components to obtain the constants of the empirical equations. Several constants have been obtained from the characterization equations given below.

$$I_n^v = V_n^v \sin \theta_n \left(-1.3759 + 0.0006V_n + -1.4246 \sin 2\phi_n + 0.051 \cos 2\phi_n + 0.0158I_{px} + -0.2322I_{py}^2 \right) \quad (6.3)$$

$$I_{mnlv} = 1.0937 + -0.6057I_{px} + 0.0825I_{px}^2 + -0.0486I_{py} + 0.0101I_{py}^2 \quad (6.4)$$

$$I_n^{sf} = I_n - I_n^v - I_{mnlv} \quad (6.5)$$

where

I_{mnlv} is negative sequence magnitude after motor loading correction,

V_{px} , V_{py} are real and imaginary value of positive sequence voltage,

I_{px} , I_{py} are real and imaginary value of positive sequence current, and ϕ_n (orientation

of unbalance voltage) = $\text{atan} \left(\frac{V_{nx}}{V_{ny}} \right)$.

Unlike the previous compensation techniques, this technique shows only the magnitude of the shorted turn fault and is given in Figure 6.4.

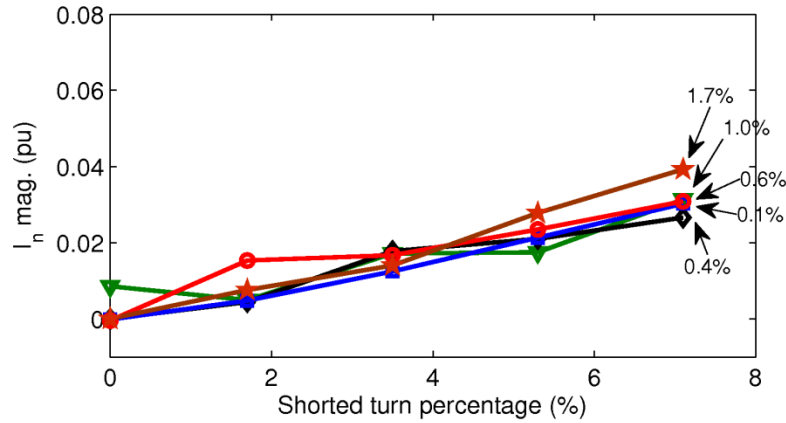


Figure 6.4 Shorted turn negative sequence current after the voltage unbalance and the load compensation based on the empirical formulas.

The negative sequence current similar to the impedance compensation technique (given in Figure 6.3) also shows an increasing magnitude with the severity of shorted turn faults. Hence, this technique may be more suitable for the real implementation compare with the previous techniques. This technique does not also require a large database to analyze the measured negative sequence voltage and current for inherent asymmetry and load compensations. However, compare with the previous negative sequence impedance compensation technique, this technique does not show a better magnitude uniformity along the shorted turn percentage. The deviation of magnitude may be caused by lack of reference points required for accurate least square estimations. In addition, it was found that the phasor can not be implemented easily although the phase angle information is useful to classify the real causes of the negative sequence current.

As shown, three compensation techniques demonstrated here have some limitations. The previous test results have shown that negative sequence current compensation techniques are necessary to obtain accurate values of the negative sequence currents. Hence, to overcome these limitations and to increase accuracy a novel technique will be discussed in the next section.

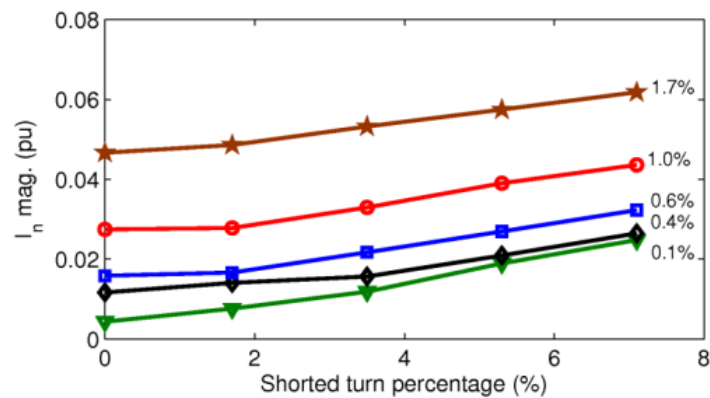
6.3 The New Compensation Methods for Negative Sequence Current Estimation

A detailed step by step explanation of the novel negative sequence compensation method that is based on the phasor extractions will be given in this

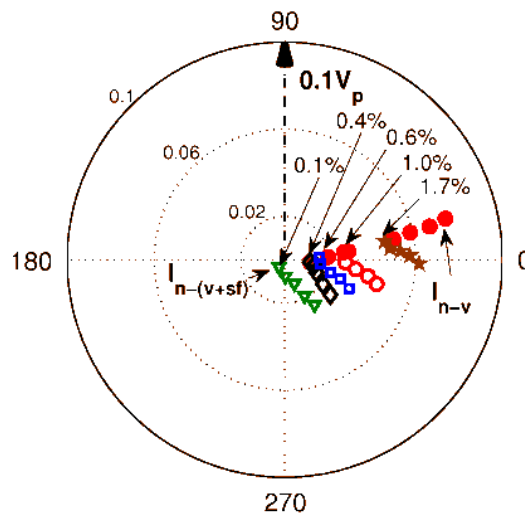
section. Two different cases will be investigated: the compensation of voltage unbalance and inherent asymmetry under shorted turn faults, and the compensation of voltage unbalance and inherent asymmetry with motor loading variation under shorted turn faults.

6.3.1 Compensation of Voltage Unbalance and Inherent Asymmetry

The previous test data without motor loading (Figure 6.1) is used in this study. The implemented techniques are divided into three steps. The first step shows the measured negative sequence currents using calibrated sensors, which is given in Figure 6.5.



(a)



(b)

Figure 6.5 The measured negative sequence currents under voltage unbalance variations showing (a) the magnitude and (b) the phasor plot.

The measured negative sequence shows that both the voltage imbalance and the shorted turn faults affect the negative sequence current (see Figure 6.5 (a)). Under

near zero supply voltage unbalance (0.1%), the negative sequence current is roughly proportional to the number of shorted turns. For example, under 7%, a shorted turn fault produces a small amount of negative sequence current 0.02 pu. However, a healthy motor (zero shorted turns), a 1% of supply voltage unbalance can produce a comparable magnitude of negative sequence current, which shows the necessity of the supply voltage unbalance compensation. The phasor plot in Figure 6.5 (b) shows that the phase angle of the negative sequence current component due to the supply voltage unbalance (about $+15^\circ$) was substantially different than under the shorted turn fault (about -45°). These phase angles are heavily dependent on the supply voltage phasors and the faulty phase.

In the test results shown, for all levels of the voltage unbalance, the negative sequence current magnitude increases with fault severity. This result however is dependent on the phasor summation of the negative sequence current component due to the fault and due to the supply voltage unbalance. Depending on the relative phase angle of these two current components, for a given value of voltage unbalance, a shorted turn fault may also have little effect on the magnitude of the total negative sequence current or, in fact, may cause it to decrease. Thus, the compensation must be based on a phasor calculation rather than the magnitudes only.

Figure 6.6 shows the test results after the compensation of the negative sequence supply voltage using the calibration curve given earlier in Figure 5.14. The sensitivity of the negative sequence current to the supply voltage unbalance is largely eliminated allowing the influence of the shorted turn fault to be more evident. In the phasor plot, the close correlation between the results under 0.1% and 1.7% VUF is shown.

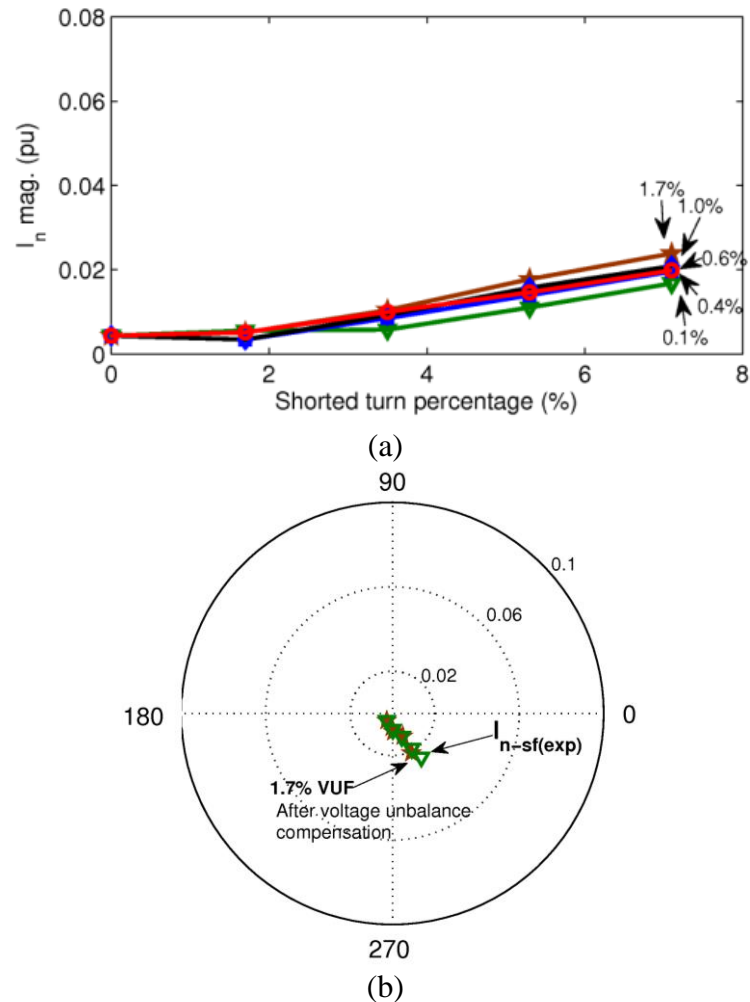


Figure 6.6 The negative sequence current after voltage unbalance elimination: (a) the magnitude and (b) phasor diagram.

The presence of inherent asymmetry means that the negative sequence current is non-zero in a healthy machine. This makes it difficult to distinguish small shorted turn faults of less than 2% for this machine. Therefore, the inherent asymmetry elimination is applied.

The final figure given in Figure 6.7 shows compensation results for both the voltage unbalance and the inherent asymmetry. Note that the compensation method reduces the negative sequence current to near zero for healthy machines allowing even small level of faults (larger than 1% shorted turns) to be distinguished. It also produces a nearly ideal linear relationship between the fault severity and the negative sequence current, and further reduces the sensitivity to the supply voltage unbalance. The phasor plot shows the result for the healthy motor now lies at the origin. Figure 6.7 also shows that the negative sequence compensation can be very practical to eliminate the disturbances. Under no load condition, the calculation shows clear and

good results. However, it is important to consider the load levels which will be presented in the following section.

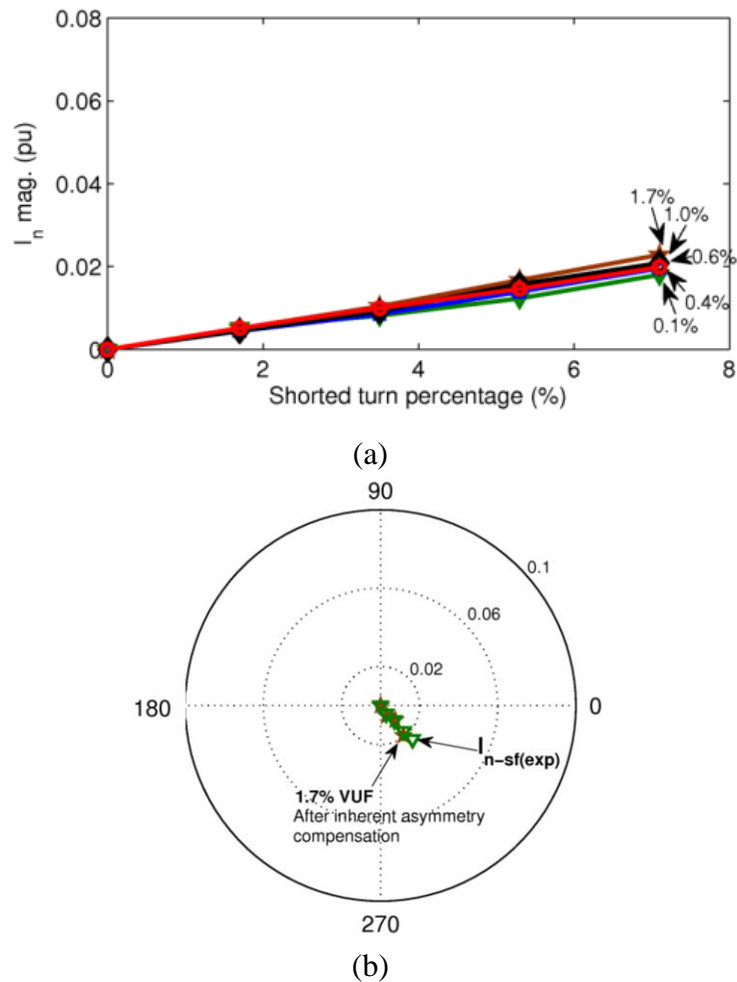


Figure 6.7 The negative sequence after inherent asymmetry elimination showing (a) the magnitude and (b) the phasor diagram.

6.3.2 Compensation of Voltage Unbalance and Inherent Asymmetry under Different Motor Loading

The combination of shorted turn fault, inherent asymmetry, voltage unbalance and load variations are investigated. As mentioned previously, the voltage unbalance was introduced using external resistors. The motor loading were increased in seven steps, and a percentage of sorted turn fault is applied in each step. The measured negative sequence currents are given in Figures 6.8 - 6.10.

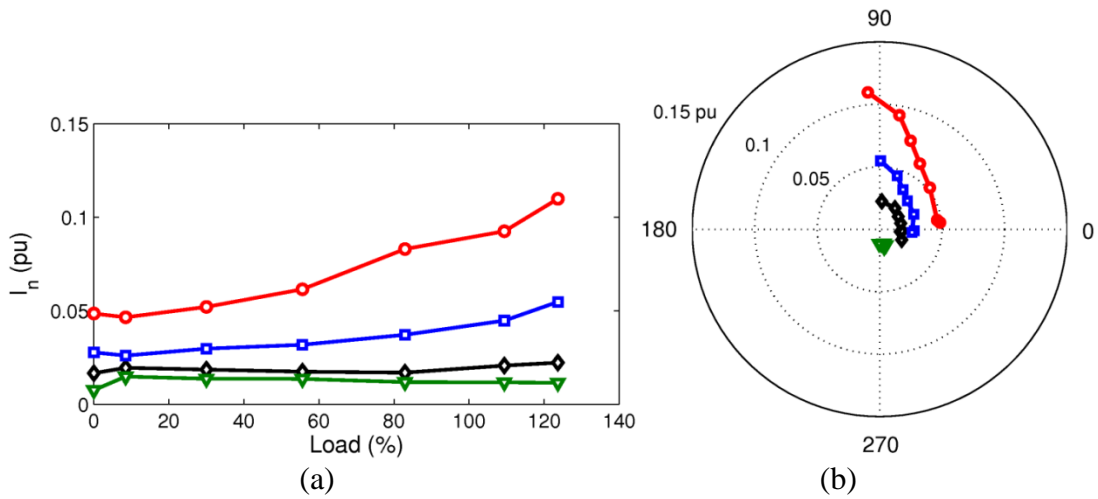


Figure 6.8 The negative sequence current of 1.7% shorted turn faults under load variation and voltage unbalance employing external resistors, $r_{ext}=0\Omega$ (triangle), $r_{ext}=1\Omega$ (diamond), $r_{ext}=2\Omega$ (square), $r_{ext}=4\Omega$ (circle), showing (a) the magnitude and (b) the phasor trajectory.

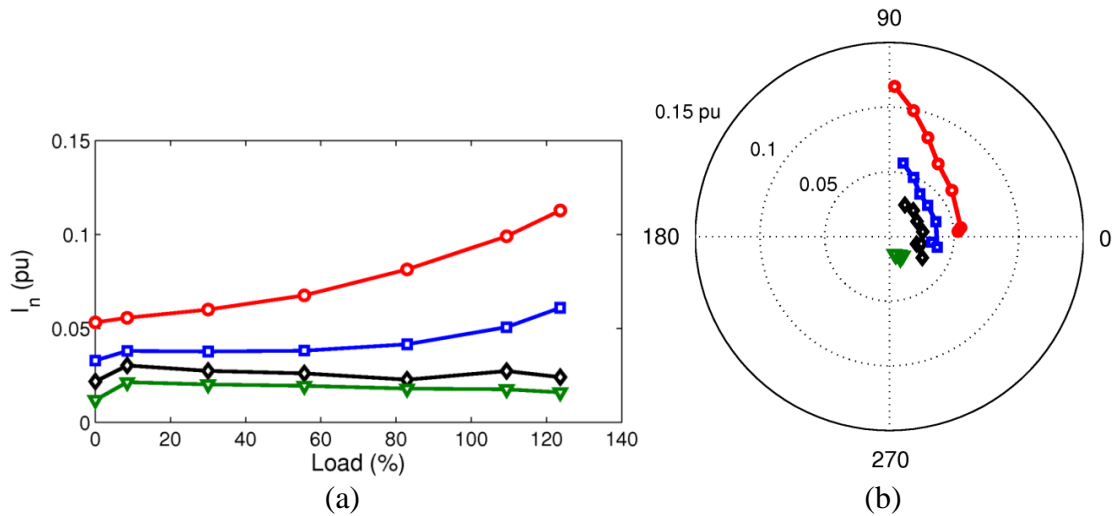


Figure 6.9 The negative sequence current of 3.5% shorted turn faults under load variation and voltage unbalance employing external resistors, $r_{ext}=0\Omega$ (triangle), $r_{ext}=1\Omega$ (diamond), $r_{ext}=2\Omega$ (square), $r_{ext}=4\Omega$ (circle), showing (a) the magnitude and (b) the phasor trajectory.

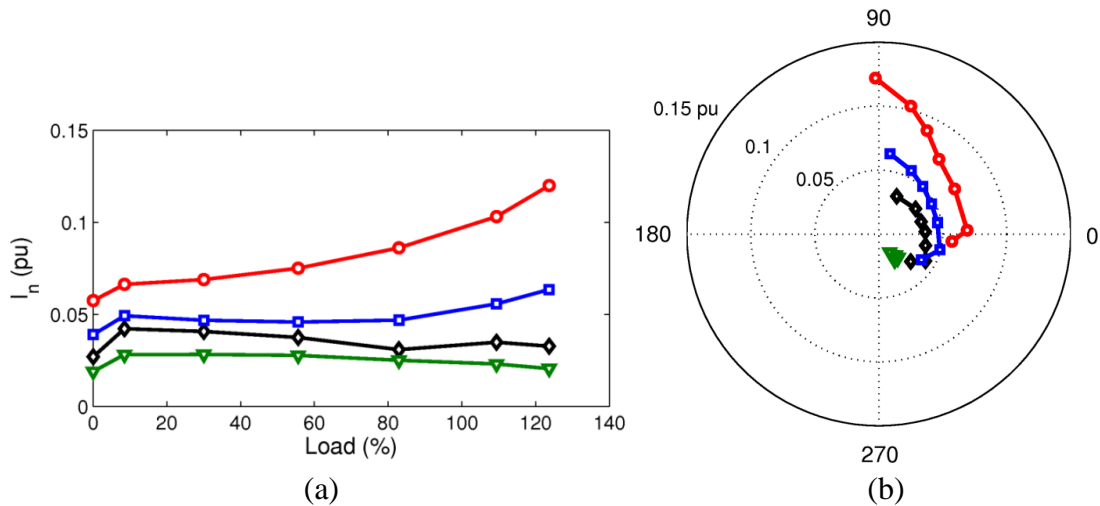


Figure 6.10 The negative sequence current of 5.3% shorted turn faults under load variation and voltage unbalance employing external resistors, $r_{ext}=0\Omega$ (triangle), $r_{ext}=1\Omega$ (diamond), $r_{ext}=2\Omega$ (square), $r_{ext}=4\Omega$ (circle), showing (a) the magnitude and (b) the phasor trajectory.

The above figures summarize the test results of the negative sequence current under various levels of the shorted turn faults: 1.7%, 3.5% and 5.3% and under varying motor loads (from no load up to 123% load) and the voltage unbalance variations using external resistors (1 Ω , 2 Ω and 4 Ω) in one phase. As it can be seen in the figure, the negative sequence currents increase proportionally with the number of shorted turn as well as the level of voltage unbalances. The percentage of loading also affects the measured negative sequences specifically under higher value of the voltage unbalances. In addition, it can be observed that at 2 Ω and 4 Ω external resistor values, the magnitude of negative sequences increase with the loading. In these external resistance values, the voltage unbalance factor varies from 0.81% to 1.65% respectively, as the motor loading changes from 0% to above the rated load of 123,7%. However under no or small value of external resistor (1 Ω), the magnitude of negative sequence slightly decreases with the motor loading. The rotor type and the level of eccentricity may contribute to this decrease under loading condition as described in Section 5.4.3.

The effects of loading and the voltage unbalance are also confirmed in the trajectory figure of the negative sequences in phasor domain. The phasor angles of the measured negative sequence (similar to the result given in Figure 5.19, from 317 $^{\circ}$ to 95 $^{\circ}$) are mostly affected by the voltage unbalance under the load variations. In addition, the increase in the voltage unbalance (using 0 Ω to 4 Ω external resistor in one phase) also shift the angle of negative sequence under light loads (from 317 $^{\circ}$ to

348⁰). These phasor angles show that when shorted turn, voltage unbalance and motor load are considered simultaneously, the identifications of the true negative sequence due to the shorted turn fault only can be very difficult to determine.

As illustrated in Figures 6.8, 6.9 and 6.10, the magnitudes of negative sequence currents due to the shorted turn fault also looks very difficult to visually identify due to the influence of the voltage unbalance magnitude under load variations. Under the rated motor load and under 1.7%, 3.5% and 5.3% of shorted turn faults using the 1 Ω external resistor, the per unit values of negative sequence currents are 0.021 pu, 0.027 pu and 0.035 pu respectively. Under similar fault levels but at 2 Ω external resistor, the negative sequence current magnitudes are 0.045 pu, 0.051 pu, and 0.056 pu under the rated motor load. Similarly, the external resistance of 4 Ω gives 0.093 pu, 0.099 pu and 0.105 pu negative sequence currents. In other words, under the same value of external resistance operation and at the rated load, the differences between the magnitudes of the measured negative sequence current due to the shorted turn faults can be very small hence difficult to determine the number of shorted turn faults.

To understand the effect of the shorted turn faults clearly, the measured negative sequence current has to be eliminated from other effects, especially the effects of the voltage unbalance under varying load. The previous phasor extraction method can also be applied here, as shown in Figure 6.11, 6.12 and 6.13 under the operation condition describe above.

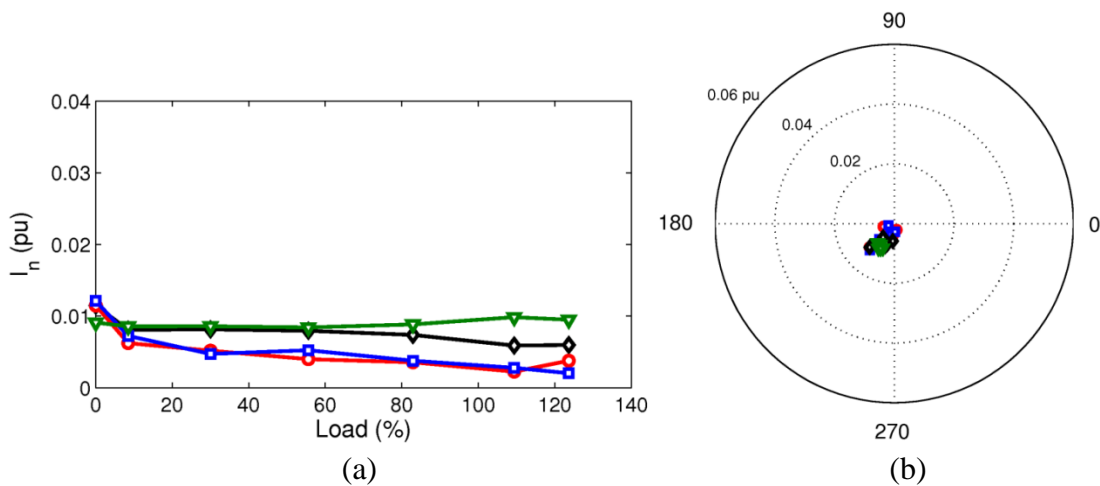


Figure 6.11 The negative sequence current under 1.7% shorted turn faults after the elimination of the load-voltage unbalance using $r_{ext}=0\Omega$ (triangle), $r_{ext}=1\Omega$ (diamond), $r_{ext}=2\Omega$ (square), $r_{ext}=4\Omega$ (circle), showing (a) the magnitude and (b) phasor trajectory.

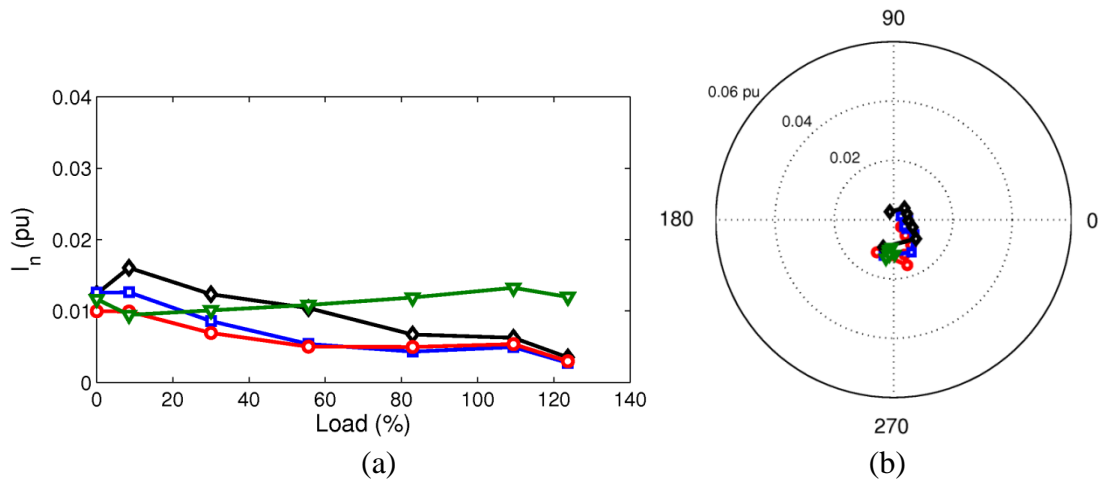


Figure 6.12 The negative sequence current under 3.5% shorted turn faults after the elimination of the load-voltage unbalance using $r_{ext}=0\Omega$ (triangle), $r_{ext}=1\Omega$ (diamond), $r_{ext}=2\Omega$ (square), $r_{ext}=4\Omega$ (circle), showing (a) the magnitude and (b) phasor trajectory.

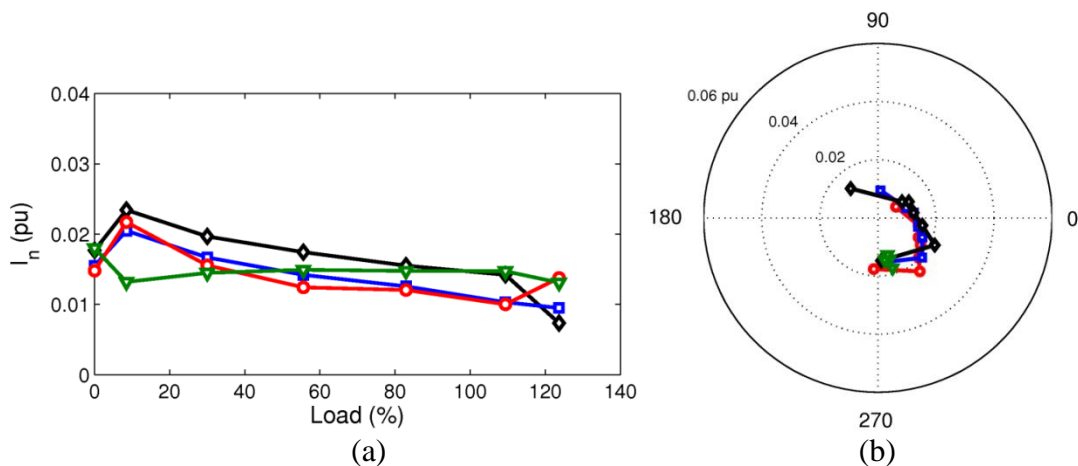


Figure 6.13 The negative sequence current under 5.3% shorted turn faults after the elimination of the load-voltage unbalance using $r_{ext}=0\Omega$ (triangle), $r_{ext}=1\Omega$ (diamond), $r_{ext}=2\Omega$ (square), $r_{ext}=4\Omega$ (circle), showing (a) the magnitude and (b) phasor trajectory.

The voltage unbalance as a function of the motor loading was discussed in Section 5.4.3. These results have shown that the measured negative sequence currents are reduced after the eliminations of the other effects, both in the magnitude and the phasor calculations. The magnitudes of negative sequence currents are reduced for about 50% to 80% while operating under small voltage unbalance (less than 0.7% VUF) at the rated load. Under higher voltage unbalances (from 0.81% to 3.6% VUF using 2 Ω and 4 Ω external resistors), about 88% up to 94% of the measured negative sequence currents due to the voltage unbalance were eliminated. After the eliminations, the remaining magnitudes of the negative sequence current can be

assumed as the shorted turn components. Note that the negative sequence magnitude decreases as the load increasing, which is similar to the results given in Figure 5.20.

Although, these elimination results show a degree of magnitude reduction, the plot of phasors appear to carry the effect of voltage unbalance under motor loading. Ideally, after the elimination, the angles of negative sequence current due to the shorted turn faults should not show any large variations at the same fault level. Hence, it can be concluded that the negative sequence currents are free from other unwanted effects. However, the phasor trajectories in Figures 6.11, 6.12 and 6.13 appear to be similar to the original data before the eliminations. For example, as in the previous results, the phasor angles in Figure 6.13 vary from about 270° (at light load) to about 90° (at full load).

The phasor trajectory analysis also shows that the negative sequence currents do not start from the origin, which indicates that inherent asymmetry exist. This inherent asymmetry also explains the difference between the values of negative sequence current after the elimination technique is applied. Figures 6.14, 6.15 and 6.16 show the test results after the inherent asymmetry eliminations are applied.

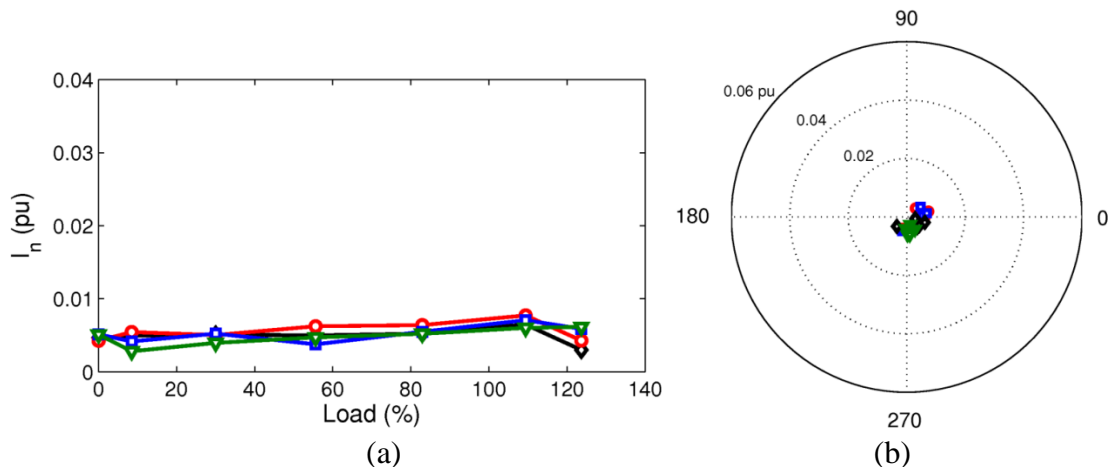


Figure 6.14 The negative sequence current of 1.7% shorted turn fault after the voltage unbalance and the inherent asymmetry elimination, using $rext=0\Omega$ (triangle), $rext=1\Omega$ (diamond), $rext=2\Omega$ (square), $rext=4\Omega$ (circle), showing (a) the magnitude and (b) the phasor trajectory

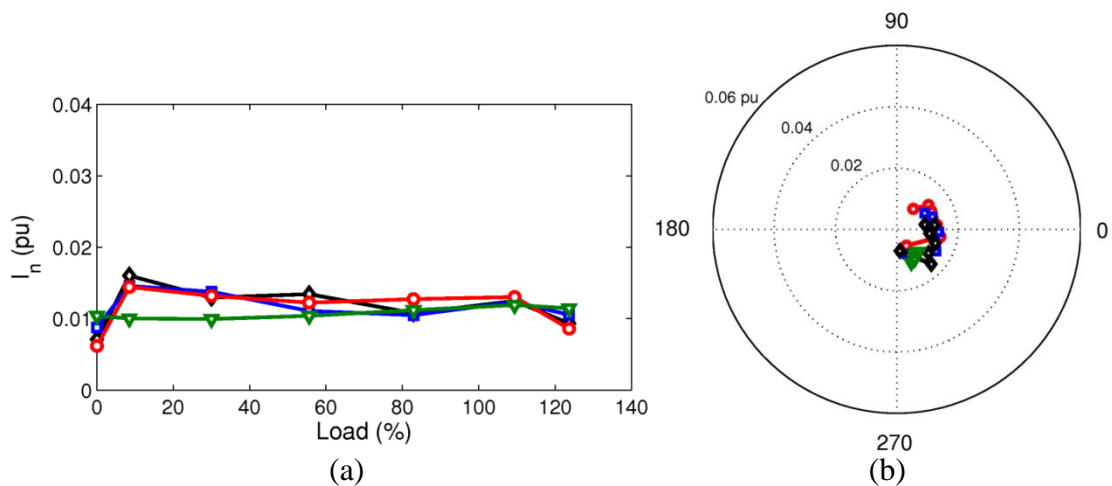


Figure 6.15 The negative sequence current of 3.5% shorted turn faults after the voltage unbalance elimination using $r_{ext}=0\Omega$ (triangle), $r_{ext}=1\Omega$ (diamond), $r_{ext}=2\Omega$ (square), $r_{ext}=4\Omega$ (circle), showing (a) the magnitude and (b) the phasor trajectory

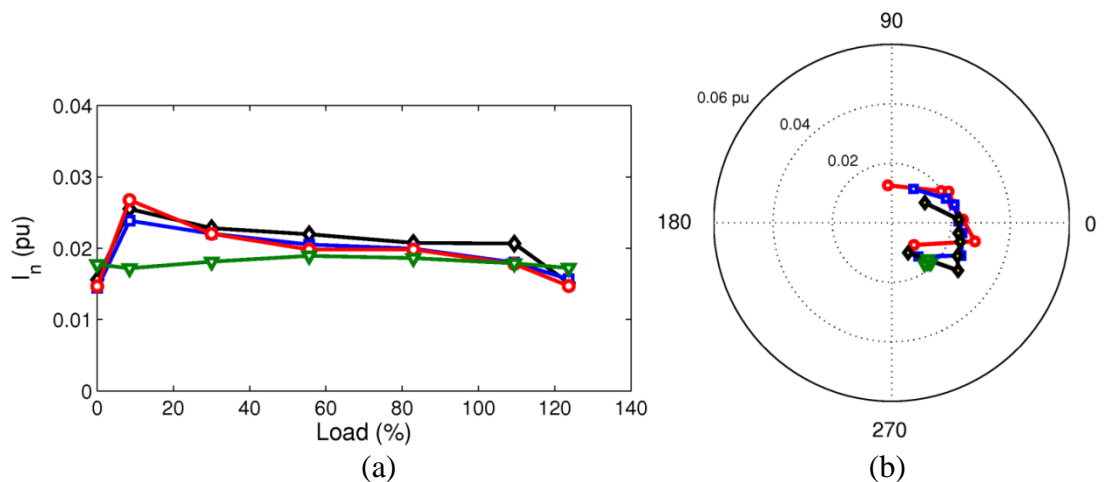


Figure 6.16 The negative sequence current of 5.3% shorted turn fault after voltage unbalance eliminations using $r_{ext}=0\Omega$ (triangle), $r_{ext}=1\Omega$ (diamond), $r_{ext}=2\Omega$ (square), $r_{ext}=4\Omega$ (circle), showing (a) the magnitude and (b) the phasor trajectories

Note that the inherent asymmetry eliminations produce more accurate results that are indicated by the small variation of the negative sequence currents at the rated load. For a comparison, the differences between the maximum and the minimum negative sequence current at the rated load using 4Ω external resistor, before and after the eliminations of inherent asymmetry shown in Figures 6.13 (a) and 6.16 (a) are 0.0047 pu and 0.0028 pu respectively. The comparison of the negative sequence currents before and after the inherent asymmetry elimination technique is given in Fig. 6.11 (a) and 6.14 (a), indicating about 0.0076 pu and 0.0017 pu variations.

Furthermore, the results of the negative sequence magnitude in Figure 6.14 (a) and 6.15 (a) shows significant differences at light loads between the result under the voltage unbalance (using 1 Ω , 2 Ω and 4 Ω external resistances) and without it (0 Ω resistance). It can be observed that the differences are much visible at the high number of shorted turn percentage (3.5% and 5.3%). The magnitude difference reaches a peak at 8.5% motor loading before decreasing, until 55% motor loading. This increase can be caused by the effect of voltage unbalances or the eccentricity fault under this loading range; which cannot be compensated completely. Furthermore, the magnitude difference might also be caused by non-linear effect of the load variation under the shorted turn faults which also can not be eliminated completely. As shown previously in Figure 5.20, the shorted turn faults themselves are a function of load due to the closed slot rotor type of the motor under test. This indicates that a precise and accurate phasors of the voltage unbalance and the eccentricity under various loads are required for the compensators.

The phasor trajectories also show that the true negative sequence currents due to the shorted turn faults are obtained as the phasors of the negative sequence currents start at the origin. At light loads, the phasors are around 315^0 , which is similar to the angle of the negative sequence current after the no load voltage unbalance compensation in Figure 6.7. This indicates that the phasor compensation is applicable to both with and without motor loading. The effect of motor loading also rotates the angle of the negative sequence current clockwise counter about 180^0 as a function of the motor loading. It should be noted here that the rated motor loading phasors should have ideally similar angle as in the light loads since the effect of voltage unbalance under load variation and the inherent asymmetry were eliminated. However, the phasor results under heavy loads show similar trajectory as in the plot of the voltage unbalance under load variation.

6.4 Conclusion

This chapter provided the detailed investigation of the negative sequence current compensation to obtain the true value of the negative sequence current that is just due to shorted turn faults. Several compensation techniques based on the analytical calculation of negative sequence currents were investigated using similar stator current data to compare the compensation technique. The experimental results

indicate that negative sequence current compensation technique can eliminate the unwanted negative sequence currents such as the voltage unbalance and the inherent asymmetry in the machine under test. However, the compensated test results demonstrate a low accuracy as indicated by the large differences of negative sequence currents under the rated load.

The chapter also provided a detailed step by step negative sequence current compensation technique based on phasor extraction. In this technique, true negative sequence current due to the shorted turn fault is extracted from the measured negative sequence current. In the first step, the negative sequence current due to the voltage unbalance is eliminated, followed by the elimination method that is due to the inherent asymmetry in the machine. An accurate plot of negative sequence current, which is capable to predict a small number of shorted turn faults (down to a single shorted turn), was given. Furthermore, the compensation method was investigated under various motor loads using similar compensation steps. The compensation of the voltage unbalance was also conducted under various motor loads. It was shown that the compensation technique can successfully eliminate the voltage unbalance under load variations and the inherent asymmetry to obtain the true negative sequence current that is due to the shorted turn faults only. However, motor loading is found to have some small influence on the final results of the compensated negative sequence currents.

Chapter 7

General Conclusions and Recommendations

7.1 Conclusions

Negative sequence current monitoring is an effective online method that is sensitive to detect stator shorted turns faults in induction machines. The method can be considered an alternative to signature analysis technique such as stator current, vibration and flux leakage monitoring. As it was preferred in a number of studies, the negative sequence current monitoring offers a reliable and fast processing (due to low computational requirements) compare to other technique which is also non-invasive. However, the negative sequence current monitoring is sensitive to even small asymmetries in the machine that may be due to small unbalanced current in the three-phases of the induction motor. Note that the current asymmetries in the machine are not only caused by the stator shorted turn faults, but are also affected by the unwanted disturbances such as the supply voltage unbalances, the measurement errors and the inherent asymmetries in the machine due to saturation, winding asymmetries and rotor eccentricity. Hence, this thesis aims to address these limitations of the negative sequence current detection and offer a practical means to be used in real fault detection system.

The literature review section of the thesis shows that previous studies only focus on the negative sequence current compensation technique. Hence, various compensation methods of the disturbances have been investigated ranging from simple look-up tables to using Neural Networks. The following compensation models have been investigated in the previous studies: negative sequence currents, negative sequence impedance, and a matrix of impedances that models the cross-coupling between the positive and negative sequence components. The previous studies however did not study the interaction between the shorted turn faults and the practical disturbances that are present in real machines, such as voltage unbalances and inherent machine asymmetries. In other words, the previous studies addressed some of the

limitations of the negative sequence techniques, but not studied the fault detection detailed under various non-idealities, non-linearities and in motor loading conditions.

Therefore, this thesis aims to address these limitations and offer solutions. To achieve the final goal, the thesis extensively utilizes accurate experimental data as well as the motor model that is developed to investigate the negative sequence currents under any motor loading conditions. The detailed investigation in this research covers all negative sequence contributors such as the motor faults (shorted turn faults, static eccentricity and broken rotor bars) and all potential disturbances (measurement asymmetry, temperature measurement, inherent asymmetry, and voltage unbalance) under a wide range of loads. In addition, unlike the previous studies, the thesis provides a step by step explanation of the negative sequence disturbance elimination method. A new detailed step by step compensation technique is also presented to eliminate inherent asymmetry in the machine as well as to eliminate the voltage unbalance under varying motor loads to obtain the true value of the negative sequence current which utilized phasor calculation. It was demonstrated that this technique allows even a single stator shorted turn faults to be detected.

In summary, in Chapter 2, a comprehensive literature review was given in order to provide an overview and to understand the of current status of the research on the negative sequence current monitoring for fault detection in induction machines. It can be summarized that the previous works can be classified under two groups:

1. theory of negative sequence involving basic phasor theory, negative sequence calculation, and negative sequence power decomposition based calculations.
2. negative sequence monitoring and compensation techniques to eliminate the non-linearity and non-ideality from the measured negative sequence current or negative sequence impedance.

It is concluded in the Chapter 2 that there is a need to understand the source of negative sequence current comprehensively. Hence, it was identified that the previous negative sequence current monitoring techniques need to be compared to understand the performance and limitations of each technique. There was also a lack of explanations in the literature about the compensation techniques that can lead to a better understanding of the monitoring techniques.

In Chapter 3, the induction motor models and machine parameters were discussed. Asymmetrical dynamic MCC induction motor model was developed which involved the review of various previous models to determine an appropriate motor model for condition monitoring. It can be concluded that the dynamic MCC model has low computational complexity that can allow simple expansion to include various electrical-related motor faults. In addition, the MCC model can provide appropriate simulation results that can be applicable to the online condition monitoring. To include in the simulation tool developed, the machine parameters of the induction motor under test were determined to include the effect of the closed slot rotor type to ensure more accurate simulation results. In this chapter, the dynamic motor model validation using experimental results as well as a steady state T-model has shown that the performance of motor model developed is very close to the real motor operation. The steady state and dynamic behavior of the negative sequence current is also studied in the chapter.

In chapter 4, one of the most critical issues, the accuracy of measurement is studied. It was demonstrated that the negative sequence current monitoring technique requires an accurate calibration of the measurement channels. The investigations revealed that the negative sequence current due to the measurement errors can be avoided if the asymmetrical gain and angle between three or two measurement channels can be minimized. This means that the differential gain calibration in sensors plays an important role in this negative sequence current measurement. The effects of the temperature were also shown under two extreme cases: hot and cold measurements. It was concluded that the effect of temperature may slightly lower the accuracy of the negative sequence current monitoring especially when the temperature cannot be kept constant during the measurement. The chapter also provides an online calibration technique to overcome any measurement asymmetry system during online operation. Two calibration techniques have been discussed in the chapter including: calibration using baseline information and calibration using differential gain correction.

Chapter 5 provides a comprehensive approach to understand negative sequence current condition monitoring in induction motors. In this chapter, the investigation was not only focused on motor faults, but also on the disturbances. The shorted turn model of the motor under test based on the asymmetrical MCC and the shorted turn test set up was presented and explained. The disturbances in the negative

sequence current condition monitoring, such as inherent asymmetry and voltage unbalance, were also explained in detail. It was demonstrated in this chapter that the negative sequence currents increase with the level shorted turn faults. It was concluded that the inherent asymmetry needs to be determined to improve the accuracy of condition monitoring and to identify the base line value of the negative sequence current. In addition, it was shown that the negative voltage unbalances that commonly exist in the voltage supply may give false alarms. The acceptable value of the voltage unbalance in ac supply can produce much higher negative sequence magnitude than the shorted turn fault. Furthermore, it is shown that the motor loading affects the negative sequence current under both in the case of faults and due to the disturbances. The voltage unbalance has found to have a greater effect on the negative sequence current with increase in the magnitude of negative sequence current as well as the shift in the phasor trajectory angle. Due to the effect of closed slot rotor type, the increase in load decreases the magnitude of negative sequence current slightly under a larger shorted turn percentage. The chapter also examined the effect of other common machine faults such as the eccentricity and the broken rotor bar fault. It is shown that both of these faults increase the negative sequence current slightly but showing a much clear and unique phasor angle compare to the shorted turn fault and the other disturbances.

Chapter 6 investigated a new method for the compensation of the disturbances to obtain a true negative sequence current that is due to the real faults. The previous of negative sequence current compensation techniques were also compared in this chapter to obtain a better understanding of these techniques. The chapter demonstrated that further research is still required to understand the impact of each disturbance. The chapter provided step by step negative sequence current compensation technique using phasor elimination method. The phasor compensation technique has shown that the voltage unbalance can be eliminated from the measured negative sequence. In addition, it is shown that the inherent asymmetry elimination increases the measurement accuracy allowing even a very small percentage of the induction motor faults (1 shorted turn) to be identified. The effect of the motor loading was also investigated under the combination of shorted turn faults, inherent asymmetry and supply voltage unbalances which are usually present simultaneously in a real machine. The voltage unbalances under various motor loading were eliminated followed by the

inherent asymmetry corrections. The results have shown that the magnitude on the negative sequence current due to the shorted turn faults can be obtained accurately. However, the compensation results of phasor angle seem to be affected by the motor loading especially at high percentage of the shorted turn faults.

7.2 Recommendations

Although, this thesis demonstrates a comprehensive investigation of the negative sequence current for condition monitoring at the induction motor that has shorted turn fault only, further comprehensive research is required to investigate other potential single and combination faults. In addition, further work is needed to use the method proposed here in a real time online monitoring of machines. In such study, an online model can be developed to obtain a detailed negative sequence current reference under various practical voltage unbalance and motor loads. Such an online motor model reference can replace various compensation databases from the measured negative sequence current.

There is also need for further research improves the voltage unbalance compensation under motor loadings, which may include an additional angle shift in the phasor compensation stage during motor loading. This approach can also improve the accuracy to identify the causes of the negative sequence current. Finally, a programmable ideal three-phase power supply can be used to eliminate the non linier effect of the supply unbalance and harmonics on the compensation technique proposed.

References

- [1] G. K. Singh, and S. A. S. Al Kazzaz, "Induction machine drive condition monitoring and diagnostic research—a survey," *Electric Power Systems Research*, vol. 64, pp. 45-158, 2003.
- [2] B. Mirafzal, and N.A.O. Demerdash, "On innovative methods of induction motor interturn and broken-bar fault diagnostics," *IEEE Transactions on Industry Applications*, vol. 42, pp. 405-414, March/April 2006.
- [3] O. V. Thorsen, and M. Dalva, "Failure identification and analysis for high-voltage induction motors in the petrochemical industry," *IEEE Transactions on Industry Applications*, vol. 35, pp. 810 - 818, July/August 1999 1999.
- [4] R. Supangat, J. Grieger, N. Ertugrul, W. L. Soong, D. A. Gray, and C. Hansen, "Investigation of static eccentricity fault frequencies using multiple sensors in induction motors and effects of loading," in *IECON 2006 - 32nd Annual Conference on IEEE Industrial Electronics, November 6, 2006 - November 10, 2006*, Paris, France, 2006, pp. 958-963.
- [5] R. Supangat, N. Ertugrul, W. L. Soong, D. A. Gray, C. Hansen, and J. Grieger, "Broken rotor bar fault detection in induction motors using starting current analysis," in *2005 European Conference on Power Electronics and Applications, September 11, 2005 - September 14, 2005*, Dresden, Germany, 2005.
- [6] S. Grubic, J. M. Aller, B. Lu, and T. G. Habetler, "A survey on testing and monitoring methods for stator insulation systems of low-voltage induction machines focusing on turn insulation problems," *IEEE Transactions on Industrial Electronics*, vol. 55, pp. 4127-4136, 2008.
- [7] G. B. Kliman, W. J. Premerlani, R. A. Koegl, and D. Hoeweler, "A new approach to on-line turn fault detection in AC motors," in *Conference Record of the 1996 IEEE Industry Applications 31th IAS Annual Meeting. Part 1 (of 4), October 6, 1996 - October 10, 1996*, San Diego, CA, USA, 1996, pp. 687-693.
- [8] M. Arkan, D. K. Perovic, and P. Unsworth, "Online stator fault diagnosis in induction motors," *IEE Proceedings: Electric Power Applications*, vol. 148, pp. 537-547, 2001.
- [9] M. Arkan, D. Kostic-Perovic, and P. J. Unsworth, "Modelling and simulation of induction motors with inter-turn faults for diagnostics," *Electric Power Systems Research*, vol. 75, pp. 57-66, 2005.
- [10] A. H. Bonnett and C. Yung, "Increased efficiency versus increased reliability," *IEEE Industry Applications Magazine*, vol. 14, pp. 29-36, 2008.
- [11] J. Sottile, F. C. Trutt, and J. L. Kohler, "Condition monitoring of stator windings in induction motors: Part II - Experimental investigation of voltage mismatch detectors," *IEEE Transactions on Industry Applications*, vol. 38, pp. 1454-1459, 2002.
- [12] A. Bellini, F. Filippetti, C. Tassoni, and G.-A. Capolino, "Advances in diagnostic techniques for induction machines," *IEEE Transactions on Industrial Electronics*, vol. 55, pp. 4109-4126, 2008.
- [13] X. Luo, Y. Liao, H. A. Toliyat, A. El-Antably, and T. A. Lipo, "Multiple coupled circuit modeling of induction machines," *IEEE Transactions on Industry Applications*, vol. 31, pp. 311-317, 1995.

- [14] R. M. Tallam, T. G. Habetler, and R. G. Harley, "Self-commissioning training algorithms for neural networks with applications to electric machine fault diagnostics," *IEEE Transactions on Power Electronics*, vol. 17, pp. 1089-1095, 2002.
- [15] H. Razik, H. Henao, and R. Carlson, "An induction machine model including interbar currents for studying performances during transients and steady state," *Electric Power Systems Research*, vol. 79, pp. 181-189, 2009.
- [16] E. Sarani, K. Abbaszadeh, and M. Ardebili, "Modeling and simulation of turn-fault and unbalance magnetic pull in induction motor based on magnetic equivalent circuit method," Ningjing, China, 2005, pp. 52-56.
- [17] C. Rojas, M. G. Melero, M. F. Cabanas, J. M. Cano, G. A. Orcajo, and F. Pedrayes, "Finite element model for the study of inter-turn short circuits in induction motors," in *2007 IEEE International Symposium on Diagnostics for Electric Machines, Power Electronics and Drives, SDEMPED, September 6, 2007 - September 8, 2007*, Cracow, Poland, 2007, pp. 415-419.
- [18] P. T. Tavner, and J. Penman, *Condition monitoring of electrical machines*. Letchworth, England: Research Studies Press LTD, John Wiley and Sons Inc, 1987.
- [19] W. T. Thomson and M. Fenger, "Current signature analysis to detect induction motor faults," *IEEE Industry Applications Magazine*, vol. 7, pp. 26-34, 2001.
- [20] _____. (2009, 12 November). *The EASA Report: Typical Causes of Winding Failures in Three-Phase Stator Windings*. Available: <http://rescuemotors.com/motor%20windings.html>
- [21] C. L. Fortescue, "Method of symmetrical co-ordinates applied to the solution of polyphase networks," *American Institute of Electrical Engineers -- Proceedings*, p. 87, 1918.
- [22] S. Williamson and K. Mirzoian, "Analysis of Cage Induction Motors with Stator Winding Faults," *IEEE Transactions on Power Apparatus and Systems*, vol. PAS-104, pp. 1838-1842, 1985.
- [23] G. B. Kliman, W. J. Premerlani, R. A. Koegl, and D. Hoeweler, "Sensitive, on-line turn-to-turn fault detection in AC motors," *Electric Machines and Power Systems*, vol. 28, pp. 915-927, 2000.
- [24] R. M. Tallam, T. G. Habetler, and R. G. Harley, "Transient model for induction machines with stator winding turn faults," *IEEE Transactions on Industry Applications*, vol. 38, pp. 632-637, 2002.
- [25] M. Arkan and P. J. Unsworth, "Stator fault diagnosis in induction motors using power decomposition," in *Proceedings of the 1999 IEEE Industry Applications Conference - 34th IAS Annual Meeting, October 3, 1999 - October 7, 1999*, Phoenix, AZ, USA, 1999, pp. 1908-1912.
- [26] R. M. Tallam, T. G. Habetler, R. G. Harley, D. J. Gritter, and B. H. Burton, "Neural network based on-line stator winding turn fault detection for induction motors," in *35th IAS Annual Meeting and World Conference on Industrial Applications of Electrical Energy, October 8, 2000 - October 12, 2000*, Rome, Italy, 2000, pp. 375-380.
- [27] R. M. Tallam, T. G. Habetler, and R. G. Harley, "Continual on-line training of neural networks with applications to electric machine fault diagnostics," in *2001 IEEE 32nd Annual Power Electronics Specialists Conference, June 17, 2001 - June 21, 2001*, Vancouver, BC, Canada, 2001, pp. 2224-2228.
- [28] R. M. Tallam, T. G. Habetler, and R. G. Harley, "Experimental testing of a neural-network-based turn-fault detection scheme for induction machines under

- accelerated insulation failure conditions," in *Diagnostics for Electric Machines, Power Electronics and Drives, 2003. SDEMPED 2003. 4th IEEE International Symposium on*, 2003, pp. 58-62.
- [29] J. L. Kohler, J. Sottile, and F. C. Trutt, "Condition monitoring of stator windings in induction motors: Part I - Experimental investigation of the effective negative-sequence impedance detector," *IEEE Transactions on Industry Applications*, vol. 38, pp. 1447-1453, 2002.
- [30] J. L. Kohler, J. Sottile, and F. C. Trutt, "Alternatives for assessing the electrical integrity of induction motors," *IEEE Transactions on Industry Applications*, vol. 28, pp. 1109-1117, 1992.
- [31] S. B. Lee, R. M. Tallam, and T. G. Habetler, "A robust, on-line turn-fault detection technique for induction machines based on monitoring the sequence component impedance matrix," *IEEE Transactions on Power Electronics*, vol. 18, pp. 865-872, 2003.
- [32] F. C. Trutt, J. Sottile, and J. L. Kohler, "Detection of electrical winding deterioration in induction motors," *Electric Power Components and Systems*, vol. 29, pp. 1025-1033, 2001.
- [33] J. L. Kohler, J. Sottile, and F. C. Trutt, "Alternatives for assessing the electrical integrity of induction motors," *IEEE Trans. Energy Conv.*, vol. 28, pp. 1109-1117, 1992.
- [34] V. N. Ghate, S. V. Dudul, and G. M. Dhole, "Generalized model of three-phase induction motor for fault analysis," Novosibirsk, Russia, 2008, pp. 232-237.
- [35] C. Mishra, A. Routray, and S. Mukhopadhyay, "Experimental validation of coupled circuit model and simulation of eccentric squirrel cage induction motor," Mumbai, India, 2006, pp. 2348-2353.
- [36] A. F. Alshandoli, "Model-predicted induction motor behaviour under different operating conditions," Lahore, Pakistan, 2007.
- [37] B. Liang, B. S. Payne, A. D. Ball, and S. D. Iwnicki, "Simulation and fault detection of three-phase induction motors," *Mathematics and Computers in Simulation*, vol. 61, pp. 1-15, 2002.
- [38] M. Ojaghi and J. Faiz, "Extension to Multiple Coupled Circuit Modeling of Induction Machines to Include Variable Degrees of Saturation Effects," *IEEE Transactions on Magnetics*, vol. 44, pp. 4053-4056, 2008.
- [39] S. Nandi, "A detailed model of induction machines with saturation extendable for fault analysis," *IEEE Transactions on Industry Applications*, vol. 40, pp. 1302-1309, 2004.
- [40] S. Nandi, "An Extended Model of Induction Machines with Saturation Suitable for Fault Analysis," Salt Lake City, UT, United states, 2003, pp. 1861-1868.
- [41] S. Nandi, R. M. Bharadwaj, and H. A. Toliyat, "Mixed eccentricity in three phase induction machines: Analysis, simulation and experiments," Pittsburgh, PA, United states, 2002, pp. 1525-1532.
- [42] O. Jasim, C. Gerada, M. Sumner, and J. Arellano-Padilla, "A simplified model for induction machines with faults to aid the development of fault tolerant drives," Poznan, Poland, 2008, pp. 1173-1180.
- [43] O. Jasim, C. Gerada, M. Sumner, and J. Arellano-Padilla, "Investigation of induction machine phase open circuit faults using a simplified equivalent circuit model," Vilamoura, Algarve, Portugal, 2008.
- [44] S. D. Sudhoff, B. T. Kuhn, K. A. Corzine, and B. T. Branecky, "Magnetic equivalent circuit modeling of induction motors," *IEEE Transactions on Energy Conversion*, vol. 22, pp. 259-270, 2007.

- [45] V. Ostovic, "Simplified approach to Magnetic Equivalent-Circuit Modelling of Induction Machines," *IEEE Transactions on Industry Applications*, vol. 24, pp. 308-316, 1988.
- [46] H. Henao, C. Martis, and G.-A. Capolino, "An equivalent internal circuit of the induction machine for advanced spectral analysis," *IEEE Transactions on Industry Applications*, vol. 40, pp. 726-734, 2004.
- [47] C. Gerada, K. J. Bradley, M. Sumner, and P. Sewell, "Evaluation of a Vector Controlled Induction Motor Drive using the Dynamic Magnetic Circuit Model," Salt Lake City, UT, United states, 2003, pp. 862-869.
- [48] C. Gerada, K. J. Bradley, M. Sumner, and P. Wheeler, "Operating induction motor drives with turn-to-turn faults," San Antonio, TX, United states, 2005, pp. 770-776.
- [49] K. Komeza and M. Dems, "Finite-Element and Analytical Calculations of No-Load Core Losses in Energy-Saving Induction Motors," *IEEE Transactions on Industrial Electronics*, vol. 59, pp. 2934-2946, 2012.
- [50] J. Faiz, B. M. Ebrahimi, B. Akin, and H. A. Toliyat, "Finite-Element Transient Analysis of Induction Motors Under Mixed Eccentricity Fault," *IEEE Transactions on Magnetics*, vol. 44, pp. 66-74, 2008.
- [51] E. Dlala and A. Arkkio, "A General Model for Investigating the Effects of the Frequency Converter on the Magnetic Iron Losses of a Squirrel-Cage Induction Motor," *IEEE Transactions on Magnetics*, vol. 45, pp. 3303-3315, 2009.
- [52] L. Aarniovuori, L. Laurila, M. Niemela, and J. Pyrhonen, "Comparison of the induction motor simulation models: analytical and FEM in drive system controlled with direct torque control," in *International Symposium on Power Electronics, Electrical Drives, Automation and Motion, 2008. SPEEDAM 2008*, 2008, pp. 1282-1285.
- [53] J. Faiz, B. M. Ebrahimi, and M. B. B. Sharifian, "Different faults and their diagnosis techniques in three-phase squirrel-cage induction motors-a review," *Electromagnetics*, vol. 26, pp. 543-569, 2006.
- [54] C. Delmotte-Delforge, H. Henao, G. Ekwe, P. Brochet, and G. A. Capolino, "Comparison of two modeling methods for induction machine study: Application to diagnosis," *COMPEL - The International Journal for Computation and Mathematics in Electrical and Electronic Engineering*, vol. 22, pp. 891-908, 2003.
- [55] S. Nandi, "Modeling of induction machines including stator and rotor slot effects," *IEEE Transactions on Industry Applications*, vol. 40, pp. 1058-1065, 2004.
- [56] P. M. Santos, M. B. R. Correa, C. B. Jacobina, E. R. C. Da Silva, A. M. N. Lima, G. Didiery, H. Raziky, and T. Lubiny, "A simplified induction machine model to study rotor broken bar effects and for detection," in *37th IEEE Power Electronics Specialists Conference 2006, PESC'06, June 18, 2006 - June 22, 2006*, Jeju, Republic of Korea, 2006.
- [57] J. Faiz and B. M. Ebrahimi, "Determination of number of broken rotor bars and static eccentricity degree in induction motor under mixed fault," *Electromagnetics*, vol. 28, pp. 433-449, 2008.
- [58] R. Zhang and X. Wang, "On-line broken-bar fault diagnosis system of induction motor," *Transactions of Tianjin University*, vol. 14, pp. 144-147, 2008.
- [59] A. Barbour and W. T. Thomson, "Finite element analysis and on-line current monitoring to diagnose airgap eccentricity in 3-phase induction motors," Cambridge, UK, 1997, pp. 150-154.

- [60] W. T. Thomson and A. Barbour, "On-line current monitoring and application of a finite element method to predict the level of static airgap eccentricity in three-phase induction motors," *IEEE Transactions on Energy Conversion*, vol. 13, pp. 347-355, 1998.
- [61] R. R. Schoen and T. G. Habetler, "Evaluation and implementation of a system to eliminate arbitrary load effects in current-based monitoring of induction machines," *IEEE Transactions on Industry Applications*, vol. 33, pp. 1571-1577, 1997.
- [62] J. F. Watson, N. C. Paterson, and D. G. Dorrell, "Use of finite element methods to improve techniques for the early detection of faults in 3-phase induction motors," *IEEE Transactions On Energy Conversion*, vol. 14, pp. 655-660, 1999.
- [63] A. Barbour and W. T. Thomson, "Finite element study of rotor slot designs with respect to current monitoring for detecting static airgap eccentricity in squirrel - cage induction motors," New Orleans, LA, USA, 1997, pp. 112-119.
- [64] P. C. Krause, O. Wasynczuk, and S. D. Sudhoff, *Analysis of electric machinery and drive system*, Second ed. NJ, USA: IEEE Press, 2002.
- [65] C. De Angelo, G. Bossio, S. Giaccone, G. O. Garcia, J. Solsona, and M. I. Valla, "Model based stator fault detection in induction motors," in *IECON 2006 - 32nd Annual Conference on IEEE Industrial Electronics, November 6, 2006 - November 10, 2006*, Paris, France, 2006, pp. 1095-1100.
- [66] S. Chen, "Induction machine broken rotor bar diagnostics using prony analysis," Electrical and Electronic Engineering, University of Adelaide, Adelaide, 2008.
- [67] C.-M. Ong, *Dynamic Simulation of Electric Machinery: Using MATLAB/Simulink*: Prentice Hall, 1998.
- [68] _____. (1995, 12 December 2010). "Coordinated" Motor Circuit Protection, A Guide to Understanding: Short-Circuit Protection Devices, Overload Protection Devices, and Coordinated Protection. Available: <http://literature.rockwellautomation.com/idc/groups/literature/documents/br/193-br001-en-p.pdf>
- [69] A. Boglietti, A. Cavagnino, and M. Lazzari, "Modelling of the closed rotor slot effects in the induction motor equivalent circuit," *2008 International Conference on Electrical Machines (ICEM'08)*, pp. 1-44, 2008 2008.
- [70] S. Williamson and M. C. Begg, "Calculation of the bar resistance and leakage reactance of cage rotors with closed slots," *IEE Proceedings B Electric Power Applications*, vol. 132, pp. 125-132, 1985.
- [71] A. von Jouanne and B. Banerjee, "Assessment of voltage unbalance," *IEEE Transactions on Power Delivery*, vol. 16, pp. 782-790, 2001.
- [72] M. C. Harke and R. D. Lorenz, "The Spatial Effect and Compensation of Current Sensor Differential Gains for Three-Phase Three-Wire Systems," *IEEE Transactions on Industry Applications*, vol. 44, pp. 1181-1189, 2008.
- [73] C. Younghoon, T. LaBella, and L. Jih-Sheng, "A Three-Phase Current Reconstruction Strategy With Online Current Offset Compensation Using a Single Current Sensor," *IEEE Transactions on Industrial Electronics*, vol. 59, pp. 2924-2933, 2012.
- [74] I. Won-Sang, H. Seon-Hwan, K. Jang-Mok, and C. Jeaho, "Analysis and compensation of current measurement errors in a doubly fed induction generator," in *Energy Conversion Congress and Exposition, 2009. IEEE ECCE 2009*, 2009, pp. 1713-1719.
- [75] J. Han-Su, H. Seon-Hwan, K. Jang-Mok, U. K. Cheul, and C. Cheol, "Diminution of Current-Measurement Error for Vector-Controlled AC Motor

- Drives," *IEEE Transactions on Industry Applications*, vol. 42, pp. 1249-1256, 2006.
- [76] M. C. Harke, J. M. Guerrero, M. W. Degner, F. Briz, and R. D. Lorenz, "Current Measurement Gain Tuning Using High-Frequency Signal Injection," *IEEE Transactions on Industry Applications*, vol. 44, pp. 1578-1586, 2008.
- [77] S. M. A. Cruz and A. J. M. Cardoso, "Multiple Reference Frames Theory: A New Method for the Diagnosis of Stator Faults in Three-Phase Induction Motors," *IEEE Transactions on Energy Conversion*, vol. 20, pp. 611-619, 2005.
- [78] Y. Jangho, L. Kwanghwan, L. Kwang-Woon, L. Sang Bin, and Y. Ji-Yoon, "Detection and Classification of Stator Turn Faults and High-Resistance Electrical Connections for Induction Machines," *IEEE Transactions on Industry Applications*, vol. 45, pp. 666-675, 2009.
- [79] R. M. Tallam, S. B. Lee, G. C. Stone, G. B. Kliman, J. Yoo, T. G. Habetler, and R. G. Harley, "A survey of methods for detection of stator-related faults in induction machines," *IEEE Transactions On Industry Applications* vol. 43, pp. 920-933, 2007.
- [80] Y. Jangho, C. Jintae, L. Sang Bin, and Y. Ji-Yoon, "Online Detection of High-Resistance Connections in the Incoming Electrical Circuit for Induction Motors," *IEEE Transactions on Industry Applications*, vol. 45, pp. 694-702, 2009.
- [81] J. T. Taylor, *The vibration ahandbook, A practical guide for solving rotating machinery problems*, First ed. Tampa Florida: Vibration Consultan Inc., 1994.
- [82] W. T. Thomson, "A review of on-line condition monitoring techniques for three phase squirrel induction motors – past, present and future," in *Proc. IEEE Int. Symp. Diagnostics Electrical Machines, Power Electronics Drives*, Gijon, Spain, 1999, pp. 3–18.
- [83] W. T. Thomson, and A. Barbour, "On-line current monitoring and application of a finite element method to predict the level of static airgap eccentricity in three-phase induction motors," *IEEE Transactions Energy Conversion*, vol. 13, pp. 347–354, 1998.
- [84] S. Nandi, H. A. Toliyat, and X. Li, "Condition monitoring and fault diagnosis of electrical motors—A review," *IEEE Transactions Energy Conversion*, vol. 20, pp. 719-729, December 2005 2005.
- [85] W. R. Finley, and M. M. Hodowanec, "Selection of copper vs aluminium rotors for inducton motors," in *47th Annual Petroleum and Chemical Industry Conference*, 2000, pp. 187 - 197.
- [86] Y. Han, and Y. H. Song, "Condition monitoring techniques for electrical equipment—A literature survey," *IEEE Transactions on Power Delivery*, vol. 18, pp. 4-13, 2003.
- [87] N. Ertugrul, *LabVIEW for Electric Circuits, Machines, Drives, and Laboratories*: Prentice Hall., 2002.

Appendix

A.1 Steady State Induction Motor Model

Several methods have been introduced in the field of induction motor modeling. The best known model for understanding the characteristics of an induction motor is the steady state T model or per-phase equivalent circuit. This model is useful to predict various steady state performance aspects: such as variation of currents, resistances, speeds, torques, and efficiencies. These parameters can provide beneficial information for further dynamic model development. In addition, the T model has been able to incorporate iron loss which cannot be done in conventional dq dynamic methods. This model is also widely employed by field analysts and motor designers. In this section, the steady state model will be presented, including the parameter analysis.

The ideal induction motor can be understood as a generalized transformer. The induction motor has two circuits: rotor side and stator, which can be illustrated as a transformer, shown in Figure A.1 below.

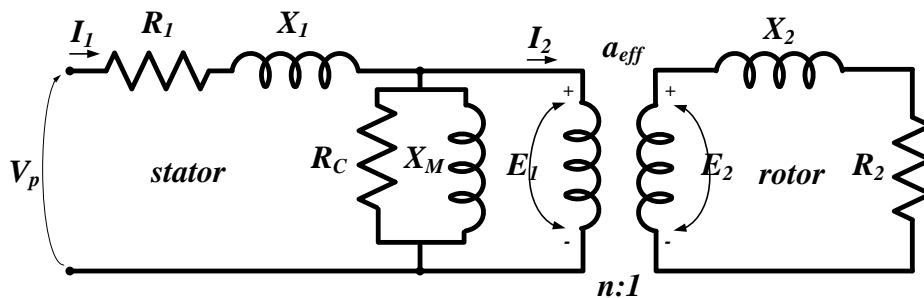


Figure A.1 Induction motor full equivalent circuit

As can be seen in Figure A.1, several important circuit parameters are illustrated. Shown in the figure for the stator side, the parameters of equivalent circuit are phase voltage (V_p), the phase current (I_1), resistance of the stator winding (R_1), reactance of the stator leakage (X_1), resistance of the core loss (R_c), and magnetizing reactance (X_m). For the rotor side, the parameters are rotor leakage reactance (X_2) and rotor resistance (R_2). The stator and rotor sides, which have specific turns ratio (a_{eff}), are separated by an air gap.

Similar to the electric transformer, it is not easy to apply the standard circuit analysis to the rotor side for an induction motor. In addition, measuring the parameter in the rotor sides, especially for the squirrel cage induction motor, can be difficult because of limited direct access to the rotor side. Therefore, one of the approaches to understand the rotor parameters of an induction motor is by referring the rotor voltage and rotor current to the stator.

Unlike the electric transformer, the real rotor side of an induction motor operates at a different frequency to the stator side [87]. The frequency of rotor refers to the frequency of the stator because the rotor is running at slip frequency, i.e. $f_{rotor}=sf$. This implies that the leakage reactance of the rotor (X_2) varies with the slip frequency changes, and the rotor resistance R_2 is constant. In this equivalent model, the rotor frequency is referred to the stator side. Therefore, the rotor frequency uses a constant frequency of the stator, or, in other words, constant rotor leakage reactance and variable effective of rotor resistance (R_2'/s).

Figure A.2 below shows the parameters of the rotor such as the rotor current referred to the stator side (I_2'), rotor leakage reactance referred to the stator (X_2'), and rotor resistance referred to the stator side (R_2'/s).

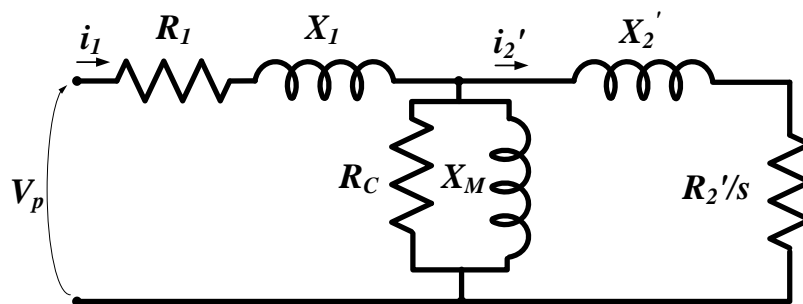


Figure A.2 Induction motor full equivalent circuit referred to stator frequency

Based on this equivalent circuit, the actual secondary parameters can be calculated. In this equivalent circuit, the rotor frequency is assumed constant, similar to the stator frequency. In addition, the rotor leakage reactance and the rotor resistance can also be assumed constant according to the slip. These referred values, such as R_2' , X_2' and I_2' , can be illustrated using actual value of R_2 , X_2 and I_2 respectively, using turn ratio between the stator and the rotor (n). In order to identify circuit parameters shown in Figure A.2, the three tests that will be discussed in the following sections can be carried out.

A.1.1 DC Test

Under a balanced winding circuit, the stator DC resistance is measured between two stator terminals, while the third terminal is open-circuited. The DC supply is applied to the circuit as illustrated in Figure A.3. The measurement per stator phase is then taken to two combinations terminals, where the average of the total three measurements is taken as the DC resistance (R_1). The final resistor measurement also considers the skin effect as given in Equation A.1.

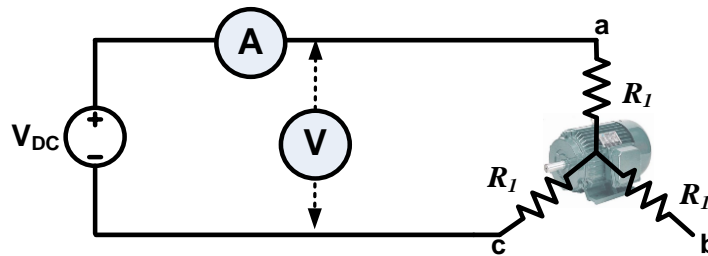


Figure A.3 The DC motor test set up

$$R_1 = 0.5 \frac{V_{DC}(1+0.05)}{I_{DC}} \quad (\text{A.1})$$

A.1.2 Block Rotor Test

The block rotor test is done by clamping the rotor, so the rotor is not allowed to turn, or slip = 1, and $R_2'/s = R_2$. The reduced voltage (V_{br}) is also applied to reach the rated current (I_{br}). Due to this reduced voltage, the magnetizing branch is considered insignificantly small and can be omitted. The equivalent circuit of this block rotor test is presented in Figure A.4.

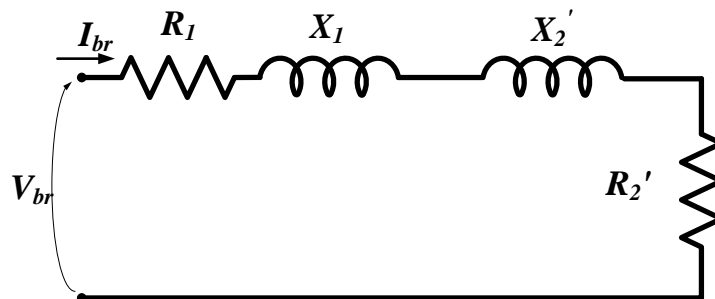


Figure A.4 Block rotor test equivalent circuit

Using this test, several parameters can be identified, such as X_1 , X_2' and R_2' . These quantities can be derived based on the measurement of V_{br} , I_{br} , and I_{br} .

A.1.3 No Load Test

For other required parameters, such as R_c and X_m , the no load test can be performed. In this test, the rated voltage is implemented to the stator of the motor, without any mechanical load. The motor runs close to synchronous speed, therefore the slip can be very small. The small slip causes a very big value of R_2'/s . This means that the rotor current can be ignored. Based on this assumption, the equivalent circuit in Figure A.2 can be modified into Figure A.5.

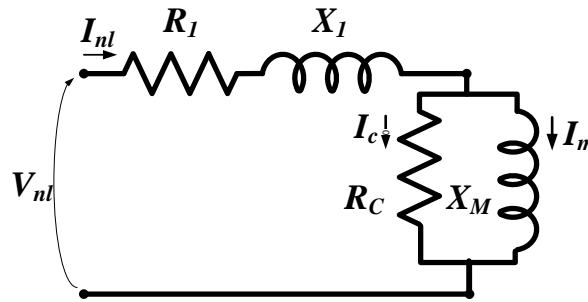


Figure A.5 No load test equivalent circuit

After completing the input parameters requirement for the full equivalent circuit, the next step is performing the standard circuit analysis of Figure A.2. The total impedance across the full equivalent circuit of Figure A.5 is presented by Equation A.2 below, where ($//$) is the parallel impedance calculation.

$$Z = R_1 + jX_1 + (R_c // jX_m) // (R_2'/s + jX_2') \quad (\text{A.2})$$

The R value of phase current input can be calculated from rms value. The phase voltage V_1 , and the magnitude of impedance $|Z_1|$ is given below.

$$I_1 = \frac{V_1}{|Z_1|} \quad (\text{A.3})$$

The input power can be calculated using the phase angle between the voltage and the stator current.

$$P_{in} = V_1 I_1 \cos \theta \quad (\text{A.4})$$

The rotor current can be obtained using Equation A.5 which also be utilized to obtain the shaft torque (T_m). The torque required by mechanical load which considers all three-phase motors can be presented by the Equation A.6.

$$\mathbf{I}_2 = n \frac{\mathbf{V}_1 - \mathbf{I}_1 (R_1 + jX_1)}{(R_2'/s + jX_2')} \quad (\text{A.5})$$

$$T_m = \frac{P_{AG}}{\omega_s} = \frac{3I_2'^2 R_2'}{s\omega_s} \quad (\text{A.6})$$

The notation ω_s is the angular synchronous speed and P_{AG} is the air gap power flowing from stator to rotor. The power output of the motor and the efficiency of the motor can be solved using the following equations. In these equations, the total power output considers power rotor loss, including losses from rotor copper, windage and friction.

$$P_{out} = P_m - P_{rotor_loses} \quad (\text{A.7})$$

$$P_{out} = T_m \omega_r - (P_{rotor_copper_loss} + P_{windage+friction}) \quad (\text{A.8})$$

where P_m is mechanical power output, and $\omega_r = \omega_s (1-s)$ is angular rotor speed.

The motor efficiency can be given as

$$\eta\% = \frac{P_{out}}{P_{in}} 100 \quad (\text{A.9})$$

$$\eta\% = \frac{\omega T_m - (P_{rotor_copper_loss} + P_{windage+friction})}{3V_1 I_1 \cos \theta} 100 \quad (\text{A.10})$$

For Torque:

$$\left. \begin{aligned} T_{mechanical/induced} = T_m &= \frac{60P_m}{2\pi n} = \frac{P_m}{\omega_r} = \frac{P_{ag}}{\omega_s} \\ T_{output/load} = T_o &= \frac{60P_o}{2\pi n} = \frac{P_{out}}{\omega_r} \end{aligned} \right\} \quad (\text{A.11})$$

$$\left. \begin{aligned} T_{starting} &= \frac{3(V_{supply-p})^2}{\omega_s} \frac{R_2}{[(R_1 + R_2)^2 + (X_1 + X_2)^2]} \\ T_{max} &= \frac{3(V_{supply-p})^2}{2\omega_s} \frac{1}{[R_1 + \sqrt{R_1^2 + (X_1 + X_2)^2}]} \end{aligned} \right\} \quad (\text{A.12})$$

$$\text{Maximum Slip: } S_{\max} = \frac{R_2}{\sqrt{R_1^2 + (X_1 + X_2)^2}} \quad (\text{A.13})$$

A.2 Dynamic Motor Model's Parameters

A.2.1 The Motor Model Inductances

To calculate the inductances of induction motor in the Chapter 3 the equations are shown in the following discussion. The mutual-inductances between two windings can be presented as

$$L_{xy} = \mu_0 N_x N_y \left(\frac{rl}{g} \right) \frac{\pi}{4} \cos \alpha = N_x N_y A_g \cos \alpha \quad (\text{A.14})$$

where, N_x and N_y are the effective number of turns of x and y windings, and α is the angle displacement between the magnetic angles of two windings. The variable of A_g can be formulated as the machine constant, which depends on airgap length g , the axial length l of the machine, radius r , and the permeability of free space μ_0 .

In the case of self-inductance, the stator phase as , the total self-inductance consists of the magnetizing inductances L_m and leakage inductances L_{ls} as given in Equation A.15. Because of self-inductance, the angle displacement can be set $\alpha = 0$. Therefore the L_m and L_{ls} of the symmetrical stator phase ($N_x = N_y = N_s$) which consider the other two stator phase winding, is defined in Equation A.16 and A.17 respectively. Therefore, the total self-inductance can be redefined as given in Equation A.18

$$L_{as} = L_m + L_{ls} \quad (\text{A.15})$$

$$L_m = \frac{3}{2} N_s^2 A_g \quad \text{or} \quad A_g = \frac{2}{3} \frac{L_m}{N_s^2} \quad (\text{A.16})$$

$$L_{ls} = N_s^2 A_l \quad \text{or} \quad A_l = \frac{L_{ls}}{N_s^2} \quad (\text{A.17})$$

$$L_{as} = L_{mas} + L_{las} = N_a^2 A_g + N_a^2 A_l = \frac{N_a^2}{N_s^2} \left(\frac{2}{3} L_m + L_{ls} \right) = N_a^2 L_{mfs} \quad (\text{A.18})$$

The following equations summarize the previous matrix inductances of the motor models. It is assumed that each of the stator phases as , bs and cs has a number

of turns, N_a , N_b and N_c respectively. In addition, because the number of turns of the rotor in each phase is assumed similar, the rotor winding in each phase ar , br and cr can be presented by $N_{ar} = N_{br} = N_{cr} = N_r$. The stator self-inductances can be given as

$$L_{asas} = \frac{N_a^2}{N_s^2} \left(L_{ls} + \frac{2}{3} L_m \right), \quad L_{bsbs} = \frac{N_b^2}{N_s^2} \left(L_{ls} + \frac{2}{3} L_m \right), \quad L_{cscs} = \frac{N_c^2}{N_s^2} \left(L_{ls} + \frac{2}{3} L_m \right). \quad (\text{A.19})$$

In addition, the stator mutual-inductances are derived from Equation A.14 by setting the $\alpha = 2\pi/3$ which are given below.

$$L_{asbs} = L_{bsas} = \left(-\frac{1}{2} N_a N_b \right) \left(\frac{2}{3} \frac{L_m}{N_s^2} \right) = -\frac{1}{3} \frac{N_a N_b}{N_s^2} L_m, \quad (\text{A.20})$$

$$L_{ascs} = L_{csas} = -\frac{1}{3} \frac{N_a N_c}{N_s^2} L_m, \quad (\text{A.21})$$

$$L_{bscs} = L_{csbs} = -\frac{1}{3} \frac{N_b N_c}{N_s^2} L_m. \quad (\text{A.22})$$

Because the rotor is assumed under the symmetrical winding, the rotor self and mutual-inductances can be given as

$$L_{arar} = L_{brbr} = L_{cr cr} = L_r \frac{2}{3} \frac{N_r^2}{N_s^2} L_m \quad (\text{A.23})$$

$$L_{arbr} = L_{arcr} = L_{br cr} = L_{brar} = L_{crar} = L_{crbr} = -\left(\frac{1}{2} \right) \left(\frac{2}{3} \frac{N_r^2}{N_s^2} L_m \right) \quad (\text{A.24})$$

In the case of rotor-stator mutual-inductances, the rotor phase angle is displaced from the stator by the variable quantity of electrical angle θ_r . The sine cosine variables of rotor to stator mutual-inductance \mathbf{L}_{abc}^{sr} have been presented previously. Hence, the peak mutual-inductances are presented in the following equations

$$\left. \begin{aligned} L_{asar} = L_{asbr} = L_{as cr} &= \frac{2}{3} \frac{N_a N_r}{N_s^2} L_m, L_{bsar} = L_{bsbr} = L_{bs cr} = \frac{2}{3} \frac{N_b N_r}{N_s^2} L_m, \\ L_{csar} = L_{csbr} = L_{cs cr} &= \frac{2}{3} \frac{N_c N_r}{N_s^2} L_m \end{aligned} \right\} \quad (\text{A.25})$$

A.2.2 The Inductances of the Stator Fault Model

Under the stator faults model, the stator self-inductances consist of shorted turns (N_{sh}) and unshorted turns (N_{us}) parts. Therefore, the self-inductances of the phases as , bs and cs in Equation A.18 can be modified to include these parts as given

$$L_{asas} = \frac{N_{us}^2}{N_s^2} \left(L_{ls} + \frac{2}{3} L_m \right) + 2N_{us} N_{sh} \left(\frac{2}{3} \frac{L_m}{N_s^2} \right) + \frac{N_{sh}^2}{N_s^2} \left(L_{ls} + \frac{2}{3} L_m \right) \quad (\text{A.26})$$

$$L_{bsbs} = L_{cscs} = \frac{N_s^2}{N_s^2} \left(L_{ls} + \frac{2}{3} L_m \right) \quad (\text{A.27})$$

In addition, the stator mutual-inductances of Equation A.20 can be written under faults condition

$$L_{asbs} = L_{bsas} = -\frac{1}{3} \frac{N_a N_s}{N_s^2} L_m = -\frac{1}{3} \frac{N_{us}}{N_s} L_m - \frac{N_{sh}}{N_s} L_m \quad (\text{A.28})$$

$$L_{ascs} = L_{csas} = L_{bsas} \quad (\text{A.29})$$

$$L_{bscs} = L_{csbs} = -\frac{1}{3} L_m \quad (\text{A.30})$$

The stator to rotor mutual-inductances also need to be modified. The Equation A.24 under stator shorted turn faults conditions can be rewritten

$$\left. \begin{aligned} L_{asar} = L_{asbr} = L_{ascr} &= \frac{2}{3} \frac{N_a N_r}{N_s^2} L_m = \frac{2}{3} \frac{N_{us} N_r}{N_s^2} L_m + \frac{2}{3} \frac{N_{sh} N_r}{N_s^2} L_m \\ L_{bsar} = L_{bsbr} = L_{bscr} &= L_{csar} = L_{csbr} = L_{cscr} = \frac{2}{3} \frac{N_s N_r}{N_s^2} L_m \end{aligned} \right\} \quad (\text{A.31})$$

A.2.3 Resistance of The Rotor Asymmetry Model

The rotor resistance after transformations $qd0$ is obtained by transformation

$$\mathbf{r}_{qd0}^r = \mathbf{T}_{qd0}(-\theta_r) \mathbf{r}_{abc}^r \mathbf{T}_{qd0}(-\theta_r)^{-1} \quad \text{where the matrix elements are}$$

$$\begin{aligned}
r_{11}^r &= \frac{2}{3} \left[r_{ar} \cos^2(\theta_r) + r_{br} \cos^2\left(\theta_r + \frac{2\pi}{3}\right) + r_{cr} \cos^2\left(\theta_r - \frac{2\pi}{3}\right) \right] \\
r_{12}^r &= -\frac{1}{3} \left[r_{ar} \sin(2\theta_r) + r_{br} \sin\left(2\left(\theta_r + \frac{2\pi}{3}\right)\right) + r_{cr} \sin\left(2\left(\theta_r - \frac{2\pi}{3}\right)\right) \right] \\
r_{13}^r &= \frac{2}{3} \left[r_{ar} \cos \theta_r + r_{br} \cos\left(\theta_r + \frac{2\pi}{3}\right) + r_{cr} \cos\left(\theta_r - \frac{2\pi}{3}\right) \right] \\
r_{21}^r &= r_{12}^r \\
r_{22}^r &= \frac{2}{3} \left[r_{ar} \sin^2(\theta_r) + r_{br} \sin^2\left(\theta_r + \frac{2\pi}{3}\right) + r_{cr} \sin^2\left(\theta_r - \frac{2\pi}{3}\right) \right] \\
r_{23}^r &= \frac{2}{3} \left[r_{ar} \sin \theta_r + r_{br} \sin\left(\theta_r + \frac{2\pi}{3}\right) + r_{cr} \sin\left(\theta_r - \frac{2\pi}{3}\right) \right] \\
r_{31}^r &= r_{13}^r \\
r_{32}^r &= \frac{1}{2} r_{23}^r \\
r_{33}^r &= \frac{1}{3} (r_{ar} + r_{br} + r_{cr})
\end{aligned} \tag{A.31}$$

When $r_{ar} = r_{br} = r_{cr} = r_r$ the elements of $r_{11} = r_{22} = r_{33} = r_r$ and other elements can be signed zero.

List of Publications

Bakhri, S.; Ertugrul, N.; Soong, W.L.; Arkan, M., "Investigation of negative sequence components for stator shorted turn detection in induction motors," Universities Power Engineering Conference (AUPEC), 2010 20th Australasian, Christchurch, New Zealand, 5-8 Dec. 2010.

Bakhri, S.; Ertugrul, N.; Soong, W. L., "Practical issues on negative sequence current monitoring for condition monitoring in induction motors," Universities Power Engineering Conference (AUPEC), 2012 22nd Australasian, Bali, Indonesia, 26-29 Sept. 2012.

Bakhri, S.; Ertugrul, N.; Soong, W. L., "Negative sequence current compensation for stator shorted turn detection in induction motors," IECON 2012 - 38th Annual Conference on IEEE Industrial Electronics Society ,Montreal, Canada, pp.1921,1926, 25-28 Oct. 2012.

Bakhri, S.; Ertugrul, N.; Soong, W. L., "Detailed Investigation of Negative Sequence Current Compensation for Stator Shorted Turn Detection Technique in Induction Motors" *IEEE Transactions on Energy Conversion*, 2013 (pending publications)